

MEASUREMENT OF UNFOLDED DIFFERENTIAL
CROSS-SECTIONS OF $ZZ(4\ell)$ PRODUCTION IN
ASSOCIATION WITH TWO JETS AT $\sqrt{s} = 13$ TEV WITH THE
ATLAS DETECTOR AND THERMAL CHARACTERISATION
OF ITK PIXEL OUTER END-CAP LOCAL SUPPORTS FOR THE
PHASE-II UPGRADE

Matteo D'Uffizi



A thesis submitted to
The University of Manchester
for the degree of Doctor of Philosophy
in the Faculty of Science and Engineering

School of Natural Sciences
Department of Physics and Astronomy

2023

Blank Page

Contents

List of figures	7
List of tables	13
List of acronyms	15
Abstract	21
Declaration	23
Copyright	24
Acknowledgements	25
Preface	27
1. Introduction	29
2. Theory	33
2.1. Formalism	33
2.2. The Standard Model	36
2.2.1. Quantum Electrodynamics	38
2.2.2. Quantum Chromodynamics	40
2.2.3. Electroweak interactions and unification	42
2.2.4. Electroweak symmetry breaking	45
2.2.5. The SM Lagrangian	47
2.2.6. SM limitations and beyond	48
2.3. Physics of Hadron Colliders	50
2.3.1. Parton Distribution Functions	51
2.3.2. Matrix elements and cross-sections	51

2.4. Physics modelling and event simulation	54
2.4.1. Parton shower	56
2.4.2. Hadronisation	57
2.4.3. Matching and merging	58
2.4.4. Monte Carlo event generators	59
2.5. Jet reconstruction	61
3. The ATLAS experiment	63
3.1. The Large Hadron Collider	63
3.2. The ATLAS detector	69
3.2.1. Coordinate system	70
3.2.2. Inner Detector	71
3.2.3. Electromagnetic and Hadronic Calorimeters	74
3.2.4. Muon spectrometer	78
3.2.5. Trigger and Data Acquisition system	80
3.2.6. Luminosity detector	81
3.3. Object reconstruction in ATLAS	83
3.3.1. Tracks and vertices	83
3.3.2. Electrons and photons	85
3.3.3. Muons	87
3.3.4. Jets	90
3.3.5. Taus	93
3.3.6. Missing transverse momentum	94
3.4. Simulation of the ATLAS detector	95
4. Thermal characterisation of ITk Pixel Outer Endcaps local supports	97
4.1. ITk Pixel upgrade	98
4.2. Local supports and thermal requirements	99
4.3. Thermal characterisation measurement	102
4.3.1. Experimental set-up and measurement procedure	103
4.3.1.1. Experimental setup	103
4.3.1.2. Calibration	104
4.3.1.3. Reference system	105
4.3.2. Analysis framework	105
4.3.2.1. Shape recognition	106
4.3.2.2. Timing measurement	107
4.3.2.3. Temperature profiles and fitting	109

4.3.2.4. Evaluation of the results and identification of defects	109
4.4. Measurements with prototypes	111
4.4.1. Prototype L3.5	113
4.4.2. Prototype L3.4	116
4.4.3. Prototype L2.1	118
4.4.4. Comparison with TFM measurements	121
4.5. Towards production of the local supports	124
5. Differential cross-section of $ZZ + jj$ production at $\sqrt{s} = 13$ TeV	127
5.1. Introduction	127
5.2. Data and MC simulation	130
5.3. Analysis definition and event selection	135
5.3.1. Object reconstruction and identification	135
5.3.2. Event selection	137
5.3.3. Signal regions and measured observables	140
5.4. Measured distributions	143
5.5. Backgrounds	144
5.6. Unfolding	151
5.6.1. Fiducial phase space	154
5.6.2. Iterative Bayesian unfolding	155
5.6.3. Regularisation of the unfolding procedure	158
5.6.4. Unfolding validation	164
5.7. Bootstrap and statistical correlation	166
5.8. Systematic uncertainties	167
5.8.1. Theoretical uncertainties	169
5.8.2. Experimental systematics	172
5.8.3. Unfolding systematics	174
5.8.4. Breakdown of the uncertainties	175
5.9. Unfolded differential cross-sections	178
5.10. EFT interpretation	179
6. Conclusions	191
A. Appendix	195
A.1. Additional plots of the $ZZjj$ cross-section measurement	195

Blank Page

List of figures

2.1. Standard Model production cross-sections measured with the ATLAS experiment in proton-proton collisions at a varying centre of mass energy.	49
2.2. The CT14 parton distribution functions at $Q = 2 \text{ GeV}$	52
2.3. Drawing of a simulated hadron-hadron collision.	55
3.1. Schematic of the accelerator complex at CERN.	64
3.2. Cumulative of the luminosity delivered by the LHC in Run2.	68
3.3. ATLAS Run 2 pile-up.	68
3.4. Schematics of the reference system used in ATLAS.	71
3.5. 3D model of the cross section of the Inner Detector barrel region.	72
3.6. Design of a quadrant of the Inner Detector.	72
3.7. Layout of the ATLAS calorimeter system.	75
3.8. Drawings of an electromagnetic LAr barrel and a Tile module.	77
3.9. Transversal and longitudinal cross-sections of the MS.	80
4.1. Design of the ITk detector.	99
4.2. Exploded view of a single ITk Pixel OEC.	100
4.3. Exploded view of a ITk Pixel OEC local support and schematic of the loaded configuration with modules.	101

4.4. Longitudinal and transverse cross-sections of a HR with a defect in the glue layer.	101
4.5. Experimental setup in the laboratory at the University of Manchester.	104
4.6. Reference system used in the thermal characterisation measurement.	105
4.7. Steps of the shape recognition algorithm applied to a HR prototype.	107
4.8. Standard deviation of the temperature on the HR surface as a function of the recording time.	108
4.9. Temperature profiles extraction and fit.	110
4.10. Distribution of T_{pipe} as a function of the angle for the left view of a HR prototype.	111
4.11. Offset subtraction procedure.	112
4.12. Prototype L3.5.	114
4.13. T_{pipe} distribution for prototype L3.5.	115
4.14. Residual temperature near the peak region observed in Side A of prototype L3.5.	116
4.15. Prototype L3.4.	117
4.16. Possible defect observed in Prototype L3.4 with the thermal characterisation measurement.	117
4.17. T_{pipe} distribution for prototype L3.4.	118
4.18. Residual temperature near the peak region observed in Side A of prototype L3.4.	119
4.19. Residual temperature near the peak region observed in Side B of prototype L3.4.	119
4.20. Schematic of prototype L2.1.	120
4.21. T_{pipe} distribution for prototype L2.1.	120
4.22. Residual temperature of the peaks observed in prototype L2.1. . . .	121
4.23. TFM measurement experimental setup.	122

4.24. Average TFM measured with prototypes L3.4 and L3.5 as a function of the number of cumulative thermal and pressure cycles.	123
4.25. Average TFM measured with prototype L2.1 as a function of the number of cumulative thermal and pressure cycles.	124
5.1. Typical diagrams for the EW production of $ZZjj$	129
5.2. Typical diagrams for the strong production of $ZZjj$	130
5.3. JVT (fJVT) selection efficiency and purity.	140
5.4. Centrality threshold optimisation.	142
5.5. m_{jj} measured distributions in the VBS-Enhanced and VBS-Suppressed regions.	145
5.6. $m_{4\ell}$ measured distributions in the VBS-Enhanced and VBS-Suppressed regions.	146
5.7. $p_{T,4\ell}$ measured distributions in the VBS-Enhanced and VBS-Suppressed regions.	147
5.8. $\Delta\phi_{jj}$ measured distributions in the VBS-Enhanced and VBS-Suppressed regions.	148
5.9. $\cos\theta_{12}^*$ measured distributions in the VBS-Enhanced and VBS-Suppressed regions.	149
5.10. $S_{T,4\ell jj}$ measured distributions in the VBS-Enhanced and VBS-Suppressed regions.	150
5.11. Electron fake efficiency in the combined Z+jets and $t\bar{t}$ CR.	151
5.12. Diagram of the unfolding procedure.	152
5.13. Migration matrices for m_{jj} and $m_{4\ell}$	159
5.14. Reconstruction efficiency, fiducial fraction, purity and stability for m_{jj} and $m_{4\ell}$	160
5.15. Data-driven closure test for m_{jj} in the VBS-Enhanced region.	161

5.16. MC-based estimation of the unfolding bias in the first bin of the m_{jj} distribution in the VBS-Enhanced region.	163
5.17. Statistical uncertainty for different numbers of iterations in the unfolding procedure.	163
5.18. Fraction of non-fiducial events in the quark-initiated strong $4\ell jj$ production.	165
5.19. Selection efficiency and fraction of non-fiducial events when including an upper cut on the p_T balance of the event.	165
5.20. Unfolding injection test.	166
5.21. Correlation matrix for all the measured observables in the VBS-Enhanced region after unfolding.	167
5.22. Correlation matrices for all the measured observables in the VBS-Suppressed region after unfolding.	168
5.23. QCD scale systematic uncertainty for the strong $qq \rightarrow 4\ell$ sample.	171
5.24. Combined PDF and α_S systematic uncertainty for the strong $qq \rightarrow 4\ell$ sample.	171
5.25. JES and JER systematic uncertainties.	174
5.26. Generator choice uncertainty associated with the modelling of the quark-initiated strong $4\ell jj$ production.	175
5.27. Breakdown of the unfolded-level uncertainties as a function of m_{jj} in the signal regions.	176
5.28. Breakdown of the unfolded-level uncertainties as a function of $m_{4\ell}$ in the signal regions.	176
5.29. Unfolded differential cross-sections in the VBS-Suppressed region.	186
5.30. Unfolded differential cross-sections in the VBS-Enhanced region.	188
A.1. Δy_{jj} measured distributions the VBS-Enhanced and VBS-Suppressed regions.	196

A.2. $p_{T,jj}$ measured distributions the VBS-Enhanced and VBS-Suppressed regions.	196
A.3. $\cos \theta_{34}^*$ measured distributions the VBS-Enhanced and VBS-Suppressed regions.	197
A.4. $p_{T,4\ell jj}$ measured distributions the VBS-Enhanced and VBS-Suppressed regions.	197
A.5. Migration matrices for $p_{T,4\ell}$	198
A.6. Migration matrices for $\Delta\phi_{jj}$	198
A.7. Migration matrices for Δy_{jj}	198
A.8. Migration matrices for $p_{T,jj}$	199
A.9. Migration matrices for $\cos \theta_{12}^*$	199
A.10. Migration matrices for $\cos \theta_{34}^*$	199
A.11. Migration matrices for $p_{T,4\ell jj}$	200
A.12. Migration matrices for $S_{T,4\ell jj}$	200
A.13. Reconstruction efficiency, fiducial fraction, purity and stability for $p_{T,4\ell}$	200
A.14. Reconstruction efficiency, fiducial fraction, purity and stability for $\Delta\phi_{jj}$	201
A.15. Reconstruction efficiency, fiducial fraction, purity and stability for Δy_{jj}	201
A.16. Reconstruction efficiency, fiducial fraction, purity and stability for $p_{T,jj}$	201
A.17. Reconstruction efficiency, fiducial fraction, purity and stability for $\cos \theta_{12}^*$	202
A.18. Reconstruction efficiency, fiducial fraction, purity and stability for $\cos \theta_{34}^*$	202
A.19. Reconstruction efficiency, fiducial fraction, purity and stability for $p_{T,4\ell jj}$	202

A.20.Reconstruction efficiency, fiducial fraction, purity and stability for $S_{T,4\ell jj}$	203
A.21.Breakdown of the unfolded-level uncertainties as a function of $p_{T,4\ell}$ in the signal regions.	203
A.22.Breakdown of the unfolded-level uncertainties as a function of $\Delta\phi_{jj}$ in the signal regions.	204
A.23.Breakdown of the unfolded-level uncertainties as a function of Δy_{jj} in the signal regions.	204
A.24.Breakdown of the unfolded-level uncertainties as a function of $p_{T,jj}$ in the signal regions.	205
A.25.Breakdown of the unfolded-level uncertainties as a function of $\cos\theta_{12}^*$ in the signal regions.	205
A.26.Breakdown of the unfolded-level uncertainties as a function of $\cos\theta_{34}^*$ in the signal regions.	206
A.27.Breakdown of the unfolded-level uncertainties as a function of $p_{T,4\ell jj}$ in the signal regions.	206
A.28.Breakdown of the unfolded-level uncertainties as a function of $S_{T,4\ell jj}$ in the signal regions.	207

List of tables

2.1. Summary of the force-mediator gauge bosons in the SM.	37
2.2. Summary of the different fermions present in the SM.	38
3.1. ATLAS electromagnetic and hadronic calorimeter design resolution.	75
4.1. TFM design limits for each layer of the ITk Pixel OEC.	102
4.2. Program of measurements carried-out with prototype L3.5.	114
5.1. List of the year-dependant electron, muon and combined unprescaled triggers used in the analysis.	131
5.2. List of MC samples used in the analysis.	132
5.3. Baseline and signal requirements for the selection of electron muons and jets.	136
5.4. Outline of the event selection requirements for the lepton quadru- plet and dijet system.	138
5.5. Event selection cut-flow.	140
5.6. Binning of the observables' distributions in the VBS-Enhanced and VBS-Suppressed regions.	144
5.7. Event yield for the measured data and predictions in the VBS- Enhanced and VBS-Suppressed regions.	145
5.8. Breakdown of the systematic uncertainties for m_{jj} in the VBS-Suppressed region at unfolded level after 2 iterations.	177

5.9. Breakdown of the systematic uncertainties for m_{jj} in the VBS-Enhanced region at unfolded level after 2 iterations.	177
5.10. Expected and observed 95% confidence interval for several Wilson coefficients of dimension-6 EFT operators.	184
5.11. Expected and observed 95% confidence interval for several Wilson coefficients of dimension-8 EFT operators.	189

Acronyms

ALICE A Large Ion Collider Experiment. 65

ATLAS A Toroidal LHC ApparatuS. 7, 13, 29–31, 47–49, 61, 63, 65–71, 73–75, 78, 80–83, 87, 92–95, 97–99, 127–130, 134, 135, 137, 154, 171, 172, 179, 183, 192

BCM Beam Conditions Monitor. 81–83

BSM Beyond the Standard Model. 50, 94, 129, 164, 166, 179, 182, 183

CERN Conseil européen pour la recherche nucléaire. 7, 29, 63, 64

CKM Cabibbo-Kobayashi-Maskawa. 43, 50

CMS Compact Muon Solenoid. 29, 47, 65, 66, 97, 129, 179, 183

CR control region. 9, 148, 149, 151, 164, 172

CSC cathode-strip chamber. 78, 80

CTP Central Trigger Processor. 81

DAQ Data Acquisition. 81

DFOC different-flavour opposite-charge. 148

EFT Effective Field Theory. 14, 31, 127, 129, 143, 164–166, 179–184, 189, 193

EMEC electromagnetic end-caps. 76

EW Electroweak. 9, 30, 44, 45, 47, 48, 61, 127–129, 132–134, 137, 139–150, 163, 175, 177–179, 181, 186, 188, 192, 193, 196, 197

EWSB Electroweak Symmetry Breaking. 30

- FASER** ForwArd Search ExpeRiment. 66
- FCal** Forward calorimeter. 77
- fJVT** forward-JVT. 9, 93, 136–140, 164, 173
- FSR** Final State Radiation. 55, 57, 59
- GSC** global sequential calibration. 91
- GSF** Gaussian Sum Filter. 86
- GUT** Global Unified Theory. 50
- HEC** hadronic end-caps. 76, 77
- HL-LHC** High Luminosity LHC. 97, 194
- HLT** High Level Trigger. 81
- HR** Half-Ring. 8, 99–115, 117, 118, 121–125
- IBL** Insertable B-Layer. 72, 73, 99
- ID** Inner Detector. 7, 69, 71–73, 76, 78, 84–90, 93, 94, 97, 98, 136, 137, 139, 155, 164
- IR** Infra-red. 102, 103, 113, 114, 116–118, 122
- IS** Inner System. 98
- ISR** Initial State Radiation. 55, 57, 59
- ITk** Inner Tracker. 7, 13, 30, 31, 97–102, 124, 191
- JER** Jet Energy Resolution. 10, 91, 172–174, 193
- JES** Jet Energy Scale. 10, 91, 92, 172, 174, 193
- JVF** Jet Vertex Fraction. 92
- JVT** Jet Vertex Tagger. 9, 92, 93, 136–140, 164, 173
- LAr** liquid Argon. 7, 74, 76, 77
- LB** luminosity block. 81

- LEP Large Electron-Positron. 64
- LHC Large Hadron Collider. 7, 30, 31, 50, 51, 54, 58, 61, 63–68, 70, 71, 83, 90, 93, 97, 127, 194
- LHCb Large Hadron Collider beauty. 65, 66
- LHCf Large Hadron Collider forward. 66
- LO Leading Order. 53, 54, 58–60, 132–134, 178, 180, 193
- LUCID LUminosity measurement using Cherenkov Integrating Detector. 81–83
- MC Monte Carlo. 13, 54, 56–61, 127, 132, 134, 135, 139, 140, 150, 152, 157, 159, 161–166, 168, 170, 174, 175, 178, 192, 193
- MDT monitored drift tube. 78–80
- MoEDAL the Monopole and Exotics Detector at the LHC. 66
- MPI multi-parton interaction. 56, 59, 60, 133
- MS Muon Spectrometer. 7, 69, 78, 80, 83, 87–89, 91, 136, 155
- NLO Next-to-Leading Order. 53, 54, 58–61, 132–135, 178, 193
- NNLO Next-to-Next-to-Leading Order. 53, 133, 135
- OB Outer Barrel. 98
- OEC Outer End-cap. 7, 13, 98–102, 124
- PDF parton distribution function. 10, 51–53, 57, 132, 133, 170, 171, 178, 180, 181
- PMT photomultiplier tube. 82
- PRW pile-up re-weighting. 130, 177
- PS Proton Synchrotron. 64
- PSB Proton Synchrotron Booster. 64
- PV Primary Vertex. 85, 87, 89, 92, 94, 135
- QA Quality Assurance. 98, 102, 111–113, 124

- QC Quality Control. 30, 98, 111, 112, 123, 124
- QCD Quantum Chromodynamics. 10, 40–42, 44, 50, 52, 55, 58, 60, 128, 129, 132–135, 169, 170, 178–181
- QED Quantum Electrodynamics. 38, 40, 41, 44, 55, 154
- QFT Quantum Field Theory. 33, 38, 40, 42, 46
- RANSAC RANdom SAmple Consensus. 106, 111, 115
- RF Radio Frequency. 65
- RoI Region of Interest. 81, 106–108
- RPC resistive plate chamber. 79, 80
- SCT SemiConductor tracker. 71–73, 83, 84
- SFOC same-flavour opposite-charge. 137, 138, 148, 192
- SM Standard Model. 13, 29, 31, 33, 37, 38, 40, 43–45, 47–50, 61, 94, 129, 144, 164, 179–181, 183, 184, 189
- SND@LHC Scattering and Neutrino Detector at the LHC. 66
- SPS Super Proton Synchrotron. 29, 64
- SR signal region. 140, 142, 143, 148–150, 157, 158, 164, 170, 174, 175, 178, 193
- TFM Thermal Figure of Merit. 9, 102, 103, 113, 114, 117, 118, 120–125, 192
- TGC thin-gap chamber. 79, 80
- TOTEM TOTal cross section, Elastic scattering and diffraction dissociation Measurement at the LHC. 66
- TRT Transition Radiation Tracker. 71–73, 83, 84
- TTVA track-to-vertex association. 89, 136, 173
- VBS Vector Boson Scattering. 9–11, 13, 14, 30, 128, 131, 138–150, 157–168, 171, 174–179, 182, 184, 186, 188, 189, 192, 193, 195–207
- vdM van der Meer. 83

VR validation region. 150

Blank Page

Abstract

The measurement of differential cross-sections of the production of four charged leptons in association with two jets, using 140 fb^{-1} of high-energy collision data recorded by the ATLAS experiment at $\sqrt{s} = 13 \text{ TeV}$, is presented in this thesis. The cross-sections are measured in two phase space regions where the strong and electroweak production mechanisms are respectively enhanced. The results are unfolded to remove detector-induced effects and extrapolate the cross-sections at a fiducial-level. These are compared with theory predictions obtained from state-of-the-art Monte Carlo simulations and are found to be in reasonable agreement with the Standard Model expectations. An Effective Field Theory interpretation of the results is given, searching for anomalous weak boson self-couplings provided by several dimension-6 and dimension-8 operators.

The ITk is a new silicon tracker which will substitute the current ATLAS Inner Detector for the High-Luminosity phase of the Large Hadron Collider. Before building the detector, it is essential to assess that each local support has good thermal performance to avoid failures during operation. A non-destructive technique to evaluate the thermal performance of thermo-active structures was developed at the University of Manchester. Its application for the quality control of the ATLAS ITk pixel outer end-caps local supports is illustrated. The technique's capability to spot potential structural defects, and identify poorly performing local supports, has been tested with measurements on several prototypes. The results are presented in this thesis and show the technique's suitability for the quality control of the local supports during serial production.

Blank Page

Declaration

This work represents the combined efforts of the author and his colleagues in the ATLAS collaboration. Some of the content has been published elsewhere and/or presented to several audiences. No portion of the work referred to in the thesis, except in the few cases where explicit reference is made to the work of others, has been submitted in support of an application for another degree or qualification of this or any other university or other institute of learning.

Matteo D'Uffizi

Copyright

1. The author of this thesis (including any appendices and/or schedules to this thesis) owns certain copyright or related rights in it (the "Copyright") and s/he has given the University of Manchester certain rights to use such Copyright, including for administrative purposes.
2. Copies of this thesis, either in full or in extracts and whether in hard or electronic copy, may be made **only** in accordance with the Copyright, Designs and Patents Act 1988 (as amended) and regulations issued under it or, where appropriate, in accordance with licensing agreements which the University has from time to time. This page must form part of any such copies made.
3. The ownership of certain Copyright, patents, designs, trademarks and other intellectual property (the "Intellectual Property") and any reproductions of copyright works in the thesis, for example graphs and tables ("Reproductions"), which may be described in this thesis, may not be owned by the author and may be owned by third parties. Such Intellectual Property and Reproductions cannot and must not be made available for use without the prior written permission of the owner(s) of the relevant Intellectual Property and/or Reproductions.
4. Further information on the conditions under which disclosure, publication and commercialisation of this thesis, the Copyright and any Intellectual Property and/or Reproductions described in it may take place is available in the University IP Policy (see here¹), in any relevant Thesis restriction declarations deposited in the University Library, the University Library's regulations (see here²) and in the University's policy on Presentation of Theses.

¹<http://documents.manchester.ac.uk/DocuInfo.aspx?DocID=24420>

²<http://www.library.manchester.ac.uk/about/regulations/>

Acknowledgements

The results presented in this thesis would not have been possible without the contribution of many people with whom I had the pleasure to work throughout my Ph.D. course.

I must thank Andy for allowing me to pursue this Ph.D. at the University of Manchester and supervising my work over its entire duration. I enjoyed collaborating with you and learned a lot from our physics discussions. If I'm a better physicist today, I largely owe it to you. Thank you also for supporting me personally and professionally when I needed it.

Secondly, I would like to thank Francisca for introducing me to the world of detector R&D and for guiding me through my ATLAS qualification task (and beyond). Doing laboratory measurements with you was a pleasant and exciting alternative to data analysis, which has given me many practical skills. You were always present if I needed help or moral support, and I must thank you for that.

To the ZZjj analysis team. Without you, I would not have had a measurement to present today. Special thanks to Prajita for working with me from the start to the end of the analysis and for sharing the burden of code debugging and note writing. To Bing Li for coordinating our efforts. To Zach and Zuchen, I enjoyed working with you, even if only for a shorter time. And to all the others for the valuable advices and discussions.

I would also like to thank everyone involved in the ITk project with whom I collaborated, either at the University of Manchester or elsewhere. Thanks to Claudia for being the technical supervisor of my qualification task. To Alex, Jo, Lan, Nico, Quake and Zak for the fruitful

discussions on the infrared measurements. And to all the engineers and technicians who made it possible to carry out the measurements I reported in this thesis.

A kind thanks to my fellow PGRs and Postdocs at Manchester and CERN for the enjoyable time spent together, at work and outside. And to all the Manchester HEP department, who contributed in creating an enjoyable working environment.

Last but not least, to my parents and family for their love and support through all my choices. You taught me how to face problems with a constructive and positive attitude and always encouraged me to fulfil my dreams and interests. Thank you for that.

Preface

The author was born in 1993 in Rome, Italy. After leaning toward a scientific education in high school, he joined "La Sapienza" University in Rome to begin his higher education in physics. He obtained a B.Sc. in 2015, followed by a M.Sc. in 2018. For his M.Sc. thesis, he joined the CMS collaboration, mainly working in the field of electron reconstruction and identification. He later joined the ATLAS group at the University of Manchester to continue his studies in particle physics in a postgraduate research course under the supervision of Prof. Andrew Pilkington.

Soon after the beginning of the course, he joined the ATLAS ITk group in Manchester to do the technical work necessary to qualify as an ATLAS author. He participated in the detector upgrade activities at the University concerning the design qualification of the ITk Pixel Outer End-cap local supports. Specifically, he contributed to developing and optimising a measurement procedure to evaluate the thermal performance of the local supports, to be used for the Quality Assurance and Quality Control of the local support design and assembly procedure. The technique was documented in a Public Note [1] of the experiment, of which he was one of the two main editors. He also led many measurements with local support prototypes, whose principal results are discussed in chapter 4 of this thesis.

Alongside the ITk project, the author mainly worked on the measurement of unfolded differential cross-sections for the $pp \rightarrow ZZjj$ production using high-energy collision data collected by the ATLAS experiment at a centre-of-mass energy of $\sqrt{s} = 13$ TeV. The measurement is fully described in chapter 5 of this thesis. The results were published in a CONF Note [2] of the experiment, and a paper conversion is currently being prepared. The author was one of the primary analysers of the team, with leading contributions in almost every aspect of the measurement. He was also appointed as the editor of the internal note of the experiment documenting the analysis strategy.

Chapter 1.

Introduction

Formulating a unified theory to describe Nature’s laws is one of the ultimate quests of modern physics. The formulation of the Standard Model (SM) of particle physics represents the most successful and experimentally proven attempt in this direction, accurately describing and predicting the interactions of fundamental particles under the action of the electromagnetic, weak and strong forces. The theory postulates the unification of the electromagnetic and weak forces under the gauge symmetry described by the combined $SU(2) \times U(1)$ group [3–5]. Spontaneous breaking of this symmetry provides masses to the elementary particles via their interaction with the Higgs field [6–8]. The existence of a corresponding scalar boson, the Higgs boson, was predicted far before its experimental observation by the ATLAS and CMS experiments in 2012 [9, 10], representing one of the most important successes of the SM. The theory, however, is far from being a complete one, as it does not include gravitational interactions, and there are small inconsistencies which hint at potential effects of New Physics.

In the SM, the Z boson is one of the mediators of the weak force and is responsible for the so-called neutral current processes where the interacting particles do not change their flavour. The Z boson was discovered in 1983 with the UA1 and UA2 detectors at the CERN Super Proton Synchrotron (SPS) [11, 12]. Since then, it has been subject to many precise measurements, including its mass of approximately 91 GeV, today known with a precision of the MeV order. The main topic of this thesis is the measurement of production cross-sections¹ of $pp \rightarrow 4\ell jj$, a process that, at high energy, is largely dominated by the combined production

¹The cross-section denotes the rate at which a process occurs. See section 2.3 and section 3.1 for more detail.

of two Z bosons that consecutively decay into lepton pairs of opposite charge. The measurement utilises 140 fb^{-1} of high-energy proton-proton collision data at a centre-of-mass energy of $\sqrt{s} = 13 \text{ TeV}$ provided by the Large Hadron Collider (LHC) and recorded by the ATLAS experiment. The emission of two massive vector bosons significantly suppresses the production rate, thus constituting one of the rarest processes observed at the LHC. $ZZjj$ production occurs via strong and Electroweak (EW) interactions, making it a particularly interesting process to study both mechanisms. The pure EW production, through the Vector Boson Scattering (VBS) process, is sensitive to weak boson self-interactions, allowing to test further the Electroweak Symmetry Breaking (EWSB) mechanism and search for New Physics effects which could produce anomalous couplings. Differential cross-sections are measured for several observables characterising the kinematic properties of the $ZZjj$ system. Of particular interest, observables sensitive to the VBS process are considered, such as the invariant mass of the two jets in the final state. Others also include variables sensitive to the CP (simultaneous charge and parity transformation) nature of the interaction and variables related to the polarisation of the weak bosons. The author was heavily involved in developing almost every aspect of the analysis, with leading contributions to the event selection and binning optimisation, unfolding implementation and evaluation of the systematic uncertainties.

A second study is linked with the Phase-II upgrade of the ATLAS detector for the High-Luminosity phase of the LHC, particularly for the installation of a new Inner Tracker (ITk). The ITk, a silicon-based detector, will operate in a very harsh radiation environment, requiring an optimal cooling system to deliver good performance and prevent the damaging of the components. In the ITk pixel outer end-caps, the cooling is provided by the local supports, a carbon-based structure which holds the pixel sensors in place. The supports' thermal performance and cooling capabilities are evaluated with a technique developed at the University of Manchester, which involves the infrared thermography of the supporting structures. The non-invasive nature of the method is essential, as it allows us to use it for the Quality Control (QC) of the local supports during the serial production without impairing them. The author was involved in optimising the procedure and personally led an extensive program of measurements with local support prototypes, whose results were used to assess the technique's sensitivity and consolidate the local supports' assembly procedure.

The structure of the thesis is outlined below. Chapter 2 introduces the theoretical framework behind the SM and outlines the procedure used to simulate hadron-hadron collisions and predict cross-section values. The LHC and the ATLAS experiment are described in chapter 3. The chapter includes a discussion on the method used to experimentally measure the cross-sections and a summary of the procedures used in ATLAS to reconstruct physical objects from the detector signals. Continuing the discussion on the ATLAS detector, chapter 4 follows with an overview of the ITk upgrade and the technique used for the thermal characterisation of the pixel outer end-caps local supports. The chapter reports several measurements carried out with three different local support prototypes, all performed by the author, and it discusses the results from the perspective of the ITk design's requirements. The measurement of differential $4\ell jj$ cross-sections is presented in chapter 5. Particular emphasis is given to the implementation of the unfolding procedure and its optimisation. Unfolded differential cross-sections are reported for several observables of interest and are used to constrain the couplings of higher-dimension operators in an Effective Field Theory (EFT) interpretation of the results. Lastly, conclusions on the two measurements presented in the thesis are summarised in chapter 6.

Blank Page

Chapter 2.

Theory

This chapter summarises the theoretical framework that describes the interactions of elementary particles and is used to obtain the predictions for the measurements described in this thesis. After a brief introduction to the mathematical formalism, given in section 2.1, the Standard Model (SM) of particle physics is introduced in section 2.2. Section 2.3 follows with a discussion of the physics of hadron colliders, along with a description of the procedure used to simulate particle interactions with Monte Carlo generators, in section 2.4. A brief introduction to jets is given in section 2.5.

2.1. Formalism

The SM formulation relies on Quantum Field Theory (QFT) to describe the dynamics of particles. QFT is a broad topic, and its formalism and development are extensively covered in literature, for example in Refs. [13–15]. Only a brief introduction is given here, mainly inspired by [13, 16]. Following [13], we use a covariant relativistic notation, where a particle is determined by its space-time four-vector $x^\mu = (ct, \vec{x}) = (ct, x, y, z)$. Natural units, corresponding to $c = \hbar = 1$, will be hereafter assumed unless otherwise specified. The covariant form of the four-vector (x_μ) is obtained by the relation

$$x_\mu = g_{\mu\nu}x^\nu, \tag{2.1}$$

where the contracted indexes imply the summation over the four components and $g_{\mu\nu}$ is the metric tensor defined as

$$g_{\mu\nu} = \begin{pmatrix} 1 & 0 & 0 & 0 \\ 0 & -1 & 0 & 0 \\ 0 & 0 & -1 & 0 \\ 0 & 0 & 0 & -1 \end{pmatrix}. \quad (2.2)$$

Let us consider, for simplicity, a system described by a single field $\phi(x)$. In analogy with the classical approach, we can determine the system's dynamics from the principle of least action. The action is defined as the time integral of the system's Lagrangian (L), namely

$$S = \int L dt = \int_{\Omega} \mathcal{L}(\phi, \partial_{\mu}\phi) d^4x. \quad (2.3)$$

The term $\mathcal{L}(\phi, \partial_{\mu}\phi)$ corresponds to the Lagrangian density, which depends on the field and its partial derivatives¹, and is trivially related to the Lagrangian by an integral over the spatial volume. Imposing a null variation of the action $\delta S = 0$, eq. (2.3) leads to the Euler-Lagrange equation,

$$\frac{\partial \mathcal{L}}{\partial \phi} - \partial_{\mu} \frac{\partial \mathcal{L}}{\partial (\partial_{\mu}\phi)} = 0, \quad (2.4)$$

thus determining the equation of motion of the system. Similarly, we can introduce the conjugate momentum field

$$\pi(x) = \frac{\partial \mathcal{L}}{\partial \dot{\phi}}, \quad (2.5)$$

where $\dot{\phi}$ represents the time derivative of the field. The Hamiltonian density (\mathcal{H}) is then defined as

$$\mathcal{H} = \pi(x)\dot{\phi}(x) - \mathcal{L}(\phi, \partial_{\mu}\phi), \quad (2.6)$$

¹The partial derivative ∂_{μ} is equivalent to $\frac{d}{dx^{\mu}}$ and corresponds to the covariant four-vector generalisation of the gradient operator.

in a way that, as for the Lagrangian, the density is related to the Hamiltonian (H) of the system by a volume integral over the spatial coordinates.

In analogy with quantum mechanics, we can interpret the field and its conjugate as operators and apply the canonical quantisation via the imposition of the commutator relations

$$\begin{aligned} [\hat{\phi}(\mathbf{x}, t), \hat{\pi}(\mathbf{y}, t)] &= i\delta(\mathbf{x} - \mathbf{y}), \\ [\hat{\phi}(\mathbf{x}, t), \hat{\phi}(\mathbf{y}, t)] &= [\hat{\pi}(\mathbf{x}, t), \hat{\pi}(\mathbf{y}, t)] = 0. \end{aligned} \quad (2.7)$$

Without going into details of the computation, the quantisation of the field operators gives rise to creation and annihilation operators, which add or remove particles of given momenta to a Fock state $|\psi\rangle$. The operators' actions lead to a state characterised by an occupancy of integer value, thus obeying Bose-Einstein statistics. In this context, a particle corresponds to the excitation of a particular Fourier mode of the field, which, in turn, is the superposition of all possible modes [16]. When measuring the energy of the ground state $E_0 = \langle 0|H|0\rangle$, one could find the quantity to be divergent. This problem can be circumvented with the so-called renormalisation procedure, changing the energy scale such that $E_0 = 0$. The scale variation is justified as measuring an absolute energy value experimentally is impossible. Using the Schrödinger picture, where the time dependence is uniquely carried by the Fock states, the temporal evolution of a state $|\psi(t)\rangle$ from the initial configuration $|\psi(t_0)\rangle$ is expressed as

$$|\psi, t\rangle = \hat{U}(t, t_0)|\psi, t_0\rangle, \quad (2.8)$$

where $\hat{U}(t, t_0) = e^{-iH(t-t_0)}$ is the time evolution operator.

Consider now the case where the particles in a system interact with each other, e.g. scattering, which is more closely related to the physics of particle colliders studied in this thesis. We can think of the Hamiltonian density of the system as being composed of two different terms, one related to the free fields (\mathcal{H}_0) and the other purely describing the interaction process (\mathcal{H}_I), namely

$$\mathcal{H} = \mathcal{H}_0 + \mathcal{H}_I. \quad (2.9)$$

The interactions typically happen in a short time-scale $-\infty \ll t \ll +\infty$, and the initial ($|i, t = -\infty\rangle$) and final ($|f, t = +\infty\rangle$) states can be asymptotically described

by the free field theory. The transition between the two states is probabilistic and is governed by the unitary operator S-matrix of elements

$$S_{fi} = \langle f, t = +\infty | \hat{U}(t, t_0) | i, t_0 = -\infty \rangle. \quad (2.10)$$

The cross-section of the process $i \rightarrow f$ is proportional to the scattering amplitude squared, $|S_{fi}|^2$, which indicates the transition probability between the two states. The unitarity condition $\sum_f |S_{fi}|^2 = 1$ ensures the probability is well-defined. Provided the energy scale at which $\mathcal{H}_{\mathcal{I}}$ operates is small, a perturbative approach is possible, and eq. (2.10) can be expressed in the Dirac picture² as a series expansion in powers of the interaction Hamiltonian. If the interaction strength (i.e. the coefficient of the expansion) is smaller than unity, the series can be truncated, approximating S_{fi} at a finite order. An example is the electromagnetic electron-photon interactions, where the coupling strength is given by the fine structure constant $\alpha_{EM} \approx \frac{1}{137}$. The S-matrix expansion and truncation is equivalent to the computation of the scattering amplitude via the Feynman rules³, where one sums the contributions from all the possible diagrams describing the $i \rightarrow f$ process, up to a given order.

2.2. The Standard Model

The Standard Model of particle physics is a unified theory which describes the interactions caused by three out of the four fundamental forces, the electromagnetic, weak and strong forces. The three forces are mediated by integer-spin⁴ gauge bosons, corresponding to the photon (γ), the gluon⁵ and the W^\pm, Z bosons. The photon mediates electromagnetic interactions, the gluon is responsible for the

²In the Dirac picture, also known as the Interaction picture, the time dependence of the operators relies only on the free field Hamiltonian, while the time evolution of the states depends on the perturbative Hamiltonian. The operators in the two pictures are related by the transformation $\phi_I(t) = e^{iH_0 t} \phi_S e^{-iH_0 t}$, where the indexes I and S denote the Interaction and Schrödinger pictures respectively.

³The Feynman diagrams are a pictorial representation of the interaction processes which allow to directly compute the scattering amplitudes from a defined set of rules (see, for example, chapter 7 of Ref. [13]).

⁴The spin of a particle denotes its intrinsic angular momentum.

⁵As described in section 2.2.2, there are eight different types of gluonic fields. However, since they are experimentally indistinguishable, it is more convenient to refer to them as a single entity.

strong interactions, and the W^\pm and Z bosons are the mediators of the weak force. The principal properties of the gauge bosons are summarised in table 2.1.

Along with the vector bosons, there are additional 12 fermions with half-integer spin, subdivided into six leptons and six quarks and arranged into three generations of particles with an increasing mass scale. They are listed in table 2.2. For each fermion, there exists an identical anti-particle with opposite quantum number values. Both leptons and quarks carry an electrical charge (Q) and a weak isospin charge (\mathbf{I}), while only quarks also present a colour charge (C). The electric and isospin charges can be combined in the so-called weak hypercharge (Y) via the relation $Q = I_z + Y/2$, where I_z denotes the third component of the isospin. Colour-charged free states have not been observed in nature, giving rise to the concept of colour confinement, where quarks of different colours combine to form neutral bound states. The combination of a $q\bar{q}$ pair forms a class of particles called mesons, while three quarks create a baryon. The most common baryons are the protons (p) and neutrons (n), which are the basic constituents of the atoms' nuclei and correspond respectively to a uud and udd state.

Interaction	Particle	Symbol	Charge	Spin	Mass [GeV]
Electromagnetic	Photon	γ	0	1	0
Weak	W-boson	W^\pm	± 1	1	80.377 ± 0.012
	Z-boson	Z	0	1	91.1876 ± 0.0021
Strong	Gluon	g	0	1	0

Table 2.1.: Summary of the force-mediator gauge bosons in the SM. The electric charge is given in units of elementary charge, and the mass values are taken from the summary tables provided by the 2022 Particle Data Group review [17].

The SM Lagrangian describes the interactions between the different fermionic and bosonic fields and is invariant under gauge transformations of the combined group

$$SU(3)_C \times SU(2)_L \times U(1)_Y, \quad (2.11)$$

Family	Generation	Particle	Symbol	Charge	Spin	Mass
Quarks	I	up	u	$2/3$	$1/2$	2.16 MeV
		down	d	$-1/3$	$1/2$	4.67 MeV
	II	charm	c	$2/3$	$1/2$	1.27 GeV
		strange	s	$-1/3$	$1/2$	93.4 MeV
	III	top	t	$2/3$	$1/2$	172.7 GeV
		bottom	b	$-1/3$	$1/2$	4.18 GeV
Leptons	I	electron	e	-1	$1/2$	0.511 MeV
		electron neutrino	ν_e	0	$1/2$	< 1.1 eV
	II	muon	μ	-1	$1/2$	105.66 MeV
		muon neutrino	ν_μ	0	$1/2$	< 0.19 MeV
	III	tau	τ	-1	$1/2$	1776.9 MeV
		tau neutrino	ν_τ	0	$1/2$	< 18.2 MeV

Table 2.2.: Summary of the different fermions present in the SM. The electric charge is given in units of elementary charge, and the mass values are taken from the summary tables provided by the 2022 Particle Data Group review [17].

where U stand for unitary, S for special⁶, and the number in brackets is the dimension of the group. The subscripts C , L and Y respectively denote the colour charge, left-handedness (see section 2.2.3) and weak hypercharge. The concept of symmetry is fundamental in QFT. Noether's theorem [18] tells us that, if the Lagrangian is invariant under some continuous transformation, there must be a conserved current which leads to the existence of a conserved scalar quantity that is constant over time. In the SM Lagrangian, the symmetry described by eq. (2.11) directly corresponds to the conservation of the quantum numbers associated with the colour charge, electric charge and the third component of the weak isospin. The different terms in eq. (2.11) are discussed in more detail in the following sections.

2.2.1. Quantum Electrodynamics

Quantum Electrodynamics (QED) describes the interactions between electrically charged fermions and massless photons and can be considered as a prolongation of the classic electromagnetic theory in a QFT framework. Fermions with half-integer spin satisfy the Pauli exclusion principle and, thus, obey Fermi-Dirac

⁶In a special group, the matrix representation of a generic element has a determinant equal to unity.

statistics. We discussed in section 2.1 that quantised field operators, which satisfy the commutation relation given in eq. (2.7), lead to the creation of bosons. Fermions, on the other hand, can be produced by replacing the commutation rules in eq. (2.7) with anti-commutation relations. The equation of motion for a fermion of rest mass m corresponds to the Dirac equation⁷, which is derived from the Lagrangian density

$$\mathcal{L}_{Dirac} = \bar{\psi}(i\gamma^\mu\partial_\mu - m)\psi + h.c., \quad (2.12)$$

where γ^μ are the 4×4 Dirac matrices, ψ is the four-vector spinor wave-function corresponding to the fermionic field, and $\bar{\psi} = \psi^\dagger \gamma^0$ is the adjoint field. The hermitian conjugate $h.c.$ will be henceforth omitted for the sake of brevity.

The unitary group $U(1)_Q$ is associated with a gauge transformation corresponding to a change in phase

$$\mathcal{L}' = e^{i\alpha(x)} \mathcal{L}, \quad (2.13)$$

with $\alpha(x)$ real. The Lagrangian density in eq. (2.12) is invariant under a global phase transformation, which coincides with the special case of a constant $\alpha(x)$. According to Noether's theorem, the symmetry leads to a conserved quantity corresponding to the electric charge. The invariance under a local phase transformation, however, is not preserved, as an additional term proportional to $\partial_\mu \alpha(x)$ would appear when substituting eq. (2.13) in eq. (2.12). To restore the symmetry at a local level, we introduce a four-component vector field (A_μ) which transforms according to

$$A'_\mu(x) = A_\mu(x) + \frac{1}{q_e} \partial_\mu \alpha(x), \quad (2.14)$$

where the term q_e represents the coupling constant of the interaction. In terms of A_μ , we can define the covariant derivative (D_μ) thorough the minimal substitution

$$D_\mu = \partial_\mu - iq_e A_\mu(x). \quad (2.15)$$

⁷The Dirac equation for a fermionic field ($\psi(x)$) is expressed as $i\gamma^\mu\partial_\mu\psi(x) - m\psi(x) = 0$, where the different terms are the same ones described in eq. (2.12).

This allows us to write the QED Lagrangian in a gauge invariant form, as

$$\mathcal{L}_{QED} = -\frac{1}{4}F_{\mu\nu}F^{\mu\nu} + \bar{\psi}(i\mathcal{D} - m)\psi, \quad (2.16)$$

indicating with a slashed notation the index contraction with the Dirac matrices $\mathcal{D} = \gamma^\mu D_\mu$. The additional term $-\frac{1}{4}F_{\mu\nu}F^{\mu\nu}$ is a gauge invariant kinetic term for the newly introduced field. $F_{\mu\nu}$ corresponds to the electromagnetic field strength tensor, which, in the classical theory, describes Maxwell's equations in a relativistic covariant form

$$F_{\mu\nu} = \partial_\mu A_\nu - \partial_\nu A_\mu. \quad (2.17)$$

In eq. (2.16) there is no mass term for the A_μ field, which would otherwise break the gauge invariance. This is consistent with the observation of a massless photon. Self-interactions of the photon are also not allowed, as the boson is not electrically charged.

2.2.2. Quantum Chromodynamics

Quantum Chromodynamics (QCD) is a branch of QFT that describes the strong interactions between colour-charged particles. In the SM, this is related to the gauge symmetry corresponding to the $SU(3)_C$ group, which leads to the conservation of the colour charge. This charge has three degrees of freedom, corresponding to three colour spinors of type red (R), blue (B) or green (G). The algebra of a generic special unitary group, $SU(N)$, has dimension $N^2 - 1$. For $SU(3)$, this implies that a generic element of the group can be represented by a linear combination of eight traceless hermitian generators t^a , with $a \in \{1, 2, \dots, 8\}$. They are defined with the 3×3 Gell-Mann matrices⁸ (λ^a), as $t^a = \frac{1}{2}\lambda^a$. The group

⁸The eight Gell-Mann matrices correspond to

$$\begin{aligned} \lambda_1 &= \begin{pmatrix} 0 & 1 & 0 \\ 1 & 0 & 0 \\ 0 & 0 & 0 \end{pmatrix}, & \lambda_2 &= \begin{pmatrix} 0 & -i & 0 \\ i & 0 & 0 \\ 0 & 0 & 0 \end{pmatrix}, & \lambda_3 &= \begin{pmatrix} 1 & 0 & 0 \\ 0 & -1 & 0 \\ 0 & 0 & 0 \end{pmatrix}, & \lambda_4 &= \begin{pmatrix} 0 & 0 & 1 \\ 0 & 0 & 0 \\ 1 & 0 & 0 \end{pmatrix}, \\ \lambda_5 &= \begin{pmatrix} 0 & 0 & -i \\ 0 & 0 & 0 \\ i & 0 & 0 \end{pmatrix}, & \lambda_6 &= \begin{pmatrix} 0 & 0 & 0 \\ 0 & 0 & 1 \\ 0 & 1 & 0 \end{pmatrix}, & \lambda_7 &= \begin{pmatrix} 0 & 0 & 0 \\ 0 & 0 & -i \\ 0 & i & 0 \end{pmatrix}, & \lambda_8 &= \frac{1}{\sqrt{3}} \begin{pmatrix} 1 & 0 & 0 \\ 0 & 1 & 0 \\ 0 & 0 & -2 \end{pmatrix}. \end{aligned}$$

is non-abelian, and the generators satisfy the commutation relation

$$[t^a, t^b] = if^{abc}t^c, \quad (2.18)$$

where f^{abc} are the totally asymmetric structure constants, and repeated Latin indexes imply summation.

Similarly to the $U(1)_Q$ case, a set of bosonic fields $G_\mu^a(x)$ is introduced in the Lagrangian to preserve the $SU(3)_C$ gauge symmetry. The multiplicity of the fields matches the algebraic structure of the group, thus resulting in eight different gluonic fields with covariant derivative

$$D_\mu = \partial_\mu - ig_S t^a G_\mu^a(x), \quad (2.19)$$

where g_S is the coupling constant of the strong interaction. In analogy with the electromagnetic field strength tensor in QED, we also introduce a kinetic term for $G_\mu^a(x)$ of the form

$$G_{\mu\nu}^a = \partial_\mu G_\nu^a - \partial_\nu G_\mu^a + g_S f^{abc} G_\mu^b G_\nu^c. \quad (2.20)$$

The QCD Lagrangian density can now be written as

$$\mathcal{L}_{QCD} = -\frac{1}{4} G_{\mu\nu}^a G_a^{\mu\nu} + \sum_{f \in \{u,d,c,s,t,b\}} \bar{\psi}_f (i\not{D} - m_f) \psi_f, \quad (2.21)$$

where the gluon octet index a is vertically displaced only to improve the readability. The Dirac field $\psi_f(x)$, describing a quark of specific flavour f , and its corresponding adjoint $\bar{\psi}_f(x)$ are expressed by the 3-dimensional colour wavefunctions

$$\psi_f(x) = \begin{pmatrix} \psi_{f,R}(x) \\ \psi_{f,B}(x) \\ \psi_{f,G}(x) \end{pmatrix}, \quad \bar{\psi}_f(x) = \left(\bar{\psi}_{f,R}(x) \quad \bar{\psi}_{f,B}(x) \quad \bar{\psi}_{f,G}(x) \right). \quad (2.22)$$

Differently from the photon in the QED theory, the gluons present a colour charge themselves. The presence of a charge allows for a self-coupling of the gluons, generating 3 and 4-point interaction vertices in perturbative QCD. The non-linear gluon coupling reflects in the running of the coupling strength, $\alpha_S \equiv \frac{g_S^2}{4\pi}$,

which exhibits a $(\ln Q^2)^{-1}$ dependence on the energy scale, Q^2 . For small energy values, the coupling strength increases and perturbative QCD can no longer be applied. In nature, this phenomenon corresponds to the colour confinement principle introduced in section 2.2, for which only colour-neutral states are observed. At high energy, α_s becomes small ($\alpha_s(m_Z) = 0.118$ at the Z boson mass scale), and a perturbative approach is possible. As the coupling strength decreases with the transferred momentum, at high enough energy quarks are no longer confined in a bound state, and they can be described with the free fields theory. This behaviour is known as asymptotic freedom [19].

2.2.3. Electroweak interactions and unification

The $SU(2)$ gauge symmetry is related to weak interactions and leads to the conservation of the weak isospin. In analogy with $SU(3)$, the group is characterised by an algebra of dimension $N^2 - 1 = 3$. Its fundamental representation can be identified with the three 2×2 Pauli matrices⁹ (σ_i), which satisfy the commutation and anti-commutation relations

$$[\sigma_i, \sigma_j] = 2i\epsilon_{ijk}\sigma_k, \quad \{\sigma_i, \sigma_j\} = 2\delta_{ij}\mathbf{I}, \quad (2.23)$$

where ϵ_{ijk} is the totally anti-symmetric Levi-Civita symbol, δ_{ij} is the Kronecker delta and \mathbf{I} is the 2-dimensional identity matrix.

Weak interactions are known to violate invariance under parity transformation, corresponding to a sign change of the spatial coordinates of a vector $(t, x, y, z) \rightarrow (t, -x, -y, -z)$. The concept of parity violation in weak interactions dates back to 1956, theoretically introduced by Lee and Yang [20] and later verified experimentally [21]. In the QFT formalism, this leads to the introduction of a chirality operator $\gamma^5 = i\gamma^0\gamma^1\gamma^2\gamma^3\gamma^4$ with eigenvalues $+1$ and -1 . The fermionic fields can then be expressed, in the basis of the chirality eigenstates, as the combination of a left-handed (negative chirality) and right-handed (positive chirality)

⁹The three Pauli matrices correspond to

$$\sigma_1 = \begin{pmatrix} 0 & 1 \\ 1 & 0 \end{pmatrix}, \quad \sigma_2 = \begin{pmatrix} 0 & -i \\ i & 0 \end{pmatrix}, \quad \sigma_3 = \begin{pmatrix} 1 & 0 \\ 0 & -1 \end{pmatrix}$$

state

$$\psi = \psi^L + \psi^R = \hat{P}_L \psi + \hat{P}_R \psi = \frac{1}{2}(1 - \gamma^5)\psi + \frac{1}{2}(1 + \gamma^5)\psi, \quad (2.24)$$

where we introduced the projection operators $\hat{P}_L = \frac{1}{2}(1 - \gamma^5)$ and $\hat{P}_R = \frac{1}{2}(1 + \gamma^5)$.

The parity violation principle is described in the theory by considering a different transformation rule for the opposite-chirality fields. In particular, a $SU(2)$ gauge transformation rotates left-handed fields while leaving the right-handed component untouched. Namely,

$$\begin{cases} \psi^L(x) \rightarrow \psi^{L'}(x) = e^{i\frac{1}{2}\alpha_j(x)\sigma_j}\psi^L(x), \\ \psi^R(x) \rightarrow \psi^{R'}(x) = \psi^R(x), \end{cases} \quad (2.25)$$

where $j \in \{1, 2, 3\}$ and $\alpha_j(x)$ are three real angles. The global transformation $\alpha_j(x) = \text{constant}$ leads to the aforementioned isospin charge conservation. We can write the left and right-handed fields respectively as an isospin doublet with $I_z = \pm\frac{1}{2}$ and a singlet with $I_z = 0$. For the leptons, this corresponds to

$$\psi_\ell^L = \begin{pmatrix} \nu_\ell^L \\ \ell^L \end{pmatrix}, \quad \psi_\ell^R \in \{\ell^R\}, \quad (2.26)$$

where $\ell = e, \mu, \tau$, and we neglected right-handed neutrinos ν_ℓ^R as they are not present in the SM. The same applies to quarks, with the up(down)-type field corresponding to a positive (negative) I_z . The down-type quark isospin eigenstates are, however, different from the mass eigenstates introduced in table 2.2. They can be interpreted as a mixture of the mass eigenstates and can be retrieved via the unitary transformation described by the so-called Cabibbo-Kobayashi-Maskawa (CKM) matrix [22, 23], as

$$\begin{pmatrix} d' \\ s' \\ b' \end{pmatrix} = \begin{pmatrix} V_{ud} & V_{us} & V_{ub} \\ V_{cd} & V_{cs} & V_{cb} \\ V_{td} & V_{ts} & V_{tb} \end{pmatrix} \begin{pmatrix} d \\ s \\ b \end{pmatrix}. \quad (2.27)$$

The nine parameters of the CKM matrix have four degrees of freedom and can be interpreted in terms of three rotation angles and a complex phase. The latter

is responsible for the phenomenon of CP (simultaneous charge conjugation and parity) symmetry violation in the SM.

Using the same argument as in QED and QCD, the invariance under a local transformation is restored by introducing three gauge fields W_μ^i . The non-abelian nature of the $SU(2)$ group reflects in the field strength tensor, which, in analogy with the gluon fields, can be expressed as

$$W_{\mu\nu}^i = \partial_\mu W_\nu^i - \partial_\nu W_\mu^i + g_W \epsilon_{ijk} W_\mu^j W_\nu^k. \quad (2.28)$$

The $W_\mu^{1,2}$ gauge fields can be re-written in a different basis to form the fields W_μ^- and W_μ^+ ,

$$W_\mu^\mp = \frac{1}{\sqrt{2}}(W_\mu^1 \pm iW_\mu^2) \quad (2.29)$$

With this representation, the quantised fields manifest via the charged W^\pm vector bosons and are responsible for flavour-changing processes. The third field W_μ^3 is related to the Z boson, as described below.

The simultaneous $SU(2) \times U(1)_Y$ symmetry corresponds to a unified theory describing electromagnetic and weak interactions [3–5]. The addition of the chirality-independent $U(1)_Y$ rotation invariance provides the conservation of the weak hypercharge, which relates the electric charge and the third component of the weak isospin (section 2.2). Introducing the B_μ real field to preserve the $U(1)_Y$ gauge invariance, we can write the covariant derivatives which act on the left and right-handed fields as

$$\begin{aligned} D_\mu \psi^L &= (\partial_\mu + \frac{i}{2} g_W \sigma_j W_\mu^j + \frac{i}{2} g_Y Y B_\mu) \psi^L, \\ D_\mu \psi^R &= (\partial_\mu + i g_Y Y B_\mu) \psi^R, \end{aligned} \quad (2.30)$$

with $Y = -1, -2$ respectively for ψ_ℓ^L and ℓ^R .

The unified Electroweak (EW) Lagrangian density, restricted to the first lepton generation for simplicity and in the massless approximation, results

$$\mathcal{L}_{EW, massless} = -\frac{1}{4} W_{\mu\nu}^j W_j^{\mu\nu} - \frac{1}{4} B_{\mu\nu} B^{\mu\nu} + i\bar{\psi}_e^L \not{D} \psi_e^L + i\bar{e}^R \not{D} e^R + i\bar{\nu}_e^R \not{D} \nu_e^R. \quad (2.31)$$

The Lagrangian density can be extended to include all lepton and quark generations by including the corresponding terms for each left and right-handed flavour. The gauge fields B_μ and W_μ^3 can be combined in a different basis to represent the electromagnetic field A_μ of section 2.2.1 and a field Z_μ associated with the neutral Z boson. This is achieved with a rotation defined by the Weinberg angle (θ_W), which can be expressed as

$$\begin{pmatrix} A_\mu \\ Z_\mu \end{pmatrix} = \begin{pmatrix} \cos \theta_W & \sin \theta_W \\ -\sin \theta_W & \cos \theta_W \end{pmatrix} \begin{pmatrix} B_\mu \\ W_\mu^3 \end{pmatrix}, \quad (2.32)$$

with $\sin \theta_W = \frac{g_Y}{\sqrt{g_W^2 + g_Y^2}}$ and such that $g_Y \cos \theta_W = g_W \sin \theta_W = q_e$.

2.2.4. Electroweak symmetry breaking

Adding an explicit mass term for the gauge bosons, such as $m_W^2 W_\mu^- W^{+\mu} + \frac{1}{2} m_Z^2 Z_\mu Z^\mu$, would make the Lagrangian no longer invariant under a $SU(2) \times U(1)$ transformation. A similar argument holds for the fermions. Substituting eq. (2.24) into the Dirac Lagrangian would give a mass term $-m_f(\bar{\psi}_f^L \psi_f^R + \bar{\psi}_f^R \psi_f^L)$ which mixes the left-handed isospinors with the right-handed isoscalars, and the $SU(2)_L$ gauge transformation acts differently on the two. Therefore, the bosons and fermions must acquire their masses through a different mechanism. In the SM theory, this is obtained with the spontaneous breaking of the EW symmetry, a process also known as the Higgs mechanism [6–8]. The concept of spontaneous symmetry breaking is related to a system that is invariant under a given transformation and is characterised by a degenerate ground state. The lowest-energy level of such a system is not uniquely identified but presents multiple eigenstates of the same energy, which transform according to the system's symmetry. Arbitrarily choosing one of the eigenstates to represent the ground state would, therefore, break the symmetry, as that particular solution would no longer be invariant.

For the W^\pm, Z bosons to get mass, we have to break the $SU(2)_L \times U(1)_Y$ symmetry while preserving the $U(1)_Q$ invariance, in such a way that the photon remains massless. This is achieved with the Higgs mechanism by introducing a

complex scalar field in the form of an isospin doublet with $\mathbf{I} = \frac{1}{2}$ and $Y = 1$,

$$\phi = \begin{pmatrix} \phi_1 + i\phi_2 \\ \phi_3 + i\phi_4 \end{pmatrix}, \quad (2.33)$$

with $\phi_1, \phi_2, \phi_3, \phi_4$ real fields. The Lagrangian density associated with ϕ has the form

$$\mathcal{L}_\phi = (\partial_\mu \phi)^\dagger (\partial^\mu \phi) - V(\phi), \quad (2.34)$$

with the potential being

$$V(\phi) = \mu^2 \phi^\dagger \phi + \lambda |\phi^\dagger \phi|^2. \quad (2.35)$$

The parameters λ, μ regulate the form of the potential. Choosing $\lambda > 0$ and $\mu^2 < 0$ produces a potential with a degenerate minimum¹⁰ at $\phi \neq 0$. The covariant derivative in eq. (2.35) is determined by the $SU(2)_L \times U(1)_Y$ gauge symmetry and resembles the first term of eq. (2.30), modified accordingly with the hypercharge of the field. Without loss of generality, we can choose a vacuum¹¹ in which three of the four fields composing the Higgs doublet are null, such as

$$\langle 0 | \phi | 0 \rangle = \begin{pmatrix} 0 \\ \frac{v}{\sqrt{2}} \end{pmatrix} \quad (2.36)$$

with $v = \sqrt{-\mu^2/\lambda}$. Equation (2.36) can be used to parametrise the Higgs field in terms of its distance from the vacuum expectation value. Introducing four generic real fields $\eta_1(x), \eta_2(x), \eta_3(x)$ and $H(x)$, it can be written

$$\phi(x) = \frac{1}{\sqrt{2}} \begin{pmatrix} \eta_1(x) + i\eta_2(x) \\ v + H(x) + i\eta_3(x) \end{pmatrix}. \quad (2.37)$$

¹⁰Considering a complex scalar singlet of the type $\phi(x) = \phi_1(x) + i\phi_2(x)$, the potential in eq. (2.35) for $\lambda > 0$ and $\mu^2 < 0$ assumes the shape of a Mexican hat with an unstable local maximum at $\phi = 0$ and a continuous, infinitely degenerate, minimum at $|\phi| = \sqrt{-\mu^2/2\lambda}$.

¹¹In QFT the ground state corresponds to the vacuum.

The three $\eta_i(x)$ fields are often referred to as Goldstone fields and represent non-physical massless bosons. The Goldstone fields can be eliminated from eq. (2.37) with a gauge transformation¹², also called unitary gauge. This leaves

$$\phi(x) = \frac{1}{\sqrt{2}} \begin{pmatrix} 0 \\ v + H(x) \end{pmatrix}. \quad (2.38)$$

When substituting eq. (2.38) into the Higgs field Lagrangian density of eq. (2.34), one obtains explicit mass terms for the gauge bosons. These have the form

$$\mathcal{L}_{V,\text{mass}} = m_W^2 W_\mu^- W^{+\mu} + \frac{1}{2} m_Z^2 Z_\mu Z^\mu - \frac{1}{2} m_H^2 H^2, \quad (2.39)$$

with $m_W = \frac{1}{2} v g_W$, $m_Z = \frac{m_W}{\cos \theta_W} = \frac{1}{2} v \sqrt{g_W^2 + g_Y^2}$ and $m_H = \sqrt{-2\mu^2}$. The Higgs field manifests through the neutral scalar boson H^0 of mass around 125 GeV. The observation of the Higgs boson had been a missing piece of the SM for many years, until its discovery by ATLAS and CMS in 2012 [9, 10].

The spontaneous EW symmetry breaking through the interaction with the Higgs field can also be used to provide masses to the fermions. This is done in the form of a Yukawa-type coupling, which, for a given lepton flavour, is expressed by the Lagrangian density

$$\mathcal{L}_{Yukawa} = g_\ell (\psi_\ell^L \psi_\ell^R \phi + \psi_\ell^R \psi_\ell^L \phi^\dagger), \quad (2.40)$$

where g_ℓ is a coupling constant and we considered the neutrino massless, as originally postulated in the SM theory. With a similar procedure used for the gauge bosons, it can be shown that the leptons acquire a mass $m_\ell = \frac{v g_\ell}{\sqrt{2}}$. The argument can be generalised to the different quark flavours with analogous results.

2.2.5. The SM Lagrangian

The different Lagrangian densities discussed in sections 2.2.1 to 2.2.4 can be combined to form the SM Lagrangian. Without explicitly writing the terms, we can express the SM Lagrangian as the sum of several contributions describing

¹²Equation (2.37) can be interpreted as the result of a gauge transformation $\phi' = U\phi U^{-1}$, with $U = e^{\frac{i\eta\sigma}{2v}}$. The Goldstone bosons thus vanish from the expression of ϕ' and are re-absorbed by the gauge bosons in the transformation $\sigma \mathbf{W}'_\mu = U \sigma \mathbf{W}_\mu U^{-1}$.

different interactions¹³, namely

$$\mathcal{L}_{SM} = \mathcal{L}_{Gauge} + \mathcal{L}_{Fermions} + \mathcal{L}_{Higgs} + \mathcal{L}_{Yukawa}. \quad (2.41)$$

\mathcal{L}_{Gauge} corresponds to the kinetic and interaction terms of the gauge bosons and is related to the field strength tensors. $\mathcal{L}_{Fermions}$ contains the fermionic fields with Dirac-like terms of the form $i\bar{\psi}\not{D}\psi$, which describe the interactions between fermions and between fermions and gauge bosons through the covariant derivatives. These refer to both electroweak and strong interactions and include a summation over all quark and lepton flavours. \mathcal{L}_{Higgs} is the Higgs Lagrangian discussed in section 2.2.4 from which the gauge bosons acquire their masses. \mathcal{L}_{Yukawa} , also discussed in section 2.2.4, describes the Yukawa-type interactions between the fermions and the Higgs field, which result in a mass term for the fermions proportional to the coupling strength.

The SM theory has been extensively tested and accurately describes the physics of particle interactions observed so far, such as at lepton and hadron colliders. As an example, production cross-sections for a plethora of different processes, as measured by the ATLAS experiment at different proton-proton collision energy, are shown in fig. 2.1. The observed values are found to be consistent with the SM predictions, also shown in the figure. Of particular relevance for this thesis, it is worth pointing out that the EW production of two Z bosons in association with two jets (see section 5.1) lies in the far end of the right side of the plot, corresponding to a very small cross-section value.

2.2.6. SM limitations and beyond

Despite being a very successful theory, the SM doesn't completely describe Nature's laws. The SM describes three fundamental forces by means of a gauge theory. However, it completely eludes the description of gravitational interactions due to the very different scale at which these become relevant. Gravity is described by Einstein's General Relativity, which is also a gauge theory. However, despite sharing a similar mathematical framework, it is considered to be incompatible with the SM, especially at the small scale where a quantum mechanical

¹³In addition to those listed in eq. (2.41), the complete SM Lagrangian necessitates other two extra terms, a gauge fixing term and a ghost term. The first is related to the choice of the gauge to uniquely identify the fields, and the second removes non-physical contributions from the gauge bosons, such as from quantised gluons. The origin of these terms is mathematical and exceeds the scope of this thesis. Therefore, they are not discussed here.

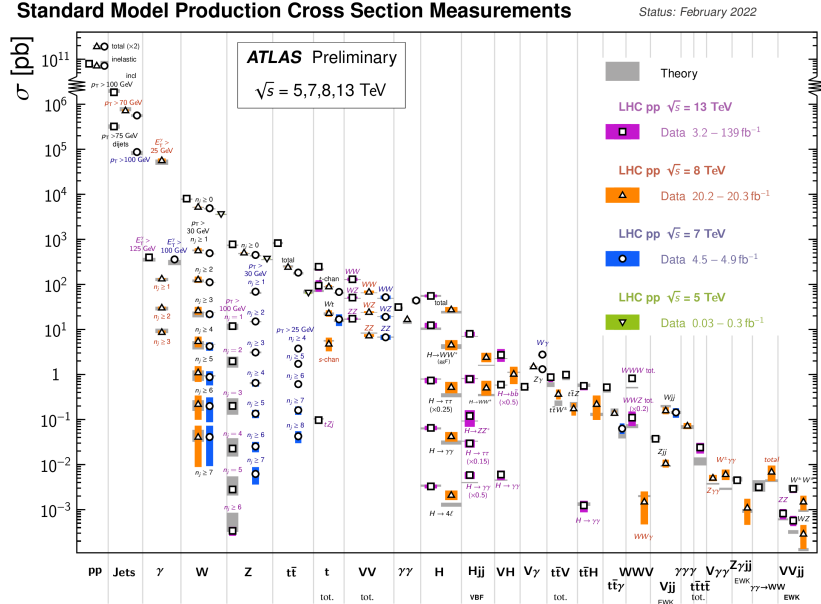


Figure 2.1.: Standard Model production cross-sections measured with the ATLAS experiment in proton-proton collisions at a centre of mass energy corresponding to $\sqrt{s} = 5$ TeV (green), 7 TeV (blue), 8 TeV (orange) and 13 TeV (fuchsia). The measurements are corrected for the branching ratios and confronted with the theoretical predictions, shown in grey. Uncertainties are plotted with a band. Figure sourced from [24]. References for the single measurements are available at the same source.

approach is necessary. Moreover, astrophysical observations suggest the existence of an additional type of matter, referred to as dark matter, which only interacts gravitationally and can't be described by the SM particles.

One of the most significant pieces of evidence of the incompleteness of the SM is the problem of the neutrino mass. In the SM, the Yukawa coupling of the neutrinos is set to zero, which originates massless particles. This conflicts with the observation of neutrino oscillations [25, 26], corresponding to a change in flavour, for which they are required to have a non-zero mass. The small neutrino mass constitutes a tiny deviation from the SM, which still accurately describes the physics of particle colliders, but points towards a possible extension of the theory. The explanation for the mass hierarchy of the different fermions, with very large mass scale difference between neutrinos and other particles, but also within the different generations of fermions, is another open problem. This is linked to the counter-intuitive idea that a single mechanism, namely the Higgs field, is responsible for the generation of particles' masses ranging over several

orders of magnitude. It also leads to the problem of naturalness, corresponding to the necessity to fine-tune the many free parameters of the SM theory to match the observations.

Another experimental hint to a possible Beyond the Standard Model (BSM) physics is given by the asymmetry between matter and anti-matter in the Universe, also referred to as baryon asymmetry. According to the cosmological inflation theory, the Big Bang should have created an equal amount of matter and anti-matter, with its consequential annihilation. Therefore, there must exist some mechanism due to which one is preferred. The so-called Sakharov conditions [27] denote three requirements needed for an asymmetric production of matter and anti-matter. Among them, there is the condition of CP symmetry violation. In the SM, this is introduced by a non-zero imaginary phase in the CKM matrix, as described in section 2.2.3. However, this is not sufficient to describe the large observed baryon asymmetry.

Similarly to the unification of the electromagnetic and weak interactions, one could think of a more comprehensive theory which, at the appropriate energy scale, unifies also QCD interactions and, ultimately, gravity. This concept is called Global Unified Theory (GUT), and a naive example would be to consider a larger group which contains the $SU(3) \times SU(2) \times U(1)$ description of the SM. This thesis will not describe any particular GUT (e.g. supersymmetry), as these models are not particularly relevant for the presented measurements. A summary of the most-known theories can be found, for example, in chapter 19 of Ref. [15].

2.3. Physics of Hadron Colliders

The measurement described in chapter 5 utilises data collected in high-energy proton-proton collisions provided by the LHC accelerator. Differently from its lepton collider predecessor, where the scattering involved elementary particles, protons are composite objects, made of three valence quarks (uud), which are held together by their interactions with gluons. These gluons can additionally produce virtual $q\bar{q}$ pairs, not necessarily of u or d flavour, that add to the mixture and could participate in the pp scattering. The valence quarks, gluons and virtual "sea" quarks are referred to as partons. The probability that a particular final state originates from the collision is given by the cross-section. An accurate calculation of the cross-section is essential to faithfully reproduce the data that

are observed experimentally. At the LHC, the presence of additional partons due to the compositeness of the protons complicates the physics modelling of the interaction and makes it more challenging to calculate cross-section values. This section briefly describes the procedure used to evaluate such cross-sections.

2.3.1. Parton Distribution Functions

Parton distribution functions (PDFs) describe the momentum distribution of the partons composing the protons and are a key ingredient for the computation of cross-sections. A generic parton (a) carries a fraction x_a of the total proton momentum (p_p), namely $p_a = x_a p_p$. The PDF $f_a(x_a, Q^2)$ denotes the probability to find the same parton a with a specific fractional momentum corresponding to x_a . The PDF depends on the momentum transfer (Q^2) of the scattering process, indicating the scale at which the proton is probed. The values of the PDFs are not known a priori, and they cannot be exactly calculated using a perturbation theory approach. Therefore, they must be constrained experimentally with high-energy collision data that can probe the internal structure of the protons. The PDFs do not depend on the interaction processes but only convey the underlying composite structure of the proton. Thus, they can be evaluated from global fits applied to multiple measurements involving the collision of protons at a desired Q^2 scale. A minimum scale is typically chosen at the GeV order to ensure the interactions occur in a perturbative regime. A non-exhaustive list of data employed in the PDF fits includes measurements of deep inelastic scattering, like those provided by the SLAC accelerator or the HERA collider, measurements of different Drell-Yan processes, or more recent vector bosons production cross-sections obtained at the LHC. Several sets of PDFs are provided by different collaborations, each obtained with a specific input dataset and fit model. These include the NNPDF3.0 [28], CT14 [29], MMHT2014 [30] and PDF4LHC15 [31] sets. The CT14 PDFs at $Q = 2$ GeV are shown in fig. 2.2. Once the PDFs for a given initial scale Q_0^2 are known, their evolution at different Q^2 values can be determined analytically. This is commonly performed with the DGLAP (Dokshitzer–Gribov–Lipatov–Altarelli–Parisi) equations [32–35].

2.3.2. Matrix elements and cross-sections

The inelastic pp collisions at the LHC, occurring at a high centre of mass energy (\sqrt{s}), are predominantly characterised by the two-body scattering of the type $2 \rightarrow N$, where N denotes the multiplicity of the final state. The interac-

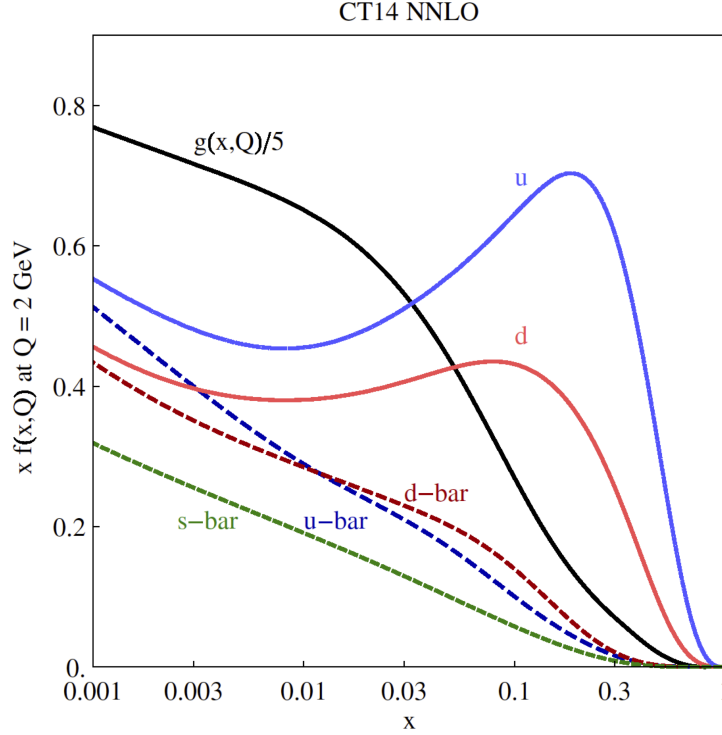


Figure 2.2.: The CT14 parton distribution functions at $Q = 2 \text{ GeV}$. The distributions for u, d, s quarks are shown in blue, red and green respectively. The PDFs for anti-quarks $\bar{u}, \bar{d}, \bar{s} = s$ are displayed in darker colours and with dashed lines. The gluon PDF (black) is suppressed by a factor of 5. Plot sourced from Ref. [29].

tion can be described as the hard scattering of two isolated partons, while the remaining constituents of the colliding protons are spectators. The collisions are characterised by a set of short and long-distance interactions. The first case is associated with a large momentum transfer and can be described perturbatively due to the asymptotic freedom property of QCD. On the other hand, long-distance interactions involve large couplings and are not in a perturbative regime. The computation of the cross-section for a generic process $pp \rightarrow X$, where X denotes the chosen final state, relies on the factorisation theorem to separate the contributions from perturbative and non-perturbative interactions [36]. In particular, the (non-perturbative) effects happening below a chosen factorisation scale μ_F are absorbed into the PDF description. The differential cross-section of the $pp \rightarrow X$

process can then be computed as

$$\frac{d\sigma_{pp \rightarrow X}(\mu_F, \mu_R)}{d\Omega} = \sum_{a,b} \int dx_a f_a(x_a, \mu_F) \int dx_b f_b(x_b, \mu_F) \frac{d\hat{\sigma}_{ab \rightarrow X}(x_a, x_b, \mu_F, \mu_R)}{d\Omega}, \quad (2.42)$$

where a, b are the colliding initial state partons with their respective PDFs $f_{a,b}$, and $\hat{\sigma}_{ab \rightarrow X}$ is the parton-level cross-section corresponding to a centre of mass energy of $\sqrt{\hat{s}} = \sqrt{x_a x_b s}$. The total cross-section is obtained by summing over all the initial state flavours and integrating over the allowed momenta. The scale μ_R is a parameter introduced to ensure the theory is renormalisable. The choice of μ_R and μ_F is arbitrary, and they are commonly set to the same scale of the momentum transfer in the hard scatter process, e.g. $\mu_R = \mu_F = Q^2$. Variations of these parameters in the cross-section computation can be one of the leading sources of uncertainty in the theory predictions, as is the case for the $ZZjj$ measurement discussed in this thesis.

The partonic differential cross-section in eq. (2.42) can be analytically computed in perturbation theory. As mentioned in section 2.1, its value is directly related to the matrix elements of the S-matrix operator. Specifically, the cross-section can be computed by summing the scattering amplitudes of all the allowed Feynman diagrams relating the initial and final states. Namely,

$$\hat{\sigma} \propto \overline{|\sum_i \mathcal{M}_i|^2}, \quad (2.43)$$

where \mathcal{M}_i is the scattering amplitude corresponding to the i -th Feynman diagram, and an average is performed over the initial particles' spin states and colour degrees of freedom. Diagrams can be included up to a certain order of the coupling constant. The lowest order is commonly referred to as Leading Order (LO) and represents the most straightforward approximation of the cross-section, which only considers the simplest diagrams. Each subsequent order increases the accuracy and complexity of the calculation, inserting an additional vertex in the form of real particle emission or virtual loop correction into the allowed diagrams. The higher-order calculations are labelled as Next-to-Leading Order (NLO), Next-to-Next-to-Leading Order (NNLO) and so on. Virtual corrections typically introduce ultraviolet divergences when integrating over the momentum. These are removed with the introduction of the renormalisation scale μ_R in eq. (2.42).

2.4. Physics modelling and event simulation

Once differential cross-sections are calculated to a specific order in perturbation theory, Monte Carlo (MC) event generators are used to make predictions for the fully hadronic final state. Inelastic pp collisions, such as those at the LHC, can lead to the formation of hundreds and hundreds of particles in the final state of an event. Charged particles in the initial and final states can emit additional photons or quarks and gluons (depending if they carry an electric or colour charge), which modify the energy distribution in the event and can also contribute to the formation of additional products in the final state. Quarks and gluons arising from the hard scatter or additional overlapping interactions cannot remain as free particles but need to form bound states of hadrons, thus increasing the particle multiplicity in the final state. As an example to demonstrate the complexity of such interactions, an illustration of a simulated hadron-hadron collision is shown in fig. 2.3. This section summarises the different procedures used to simulate final state events originating from inelastic hadron collisions. A more detailed description of the working principles of MC event generators in particle physics can be found, for example, in Ref. [37].

MC simulations take advantage of a factorisation approach to simplify the difficult computations necessary to obtain the predictions, meaning the simulation proceeds in consecutive steps, each describing a different part of the overall interaction. The different steps are outlined below.

- **Matrix elements computation.** First, the cross-section of the hard scattering is computed perturbatively with the procedure described previously in section 2.3.2, after choosing the appropriate factorisation and renormalisation scales. The desired accuracy (LO, NLO, etc.) is achieved by including matrix elements corresponding to diagrams containing up to a certain number of couplings. The computation is now automated for LO and NLO processes but rapidly becomes more challenging when including higher-order corrections. In the case of high-multiplicity final states, dedicated matrix element generators can be employed along with the main event generator. The differential cross-section must be integrated over the allowed phase space, a procedure that is often not solvable analytically due to its complexity and for the presence of large logarithms. Therefore, MC techniques are used to compute the integral numerically.

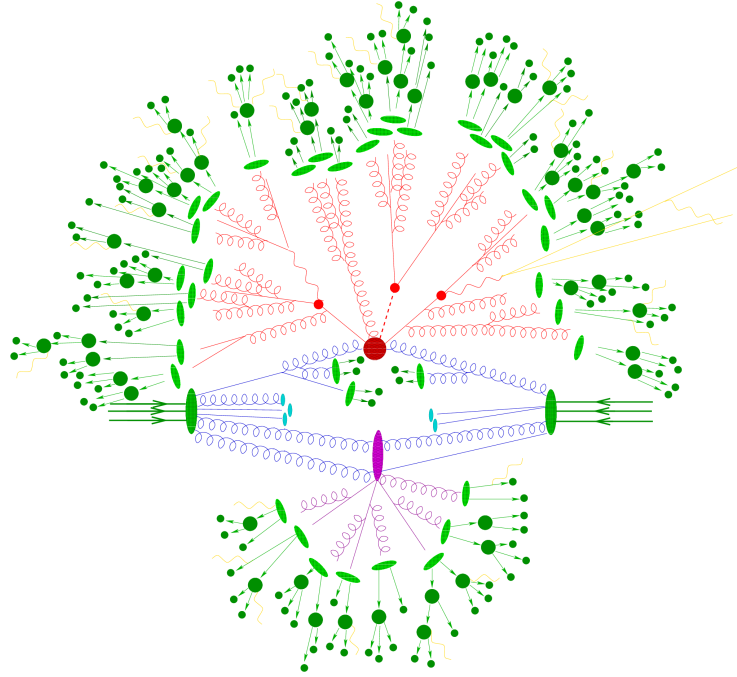


Figure 2.3.: Drawing of a simulated hadron-hadron collision. Different types of interactions are highlighted with different colours and shapes. The hard scatter of the colliding partons is depicted in red, accompanied by Bremsstrahlung and additional quark/gluon emissions as simulated by the parton shower. A secondary hard scattering interaction (underlying event) is depicted with a purple blob. Light and dark green blobs represent parton-to-hadrons and hadron decays, respectively. The radiation of soft photons is shown in yellow. Figure sourced from Ref. [38].

- **Parton shower.** As described above, charged particles can emit additional radiation that adds to the event. Depending on whether the emission occurs in the initial or final state, this phenomenon is referred to as Initial State Radiation (ISR) and Final State Radiation (FSR). The emission of additional particles through ISR and FSR is modelled using parton shower algorithms. These can simulate both the QED radiation (photons) emitted by electrically charged quarks¹⁴ and the QCD radiation stemming from the splitting of quarks and gluons. The parton shower is applied only above a cut-off energy scale, below which the partons can no longer be considered free and colour confinement must be accounted for. Parton shower is described in more detail in section 2.4.1.

¹⁴Some event generator prefer to use a different approach to simulate the electromagnetic emission, based on the YFS formalism [39], particularly in cases where additional QCD radiation is not possible.

- **Hadronisation.** After the parton shower has been developed down to the threshold scale, typically a few GeV, hadronisation takes over. This corresponds to the process by means of which colour-charged particles are grouped to form hadrons. Being a non-perturbative process, hadronisation has to be described with phenomenological models, as described in section 2.4.2.
- **Unstable hadron and τ -leptons decays.** After the hadronisation step, the final state of an event can contain a certain number of unstable particles characterised by a very short lifetime, e.g. τ -leptons or excited mesons and baryons containing heavy quark flavours. In a collider experiment, such particles decay before reaching the active material of the detector. The decays of unstable particles are therefore included in the simulation, using either experimental-constrained models or theoretical assumptions, like simplified matrix elements. The decays' simulation is closely connected with the hadronisation procedure and typically needs to be configured accordingly with the tuning of the latter.
- **Underlying event.** The underlying event refers to the additional activity from the spectator partons which accompany the main hard scatter process. Such interactions typically occur at a smaller energy scale, as most of the initial momentum is transferred in the hard scatter process. They can stem from additional radiation and fragmentation of the beam remnants or interactions between colliding spectators, the latter being referred to as multi-parton interactions (MPIs). The majority of MPIs are constituted by soft $2 \rightarrow 2$ partonic states, which then undergo parton showering and hadronisation. Event generators use different models to simulate MPIs. One of the most established procedures is based on the Sjöstrand and van Zijl model [40]. The model assumes that the semi-hard parton-parton interactions are described in average by the perturbative $2 \rightarrow 2$ matrix element, and uses Poisson statistic to correct the cross-section for the multiplicity of the interactions.

2.4.1. Parton shower

Quarks possess a colour charge and, consequently, can emit gluons, e.g. $q \rightarrow qg$. The gluons can further split into a quark-antiquark pair or a pair of gluons, namely $g \rightarrow q\bar{q}$ and $g \rightarrow gg$. The splitting of gluons and quarks can generate a cascade of strongly interacting particles. This cascade is simulated in MC event generators by

the parton shower, using an iterative procedure. The radiated particles become the new initial state for a consecutive emission until the partons' momenta are below a cut-off threshold, below which the partons are bound into colour-neutral hadrons. An upper threshold is also introduced to avoid double-counting configurations already included in the computation of the matrix elements, and is typically set to the momentum transfer of the hard scatter. The simulation of ISR and FSR is performed with a common procedure, but a different direction of execution. While the FSR trivially follows from the splitting of the hard scatter final state products, the showering of the initial state is obtained with a backward evolution, starting from the hard scatter. In particular, one computes the probability that a parton has originated from one with larger fractional momentum and at a lower scale. This is achieved thanks to the capability of evolving the PDFs at specific values of x and Q^2 with the DGLAP equations.

2.4.2. Hadronisation

After the partons have been showered down to a small momentum scale, typically of the order $O(1 \text{ GeV})$, hadronisation takes over, marking the transition between the partonic final state and the hadronic final state that is experimentally observed. The mechanism through which the partons are combined into hadrons has to be described by a model, due to the non-perturbative nature of the interactions. The two most common models used in MC generators are the Lund string model [41, 42] and the cluster model [43, 44].

- In the string model, the field lines between a quark and an antiquark are considered as a string. In the massless approximation, a $q\bar{q}$ at a time $t = 0$ and position $z = 0$ moves on the light-cone $t^2 - z^2 = 0$ [45]. The string is characterised by a potential $V = kz$, with a tension $k \approx 1 \text{ GeV fm}^{-1}$, which increases as the q and \bar{q} move apart from each other. If the initial energy is high enough, an additional $q\bar{q}$ pair can be created on the string. In case the new quark and anti-quark form a colour-neutral singlet with the original ones, the strong attraction overcomes the tension of the string, which gets split into two disconnected parts. The process is repeated iteratively until the stored energy is too low to create additional pairs. In this picture, a gluon is represented as a kink in the string connecting the $q\bar{q}$ pair, which leads to an asymmetric hadron production in the two newly created strings.

- The cluster model is based on the concept of preconfinement [46–48], which describes the tendency of the parton shower products to form colourless clusters. In the model, virtual gluons below the parton shower cut-off scale are forced to convert into a quark-antiquark pair. All the products are combined to form colour-neutral $q\bar{q}'$ pairs based on their proximity (clusters), which decay into mesons or baryons of a specific flavour and spin.

Both hadronisation models are empirical models and require a tuning of their parameters, which are constrained by experimental observations. However, these tend to be less abundant in the cluster model.

2.4.3. Matching and merging

The production of multiple partons represents one of the most common processes in proton-proton collisions at the LHC. As described above, the $2 \rightarrow N$ cross-section can be perturbatively computed using matrix elements and interfaced with parton shower, hadronisation and underlying event algorithms to simulate the complete hadronic final state. However, the final state's multiplicity may vary with the emission of additional hard partons (e.g. $2 \rightarrow N + 1$, $2 \rightarrow N + 2$, etc.), which should be simulated accordingly to provide a faithful description of the interactions. Although this can be simulated by the parton shower, the computation accuracy for the wide-angle parton emission is limited (leading logarithm in QCD). Therefore, it is preferred to include the additional parton emission in the matrix elements computation before the parton shower stage. In this procedure, the new matrix elements have to be matched (or merged) with the parton shower to provide a single prediction. Matching and merging procedures ensure there is no double-counting of emissions between the matrix elements calculations and the parton shower, and no overlapping or uncovered phase space regions. Specifically, matching refers to corrections applied to the finite-order calculation to integrate the parton shower at the targeted accuracy. Standard implementations of matching algorithms at NLO accuracy used in modern MC event generators follow the MC@NLO [49] or POWHEG [50, 51] prescriptions. Differently, merging refers to the combination of finite-order matrix elements and parton shower via the introduction of a merging scale which defines the transition between the two production mechanisms, ensuring no phase-space overlap. An example of LO merging algorithm is given by the CKKW method [52, 53], and its NLO extension provided by the MEPS@NLO prescription [54]. More details on the different

matching and merging algorithms employed by event generators can be found in Refs. [37, 55].

2.4.4. Monte Carlo event generators

Several MC events generators are employed in particle physics analyses to simulate inelastic pp collisions, differing in the approaches used to calculate matrix elements or model the different components of the interactions discussed above in this section. Matrix elements and parton shower matching and matching techniques also vary across the different event generators. Multi-purpose event generators can simulate both the hard scatter process and the concomitant soft interactions, while specialised generators focus on the computation of matrix elements or in the modelling of parton shower and hadronisation. The relevant multi-purpose generators for the measurement described in this thesis are SHERPA [56] and PYTHIA [57]. Although PYTHIA can generate LO-accurate matrix elements, it is often used in conjunction with other matrix element generators, to simulate the parton shower and hadronisation. This is the case, for example, for hard processes generated with MADGRAPH5_AMC@NLO [58] and POWHEG BOX [50, 51, 59, 60]. A summary of these event generators is given below.

- **PYTHIA** is a multi-purpose generator which can simulate both the hard and soft interactions in a hadron-hadron collision. The simulation of the hard scatter is accomplished by LO-accurate matrix elements calculations, internally provided for a set of hard-coded processes, mainly of the $2 \rightarrow 2$ type. PYTHIA is more commonly interfaced with different matrix element generators to provide modelling of the parton shower, hadronisation and underlying event. The default parton shower algorithm consists of a decreasing- p_T shower development [61], which simultaneously simulates the ISR and FSR branchings. PYTHIA is very versatile regarding the matching and merging of matrix elements and parton showers, with several algorithms available. They include, but are not limited to, the MC@NLO and POWHEG matching methods, and CKKW-L [62] and FxFx [63] merging methods. The simulation of MPIs is based on the Sjöstrand and van Zijl model. The Lund string model is used to simulate the hadronisation process.
- **SHERPA** is a multi-purpose generator capable of calculating matrix elements with a LO and NLO accuracy, using two embedded matrix element generators, AMEGIC++ [64] and COMIX [65]. AMEGIC++ is the default matrix

elements generator, whose calculations are based on a Feynman diagram approach. COMIX is an alternative generator specialised in the computation of matrix elements for high-multiplicity final states. SHERPA employs an integrated parton shower that is based on the Catani–Seymour dipole factorisation [66, 67]. Matrix elements and parton shower matching and merging are performed following the MC@NLO and MEPS@NLO prescriptions, respectively. In this scope, AMEGIC++ is also employed to calculate parton shower subtraction terms to provide NLO predictions for the emission of one parton in the final state. Virtual corrections to the NLO calculations are typically obtained from the OPENLOOPS library [68–70]. The simulation of MPIs is similar to the Sjöstrand and van Zijl model implementation in PYTHIA. The hadronisation is simulated using the SHERPA’s native AHADIC++ [71] implementation of the cluster model discussed in section 2.4.2.

- **MADGRAPH5_AMC@NLO** is the successor of MADGRAPH 5 [72]. It is a matrix element generator that performs calculations at LO and NLO accuracy for an arbitrary process. Tree-level computations are based on Feynman diagrams, with rules provided by the FEYNRULES [73] toolbox. Virtual one-loop QCD corrections are provided by the MADLOOP [74] library. Matching and merging to the parton shower is fully automated when interfacing the matrix elements to PYTHIA. Still, other generators could potentially be used for the parton shower modelling, like HERWIG [75, 76]. Different matching and merging algorithms are implemented in the generator’s framework. At NLO, matching is performed with the MC@NLO method, while merging follows the FxFx prescription. The MC samples generated with MADGRAPH5_AMC@NLO used in the $pp \rightarrow ZZjj$ cross-section measurement described in this thesis were all interfaced to PYTHIA for the simulation of the parton shower, hadronisation and underlying event.
- **POWHEG BOX** is a framework that implements the POWHEG procedure to match NLO matrix elements to the parton shower. One of the main features of this method is the reduction of the fraction of negative event weights that are commonly produced when using the MC@NLO method [77]. For example, some of these negative weights can originate from the subtraction procedure used to correct the NLO computation with the parton shower contribution. The matrix elements obtained from POWHEG BOX are then interfaced with a second generator that provides the parton shower implementation, such

as PYTHIA or HERWIG. NLO calculation for many SM processes are implemented within the POWHEG BOX framework. These include the EW $ZZjj$ production [78], one of the signal processes targeted by the cross-section measurement described in chapter 5. Also in this case, the MC samples employed in the measurement used PYTHIA to obtain the hadronic final state.

2.5. Jet reconstruction

A direct consequence of the parton shower fragmentation and hadronisation discussed in section 2.4 is the formation of a series of different particles that are emitted nearly collinear to each other. Experimentally, this is observed as a stream of collimated hadrons, which are collectively referred to as jets. A jet is an abstract object, defined by clustering close-by hadrons in an attempt to trace back the properties of the single particle which initiated the showering process. In this sense, the momentum of a jet, obtained by summing the contributions of all its single components, directly corresponds to the momentum of the original parton. Jets represent one of the most frequent experimental signatures in pp collision events at the LHC. This is the case for the measurement presented in this thesis, where two jets (dijet) are present in the final state.

Several jet algorithms have been implemented, which combine the final state particles using different clustering techniques. An example is given by cone clustering algorithms, where a jet is formed by all the particles whose trajectories fall within a cone of a predefined radius that is centred on a selected particle (typically of greater transverse momentum p_T). A different procedure is used in the anti- k_T algorithm [79], one of the most widely used jet reconstruction techniques, also used to obtain the jets in the measurement discussed in chapter 5. The anti- k_T algorithm is a combinatorial procedure that forms conglomerates from a set of initial objects based on a minimum distance metric. The distance between entries i and j is defined as

$$d_{i,j} = \min \left(\frac{1}{p_{T,i}^2}, \frac{1}{p_{T,j}^2} \right) \frac{\Delta R_{i,j}^2}{R}, \quad (2.44)$$

where $\Delta R_{i,j}$ is the angular separation¹⁵ between the two objects, and R is a radius parameter, usually set to 0.4. This quantity is then compared to the distance from

¹⁵See eq. (3.7) in section 3.2.1 for a definition of this variable as done in ATLAS.

the beam remnants, defined as $d_{i,B} = \frac{1}{p_{T,i}^2}$. If $d_{i,j} < d_{i,B}$, the two objects i and j are combined. Otherwise, if $d_{i,B} < d_{i,j}$, the object i is defined as a jet and removed from the list. The process is then repeated until no entries are left. Among the algorithm's properties, we emphasise that it is infrared and collinear safe. This means that additional splitting at small angles and soft emissions do not change the jet structure of the final state.

Chapter 3.

The ATLAS experiment

This chapter discusses the ATLAS experiment at the Large Hadron Collider (LHC). Section 3.1 introduces the LHC accelerator complex and the main experiments operating at the CERN facilities. A technical description of the ATLAS detector and its subsystems is given in section 3.2. Section 3.3 follows with a review of the techniques employed to reconstruct physical objects from the raw data acquired by the detector.

3.1. The Large Hadron Collider

The LHC is a world-leading particle accelerator built at CERN, on the France and Switzerland border. It was designed to accelerate and collide beams of protons up to a maximum centre-of-mass energy of $\sqrt{s} = 14$ TeV [80–82]. During its first running period, also referred to as Run 1 (2011-2012), the accelerator operated at a lower capacity, reaching an energy of $\sqrt{s} = 7$ TeV in the first year and $\sqrt{s} = 8$ TeV in the second. After a technical stop (Long Shut-down 1), the LHC resumed its operation in 2015 at an increased energy equal to $\sqrt{s} = 13$ TeV. A second data-taking period, called Run 2, lasted from 2015 to 2018, and it was followed by another shutdown. The year 2022 marked the beginning of Run 3, with an even higher energy of $\sqrt{s} = 13.6$ TeV. Run 3 is expected to last until 2025 and is foreseen to deliver more collision data than the two previous runs combined.

The energy of protons is increased in steps, through a chain of different particle accelerators, until it reaches the target value for collisions. Protons are initially extracted from a bottle of hydrogen gas. The atoms are ionised and injected into a linear accelerator, Linac2, which increases their energy to 50 MeV. They are then

accelerated by the Proton Synchrotron Booster (PSB) to an energy of 1.4 GeV and by the Proton Synchrotron (PS) to an energy of 26 GeV. A further acceleration up to an energy of 450 GeV occurs in the Super Proton Synchrotron (SPS) before the protons are injected in the main LHC ring and reach their final energy. The main ring of the accelerator is 26.7 km long and occupies the same tunnel which previously hosted the Large Electron-Positron (LEP) collider [83, 84]. A schematic of the accelerator complex at CERN is illustrated in fig. 3.1. In 2020, before the start of Run 3, Linac2 was replaced by a new linear accelerator Linac4 [85], which increases the proton energy at the end of the first acceleration stage to 160 MeV.

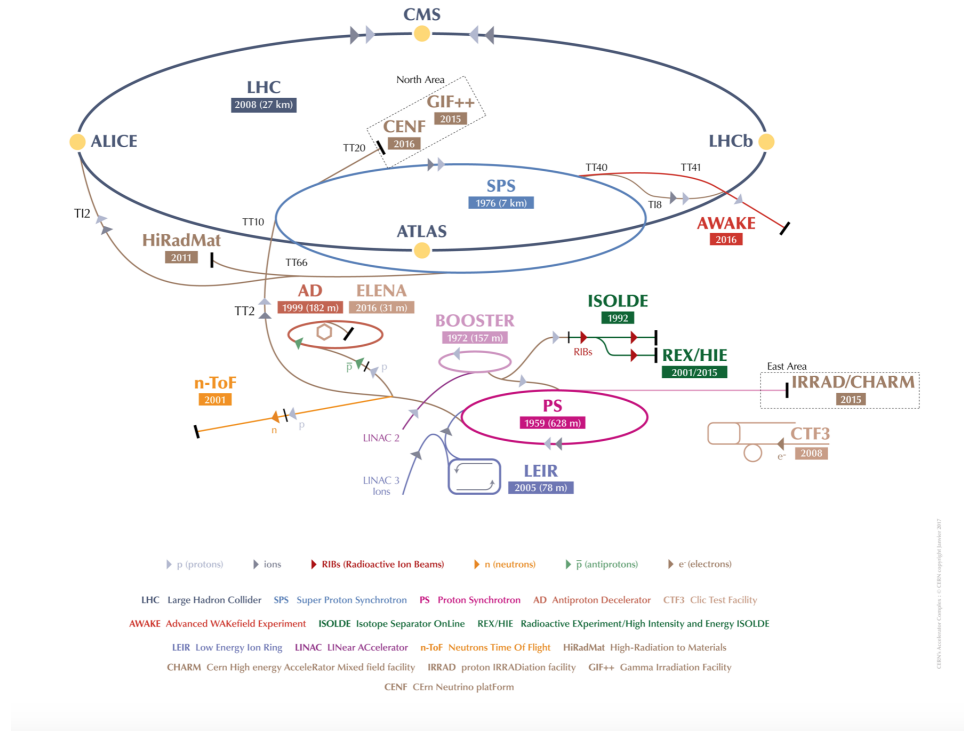


Figure 3.1.: Schematic of the accelerator complex at CERN. Figure from [86].

In the main ring of the LHC, two beams of protons travel in opposite directions, in separate beam pipes, and are made to collide at four different interaction points. The LHC ring is segmented into eight arcs, with eight additional straight sections to inject or dump the beam. The trajectory of the particles is carefully adjusted by different magnet systems. More than 1200 dipole magnets provide a 8 T magnetic field to maintain the particles in a circular trajectory. These 15 m-long electromagnets are made of superconducting coils (NbTi) driving a current of over 11 kA to generate the magnetic field. Liquid helium cools down the magnets below

2 K to ensure they operate in a superconducting state. Quadrupole magnets are used to focus the beam and regulate its vertical and horizontal spread. Sextupole, octupole and decapole magnets are also employed for smaller corrections to the trajectory. The particles are accelerated with 16 Radio Frequency (RF) cavities (8 per beam) providing an electromagnetic field, which is made to oscillate at nearly 400 MHz. Each cavity can reach a voltage of 2 MV, corresponding to a total of 16 MV per beam. The oscillating field has a synchronising effect on the particles, in such a way that they are not accelerated if they have the right energy and revolution frequency, but are either sped up or slowed down otherwise. As a consequence, the beams become segmented into bunches. In normal conditions, there are up to ≈ 2800 proton bunches per beam, each temporally separated by 25 ns from the consecutive one.

Nine experiments operate at the LHC to measure the properties of particles arising from the collisions. The largest ones, ATLAS, CMS, LHCb and ALICE, are placed at the four interaction points. They are:

ATLAS (A Toroidal LHC ApparatuS) [87] is a general-purpose detector, designed to maximise the acceptance and hermeticity to detect different particles with a typical energy in the GeV and TeV scale. Its vast physics program involves measurements of SM processes and searches for new physics, including extra dimensions and dark matter. The apparatus is fully described in section 3.2.

CMS (Compact Muon Solenoid) [88] is another general purpose detector with similar intent and performance of ATLAS. Differently from the latter, it utilises a single magnetic field provided by a superconducting solenoid from which it takes its name. Measurements performed with the CMS detector are expected to be compatible with the ones provided by ATLAS, thus ensuring the reproducibility of the results.

LHCb (Large Hadron Collider beauty) [89] is a specialised detector which focuses on the measurements of b quarks to investigate flavour physics and study the matter-antimatter asymmetry in the universe. The detector is a single-arm spectrometer composed of several sub-detector layers arranged in the forward direction.

ALICE (A Large Ion Collider Experiment) [90] specialises in the study of heavy-ion interactions. In special runs of the LHC, lead ions are made to collide to form a quark-gluon plasma, a mixture of quarks and gluons freed from their

confinement due to the extreme temperatures reached in the collisions. A general-purpose detector is used to study the quark-gluon plasma to better understand QCD interactions and the nature of confinement.

TOTEM (TOTal cross section, Elastic scattering and diffraction dissociation Measurement at the LHC) [91] is the longest experiment at the LHC, with several small sub-detectors scattered over more than 400 m along the beam line near the CMS interaction point. This experiment aims to perform precision measurements of the total pp cross-section by detecting protons which emerge from the collision in the very forward direction, an area which is not accessible by the larger experiments.

LHCf (Large Hadron Collider forward) [92] is also a forward-physics experiment, made of two detectors placed 140 m far from ATLAS on both sides. It aims to study particles that mimic cosmic rays' behaviour, thus allowing to better constrain shower models and help to calibrate larger scale experiments.

MoEDAL (the Monopole and Exotics Detector at the LHC) [93] is a small detector close to the LHCb interaction point. It aims to search for magnetic monopoles and other exotic particles that would indicate new physics beyond the SM.

FASER (ForWard Search ExpeRiment) [94] is a new detector, placed 480 m downstream of ATLAS, which started its operation in Run 3. The experiment aims to study light and weakly interacting particles that can escape from the ATLAS detector, such as neutrinos and muons, in a region where the background from well-known SM processes is suppressed.

SND@LHC (Scattering and Neutrino Detector at the LHC) [95] also started operations in Run 3 and consists of a neutrino and muon detector. It is located near ATLAS, slightly off the LHC beamline, to measure particles emerging at low angles.

The interaction rate at the LHC depends on the beam dimensions and dynamics, and it can be expressed in terms of the instantaneous luminosity (\mathcal{L}). For head-on collisions, the per-bunch instantaneous luminosity is defined as

$$\mathcal{L}_b = \frac{f_R N_1 N_2}{2\pi \Sigma_x \Sigma_y} = \frac{f_R \mu}{\sigma_{inel}}, \quad (3.1)$$

where N_1 and N_2 are the number of particles in the two colliding bunches, f_R is the LHC revolution frequency and $\Sigma_j = \sqrt{\sigma_{j,1}^2 + \sigma_{j,2}^2}$ represents the convolved beam dimensions in the $j = (x, y)$ direction (transverse plane). In the case of non-head-on collisions, the longitudinal spread of the beam contributes to the value of Σ , thus leading to a degradation of the luminosity [96]. Assuming the beams collide with a half-crossing angle (α), without any beam displacement in the transverse plane, the luminosity can be written as $\mathcal{L}_b = F \mathcal{L}_b^{(head-on)}$, with $F \propto \cos(\alpha)$. At the LHC, the beams collide with a crossing angle of about $285 \mu\text{m}$ [80], resulting in a geometrical attenuation factor of $F \approx 0.84$. As indicated in eq. (3.1), the instantaneous luminosity can also be related to the average number of interactions per bunch crossing (μ), also called pile-up term, and to the inelastic proton-proton cross-section (σ_{inel}).

The total instantaneous luminosity is obtained from eq. (3.1) by summing over the n_b colliding bunch pairs

$$\mathcal{L} = \sum_{n_b} \mathcal{L}_b = n_b \langle \mathcal{L}_b \rangle = \frac{n_b f_R \langle \mu \rangle}{\sigma_{inel}}, \quad (3.2)$$

having indicated the average per-bunch luminosity with $\langle \mathcal{L}_b \rangle$ and the average pile-up coefficient with $\langle \mu \rangle$. The LHC was designed to operate with a peak instantaneous luminosity of $\mathcal{L} = 1 \times 10^{34} \text{ cm}^{-2} \text{ s}^{-1}$. The peak instantaneous luminosity delivered by the LHC saw a continuous ramp-up from its first operation. During Run 1, it increased from $2.0 \times 10^{32} \text{ cm}^{-2} \text{ s}^{-1}$ in 2010 to $3.6 \times 10^{33} \text{ cm}^{-2} \text{ s}^{-1}$ by the end of 2011 [97]. Similarly, Run 2 started in 2015 with a peak luminosity of $5 \times 10^{33} \text{ cm}^{-2} \text{ s}^{-1}$, raised to $19 \times 10^{33} \text{ cm}^{-2} \text{ s}^{-1}$ in 2018 [98].

The interaction rate for a given process can be written as

$$R = \mathcal{L} \sigma, \quad (3.3)$$

with σ being the cross-section of the process. The total number of events occurring over a specific period is obtained by integrating eq. (3.3):

$$N = \sigma \int \mathcal{L} = L_{int} \sigma. \quad (3.4)$$

The integrated luminosity L_{int} is used to quantify the amount of data collected during a period of data acquisition. In Run 2, ATLAS recorded about 140.1 fb^{-1} of

data with quality good enough to perform physics analyses. Figure 3.2 shows a plot of the integrated luminosity delivered by the LHC and recorded by ATLAS after different periods of Run2. The luminosity-weighted distribution of the pile-up in Run 2 is also shown in fig. 3.3.

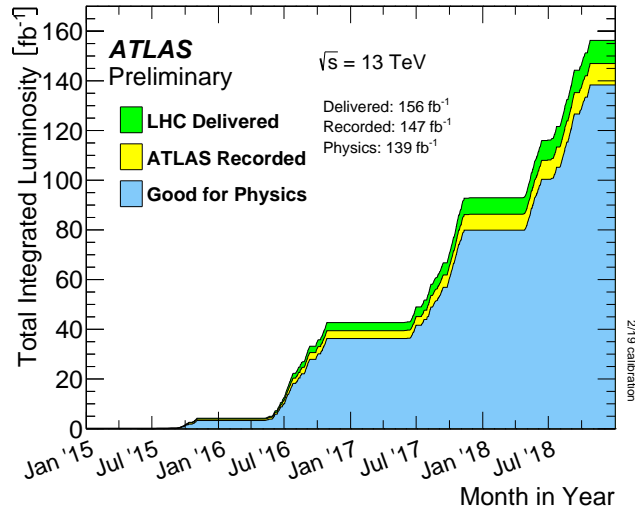


Figure 3.2.: Cumulative of the luminosity delivered by the LHC in Run2 (green). The corresponding amount of data recorded by ATLAS is shown in yellow, of which the subset having good quality for physics analyses is shown in blue. In a more recent and more precise measurement, the total Run 2 luminosity value was found to be 140.1 fb^{-1} [98]. Figure sourced from [99].

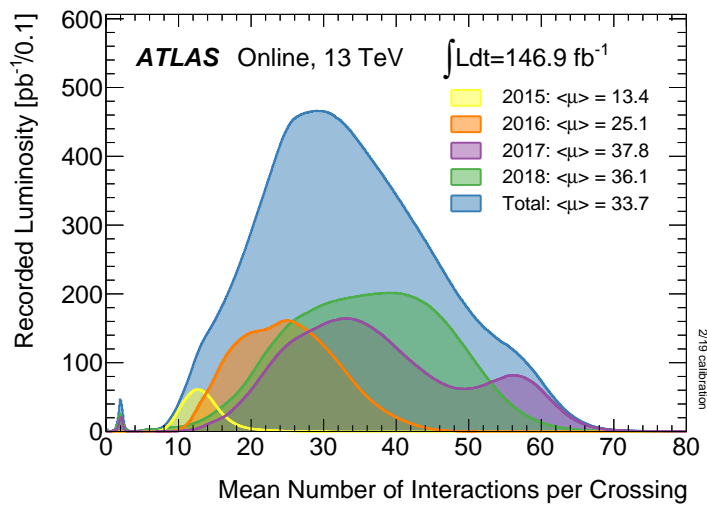


Figure 3.3.: Year specific and total luminosity recorded by ATLAS during Run 2 as a function of the average number of interactions per bunch crossing. The value of μ was obtained by inverting eq. (3.2) and assuming a cross-section of $\sigma_{inel} = 80 \text{ mb}$ for collisions at $\sqrt{s} = 13 \text{ TeV}$. Figure sourced from [99].

3.2. The ATLAS detector

A general-purpose detector such as ATLAS does not target a specific physics process but is rather designed and optimised to identify the plethora of different particles that emerge from proton collisions. The detector is massive, with a length of about 46 m and a radius of 25 m. It is located underground, in a cavern 100 m below the surface, to reduce the background induced by cosmic rays. The detector is composed of different sub-systems arranged in layers, each specialised in detecting different types of particles. A tracking detector, also referred to as Inner Detector (ID), is responsible for reconstructing the charge and momenta of charged particles travelling through it. The ID is enclosed in a solenoid magnet providing an axial field of 2 T [100] which bends the trajectory of the charged particles, thus allowing the measurement of their momentum. The following layer consists of two calorimeters, one electromagnetic and one hadronic, to measure the energy of photons, electrons and hadrons which are usually completely absorbed by them. Conversely, muons escape from the calorimeter due to their low interaction rate with matter. A dedicated Muon Spectrometer (MS) is placed after the calorimeters to measure their momenta. The spectrometer is immersed in a magnetic field up to 3.5 T produced by a toroidal magnet. In the central part of the detector, the magnet is composed of eight coils which are about 25.3 m long and arranged to form a toroid with an outer diameter of 20.1 m [101]. The forward regions of the detector are covered by two additional toroids that are placed on each side [102].

The sub-detectors of ATLAS are described in more detail in sections 3.2.2 to 3.2.4. The layered structure of ATLAS allows to discriminate between different types of particles by looking at their characteristic signatures in each sub-detector. Electrons interact with the active material of the ID, before they are absorbed in the electromagnetic calorimeter. Similarly, photons deposit their energy in the calorimeter, but leave no trace in the ID. Hadrons can also deposit a small fraction of their energy in the electromagnetic calorimeter, with the remaining part being absorbed by the hadronic calorimeter. They can also be detected by the ID depending on their electrical charge. As explained above, muons escape the detector after passing through both the ID and the MS. When they collide, protons have close to zero transverse momentum, which is a conserved quantity of the process. A non-closure of the total transverse momentum in the final state would indicate the presence of particles which were not detected. Neutrinos, and other weakly interacting particles which have a small probability of interacting with the

detector material, are therefore indirectly observed by searching for a momentum imbalance in the events.

3.2.1. Coordinate system

A conventional coordinate system is used for all the measurements performed within ATLAS. A right-handed three-dimensional Cartesian system is adopted, with origin ($x = 0, y = 0, z = 0$) corresponding to the nominal interaction point at the centre of the detector. The xy plane corresponds to the transverse plane, and the two axes \hat{x} and \hat{y} are respectively oriented toward the centre of the LHC ring and upward. The \hat{z} axis is parallel to the beam direction, and its sign defines two opposite regions of the detector, "side-A" for positive values of z and "side-C" for negative z values. Angles θ and ϕ correspond to the angle with respect to the beamline and the azimuthal angle in the transverse plane, respectively. A schematic of the reference system is given in fig. 3.4.

The kinematics of a particle is described by its momentum $\vec{p} = (p_x, p_y, p_z)$ and energy E . Due to the momentum conservation, physics analyses typically use the corresponding quantities projected on the transverse plane: $p_T = \sqrt{p_x^2 + p_y^2}$ and $E_T = E \sin \theta$. The rapidity of a particle is defined as

$$y = \frac{1}{2} \ln \left(\frac{E + p_z}{E - p_z} \right). \quad (3.5)$$

For particles with momentum much larger than their mass, eq. (3.5) can be approximated by the pseudorapidity,

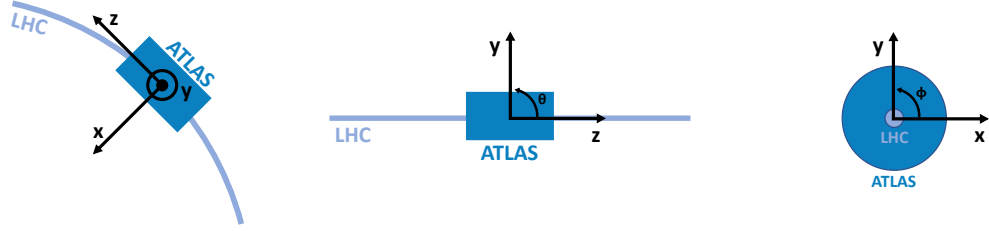
$$\eta = -\ln \left(\tan \left(\frac{\theta}{2} \right) \right). \quad (3.6)$$

Small (large) values of η correspond to a position in the central (forward) region of the detector. The pseudorapidity sign follows the same A/C-side convention of the z axis. Along with ϕ , y and η are also used to quantify the angular separation ΔR between two particles, expressed as

$$\Delta R(y, \phi) = \sqrt{(\Delta y)^2 + (\Delta \phi)^2}, \quad (3.7)$$

$$\Delta R(\eta, \phi) = \sqrt{(\Delta \eta)^2 + (\Delta \phi)^2}, \quad (3.8)$$

with Δy , $\Delta\eta$ and $\Delta\phi$ being the corresponding y, η, ϕ difference between the two particles.



(a) View from above ATLAS.

(b) View facing ATLAS.

(c) Transverse section.

Figure 3.4.: Schematics of the reference system used in ATLAS. The detector is depicted in blue, with the LHC beamline in a lighter tone. The \hat{x} axis is parallel to the ground and points toward the LHC centre. The \hat{y} axis is vertically oriented and pointing upward, while the \hat{z} axis is parallel to the beamline.

3.2.2. Inner Detector

The Inner Detector [103, 104] occupies the closest region to the nominal interaction point. With a length of about 7 m and a radius of 2.3 m, it provides full coverage in the azimuthal angle ϕ within $|\eta| < 2.5$. The ID comprises three sub-systems that employ different technologies to detect charge particles travelling in their volume. A pixel detector is placed next to the interaction point, where the track density is larger and a greater granularity is required for the vertex detection. Moving outward, the pixel detector is surrounded by a SemiConductor tracker (SCT) and a Transition Radiation Tracker (TRT). When a charged particle passes through the active material of the detector, it produces an electric signal that is registered as a hit. All the sub-systems present a layered structure, in such a way that the track of a particle can be reconstructed from a collection of hits as described in section 3.3.1. The structure of the ID can be observed in figs. 3.5 and 3.6, which show respectively a 3D visualisation of a cross-section of the central part of the ID (barrel) and a schematic of the whole detector. To achieve the physics goals of the ATLAS experiment, the ID was designed to measure the momenta of charged particles with a resolution of [87]

$$\frac{\sigma_{p_T}}{p_T} = 0.05\% \cdot p_T \oplus 1\%, \quad (3.9)$$

where σ_{p_T} is the resolution of the p_T measurement.

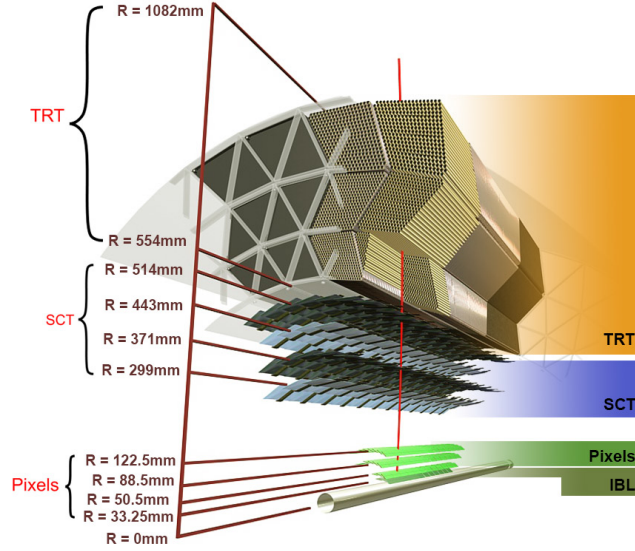


Figure 3.5.: 3D model of the cross section of the Inner Detector barrel region [105]. Different sub-systems composing the ID are placed with increasing radii from the nominal interaction point: the pixel detector (including the IBL), the SemiConductor tracker and the Transition Radiation Tracker.

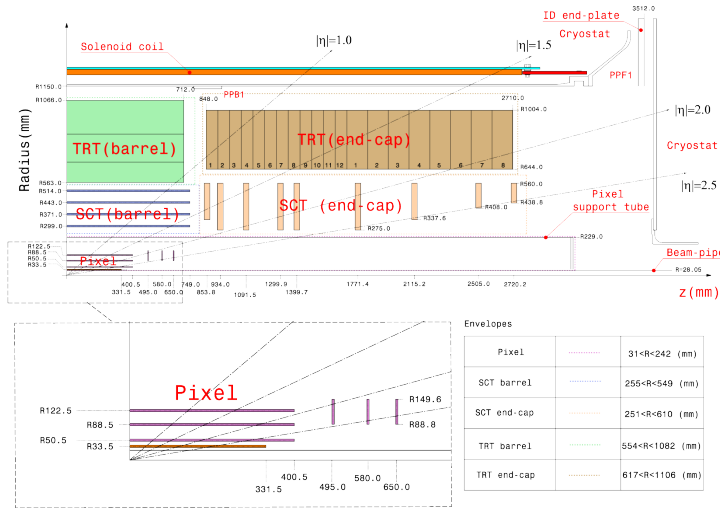


Figure 3.6.: Design of a quadrant of the Inner Detector sourced from [106]. Tracking coverage spans the full azimuthal angle and up to $|\eta| < 2.5$.

The pixel detector [107] occupies the region closest to the interaction point defined with a radius $r < 242$ mm, and comprises a barrel and two end-caps. The barrel consists of three co-axial cylinders of increasing radii (50.5 mm, 88.5 mm and 122.5 mm) enclosing the beamline and centred on the nominal interaction

point. The end-caps are placed at the sides of the barrel, each made of three identical disks placed at $|z| = 495$ mm, $|z| = 580$ mm and $|z| = 650$ mm. Charged particles are detected with planar silicon pixel sensors of average dimension $50\text{ }\mu\text{m} \times 400\text{ }\mu\text{m}$ [108]. The sensors are arranged over 1744 modules, for a total of more than 80 million channels. In the barrel, the modules are attached to long staves which are inclined 20° with respect to the azimuthal angle. In the end-caps, they are attached to the disks and subdivided into eight sectors per disk to provide adequate mechanical support and cooling. The total active area covered by the pixels amounts to around 1.7 m^2 .

After the successful completion of Run 1, during the first long shut-down, an additional layer of pixel sensors was inserted in the space between the beam pipe and the innermost layer of the pre-existing pixel detector. This Insertable B-Layer (IBL) [109, 110] complements the pixel system with around 12 million additional channels. The IBL employs sensors with smaller dimensions of $50\text{ }\mu\text{m} \times 250\text{ }\mu\text{m}$ to improve the tracking performance and to cope with the larger interaction rate and track density caused by the increased Run 2 luminosity. Both planar and 3D pixels are used. The planar pixels are an improved design of the sensors used in Run 1, while the 3D pixels are a new technology which grants greater radiation hardness.

The SCT [111, 112] is a semiconductor strip detector which surrounds the pixels in the region $242\text{ mm} < r < 560\text{ mm}$. It has a barrel and end-caps structure with a total of 63 m^2 of silicon micro-strips covering a region up to $|\eta| < 2.5$. Four cylindrical layers compose the barrel part, while nine disks are present in each end-cap. The barrel has 2112 modules of silicon micro-strips of uniform design. Each module is made of four rectangular-shaped sensors, two on the top and two on the bottom glued back to back, which have 768 readout channels at a constant pitch of $80\text{ }\mu\text{m}$ and are arranged in parallel to the \hat{z} direction. The sensors' geometry in the end-caps is more complex and driven by the necessity of achieving full coverage within the area of the disks. There are five trapezoidal sensors of different dimensions and variable pitch sizes (from approximately $57\text{ }\mu\text{m}$ to $94\text{ }\mu\text{m}$) that are grouped to form 988 modules per end-cap.

The TRT [113–115] is the outermost system of the ATLAS ID, occupying the region up to around 1066 mm from the centre. In contrast to from the previous sub-systems, the TRT does not use silicon-based detectors but gaseous ones. The key element of the detector is the strawtube (straw), a proportional drift tube

which acts both as a tracking device and an electron identification device (via the absorption of the transition radiation generated in its multi-layered walls). The straws have an axial structure, with a diameter of 4 mm, and a 31 μm -diameter gold-plated tungsten wire anode. The tubes are filled with a mixture of different gases (70% Xe, 27% CO_2 and 3% O_2) and typically operate at a high-voltage of about 1530 V. The length and orientation of the straws differ in the barrel and the end-caps. In the first case, 52544 144 cm-long straws are placed in parallel to the beam direction. Each end-cap has 122880 straws of approximately 37 cm length arranged in the radial direction.

3.2.3. Electromagnetic and Hadronic Calorimeters

The calorimeters in ATLAS are placed outside the solenoid magnet and are responsible for measuring the position and energy of particles that interact electromagnetically or strongly with their material. High-energy photons, electrons and positrons interact with the material of the electromagnetic calorimeter, initiating a shower of particles through pair production and bremsstrahlung. Similarly, hadrons produce a cascade of secondary particles in strong interactions with the material of the hadronic calorimeter. In a sampling calorimeter, like the ones used in ATLAS, multiple layers of active and absorber material are interleaved to measure the energy lost by the incoming particles in the interactions. The energy resolution of a calorimeter (σ_E) can be typically expressed as

$$\frac{\sigma_E}{E} = \frac{a}{\sqrt{E}} \oplus \frac{b}{E} \oplus c, \quad (3.10)$$

where a is the stochastic term accounting for fluctuations of the produced particles, lateral containment of the shower and the sampling nature of the measurement, b is a noise term, and c is related to inhomogeneities of the material composing the detector. The calorimeters' design performance goals are summarised in table 3.1.

Figure 3.7 illustrates the different components of the calorimeter system in ATLAS. The electromagnetic calorimeter [116], composed of a barrel and two end-caps, is made of liquid Argon (LAr) and lead-stainless-steel absorber. The use of LAr as the active material benefits from its linear energy response and radiation hardness. Furthermore, the liquid state assists in reaching perfect coverage. The electromagnetic barrel reaches a pseudo-rapidity of $|\eta| < 1.475$ and is divided into

Calorimeter	σ_E/E
Electromagnetic	$10\%/\sqrt{E} \oplus 0.7\%$
Hadronic (barrel and end-caps)	$50\%/\sqrt{E} \oplus 3\%$
Hadronic (forward)	$100\%/\sqrt{E} \oplus 10\%$

Table 3.1.: Design resolution of different calorimeter systems in ATLAS after noise subtraction [87].

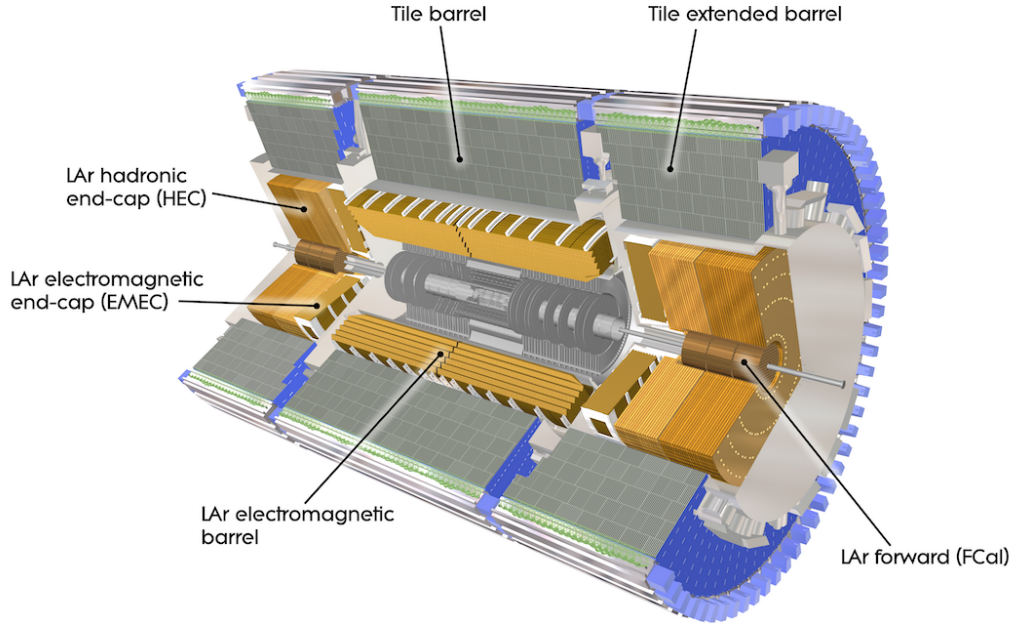


Figure 3.7.: Layout of the ATLAS calorimeter system. Figure sourced from [87].

two identical cylinders separated at $z = 0$ with a 4 mm-gap, each composed of 1024 accordion-shaped layers of Pb absorber and readout boards. The accordion shape ensures a continuous acceptance in ϕ without any gap. The barrel modules are radially segmented into three layers, as shown in fig. 3.8a. A first layer with a fine granularity allows to measure the position of incoming particles with a precision of $\Delta\eta \times \Delta\phi = 0.0031 \times 0.098$. The central layer is the thickest one, with cells of dimensions $\Delta\eta \times \Delta\phi = 0.025 \times 0.0245$ and a radiation length of around $16 X_0$, thus containing most of the electromagnetic shower¹. A coarser third layer

¹The radiation length X_0 is a characteristic of the material and indicates the distance after which an electron loses in average a factor $\left(1 - \frac{1}{e}\right)$ of its energy by bremsstrahlung.

($\Delta\eta \times \Delta\phi = 0.05 \times 0.0245$) is placed on top to measure the energy in case of longitudinal shower leakage.

The electromagnetic end-caps (EMEC) [116] expand coverage in the range $1.375 < |\eta| < 3.2$ and consist of two LAr-Pb wheels, each placed alongside the barrel at positive and negative pseudorapidity values. The wheels are subsequently divided into an inner and outer coaxial wheel separated at $|\eta| = 2.5$. The EMEC modules are similar to the barrel ones, made of the same materials and with the characteristic accordion shape. The outer wheel has a total of 768 absorber layers, while the inner has 256. An additional active layer of LAr, 1 cm-wide and 5 mm-wide respectively in the barrel and end-caps, is placed in front of the electromagnetic calorimeter up to $|\eta| < 1.8$. This presampler is necessary to measure the energy lost by the incoming particles when interacting with the dead material before the calorimeter (ID, coil, etc.).

The Tile calorimeter [117] measures the position and energy of hadrons in the barrel region $|\eta| < 1.7$. It has an inner and outer radius of 2280 mm and 4230 mm respectively, and is subdivided into three cylinders. The central barrel is 5640 mm long and spans the pseudorapidity range $|\eta| < 1$, while the two extended barrels are 2910 mm long and occupy the regions $0.8 < |\eta| < 1.7$. A 60 cm gap is allocated between each cylinder to host the electronics and services of the ID and LAr calorimeter. The building blocks of the Tile calorimeter are its wedge-shaped modules, an assembly of several plates of plastic scintillator and steel absorber, illustrated in fig. 3.8b. Each barrel cylinder contains 64 modules radially arranged, corresponding to a ϕ segmentation of 0.1 rad. The scintillating tiles are placed perpendicular to the beam direction and are staggered in depth. The light produced by the scintillators is collected by wavelength-shifting fibres and delivered to a photomultiplier for signal extraction. The modules are longitudinally segmented into three layers with a transverse readout cell of $\Delta\eta \times \Delta\phi = 0.1 \times 0.1$. The combined interaction length² amounts to a total of 7.4λ .

The hadronic end-caps (HEC) calorimeter [116] is placed right after the EMEC, of which it shares the same cryostat. Each end-cap covers the range $1.5 < |\eta| < 3.2$ and is composed of two identical, independent wheels. Similarly to the EMEC, the HEC uses LAr as its active material, while copper is used as the absorber. The sampling is achieved through layers of copper plates separated by a 8.5 mm

²The interaction length λ denotes the average distance hadrons travel in a medium before a nuclear interaction occurs.

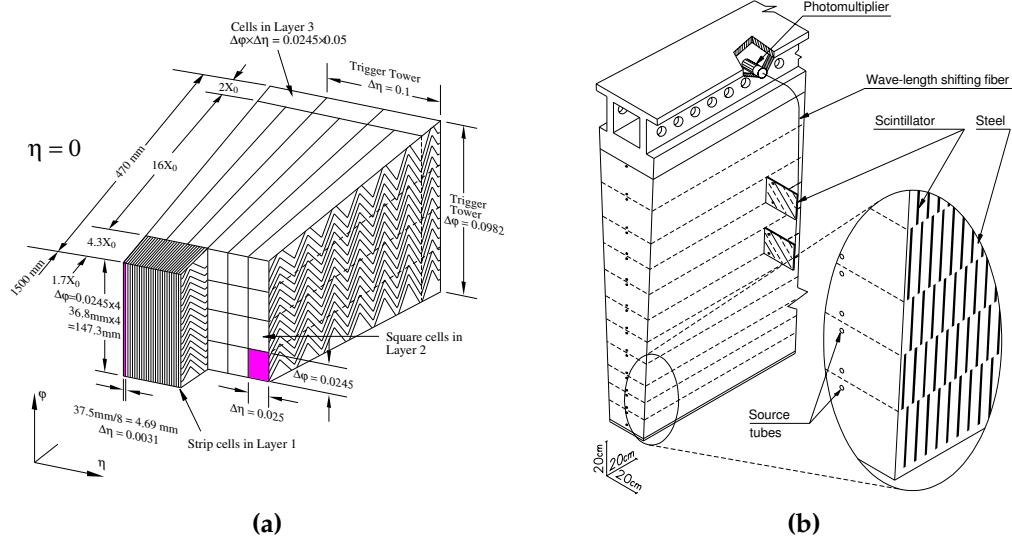


Figure 3.8.: Drawings of an electromagnetic LAr barrel (a) and a Tile (b) module. Figures sourced from [87].

gap filled with LAr. The plate's width is 25 mm in the inner wheel and 50 mm in the outer. The wheels are assembled from 32 identical modules providing a granularity of $\Delta\eta \times \Delta\phi = 0.1 \times 0.1$ up to $|\eta| < 2.5$, and $\Delta\eta \times \Delta\phi = 0.2 \times 0.2$ elsewhere.

A further calorimeter, the FCal [116, 118], covers the forward region of the detector at $3.1 < |\eta| < 4.9$. FCal is placed nearly 5 m upstream (downstream) of the interaction point, in the space between the pipe and the HEC, housed in the same cryostat. The calorimeter is segmented into three longitudinal sections, or modules, (FCal 1 to FCal 3) which provide both electromagnetic and hadronic measurements. The innermost section (electromagnetic) is composed of LAr and copper absorber, while the remaining two (hadronic) are based on LAr and tungsten. The module's geometry is the same for all three components and consists of a metallic cylinder, roughly 44 cm deep with a 45 cm outer radius, inside of which a series of concentric rods and tubes are inserted to form a matrix. The rods are as long as the module and act as electrodes. LAr fills a gap between the rod and its tube, thus establishing the sampling nature of the calorimeter. LAr gaps are smaller than in the electromagnetic barrel and end-caps, getting as small as 250 μm in FCal 1, and provide a very fast signal. FCal 1 is about $28 X_0$ deep, and the three sections reach a combined interaction length of around 10λ . This structure yields a high-density calorimeter, thus reducing potential shower

leakage in the neighbouring detectors. The very forward positioning also helps in reaching good calorimetric hermeticity.

3.2.4. Muon spectrometer

Muons typically escape the volume of the calorimeters as their electromagnetic interactions are suppressed by a factor $(m_e/m_\mu)^2 \approx (1/200)^2$. A dedicated sub-system, the Muon Spectrometer [119], is placed in the outer region of ATLAS to independently determine the momentum of charged particles escaping the inner sub-systems. The toroid magnet is incorporated into the MS, providing the necessary bending power for the momentum and charge measurement. Like the ID and the calorimeters, the MS also presents a barrel plus end-caps structure and uses several technologies to achieve good physics performance in different parts of the detector. The design resolution for the transverse momentum of 1 TeV-tracks amounts to $\frac{\sigma_{p_T}}{p_T} = 10\%$. The layout of the spectrometer is shown in fig. 3.9.

Precision tracking is achieved with monitored drift tube (MDT) chambers, used in most of the MS, up to $|\eta| < 2.7$. The chambers are rectangular in the barrel and trapezoidal in the end-caps. They consist of a series of 3 cm-diameter drift tubes containing a pressurised gas mixture. Ar and O₂ in a 93 : 7 ratio are used, due to the mixture's resistance to ageing phenomena. An axial tungsten-rhenium wire is placed at a potential of 3080 V to collect the ionised charges. The average spatial resolution for a tube is 80 μm , corresponding to 35 μm per chamber. In the barrel, the chambers are arranged in three concentric layers centred on the beamline, roughly at $r = 5\text{ m}$, 7.5 m , and 10 m . In the end-caps, the chambers form wheels in the transverse plane, displaced by 7.4 m, 10.8 m, 14 m, and 21.5 m from the interaction point at positive and negative z . The innermost layer of the end-caps ($2 < |\eta| < 2.7$) hosts cathode-strip chambers (CSCs) instead of MDTs, due to the larger flux of particles expected in this region. Despite having a slightly worse spatial resolution, the CSCs can operate at a higher rate, thus ensuring a good efficiency is maintained in this region of the detector. The CSCs are multiwire proportional chambers filled with 80% Ar and 20% O₂. The wires (anodes) are stretched in the radial direction and work at a potential of 1900 V. The wire-wire and anode-cathode spacings are constant and equal to 2.5 mm. Both cathodes are segmented into strips, one in parallel to the wire and the other perpendicularly. The orientation of the strips provides a measurement of the position in two dimensions, with the spatial resolution dependent on the readout

pitch size. A fine segmentation in the bending plane achieves a resolution of $40\text{ }\mu\text{m}$, increasing to 5 mm in the orthogonal plane. In the azimuthal plane, both barrel and end-caps are configured in eight octants, reflecting the symmetry of the magnet system. The chambers are then allocated into the octants, arranged in a short and a long layer, as shown in fig. 3.9a. The two layers partially overlap, ensuring a complete ϕ hermeticity. A small acceptance gap toward the centre of the detector, up to $|\eta| < 0.08(0.04)$ for large (short) sectors, is uncovered by the chambers to leave space for services and cables. To achieve the desired p_T resolution, the position of the chambers must be known with a precision $< 30\text{ }\mu\text{m}$. A dedicated optical alignment system is used for this purpose and also to monitor the chambers' planarity.

Resistive plate chambers (RPCs) and thin-gap chambers (TGCs) augment the precision tracking chambers in the barrel and end-caps. The purpose of these additional detectors is to provide a fast measurement, with a response time of the order of tens of ns, to trigger on muons and tag the bunch crossing. They are also used to complement the MDT's measurement with a second spatial coordinate in the non-bending (transverse) plane. Three trigger stations are located in the barrel, in the form of three concentric cylinders placed next to the MDT layers. Two of the RPCs layers are placed respectively on top and on the bottom of the middle MDT layer, while the third one is located above (below) the outer MDT layer in the long (short) sectors. Each station comprises two parallel detectors, giving a total of six hits for a track passing all the trigger stations. The RPCs are gaseous detectors made of two equidistant resistive plates (phenolic-melaminic plastic laminate) separated by a 2 mm -gap filled with $\text{C}_2\text{H}_2\text{F}_4$, Iso- C_4H_{10} and SF_6 (94.7 : 5 : 0.3). An electric field of about 4.9 kV mm^{-1} is formed between the plates inducing ionised charges to produce avalanches of electrons toward the anode. Metallic strips arranged in η and ϕ are placed on the external surface of the plates to read the signal and provide a 2D measurement of the position. In the end-caps, there are 2 and 7 layers of TGCs respectively next to the inner and middle layer of MDTs arranged in a doublet or triplet module. The TGCs are multiwire proportional chambers, consisting of a series of parallel anodes placed between two cathode plates. The wires are placed 1.8 mm apart from each other and 1.4 mm from the cathodes. The volume between the two plates is filled with a gas mixture of 55% CO_2 and 45% n- C_5H_{12} (n-pentane). Doublets and triplets units are then formed by a series of two or three chambers separated by a honeycomb spacer.

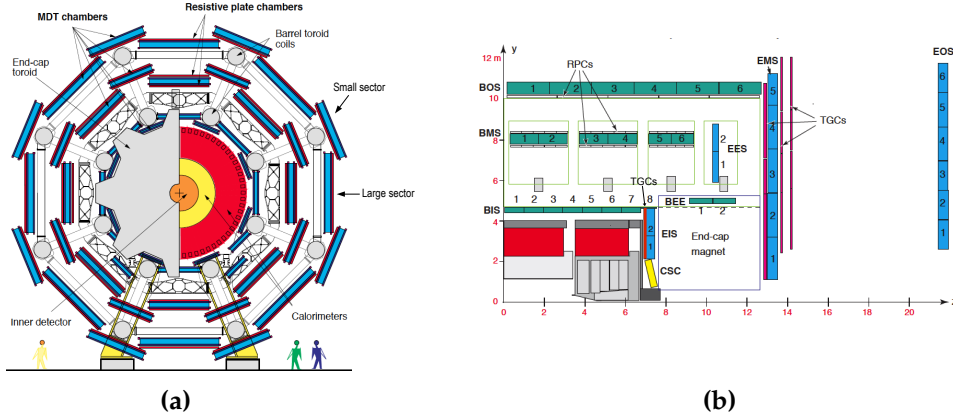


Figure 3.9.: (a) Transversal section of the MS barrel detectors in the xy plane. (b) Schematic of the MS in one quadrant of the yz plane. The MDT chambers in the barrel (end-cap) are displayed in green (blue). The TGCs, RPCs, and CSCs are shown in red, white and yellow. Figures sourced from [120].

3.2.5. Trigger and Data Acquisition system

In a standard data-taking configuration, with a bunch separation of 25 ns and an instantaneous luminosity of $\mathcal{L} = 1 \times 10^{34} \text{ cm}^{-2} \text{ s}^{-1}$, ATLAS is expected to see around 10^9 interactions each second. This enormous quantity of data would be impossible to store and process with the current technology limitations. A trigger system is, therefore, necessary to parse the stream of data acquired by the detectors and select only those events which can be of interest for physics analysis. The triggering in ATLAS is performed in a multi-staged process which performs an online data analysis to support the algorithms' decision-making.

The Level 1 (L1) trigger [121] uses custom-made electronics and is designed to operate at the bunch crossing rate of 40 MHz. L1 has an accept rate up to 100 kHz and must deliver its decisions to the front-end electronics within $2.5 \mu\text{s}$ from the bunch crossing³. To make fast decisions, L1 only uses partial information acquired by a subset of the detector, such as coarse data from the calorimeters (with a reduced granularity) and the muon trigger towers (RPCs and TGCs). Energy deposits and partial muon tracks are used for an online reconstruction of the events and to tag high-energy electrons, photons, muons, jets and hadronically decaying τ leptons. Isolation requirements on calorimetry-tagged objects can also be applied, ensuring the energy deposits are separated by a minimum ΔR . L1

³The limit depends on the front-end buffers' capacity.

decisions are made by the Central Trigger Processor (CTP), which compares the multiplicity of the tagged objects to a predefined set of up to 256 combinations. In case of a match, the spatial coordinates of the objects are also saved and passed to the following trigger stage. L1 also defines the luminosity blocks (LBs), namely short periods of data taking time (typically about 60 s each) characterised by stable beam conditions and for which an average luminosity value is computed.

The second triggering stage is performed by the High Level Trigger (HLT) [122, 123], a software-based trigger running on highly-performing processing farms. The HLT operates on the Regions of Interest (RoI's), a portion of the event restricted to the geometrical region in close proximity to the candidate objects seeded by the L1 trigger. The HLT performs a more accurate online reconstruction using full-granularity detector information within the RoI's, which typically takes about 200 μ s. To speed up the process, the reconstruction is performed in different steps with a hypothesis test in between, leading to an early rejection of the event if it does not meet the requirements. The final data rate recorded by ATLAS in Run 2 was in average around 1 kHz in 2016 and 2017 [124, 125] and 1.2 kHz in 2018 [126].

The Data Acquisition (DAQ) system [122] manages the data flow from the detector interface to the storage system and is an integrated part of the HLT. Initially, the event data is temporarily buffered in the on-detector front-end electronics accessible by the L1 trigger. Upon acceptance from L1, over 1500 optical fibres transfer the data to the readout system and its buffers, from which the data can be requested by the HLT based on the RoI information. The outcome of the HLT selection, including a classification of the event, is stored within the data structure and sent to the output nodes for storage. The DAQ system also monitors the detector-specific hardware and software necessary for data taking.

3.2.6. Luminosity detector

A precise knowledge of the luminosity is essential for the success of ATLAS's physics program, particularly for the measurements of cross-sections directly affected by it. Several methods are employed to evaluate and consolidate the instantaneous luminosity value, including dedicated detectors and algorithms which use the information from other parts of ATLAS (e.g. track multiplicity or calorimeter-seeded algorithms). The primary luminosity-sensitive detector used in Run 2 is the LUMinosity measurement using Cherenkov Integrating Detector (LUCID). The Beam Conditions Monitor (BCM) also provides a complementary

bunch-by-bunch measurement, and it was primarily used to estimate the luminosity during Run 1.

LUCID [127] is a Cherenkov detector consisting of photomultiplier tubes (PMTs) placed on both side A and C of ATLAS, nearly 17 m far from the interaction point. The PMTs are placed around the beam pipe, covering the very forward region $5.561 < |\eta| < 5.641$. In its original design, the detector was filled with C_4F_{10} gas to produce Cherenkov radiation at the passage of electrically charged particles. After an upgrade of the detector for Run 2 [128], the gas was removed to prevent saturation and migrations of secondary particles that would occur with the increased Run 2 pile-up. In the new configuration, Cherenkov light is instead produced by the 10 mm-diameter quartz window of the PMTs. There are 16 PMTs per side, grouped in four arrays that are placed at different angles along the pipe. Four additional quartz fibre bundles are connected to PMTs that are located 2 m apart and shielded from the magnetic field in a metallic box. The PMTs are calibrated either with a LED or with a radioactive ^{207}Bi source to monitor their gain and correct for any ageing effect. The PMTs are equipped with fast electronics capable of both registering hits, whenever they receive a signal above a certain threshold, and performing a charge integration over the single bunch crossings. The probability of registering a hit is related to the pile-up term μ of eq. (3.2), and the instantaneous luminosity can be obtained by counting the hits in each luminosity block. More than 100 algorithms that use different logic combinations of the PMTs are employed to precisely determine the luminosity value.

The BCM [129] is a diamond detector designed to monitor the status of the beams and provide a beam abort signal in case of an event that could compromise the safety of ATLAS. Particularly, it searches for lost protons that could interact with the collimators that protect the inner systems and could initiate a particle shower potentially hazardous for the detectors. It also monitors the interactions between the beam and the gas. The BCM detector comprises 2×4 diamond sensors ($8 \times 8 \text{ mm}^2$) which are placed at $|z| = \pm 1.84 \text{ m}$ around the beam pipe. On each side, the four sensors are arranged in a cross pattern at a radius $r = 55 \text{ mm}$, corresponding to $|\eta| \approx 4.2$. The sensors are connected to readout amplifiers, whose signal is then sent to a digitiser for analysis. The distance in z of the two modules corresponds to a time of flight which is about half of the beam separation ($\approx 12.5 \text{ ns}$), allowing to discriminate between interactions occurring in a bunch crossing and secondary showers originating upstream or downstream the centre of

ATLAS. Similarly to LUCID, several algorithms use different combinations of the hits registered by the BCM to provide a complementary luminosity measurement.

The LUCID and BCM detectors are calibrated to the absolute luminosity scale in the so-called van der Meer (vdM) scans [98, 130]. The scans are performed in special LHC runs, where the colliding beams are horizontally or vertically displaced in opposite directions. Starting from an initial configuration, which optimises the delivered luminosity, the beam separation is gradually increased to provide scans in the x and y directions. The measurement of the uncalibrated luminosity as a function of the displacement permits to measure the Σ_x and Σ_y parameters of eq. (3.1), thus providing a reference for the calibration.

3.3. Object reconstruction in ATLAS

The raw data collected by ATLAS consists of fragmented pieces of information coming from all the signals registered by the different detectors. A reconstruction procedure is needed to associate them with a physical object before they can be used in physics analyses. The offline reconstruction of different objects, including tracks, vertices, electrons, muons, photons, jets, tau leptons and missing transverse momentum, is described in this section.

3.3.1. Tracks and vertices

An electrically charged particle moving in a magnetic field is subject to the Lorentz force, resulting in a centripetal acceleration in the plane orthogonal to the magnetic field. In the case of a homogeneous field, the particle presents a helicoidal trajectory with a circumference projected in the transverse plane. The trajectory can be described by five parameters, or degrees of freedom, which, in the reference system used by ATLAS, correspond to $(d_0, z_0, \theta_0, \phi_0, \frac{q}{p})$. The impact parameters d_0 and z_0 are the distances of the perigee, the point of closest approach to the beam axis, from the xy plane and the z axis respectively. The angles (θ_0, ϕ_0) correspond to the angular coordinates of the perigee and $\frac{q}{p}$ is the ratio of the particle's charge to its momentum.

In ATLAS, the momentum reconstruction of charged particles, henceforth referred to as tracks, is performed by combining different hits registered in the layers of the Pixel, SCT and TRT detectors. Tracks associated with muons also exploit information gathered by the MS, as described in section 3.3.3. Tracking in

the ID starts by forming clusters of hits in the Pixel and SCT. Particles traversing a single tracker layer can interact with the active material of different close-by sensors, thus producing multiple signals. Adjacent hits, sharing a side or a corner of different sensors, are grouped to form a so-called space-point, a three-dimensional spatial coordinate describing the point where the particle interacted with the pixels or the strips. In the latter case, two clusters from opposite faces of the strip are needed to form a space point.

Track candidates are found from the space points using an iterative algorithm [131]. Each track candidate is seeded by a set of three space points, in such a way as to maximise the total number of possible tracks with the minimum number of points needed for an estimate of the momentum. A loose kinematic selection, with requirements on the momentum and impact parameters of the track, is applied to the seeds to improve the purity⁴. The selected seeds are then passed to a Kalman filter [132] which extrapolates the track through the subsequent layers of the ID in the outward direction, up to the SCT border. Given the very large hit multiplicity, it is not uncommon to find different track candidates sharing space points. A selection criterion is therefore necessary to choose only tracks of good quality. First, the different clusters associated with a track are weighted in such a way that hits in the detector regions with better resolution have a better score. Track candidates with missing expected space points (holes) or large χ^2 are penalised. Lastly, tracks with a higher momentum are preferred. An ambiguity solver algorithm successively deals with cluster-sharing tracks, discarding candidates failing basic quality criteria and removing clusters from tracks which contains more than two shared clusters. The parameters of these stripped tracks are re-evaluated, and the new tracks go again through the ranking selection.

A high-resolution fit is performed on accepted track candidates using artificial neural networks to estimate the cluster's position and its uncertainty. Tracks are then extended toward the TRT region with a similar procedure. Trajectories of particles arising from secondary interactions may not be found with this "inside-out" approach, as they could miss hits in the innermost layers of the ID. An additional "outside-in" search is carried out starting from track segments in the TRT which are backtracked to the inner region [133].

⁴The purity is defined as the fraction of seeds from which a good-quality track is found.

Primary Vertices (PVs) are reconstructed from the final tracks with an iterative procedure [134, 135]. The first stage, also referred to as vertex finding, consists in applying a pattern recognition algorithm to the reconstructed tracks to search for vertex candidates. A vertex seed is identified depending on the reconstructed beam spot position and the corresponding point of closest approach of the tracks. The vertex position is consequently estimated with a fit to the beam spot coordinates and the tracks' parameters, through an iterative χ^2 minimisation. The associated tracks are then weighted based on their compatibility with the vertex position, and the fit is performed a second time. Incompatible tracks are eventually discarded and reused to find additional vertex candidates. A PV candidate is considered valid if connected to at least two separate tracks. Pile-up events⁵ often contribute with additional vertices that are reconstructed together with the hard-scatter interaction vertex. The usual method to distinguish between the two is to order the vertices depending on the p_T of the associated tracks, as the hard-scatter process is more likely to present a wider transverse spread. With this logic, the hard-scatter PV is determined to be the one with the largest sum of squared transverse momenta $\sum^{(tracks)} p_T^2$.

3.3.2. Electrons and photons

Electrons (positrons) and photons are reconstructed by combining information from the tracker and the electromagnetic calorimeters. Electrons interact with both sub-detectors, thus showing a characteristic signature which consists of a track geometrically matched to an energy deposit in the calorimeter. Photons, on the other hand, do not leave a signal in the ID unless they convert mid-flight in a e^+e^- pair before reaching the calorimeter. In this case, they are identified as an energy deposit connected to either a partial track in the outer region of the ID or a two-track conversion vertex⁶. Energy deposits in the electromagnetic calorimeter that are not matched with any track or conversion vertex are identified as unconverted photons.

Due to their low mass, electrons lose a significant fraction of their energy via bremsstrahlung, an energy that is also spread along the bending direction of the magnetic field. The emitted photons are typically emitted at small angles from the electron's trajectory, resulting in multiple signals sampled across different

⁵Additional interactions that are concomitant to the hard-scatter process.

⁶A vertex associated to two opposite-charge tracks and compatible with the hypothesis of a massless particle.

close-by cells of the calorimeter. A clustering algorithm allows to recover some of this energy loss and also accounts for particles whose electromagnetic shower develops over multiple cells [136]. Electron and photon reconstruction begins by forming topologically-connected clusters (topo-clusters) in the electromagnetic and hadronic calorimeter cells. The energy measured in hadronic cells is not used in the reconstruction process but serves as a selection criterion to reject clusters with considerable hadronic leakage and reduce the contamination from misidentified hadrons. Topo-clusters are seeded by a single cell registering a signal well above the expected noise value. The cluster seed is then merged with neighbouring cells that also present an SNR (signal-to-noise ratio) larger than a distance-dependant threshold. The algorithm matches topo-clusters to ID tracks or conversion vertices and performs a new track fitting to account for radiative energy losses. An improved description of the bremsstrahlung radiation is obtained with a Gaussian Sum Filter (GSF) [137], an extension of the Kalman filter described in section 3.3.1 which uses a weighted sum of Gaussian functions to approximate the Bethe-Heitler distribution. Matched topo-clusters are later used to build super-clusters: a seed cluster is selected, and satellite clusters are added to it if they fall within a specific $\Delta\eta \times \Delta\phi$ window or if they show a converted photon topology (e.g. a shared conversion vertex).

The final electrons and photons used in physics analyses are reconstructed from the identified super-clusters. Tracks and conversion vertices are matched to the super-cluster, after a position correction and energy calibration. Tracks parameters and shower observables are used to calibrate the object's energy further. The calibration includes the use of a multivariate analysis trained on simulated data to better constrain the energy resolution and reduce the influence of the material budget present in the detector. An inter-calibration of the different layers of the calorimeter is also performed to ensure a uniform energy response. A global energy scale correction, reflecting differences in data and simulation, was measured with $Z \rightarrow e^+e^-$ events collected in a partial Run 2 dataset [136] between 2015 and 2017, and it is applied to the reconstructed electrons and photons. The total systematic uncertainty in the energy scale was evaluated to be 4×10^{-4} (2×10^{-3}) in the barrel (end-caps).

Track and shower properties are used to establish a set of criteria to select good-quality electrons and photons and reduce the contribution from hadronic jets depositing a fraction of their energy in the electromagnetic calorimeter. Two

different approaches are used for the identification of prompt electrons and photons. Electrons are identified with a likelihood discriminant [138] relying on both tracker and calorimeter information. The track requirements include selection cuts applied to impact parameters and their significance, the number of hits in the innermost tracking layers and the fraction of momentum loss. Shower shape observables account for the longitudinal and lateral spread and the fraction of energy deposited in subsequent calorimeter layers. Different working point selections are defined with a target efficiency. Loose, medium and tight selections respectively correspond to about 93%, 88%, and 80% efficiency [136, 138], with tighter working points corresponding to greater purity. The significance of the transverse impact parameter is defined as the ratio between d_0 and its uncertainty, corresponding to $d_{0,sig} = \frac{|d_0|}{\sigma(d_0)}$. Besides its usage in the likelihood discriminant, a requirement on $d_{0,sig} < 5$ is typically applied to select good-quality electrons. Similarly, a requirement on the longitudinal impact parameter (z_0), e.g. $|z_0 \sin \theta| < 0.5$ mm, can be used to select electrons originating from the PV and reduce pile-up contributions. Electron identification efficiencies were measured with the same dataset described above for the energy scale correction. The measurement relies on a tag and probe method applied to $Z \rightarrow e^+e^-$ events, which provides a set of unbiased electrons from which the efficiencies can be estimated. Identification efficiencies were measured in bins of E_T and $|\eta|$, and vary accordingly with the corresponding selection working point. The uncertainties in the identification efficiency correspond to 7% at $E_T = 4.5$ GeV, decreasing to less than 1% for higher- E_T electrons (up to $30 < E_T < 250$ GeV) [136]. Photon identification is performed with a cut-based selection on similar shower shape observables. As for electrons, loose, medium and tight working points are built [136, 139]. Loose and medium selections are the same for converted and unconverted photons, while tight identification includes a multivariate analysis separately tuned for the two classes. Along with the identification criteria, isolation requirements are often imposed to electrons and photons to further improve the selection purity. Isolation is computed at the tracker or calorimeter level by summing the contribution of contiguous tracks or energy deposit (p_T for tracks and E_T otherwise) falling within a cone of size ΔR centred on the particle's trajectory [136].

3.3.3. Muons

Muons are reconstructed using information from the different ATLAS subsystems. At their passage, muons produce tracks in the ID and the MS, allowing

for two independent momentum measurements. Calorimeters can also be used to tag muons which deposit a fraction of their energy in them. Track candidates in the MS are identified by looking for short linear segments of hits in a single muon station. The segments are found with a Hough transform [140] and later merged with an extrapolation based on the interaction point position and the hypothesis of a parabolic trajectory. Three-dimensional coordinates, obtained by associating position measurements in the precision chambers and the trigger towers, are used in a global fit to estimate the track's parameters. Incompatible hits are discarded from the track candidate, while aligned hits not initially included in the fit are added. Ambiguities may rise if multiple tracks share a large fraction of hits. In this case, redundant tracks are discarded based on their quality, with the poorest ones being rejected.

Inputs from different detectors are combined to form five classes of global reconstructed muons [141]:

- **Combined** muons are reconstructed by associating a track in the MS with one in the ID. A global fit is performed on the selected hits from both detectors, also correcting for energy loss in the calorimeters.
- **Inside-out combined** muons follow a similar approach as the previous class, but the track-matching direction is inverted, starting from the ID to the MS.
- **MS extrapolated** muons correspond to the case of standalone MS tracks with no associated counterpart in the ID. This class of muons is particularly relevant in the forward region ($2.5 < |\eta| < 2.7$), which lies outside of the ID acceptance.
- **Segment-tagged** muons are those with an ID track associated with at least one segment in the MS. They describe low- p_T muons, which can only reach the first layers of the MS, or those muons escaping the MS acceptance. In this case, the track's parameters are directly measured in the ID.
- **Calorimeter-tagged** muons are based on ID tracks matched to an energy deposit in the calorimeter compatible with the expected energy loss profile of a minimum ionising particle. These muons help to recover an acceptance loss at small pseudorapidity values caused by a gap in the MS layout.

Identification criteria are applied to the good-quality muons to reduce the non-prompt background. This mainly originates from light hadrons decaying

mid-flight into muons, whose reconstructed tracks turn out to be degraded due to the modified trajectory. Similarly to the electrons and photons case, loose, medium and tight working point selections are defined. Additionally, two special working points are tuned for low- p_T and high- p_T muons to be used in physics analyses dedicated to more exotic phase spaces, such as searches for heavy resonances or supersymmetry. All muon classes, except for MS extrapolated, are required to have at least one hit in the ID, five hits in the MS and no more than two missing hits in the combined track. The different working points accept specific classes depending on the muon (p_T, η) and also impose some constraints on the track quality measured in the two detectors⁷. A track-to-vertex association (TTVA) ensures muons are compatible with the PV and reduces the contribution from hadron decays, pile-up events and cosmic rays. The TTVA requires the PV to be as close to the muon track as $|z_0| \sin \theta < 0.5$ mm in the longitudinal direction. A requirement on the transverse track parameter significance can also be applied, usually with a cut-off value of $\frac{|d_0|}{\sigma_{d_0}} < 3$. Background muons originating from heavy-flavour hadron decays can be suppressed by selecting isolated muons. The isolation is computed similarly to the electron case, looking for additional tracks or topo-clusters in a cone around the muon. Different working points are established, which rely on either track or calorimeter-based isolation or on a combination of the two.

The muon reconstruction efficiency was measured with a tag and probe method applied to $Z \rightarrow \mu^+ \mu^-$ and $J/\psi \rightarrow \mu^+ \mu^-$ events [141]. In the range $0.1 < |\eta| < 2.5$, both Loose and Medium working points present an efficiency above 98%, decreasing to about 95% for the tight selection. The performance of the momentum reconstruction was evaluated with a complete Run 2 dataset, again from the leptonic decay channel of the above resonances [142]. The transverse momentum resolution was measured to be up to 2.3% and 3.4% in the barrel and end-caps regions respectively. The momentum scale was measured in the same $Z \rightarrow \mu^+ \mu^-$ sample with an accuracy of 0.05% – 0.15% increasing with pseudorapidity [142].

⁷The agreement between ID and MS tracks is evaluated from the q/p compatibility, defined as $\frac{|q/p_{ID} - q/p_{MS}|}{\sqrt{\sigma_{q/p,ID}^2 + \sigma_{q/p,MS}^2}}$, and from the ratio of the detector-dependent p_T difference divided by the outcome of the combined fit: $\frac{|p_{T,ID} - p_{T,MS}|}{p_{T,CB}}$.

3.3.4. Jets

Jets are one of the most frequent final state signatures in proton-proton interactions at the LHC. They consist of a stream of quasi-collinear hadrons. These hadrons can be either electrically charged or neutral, thus being detected by the tracker and/or the calorimeter. The common procedure of reconstructing jets utilises the anti- k_T clustering algorithm [79], described earlier in section 2.5, with a typical radius parameter of $R = 0.4$. The inputs used by the jet clustering algorithm can be either tracks or the topo-clusters introduced in section 3.3.2. A third option, introduced during Run 2, consists in using a combination of the two to better reconstruct the contribution of soft interactions to the energy of the jet [143]. Jets reconstructed with this method are referred to as particle-flow jets. The procedure aims to correct the energy deposits in the calorimeter with ID information, to take advantage of its better resolution. Good quality tracks are selected by requiring at least 9 hits in the silicon detector and no missing hits in the pixel region. They must also fall within the tracker acceptance $|\eta| < 2.5$ and have a minimum transverse momentum of $p_T > 0.5 \text{ GeV}$. The momentum resolution in the ID decreases with the particle's energy, in which case the particle-flow procedure would not improve the results obtained from topo-clusters. Therefore, tracks whose transverse momentum exceeds $p_T > 40 \text{ GeV}$ are not considered⁸. The selected tracks are then geometrically matched to the topo-clusters depending on the angular separation and the cluster's width. An energy subtraction procedure is performed on matched tracks to avoid double-counting of the signal in the tracker and the calorimeter. The expected energy deposit that a track would leave in the calorimeter is extrapolated from ID information and consequently subtracted cell-by-cell in the corresponding topo-cluster. The algorithm also accounts for the cases where the energy is split between different clusters and decides whether to merge them. If the remaining energy in a cell after the subtraction procedure is compatible with the hypothesis of shower fluctuation, the cell is removed. The final output of the particle-flow algorithm corresponds to the set of selected tracks and the surviving topo-clusters, which can later be used to reconstruct jets with the aforementioned anti- k_T method.

The energy of the reconstructed jets needs to be corrected and calibrated.

⁸This requirement was later replaced by a more sophisticated cut depending on both the track p_T and the energy deposits in a cone of aperture $\Delta R < 0.15$ around the particle [144]. This cut prevents the subtraction procedure from being executed in case of a very dense environment, where the selected track is not isolated.

- Energy deposits from pile-up interactions occurring during the same or consecutive bunch-crossings can add to the reconstructed energy of a jet. This contribution is subtracted with an energy correction based on the jet area, evaluated from the ghost association [145, 146] of soft particles to the jet, and the momentum density. A residual correction depending on $\langle \mu \rangle$ and the number of primary vertices is also applied at this stage.
- A Jet Energy Scale (JES) calibration accounts for detector effects, such as different calorimeter response and energy loss in non-active material, to restore the energy scale to that of the truth particles. This is done by applying a correction for the jet energy response determined using simulations.
- An absolute η calibration is necessary to correct a bias in the measured jet pseudorapidity caused by shape and material differences of the sub-detectors, particularly in the barrel, end-caps and forward transition regions [144]. Similarly to JES, the η calibration is also based on a simulation.
- Because jets are composite objects, the energy response and shower development depend on their structure. For example, the hadronic shower of gluon-initiated jets tends to be wider and shorter than quark-initiated ones. The so-called global sequential calibration (GSC) uses information from the different detectors to improve the jet energy resolution without altering the average response. The GSC is applied through a series of multiplicative corrections derived from jet observables, such as shower shape, tracking information and activity in the MS.
- The final set of corrections corresponds to the *in situ* calibration, which suppresses the remaining differences between data and simulation. Dijet events are used for an η intercalibration of central and forward jets, to equalise the response across the two regions of the detector. The p_T balance of hadronic events is measured in $Z/\gamma + jet$ events and compared to the well-calibrated boson's. Lastly, multijet events are used to cross-calibrate high- p_T jets with a set of low- p_T ones.

The Jet Energy Resolution (JER) was measured with a partial Run 2 dataset of dijet events [144]. The JER for particle-flow jets was found to be varying between 25% and 4% depending on the jet p_T , with an absolute uncertainty decreasing from 1.5% to 0.5%. The same study also provided an evaluation of the systematic

uncertainties related to the JES , which were measured to be between 1% and 5% for central jets.

In addition to the low- p_T particles that add to the jets, described above, pile-up interactions can also produce high- p_T jets directly, which are reconstructed along with the hard-scatter products. To reduce the number of pile-up jets, ATLAS uses a likelihood discriminant called the Jet Vertex Tagger (JVT) [147], which is based on tracking and vertex information. The discriminant is constructed using two different jet variables, described below.

- For each jet, the JVF (Jet Vertex Fraction) expresses the p_T fraction of matched tracks associated with a specific reconstructed PV. It can be computed for any desired PV but typically refers to the hard-scatter one. The JVF is defined as

$$\text{JVF}(j_i, \text{PV}_k) = \frac{\sum_l p_T(\text{track}_l^{(j_i)}, \text{PV}_k)}{\sum_m \sum_n p_T(\text{track}_n^{(j_i)}, \text{PV}_m)}, \quad (3.11)$$

where j_i and PV_k are respectively the selected jet and PV, the numerator is the scalar p_T sum of the tracks matched to both j_i and PV_k , and the sum in the denominator runs over all the tracks matched to j_i and all the reconstructed PVs. The JVF can assume a value between 0 and 1, with hard-scatter jets typically showing larger values. The denominator of eq. (3.11) depends on the luminosity of the collisions and shows a linear increment with the number of pile-up tracks. A correction is applied to the denominator to remove this dependence before using JVF for the JVT evaluation.

- The variable R_{p_T} denotes the p_T fraction of the tracks in a jet that are associated with the hard-scatter PV, namely

$$R_{p_T}(j_i) = \frac{\sum_k (\text{track}_k^{(j_i)}, \text{PV}_0)}{p_{T,j_i}}, \quad (3.12)$$

where the scalar p_T sum is performed over the tracks matched to j_i and the hard-scatter vertex, PV_0 , and p_{T,j_i} is the fully calibrated transverse momentum of j_i . R_{p_T} has a similar trend as JVF, with hard-scatter jets presenting a large value, while pile-up jets peak at zero.

A k-nearest neighbour algorithm [148] is employed to evaluate a 2D likelihood from a set of simulated dijet events, combining the JVF and R_{p_T} variables.

The JVT relies on tracking information, which is not available for jets in the forward region of the detector. Outside of the ID acceptance, a different discriminant, the forward-JVT (fJVT) [149], is used to reduce the contribution from pile-up jets. The JVT and R_{p_T} variables are used to identify central pile-up jets originating from secondary strong interactions from a background of stochastic pile-up jets⁹. These are then associated to the pile-up vertex $PV_{i \neq 0}$ which yields the largest $R_{p_T}^{(i)}$. For any pile-up vertex the missing transverse momentum vector ($\langle \mathbf{p}_{T,i}^{miss} \rangle$) is computed as

$$\langle \mathbf{p}_{T,i}^{miss} \rangle = -\frac{1}{2} \left(\sum_{\text{track} \in PV_i} k \mathbf{p}_{T,\text{track}} + \sum_{j \in PV_i} \mathbf{p}_{T,j} \right), \quad (3.13)$$

where $\mathbf{p}_T = (p_{T,x}, p_{T,y})$ denotes the vectorial expression for the transverse momentum, and the weight $k = 2.5$ accounts for differences between the p_T of jets and tracks, optimised to reject forward pile-up jets [149]. A forward pile-up jet of transverse momentum vector $\mathbf{p}_{T,j}$ is expected to show a significant fraction of missing transverse momentum aligned in the same direction of $\mathbf{p}_{T,j}$. The fJVT discriminant is therefore constructed as the projection

$$\text{fJVT}_i = \frac{\langle \mathbf{p}_{T,i}^{miss} \rangle \cdot \mathbf{p}_{T,j}}{|\mathbf{p}_{T,j}|}, \quad (3.14)$$

with the index i referring to a specific pile-up vertex. fJVT is computed for all vertices, and the forward jet is considered a pile-up jet if the maximum value is larger than a certain threshold. Different thresholds of the JVT and fJVT discriminants are used to define a medium and a tight selection working points. The thresholds vary for EMTopo and PFlow jets and depend on their η and p_T . The two taggers play a significant role in the event selection used for the measurement of $ZZjj$ production cross-section, described in chapter 5.

3.3.5. Taus

Tau leptons (τ) produced at the LHC cannot be directly detected by ATLAS due to their very short lifetime. They typically decay before reaching the active material of the detector and must be reconstructed from the decay products. The branching ratio of the hadronic decay channel ($\tau \rightarrow h + \nu_\tau$) is about 65%, and most

⁹The term stochastic refers to jets formed by particles stemming from different interactions. Such jets typically present a small value of R_{p_T} , calculated for any pile-up vertex different from PV_0 .

decays include charged and neutral pions. Tau leptons are outside of the scope of this thesis, and their reconstruction is only briefly introduced. More details can be found in refs. [150, 151]. The hadronically decaying τ -leptons reconstruction is seeded by jets formed with the anti- k_T algorithm using a $R = 0.4$ radius, as described in section 3.3.4. A τ vertex is then identified as the vertex candidate with the largest p_T fraction in a $\Delta R = 0.2$ cone around the jet axis. Tau leptons are identified with a recurrent neural network analysis [152] which provides different working point selections.

3.3.6. Missing transverse momentum

Weakly-interacting particles, such as SM neutrinos and potential BSM particles, escape the volume of the detector without interacting with its active components. Due conservation of momentum, the total transverse momentum in the final state of a pp collision should be equal to zero. A momentum imbalance in the transverse plane of an event would then indicate the presence of undetected particles. The imbalance is measured in terms of missing transverse momentum, a 2-dimensional vector in the xy plane of components $\mathbf{E}_T^{miss} = (E_x^{miss}, E_y^{miss})$.

The reconstruction of \mathbf{E}_T^{miss} is a demanding and susceptible to imprecision task, as it involves information from all the different sub-systems of ATLAS. The missing transverse momentum is defined as the negative vector sum of the p_T of all the reconstructed objects in an event [153]:

$$\mathbf{E}_T^{miss} = - \left(\sum_{i \in \{e, \gamma, \tau, \mu, jet\}} \mathbf{p}_{T,i} \right) - \left(\sum_{j \in \{\text{soft objects}\}} \mathbf{p}_{T,j} \right). \quad (3.15)$$

The first term of the sum corresponds to the contribution from all the objects produced in the hard-scatter process that have been reconstructed and calibrated with the different procedures introduced above. The second term, or "soft" term, assembles all the remaining signals (tracks only) associated with the PV of the event but not with other hard objects. These include the products of the underlying event and pile-up interactions and those particles whose signals fail the selection criteria of hard objects. To avoid double counting signals of the same particle, which might be independently reconstructed in different detectors (e.g. an electron reconstructed from a track in the ID and a jet in the calorimeter), the objects are selected with a different priority. With descending priority, the order of the

different particles is electrons, photons, τ -leptons and jets. Low-priority objects that are geometrically matched with higher-priority ones are discarded. Muons can only overlap with jets and always have higher priority. Either EMTopo or PFlow jets can be used in the computation of E_T^{miss} . In a study using data collected in 2015-2016, the second, more recent, jet category showed some improvements in the reconstruction performance [154].

3.4. Simulation of the ATLAS detector

The event generation described in section 2.4 provides a prediction on the true final states originating from hadron collisions, also referred to as fiducial or particle-level prediction in the following chapters of this thesis. Such prediction is typically different from what is observed experimentally, as the detectors have a finite acceptance, efficiency and resolution, which can alter the measured observables. A detector-level prediction can be obtained by interfacing the generated true event with a second simulation, describing the detector response. In ATLAS, the detector simulation [155, 156] is based on a model of the detector's geometry implemented in *Geant4* [157]. The simulation accounts for the interactions between the final state particles of the true prediction and the different materials composing the detector. A second step, called digitisation, translates the event signatures into signals read by the detector. These are analogous to real data signals and can be used in the same object reconstruction procedure described above.

Blank Page

Chapter 4.

Thermal characterisation of ITk Pixel Outer Endcaps local supports

Between 2026 and 2029¹, the LHC will undergo a series of upgrades aimed at increasing its instantaneous luminosity up to a peak value of $\mathcal{L} = 7.5 \times 10^{34} \text{ cm}^{-2} \text{ s}^{-1}$. This so-called High Luminosity LHC (HL-LHC) project [158] is foreseen to last over a period of about ten years and deliver up to 3000 fb^{-1} of collision data to both ATLAS and CMS experiments.

An increment in luminosity directly corresponds to a larger number of interactions per bunch-crossing. Around 200 interactions are expected to occur in each bunch crossing, which is much larger than the 34 that was typical of Run2. The higher track density poses a challenge for the track reconstruction, along with increased sensor occupancy and the amount of data to be transmitted. More interactions also produce a larger dose of radiation that the detector has to withstand: a non-ionising fluence of $10^{16} \text{ n}_{\text{eq}}/\text{cm}^2$ and an ionising dose of 5 MGy are expected in the region close to the interaction point. The current ATLAS ID cannot survive this harsh environment while providing the current physics performance. Therefore, it will be replaced by a new Inner Tracker (ITk) detector during the ATLAS Phase-2 upgrade[159]. The ITk is an all-silicon tracker detector, designed to deliver the same or better performance than the ID. It's composed of a Pixel detector near the interaction point, surrounded by a Strip detector [160, 161].

The University of Manchester is widely involved in the design and production of the outer end-caps of the Pixel Detector and, in particular, of their local supports.

¹Current schedule updated in January 2022.

Section 4.1 illustrates the design of the Pixel detector, while section 4.2 describes the local supports and their assembly procedure, with insights on possible issues that can occur during it. To guarantee that the local support design meets the operational requirements, and to ensure faulty pieces are not used when building the detector, Quality Assurance (QA) and Quality Control (QC) protocols were established. A technique to assess the thermal performance of the local support was developed at the University of Manchester [1] and will be used during the serial production. The original concept of the technique was implemented in a previous work by another member of the Manchester team [162], whilst the author of this thesis collaborated to its further development and optimisation for the measurement of local support prototypes. All the results presented here were also obtained from measurements led by the author. A complete description of the method, along with a list of the experimental apparatus used for the measurements, is given in section 4.3. The technique's sensitivity and effectiveness have been tested with several prototypes. The results are reported in section 4.4. Lastly, section 4.5 gives an insight on the foreseen technique's employment during the local supports' production.

4.1. ITk Pixel upgrade

The latest design of the entire ATLAS ITk detector [163] is shown in fig. 4.1. Compared to the ID, the pseudorapidity coverage is extended up to $|\eta| < 4$, thus expanding the track reconstruction to the forward region. With its three different sub-systems, the Pixel detector constitutes the innermost part of the ITk. The Inner System (IS) covers the region closest to the nominal interaction point and comprises two different layers, also referred to as L0 and L1. An Outer Barrel (OB) surrounds the IS in the central region of the detector, with two additional Outer End-caps (OECs) placed on each of its sides. Both OB and OECs are composed of three concentric layers, named L2, L3 and L4. The IS is designed to be removable and will be replaced after about 2000 fb^{-1} of data-taking due to radiation damage.

The detector is populated with different types of modules made of pixel sensors coupled to novel ASICs implemented in 65 nm CMOS technology. A mixture of planar n-in-p and 3D silicon pixel sensors are employed. 3D sensors are used in L0, as their structure is more resilient to radiation damage. They are assembled in "Triplets" modules made of three adjacent ASIC-sensor pairs arranged in a linear or curved shape, depending on the detector's geometry they must cover.

In the other parts of the detector, single planar sensors are bump-bonded to four different ASICs, forming a so-called "Quad" module. The small pitch of the pixels ($25 \times 100 \mu\text{m}^2$ and $50 \times 50 \mu\text{m}^2$) increases the z_0 resolution up to a factor 2 compared to the Run 2 value [163].

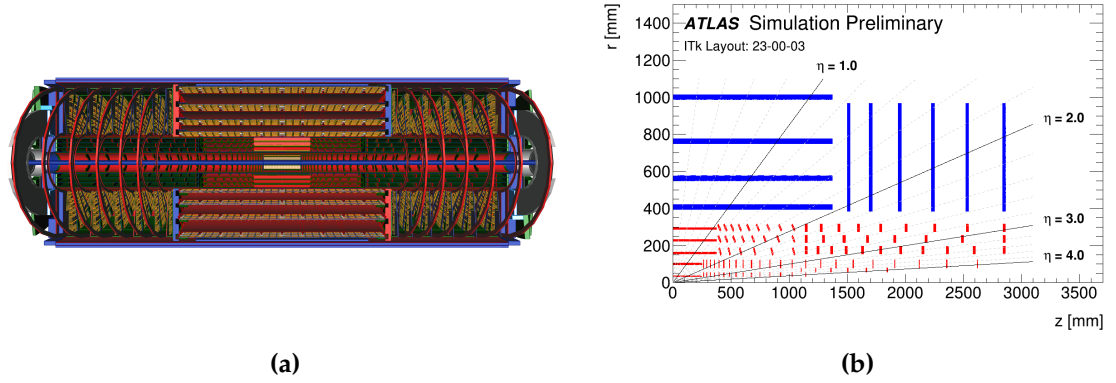


Figure 4.1.: Design of the ITk detector (a) and schematic of one quadrant of the detector (b) with the latest configuration [163]. The Pixel detector is shown in red in (b), while the Strip detector is in blue.

The OECs are the object of study of this work, and their structure is illustrated in fig. 4.2². They occupy the detector region defined by $1114 \text{ mm} < |z| < 3018 \text{ mm}$ and $114 \text{ mm} < R < 327 \text{ mm}$. In each end-cap, three concentric semi-cylindrical structures (global supports) of different radii host several half-ring-shaped local supports (see section 4.2) on which the modules are attached. These Half-Rings (HRs) are arranged in arrays along the beam direction: there are 11 HRs in L2, 8 in L3 and 9 in L4. The HRs are populated with a different number of quad modules (32, 44 and 52), which adds up to more than a thousand per end-cap. The modules are evenly placed on both faces of the HR, in such a way that the gap between two adjacent modules on one side is covered by another module on the opposite side. This ensures full coverage in both η and ϕ directions.

4.2. Local supports and thermal requirements

The ITk Pixel OEC local supports are responsible for the mechanical stability of the sensors and are an integrated part of the cooling system. Their design is based on the technology used for the current ATLAS IBL. They present a carbon-based structure which provides good thermal conductivity and a small density (a low

²For a detailed description of the other sub-systems, we refer to [160, 163].

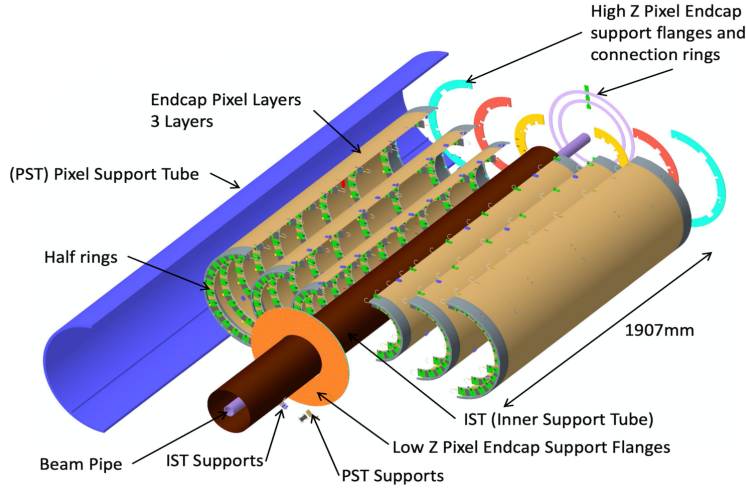


Figure 4.2.: Exploded view of a single ITk Pixel OEC [164].

material budget in the detector volume is important to reduce conversion). An HR is made of two half-sandwiches of co-cured [165, 166] carbon fibre face-sheet (a three-ply pre-preg) and carbon foam. A titanium pipe is embedded into the foam core to bring the coolant to the modules. An exploded view of the HR components can be seen in fig. 4.3a. An end closeout and an electrical break are placed on both ends of the pipe, respectively, to stabilise it and insulate the HR from the rest of the detector. In the loaded configuration, a Kapton bus tape and the modules are glued on the HR surface as shown in fig. 4.3b. The average radius of the local supports corresponds to 174.6 mm in Layer 2, 234.65 mm in Layer 3 and 294.7 mm in Layer 4.

To produce a HR, several trapezoid tiles are cut out of a carbon foam block. They are then assembled into a half-ring shape and put over the three pre-preg layers to build a single half-sandwich. After co-curing, the half-sandwich is thinned to the required dimensions and a groove for the pipe is machined. A graphite-doped epoxy is deposited on the pipe, which is then inserted in the groove. The same non-doped glue is also deposited on the rest of the exposed foam, and another half-sandwich is placed on top. The assembled object is let cure at room temperature in a vacuum chamber for several hours. The doped glue enhances the thermal conductivity [167, 168] and connects the different parts of the HR to form a thermal path between the pipe and the sensors. If the glue layer is not uniform due to assembly issues, the thermal path can be compromised, and defective areas with lower cooling capabilities can form. This is illustrated in

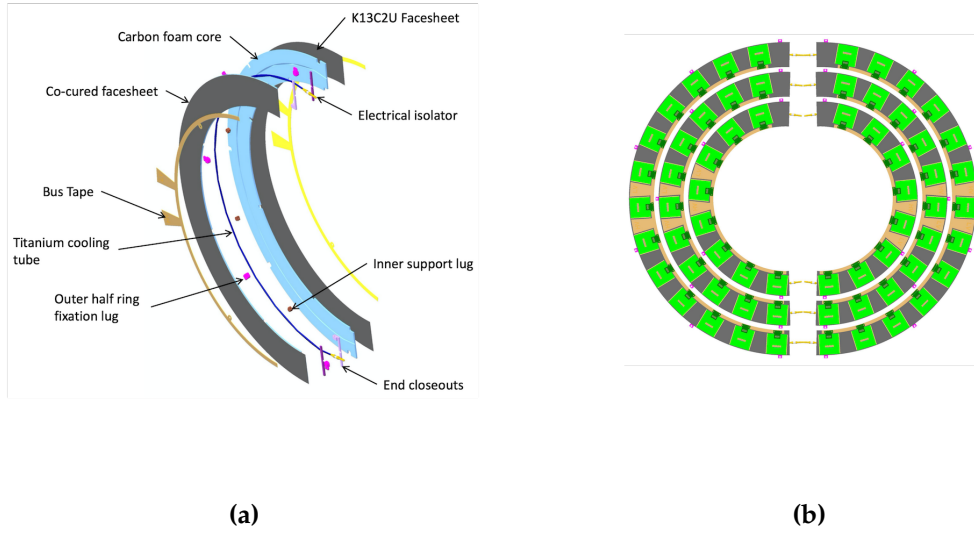


Figure 4.3.: Exploded view of a ITk Pixel OEC local support [164] (a) and schematic of the loaded configuration with modules (b). The modules are placed in such a way that an additional module on the opposite face of the HR covers the space between two adjacent modules.

fig. 4.4 where longitudinal and transversal cross-sections of a HR are shown with a defect in the glue layer depicted in red.



Figure 4.4.: Longitudinal (a) and transverse (b) cross-sections of a HR with a defect in the glue layer depicted in red. Figures sourced from [1].

Proper cooling of the sensors is essential for their correct functioning and their preservation. One of the effects of radiation damage is to increase the leakage current in the semiconductor sensors due to newly created generation-recombination centres [169]. Since the leakage current also increases with temperature, and more current would produce more heat, the temperature must be kept under control

to prevent the so-called thermal runaway [160, 170] phenomenon. This occurs when the temperature is high enough to enter a positive-feedback loop which will exponentially increase its value, thus leading to the eventual malfunction or damage of the sensors. The ATLAS ITk employs bi-phase CO₂ to provide a uniform cooling in the detector area down to -35°C .

To ensure the power dissipation of the modules doesn't reach the thermal runaway condition, a design requirement on the thermal performance of the HRs is imposed. This is given in terms of Thermal Figure of Merit (TFM), which can be interpreted as the thermal impedance of the local support and is defined as:

$$\Gamma = \frac{T_{\text{sensor}} - T_{\text{coolant}}}{W/S}, \quad (4.1)$$

where the numerator is the temperature difference between the boiling coolant in the pipe and the (hottest) point on the sensor, and the denominator is the module's power per area unit. A low value of TFM indicates the temperature of the sensor is close to that of the coolant and is therefore preferred. The requirements for the OECs are listed in table 4.1.

Pixel OEC Layer	Maximum TFM [$\text{K cm}^2 \text{ W}^{-1}$]
2	28.85
3	32.43
4	34.76

Table 4.1.: TFM design limits for each layer of the ITk Pixel OEC. [171].

4.3. Thermal characterisation measurement

The TFM can be measured by attaching artificial heaters (e.g. a resistive silicon plate) to the HR, which simulates the power consumption of the modules. A more detailed description of this measurement, as done at the University of Manchester, is given in section 4.4.4. However, this process is destructive for the HR, as the heaters need to be glued on its surface and cannot be removed afterwards without possibly compromising it. Therefore, the TFM is only measured with prototypes for the HR design qualification (QA) and cannot be used as a quality criterion during serial production. The thermal characterisation technique described in this section was developed as an alternative to the TFM measurement and is based

on the Infra-red (IR) thermography of an HR structure. IR cameras can detect temperature changes in an object by converting their infrared radiation into an image which can then be analysed to inspect the object's structure. The functioning principle of these cameras is the same as standard cameras that operate in the eye spectrum. IR thermography is therefore completely safe for the object under study and is widely used in the R&D sector.

4.3.1. Experimental set-up and measurement procedure

Similarly to the TFM measurement, the concept beyond the thermal characterisation strategy is to emulate the operating conditions of the running experiment and test the behaviour of the local supports. Instead of using heaters to reproduce the modules' dissipation, an HR is placed in a controlled environment at a high temperature (45 °C) and is connected to a cooling system. After thermal equilibrium is reached, the coolant (water at 10 °C) is let flow inside the HR pipe by activating a mechanical switch. The complete cooling process is recorded with an IR camera and exported as a video for an off-line analysis. The video recording is essential as it allows to analyse, frame by frame, different stages of the cooling, and also provides a time measurement.

The procedure can be repeated with different flowing directions of the coolant, as this gives more contrast to a particular zone of the subject (the fluid is colder at the inlet). With the experimental setup at the University of Manchester, only a portion of the HR enters the camera's field of view. Hence, two separate measurements are needed to cover the whole area. In normal conditions, the heat path in the HR goes from the pipe wall to the closest face-sheet. The measurement is therefore repeated with the HR facing upwards or downwards (referred to as Side A and Side B) to inspect both surfaces. This gives a total of eight different measurements (four if the cooling direction is not switched).

4.3.1.1. Experimental setup

The equipment used at the University of Manchester to perform the measurements consists in:

- **IR Camera** FLIR SC7500 Series [172] with a temperature resolution of 25 mK at 25 °C. The camera is equipped with a lens of fixed focal length equal to 12 mm and aperture F/2.

- **Climate chamber** MKT 240 [173].
- **Humidity and temperature sensor** Sensirion EK-H4 [174].
- **Movable stage** [175] to adjust the camera position.
- **Chiller** HAAKE C10 [176].

The configuration of the instruments with a HR placed inside the climate chamber can be seen in fig. 4.5

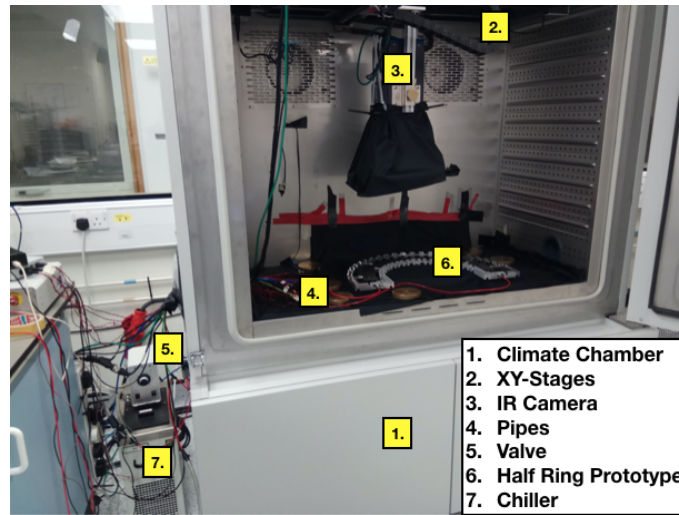


Figure 4.5.: Experimental setup in the laboratory at the University of Manchester.

4.3.1.2. Calibration

Before any set of measurements is taken, the camera needs to be calibrated to ensure it provides a correct temperature reading of the subject. The principal correction to be applied is related to the emissivity of the HR. The emissivity of an object denotes its radiative properties. It is defined as the fraction of the radiation emitted at a given temperature with respect to the one emitted by a black body at the same temperature: $\epsilon = W_{obj}/W_{bb}$. In a black body, which is a perfect emitter, the radiation directly corresponds to its temperature, and the emissivity is equal to unity. The emissivity of the HR was measured in a previous study [1] and is used as a parameter in the camera's software to correct the temperature values. Ambient radiation reflected by the HR can also affect the measured temperature. A reflective apparent temperature is measured by placing an aluminium foil in the camera's field of view. The foil reflects all of the ambient radiation, which can be measured with the camera and subtracted in the final recording. The different

pixel sensors of the camera can have a different response to the detected radiation between each other. A non-uniformity correction is applied to inter-calibrate their response. This is performed by acquiring 100 consecutive frames of a subject with uniform temperature distribution (a black nylon, polyurethane-coated fabric [177]) and, from the average value, a pixel-by-pixel offset correction is applied. This procedure is automated in the camera's software.

4.3.1.3. Reference system

In the measurement procedure and its subsequent analysis, we define a reference system where the centre of the HR corresponds to the origin. The HR is then placed as a "U" shape occupying the III and IV quadrants of a Cartesian plane. Similarly, in polar coordinates, the pole corresponds to the centre, and the HR occupies a region with angle $\phi \in [-\pi, 0]$. In this configuration, we also define the "left" and "right" views of the HR, as given in fig. 4.6.

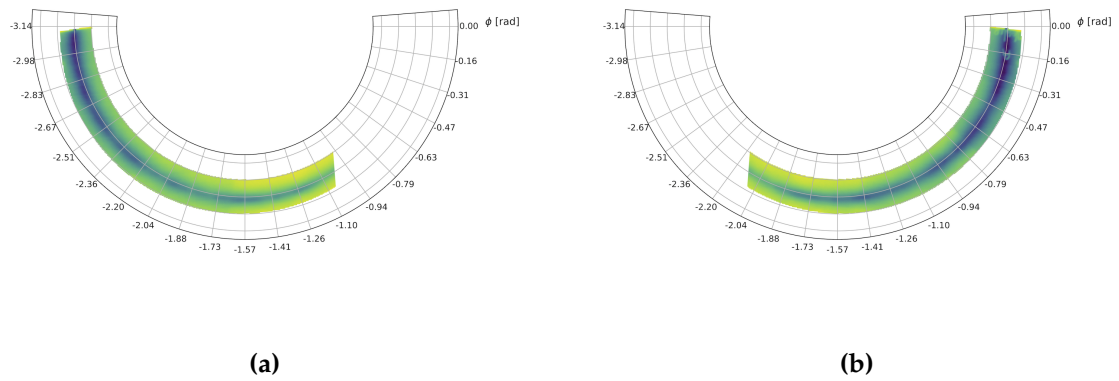


Figure 4.6.: Reference system used in the thermal characterisation measurement. The HR centre corresponds to the origin, and the angle spans from 0 to π . The HR is portrayed from its left (a) and right (b) views. Darker colours correspond to colder temperatures.

4.3.2. Analysis framework

The recorded frames are exported in a readable format and analysed with a framework fully coded in python3 [178]. The raw data consist of a matrix containing the temperature values read by each pixel of the camera and the time of the recording. The four principal steps in the analysis procedure are described in detail in the paragraphs below.

4.3.2.1. Shape recognition

The first step of the analysis has the purpose of identifying the portion of the recorded frame corresponding to the HR surface and separate it from the background. This is achieved using tools provided by the `scikit-image` [179] package in python. The different actions performed in this step are illustrated in fig. 4.7.

An edge detection algorithm, called Canny filter [180], is applied to the data to find all the points lying along the contour of the HR (fig. 4.7b). The filter also performs a Gaussian smoothing of the image to suppress the noise and reduce the possibility of false identification. The strength of the smoothing is regulated by the width of the Gaussian function to which the raw data is convoluted. The Canny filter employs an hysteresis thresholding to discriminate between the real edges of the subject and the false ones originating from the noise. The threshold value must be given in input to the filter and should be chosen appropriately depending on the analysed image. To automatise the process and avoid the necessity of a manual input for each measurement, an initial value is chosen by applying Otsu's method [181]. The method relies on the concept that the grey-level histogram of the image is characterised by distinct peaks corresponding to the foreground and background objects, and provides an optimal threshold to distinguish between the two. In case of necessity, an iterative correction is further applied to the provided threshold value until a good result is obtained.

After the edge points have been found, they are used to estimate a mathematical model to describe the shape of the HR. The model consists of two circles of different radii to represent the curved edges of the ring, plus a straight line for the transversal edge (only one line is needed as the HR is not portrayed in full). The method is versatile and can be adapted to other geometries to study different subjects. The parameters of the model are found with a RANdom SAMple Consensus (RANSAC) [182] fit applied to the points found by the Canny filter (fig. 4.7c). The algorithm is advantageous if the dataset contains outlier points which do not belong to the considered model. The randomness of the algorithm consists of the initial selection of a subset of points from which the model's parameters are estimated. All the points are then classified as inliers or outliers depending if they fall within a certain threshold from the model's prediction. The procedure is repeated several times until the model with the maximum number of inliers is found. The model obtained from the fit defines a Region of Interest (RoI) that can

be used to build a boolean mask to be applied to all the frames to extract the HR (fig. 4.7d).

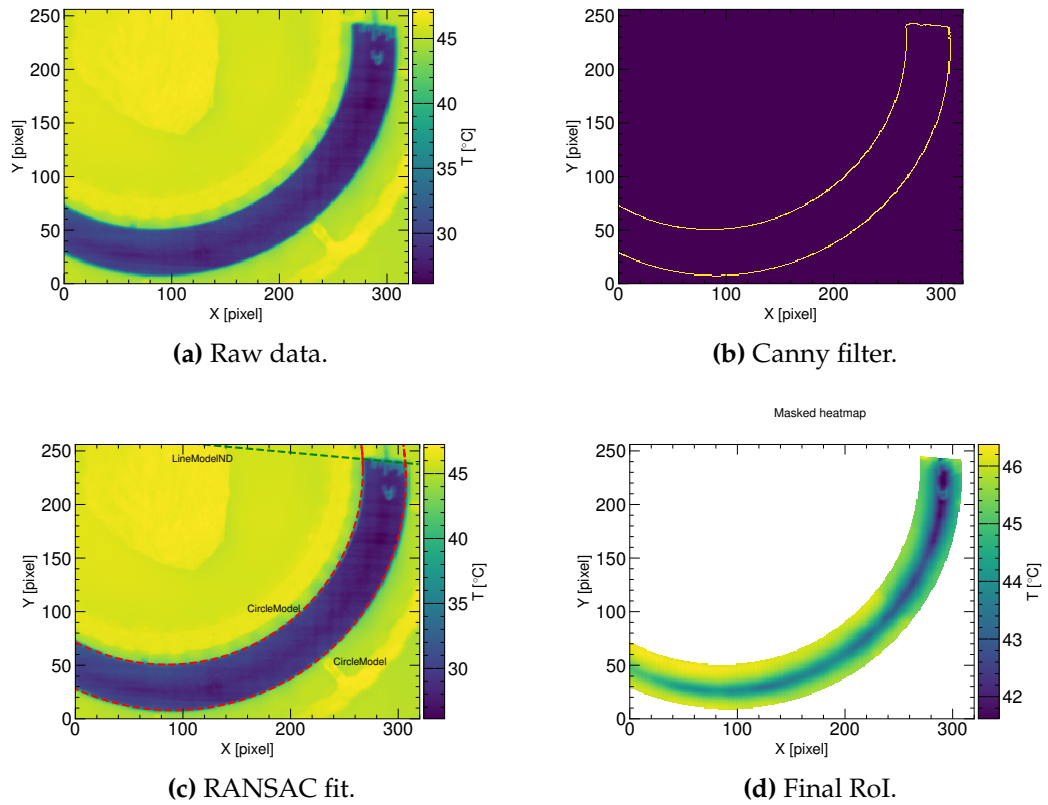


Figure 4.7.: Steps of the shape recognition algorithm applied to a HR prototype. (a) Raw data measured with the IR camera. (b) Edge points found with the Canny filter. (c) RANSAC fit (dashed lines) to the edges. The model consists of two circles (red) and a straight line (green). (d) Cut-out of the RoI from the raw frame [1].

4.3.2.2. Timing measurement

The successive step of the analysis corresponds to the evaluation of the cooling start time. This value provides a reference point for selecting the subsequent frames to be analysed. It also allows to synchronise different sets of measurements for a direct comparison of their results. The video of the cooling is recorded at 50 Hz, corresponding to a temporal separation of 20 ms between two consecutive frames. The standard deviation of the temperature on the HR surface (σ_T), as a function of the recording time, can be used as an indicator of the cooling stage. The standard deviation in each frame is computed from the temperature values registered by the different pixels of the camera, which belong to the reconstructed

RoI. At thermal equilibrium, before the cooling starts, the temperature is uniform across the HR, and σ_T is close to zero and constant over time. When the coolant is injected through the inlet, the surface on top of the pipe becomes colder, producing a gradient in the temperature distribution, resulting in the rise of σ_T . The latter continues to increase as the HR is cooled down, until a maximum is reached. After a plateau region near the maximum, the distribution eventually drops again as the temperature stabilises. The overall trend of the σ_T distribution can be seen in fig. 4.8. The cooling start time t_0 corresponds to the time at which the σ_T curve starts rising and is found by fitting two linear functions respectively to the region before and immediately after this point. The intersection of the two lines defines t_0 . The procedure is explained in fig. 4.8a. The set of points on which the linear fit is performed is not fixed, but it's found by including the maximum number of points which give the smallest χ^2 . The value of t_0 can be used as a reference point to compare sets of measurements acquired at different times, as shown in fig. 4.8b. The plots show the σ_T distribution for different measurements performed on the same prototype, after an offset correction on the time has been applied. It is clear how the different curves are synchronised and present a similar behaviour, with small differences in the rising slope due to differences in the environmental conditions.

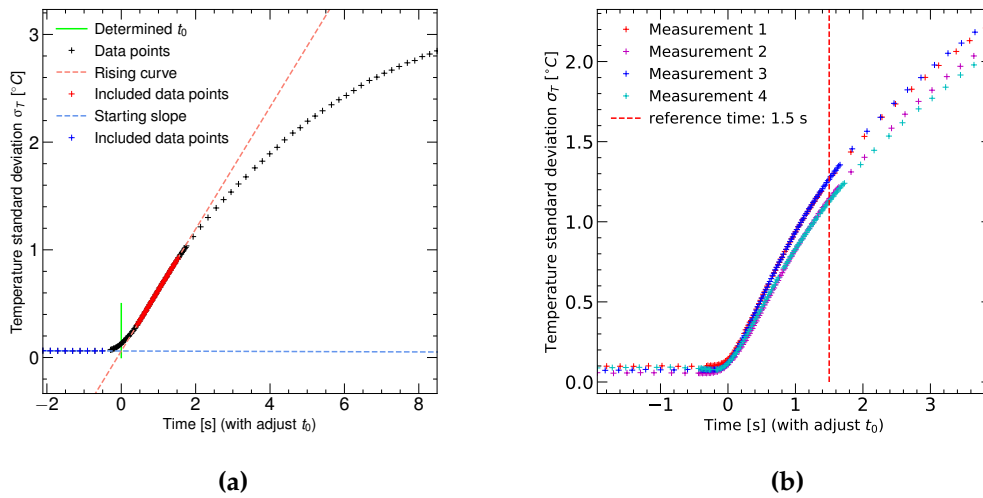


Figure 4.8.: Standard deviation of the temperature on the HR surface (σ_T) as a function of the recording time. (a) Fit to measure the cooling start time. (b) Comparison of σ_T for different measurements performed on the same HR prototype, after time adjustment with respect to t_0 . [1].

4.3.2.3. Temperature profiles and fitting

In the third step of the analysis, a single frame is selected at a given time t^* . Several temperature profiles are measured in the radial direction of the HR at different angles. The temperature in each profile is expected to have a negative Gaussian distribution, with the minimum corresponding to the point on the HR surface directly above the pipe position. The pipe groove is slightly displaced from the centre of the trapezoids towards the outer edge of the HR, resulting in asymmetric tails in the temperature distribution. We define a Gaussian function with different widths to model the profiles:

$$T(x) = \begin{cases} T_{max} - T_{diff} \cdot \exp\left(\frac{-(x-\mu)^2}{2 \cdot \sigma_{left}^2}\right) & \text{for } x \leq \mu \\ T_{max} - T_{diff} \cdot \exp\left(\frac{-(x-\mu)^2}{2 \cdot \sigma_{right}^2}\right) & \text{for } x > \mu \end{cases}, \quad (4.2)$$

where T_{max} and T_{diff} are respectively the maximum temperature and the maximum temperature difference in the profile, μ corresponds to the distance of the minimum from the inner edge of the HR (the pipe position) and $\sigma_{L,R}$ are the two widths of the asymmetric Gaussian distribution. All of the parameters above are evaluated with a fit to the temperature profile and used at a later stage to assess the thermal performance of the HR. Examples of the profile extraction and the profile fitting are reported in fig. 4.9.

4.3.2.4. Evaluation of the results and identification of defects

The parameters of eq. (4.2) can be used to evaluate the cooling capabilities of the HR and identify defective areas where the thermal performance is less effective. Both μ and $\sigma_{L,R}$ are indicative of the pipe position and could be used to spot eventual misalignments in the assembly procedure. The temperature on top of the pipe position (T_{pipe}), defined as $T_{max} - T_{diff}$, was found to be an observable sensitive to inefficiencies in the heat propagation [1]. In the absence of any defect, T_{pipe} is expected to linearly increase from the inlet position to the outlet, as the coolant is heated up while it flows through the pipe. Any peak in the temperature distribution would be a sign of a potential structural defect which is impairing the cooling capabilities of the HR. The slope of the T_{pipe} distribution, and the magnitude of the peaks, strongly depend on the time chosen during the previous step of the analysis. Early in the cooling process, the peaks would result smaller or not visible at all because of the small temperature gradient across the HR surface.

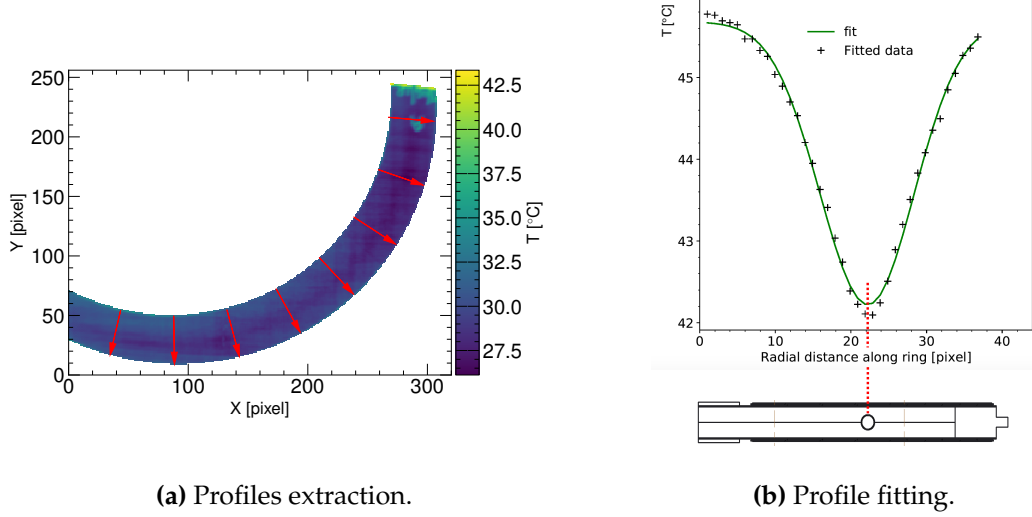


Figure 4.9.: (a) Temperature profiles are extracted from the HR surface in the radial direction for different angles, as shown by the red arrows. (b) Fit to a temperature profile (green line) with the corresponding position shown by a cross-section of the HR [1]. Uncertainties are not showed in the plot.

Conversely, if the time is too late, the T_{pipe} distribution would be no longer linear as the HR is uniformly cold. A value of $t^* = t_0 + 1.5\text{ s}$ was empirically found to provide good sensitivity to defects while maintaining a linear behaviour [1]. To assess if the fit is descriptive of the data, the T_{pipe} distribution is also compared to that obtained from the raw data by selecting the minimum measured temperature in each profile. The two distributions typically show very similar results, but the fit is more robust to data fluctuations.

An example of T_{pipe} distribution is reported in fig. 4.10, which shows the left view of a well-performing HR. The little bumps observed in the distribution (e.g. at $\phi \approx -2$) are too small to cause any significant difference in the thermal performance. More details on the peak amplitude and their effects are given in section 4.4. Depressions like the one observed at $\phi \approx -1.4$ have been associated with alterations (scratches) of the HR face-sheet, which result in a smaller temperature measured by the camera.

Some corrections are applied to the results when comparing different sets of measurement in such a way that the different distributions result aligned. Misalignments in the angle position are accounted for by requiring the leftmost (rightmost, depending on the HR view) to start at a value of $-\pi$ (0). The absolute

value of T_{pipe} can also vary for different measurements due to changes in the environment conditions³. A constant temperature offset can be subtracted from the data without losing information, as the slope of the distribution does not change. A single measurement is chosen as a reference, and the offset correction is applied to the others. The offset value is computed by measuring the average distance between the selected T_{pipe} curve and the reference one. A linear fit with the RANSAC algorithm is applied to exclude eventual peaks from the offset computation. The procedure is illustrated in fig. 4.11.

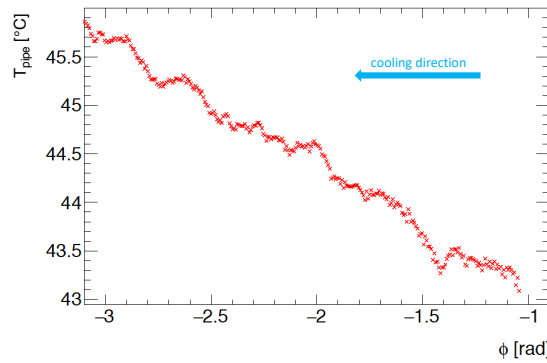


Figure 4.10.: Distribution of T_{pipe} as a function of the angle for the left view of a HR prototype. The cooling direction goes from the right to the left. A linear trend indicates the cooling process is behaving as expected. Peaks in the distribution would indicate potential defects.

4.4. Measurements with prototypes

This section describes the measurements carried-out on HR prototypes at the University of Manchester. Some preliminary tests to evaluate the sensitivity of the thermal characterisation technique were carried-out with small pieces of a HR before the time of this study and are available in [1]. Results obtained with entire Layer 2 and Layer 3 local support prototypes are reported⁴ here. For the sake of brevity, only prototypes of interest are included.

As part of the thermal QA and QC of the HRs, some stress-tests are performed to check the resistance of the local supports to extreme variations of the envi-

³The climate chamber can only provide a temperature stable within 2 °C. Humidity and room temperature can also affect the measurement.

⁴Layer 4 local supports will be produced in Italy with a similar procedure.

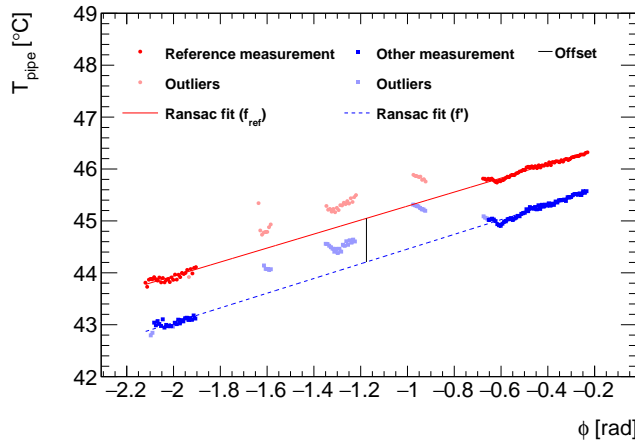


Figure 4.11.: Procedure to subtract a temperature offset to compare different results. The reference measurement (red) and a second measurement (blue) are fitted with a linear model using the RANSAC algorithm to exclude eventual peaks in the distribution. The average temperature difference between the two lines (black) gives the offset value. The four gaps in the temperature distributions are due to silicon heaters glued to the HR surface, which obstruct the camera's view (see section 4.4) [1].

ronmental conditions. The HRs are made of materials characterised by different thermal expansion coefficients. The non-uniform response to temperature changes may provoke structural damage in the local supports caused by the stretching of the components, especially near the glue layer. The prototypes undergo a process of thermal cycling during which the environment temperature (the HR is placed inside the climate chamber) is varied between -55°C and 60°C over several hours. The two limits correspond to the minimum expected temperature during operation and to the highest temperature expected during shipment and storage, with safe factors applied. Measurements of TFM and thermal characterisation are performed before and after cycling, to check for any change in the HR performance. The pipe's resistance to change in pressure is also assessed in a similar procedure. A HR prototype is filled with water and its pipe is attached to a hydraulic pump which raises the pressure up to 162 bar. The same thermal measurements are also performed between pressure cycling. The number of total cycles varies for the QA and the QC. In the first case, the prototypes undergo up to 100 thermal cycles and 100 pressure cycles for the design qualification. These numbers correspond to the expected cycles during operation for the entire lifetime of the detector. During the serial production of the local supports, the cycling is performed only once to significantly reduce the amount of dead time.

4.4.1. Prototype L3.5

Prototype L3.5 is a Layer 3 local support prototype assembled at the University of Manchester. It is the first prototype to be thoroughly tested with a complete thermal and pressure cycling chain. Pictures of the two sides of the HR are shown in fig. 4.12. Silicon heaters (the silver squares in the picture) of the same size as the quad modules are attached to the HR surface to allow the measurement of the TFM. The heaters are highly reflective objects, and the IR camera cannot detect the temperature of the area they occupy. Three heaters occupy the central part of Side B, with the same configuration that will be used in the loaded local supports. Additionally, Side A has two heaters placed in the gap region formed by the heaters on the opposite face of the HR. A piece of glass was glued to the surface of Side B for loading tests.

The complete program of measurements carried out on prototype L3.5 is listed in table 4.2. The cycling procedure was executed in different steps, with measurements of the thermal performance carried-out in between. Thermal cycling was done in steps of 10, 20, 30, and 40 cycles, while pressure cycling in steps of 10, 40 and 50 cycles, to reach the total number of cycles needed for the QA protocol. After step 9, the cooling system's valve, used in the thermal characterisation measurement to inject the coolant in the HR, broke and had to be replaced. The cooling process was observed to be slower with the new equipment, likely due to changes in pressure and velocity of the fluid, resulting in a different σ_T distribution. The difference was significant enough to de-synchronise the measurements and alter the T_{pipe} slope. An adjustment in timing was necessary to compare the results obtained before and after the valve replacement. A new time of $t^* = t_0 + 2.3 \text{ s}$ was empirically found to yield a T_{pipe} distribution with a similar slope as before.

The results of the thermal characterisation measurements after a different number of thermal and pressure cycles are reported in fig. 4.13 (only a subset of table 4.2 is shown). The plots show the T_{pipe} distribution for the left and right views of each side of the HR. The cooling direction follows the view of the HR (from the left to the right side in the left view of the HR and vice-versa) to enhance the temperature gradient in the region. The area occupied by the heaters and the glass piece is manually removed from the frame for the reasons explained above. Some spikes in the T_{pipe} distribution are present near the heaters' position and are

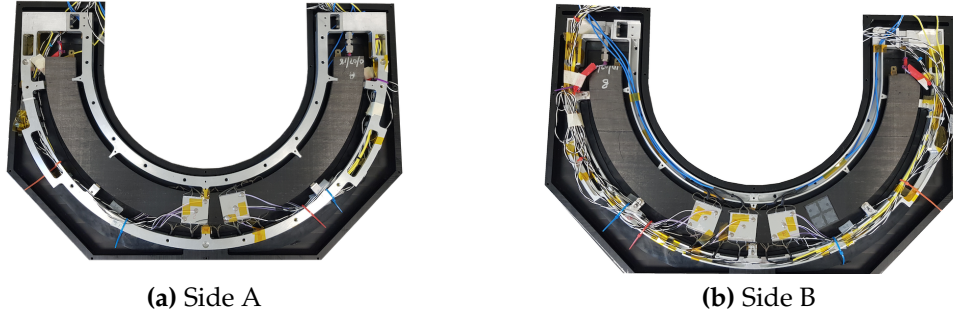


Figure 4.12.: Prototype L3.5 (Layer 3). The silver squares are silicon heaters attached to the surface of the HR to measure its TFM. The transparent square visible on Side B (b) to the right of the heaters is a piece of glass used in loading tests. The deposited glue is visible underneath it, with the shape of four smaller square-like layers.

Step	Action	Step	Action
1	TFM + IR	9	TFM + IR
2	10 temperature cycles	10	10 pressure cycles
3	TFM + IR	11	TFM + IR ^(*)
4	20 temperature cycles	12	40 pressure cycles
5	TFM + IR	13	TFM + IR ^(*)
6	30 temperature cycles	14	50 pressure cycles
7	TFM + IR	15	TFM + IR ^(*)
8	40 temperature cycles		

Table 4.2.: Program of measurements carried-out with prototype L3.5. IR denotes the thermal characterisation with the infrared measurement. Measurements marked with a (*) were performed with a new valve in the cooling system.

caused either by border effects which alter the temperature profiles, for example around $\phi \approx -1.6$ of fig. 4.13b, or by the presence of wires, like at $\phi \approx -1.3$ in the same plot. This apparent temperature rise is non-physical and should not be interpreted as a defect in the prototype. The regions close to the straight edge of the HR also present some border effects (they were also marked to indicate the side's name) and were therefore removed from the plots.

The T_{pipe} distributions present the expected linear behaviour, with the exception of the right view of Side A (fig. 4.13b), where a wide peak is observed around $\phi \approx -0.7$. Another peak is also observed in the right view of Side B, which is significantly smaller than the previous one. The peaks do not manifest a counter-

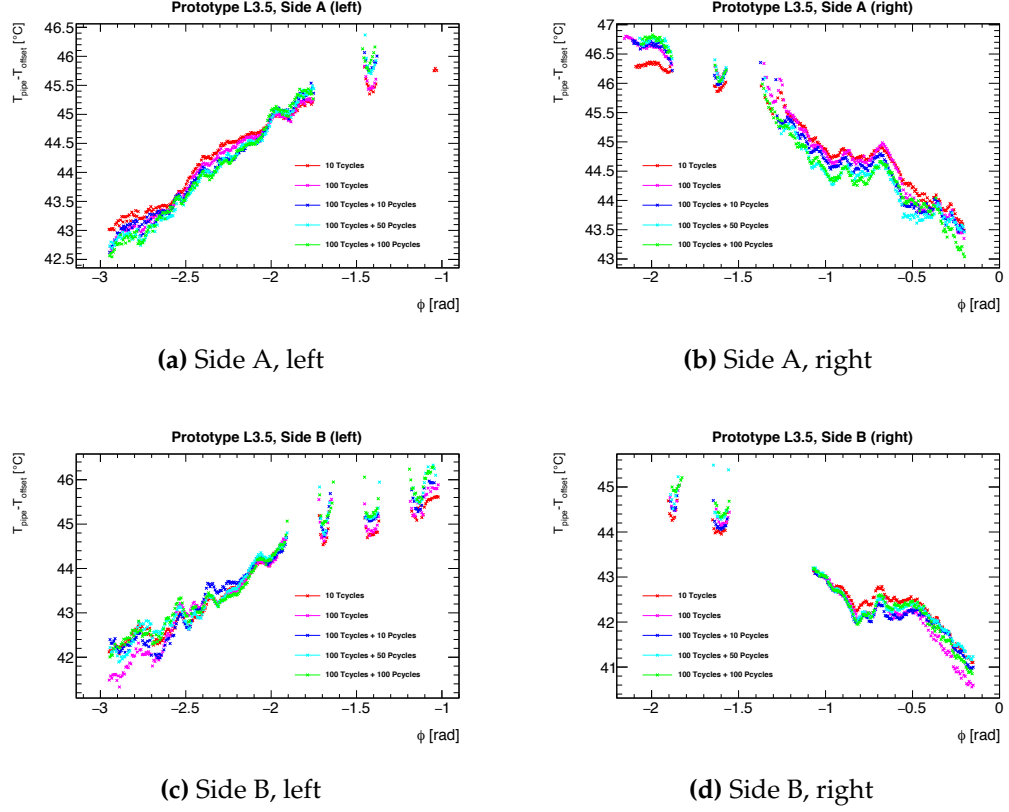


Figure 4.13.: Distribution of T_{pipe} as a function of the angle for the left and right views of Side A and Side B of prototype L3.5. Measurements after 10 and 100 cumulative thermal cycles are shown respectively in red and fuchsia. Additional measurements after 10, 50 and 100 cumulative pressure cycles are shown in blue, cyan and green.

part on the opposite side of the HR⁵, hinting at a possible defect in the glue layer between the pipe and the foam of the corresponding side, or in the foam itself. The results of the different measurements have been aligned following the procedure described in section 4.3.2.4. Overall, they show the same trend after different numbers of thermal and pressure cycles, with minimal differences in slope caused by a change in the environment at the time of the measurement. The overlap of the T_{pipe} distributions suggests that cycling did not alter the thermal capabilities of the HR, proving its resistance to temperature and pressure variations. The peak observed in Side A is further studied to better understand its magnitude and evaluate its evolution after cycling. A linear fit with the RANSAC algorithm is performed to the T_{pipe} distribution and a residual temperature is computed

⁵Side A and side B are reversed, meaning the right view of one side corresponds to the left view of the other.

as $T_{res} = T_{pipe}^{(Data)} - T_{pipe}^{(Fit)}$. The residual temperature in the peak region is shown in fig. 4.14. A flat 0.05°C systematic uncertainty is applied to T_{res} to account for small variations of the environmental conditions and of the analysis procedure. The value corresponds to the average spread in ϕ of T_{res} , found by subsequently repeating the measurement with the IR camera multiple times and applying the full analysis chain to the data. The plot confirms the hypothesis that the thermal performance of the prototype does not worsen after cycling. The peak has a magnitude of about 0.5°C , which does not increase in the following measurements. A slight increment is observed after 100 thermal cycles but is consistent within uncertainties.

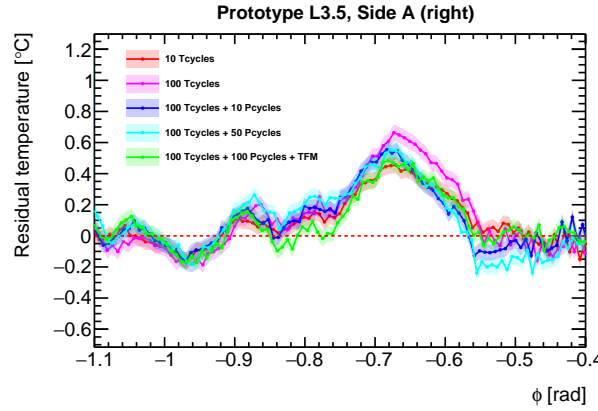


Figure 4.14.: Residual temperature near the peak region observed in Side A of prototype L3.5 (see fig. 4.13b). Measurements after 10 and 100 cumulative thermal cycles are shown respectively in red and fuchsia. Additional measurements after 10, 50 and 100 cumulative pressure cycles are shown in blue, cyan and green.

4.4.2. Prototype L3.4

Prototype L3.4, displayed in fig. 4.15, is another Layer 3 prototype, also assembled at the University of Manchester in the same period as its L3.5 counterpart. A different test strategy was adopted with this prototype with respect to L3.5. A thermal characterisation measurement was performed with the bare prototype to search for potential defects and install heaters on their position. The IR thermography results unveiled different peaks in the T_{pipe} distribution. The largest of them, located on Side B around $\phi \approx -0.75$ and shown in fig. 4.16a, was selected for the operation. Two heaters were glued on Side B near the peak area, one exactly on the peak position and the other on its side, as indicated in fig. 4.16b. An additional

heater was placed on Side A in between. The standard three heaters in the HR central region were also included.

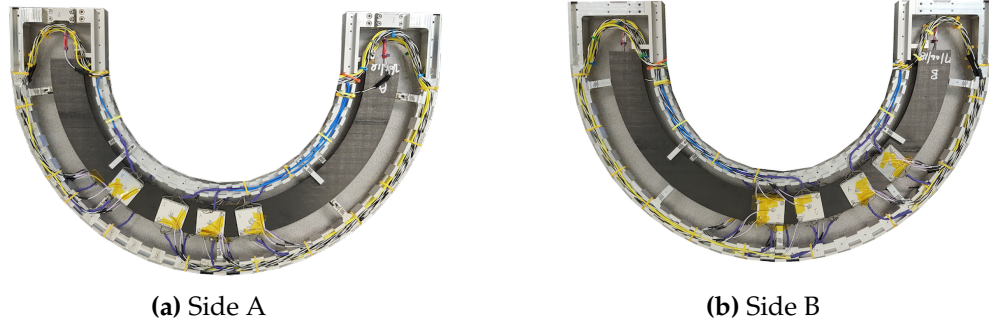


Figure 4.15.: Prototype L3.4 (Layer 3). The silver squares are silicon heaters attached to the surface of the HR to measure its TFM.

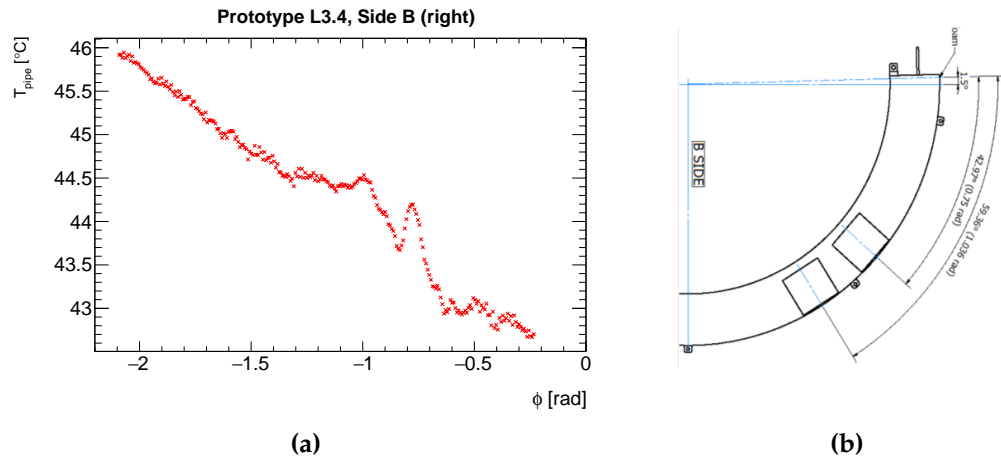


Figure 4.16.: (a) Possible defect observed in Prototype L3.4 with the thermal characterisation measurement. (b) Silicon heaters were glued on the HR surface on the area identified by the IR camera to allow the measurement of the TFM [1].

A similar program of measurement as the one listed in table 4.2 was implemented, with a slight change in the thermal cycling steps to match the pressure cycling ones. The results of the thermal characterisation are reported in fig. 4.17, with the same configuration discussed for fig. 4.13. Similarly to L3.5, the T_{pipe} distributions present a linear behaviour which doesn't change after cycling. Another peak of similar size as the one observed in the previous prototype was found on Side A around $\phi \approx -0.47$ (fig. 4.17b). The same region also presents two more peaks of smaller amplitude. The residual temperature for the largest peak in Side A is shown in fig. 4.18, indicating no degradation after cycling.

After the full program of measurements was completed, the heaters were carefully removed from the HR in the attempt to measure the defective area once again with the IR technique. T_{res} is compared with the first result obtained before glueing the heaters and shown in fig. 4.19. An increment in the peak magnitude hints at a possible worsening of the thermal performance.

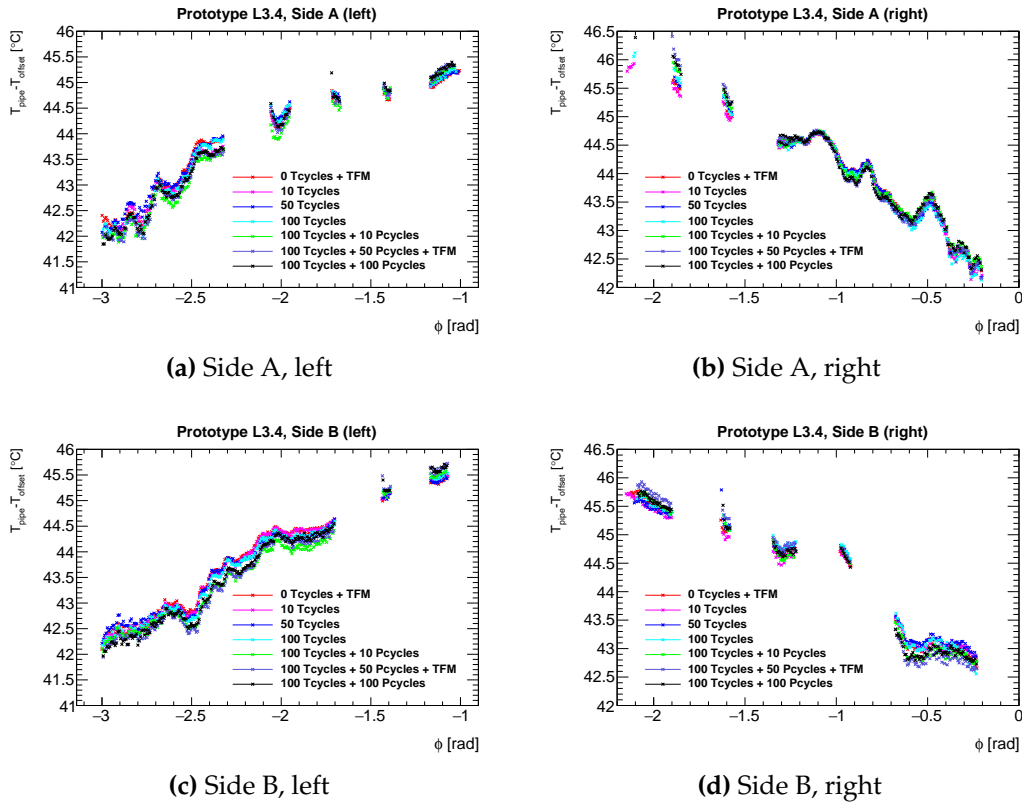


Figure 4.17.: Distribution of T_{pipe} as a function of the angle for the left and right views of Side A and Side B of prototype L3.4 for different numbers of cumulative thermal and pressure cycles [1]. The label "+TFM" indicates that the infrared measurement was carried out only after performing the measurement of TFM. Otherwise, the results were obtained soon after the cycling procedure.

4.4.3. Prototype L2.1

Prototype L2.1 is a Layer 2 local support built with intentionally implanted defects to further understand the impact of issues in the assembly procedure. The defects are summarised in fig. 4.20. The most relevant one consists of a portion of the pipe embedded in the HR without glue and is placed in the left part of Side B (shown on the right in the figure). Measurements with the IR camera are performed, and the results are given in fig. 4.21. Two adjacent peaks are observed

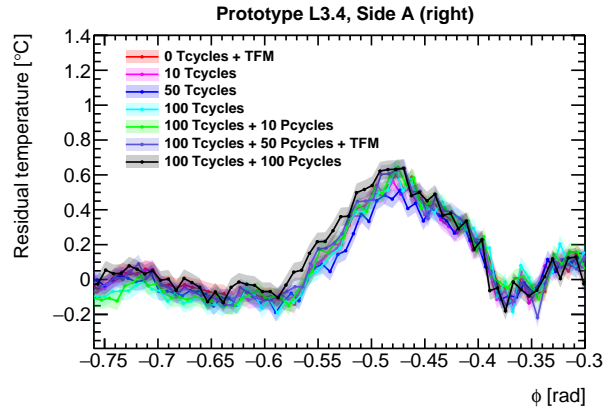


Figure 4.18.: Residual temperature near the peak region observed in Side A of prototype L3.4 (see fig. 4.13b) for different numbers of cumulative thermal and pressure cycles [1].

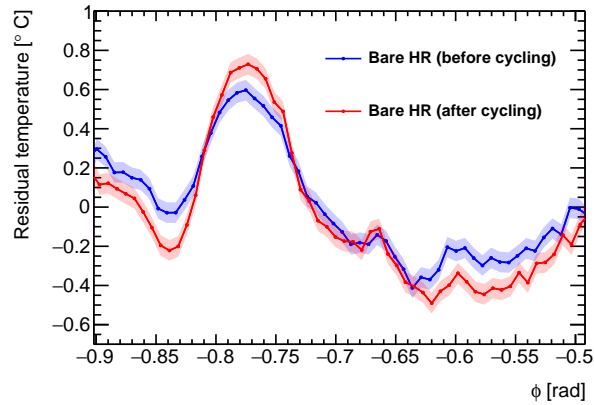


Figure 4.19.: Residual temperature near the peak region observed in Side B of prototype L3.4 (see fig. 4.16a) before mounting the heaters (blue) and after the full program of measurement (red) [1].

close to the no-glue region in both Side A and Side B, respectively shown in figs. 4.21b and 4.21c, further proving the capability of the thermal characterisation technique to identify defects. The magnitude of the peak, shown in fig. 4.22a is larger than the precedent observations made with prototypes L3.4 and L3.5. A broad peak, the largest among all others, was also found around $\phi \approx -2.7$ in Side A and is not associated with a known defect, meaning that this defect was accidentally introduced during the assembly process. The residual temperature is reported in fig. 4.22b. All the plots report four different sets of measurements, carried out with the same experimental configuration to check the consistency of the results. The different T_{pipe} distributions and peak amplitudes present similar features, with minor differences attributed to changes in the environment

conditions. The peaks have been further studied with measurements of the TFM by mounting heaters on the identified areas, as done with prototype L3.4. These are discussed in section 4.4.4.

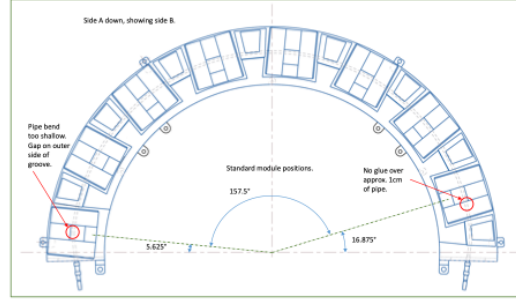


Figure 4.20.: Schematic of prototype L2.1 (Side B) with the defects intentionally included in the assembly procedure.

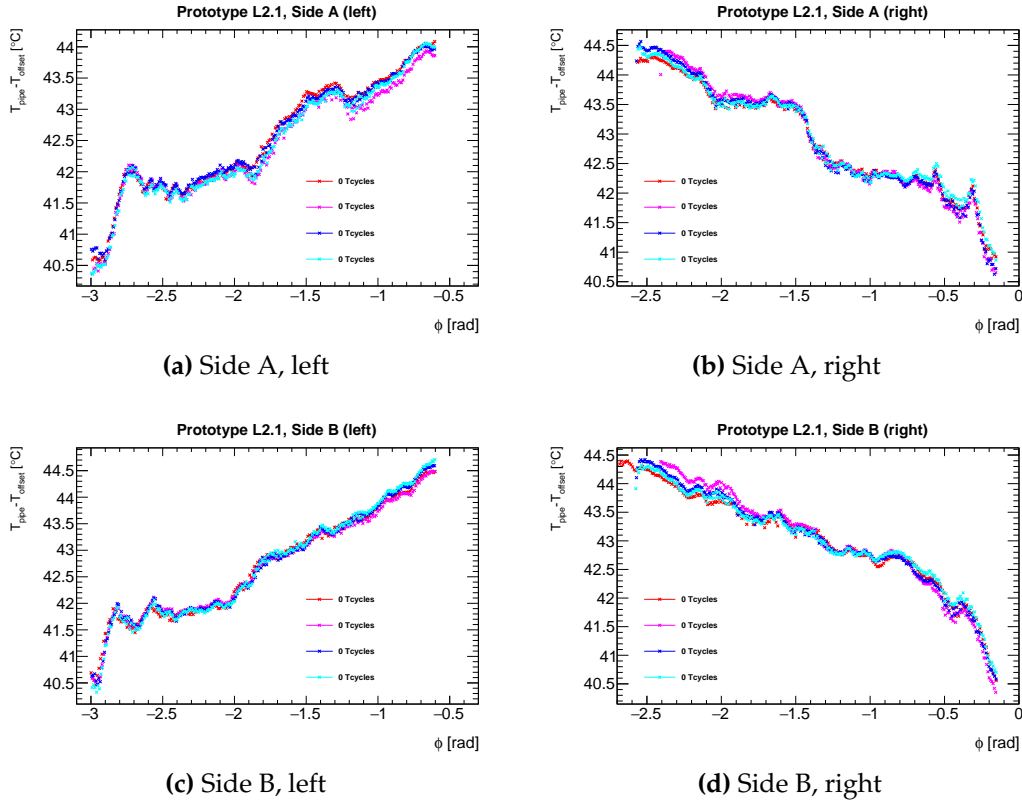


Figure 4.21.: Distribution of T_{pipe} as a function of the angle for the left and right views of Side A and Side B of prototype L2.1. Different colours represent different sets of measurements carried out with the same configuration to check the consistency of the results. The prototype did not undergo thermal or pressure cycling before the measurement.

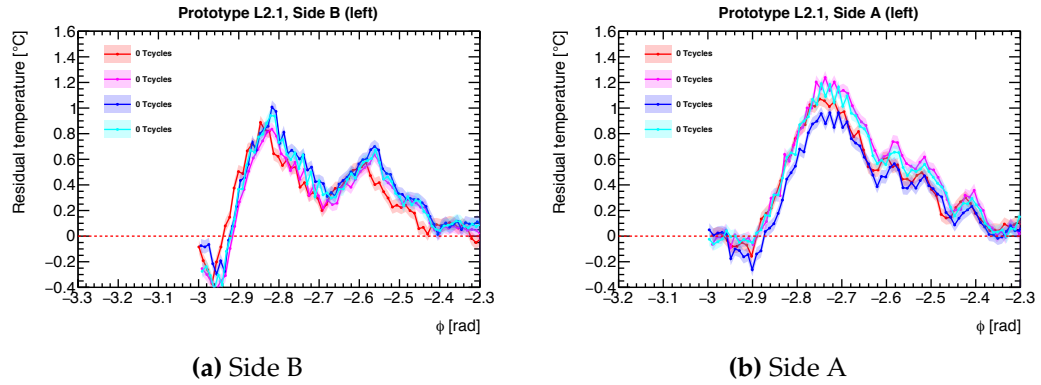


Figure 4.22.: Residual temperature of the peaks observed in the thermal characterisation measurement carried-out on prototype L2.1. Different colours represent different sets of measurements carried out with the same configuration to check the consistency of the results. The prototype did not undergo thermal or pressure cycling before the measurement.

4.4.4. Comparison with TFM measurements

Measurements of the TFM were carried out in parallel to the thermal characterisation of the local support prototypes with the purpose of correlating the results of the two techniques and establish a criterion to reject under-performing HRs in the serial production. These particular measurements were done by another member of the Manchester team, so only a brief description is given here.

As described in section 4.3, silicon heaters are attached to the surface of the HR to simulate the heat produced during the operation of the pixel modules. The heaters have a known resistance of about $3\ \Omega$ and are powered up to simulate the power consumption of the real modules. NTC (negative temperature coefficient) sensors are soldered to the heaters to measure their temperature during the procedure. The resistors are attached to a VOLTRON (VOLTage to Temperature ReadOut iNstrument) board [183] read by an Arduino MEGA board [184]. Typically, three resistors per heater are used, with one placed at the centre of the plate and two at opposite corners. The configuration of the NTCs for the heaters in the central region of the HR is illustrated in fig. 4.23a. The HR is vertically attached to a cooling system, like in fig. 4.23b, which provides CO_2 at $-10\ ^\circ\text{C}$ with a flow of $0.7\ \text{g s}^{-1}$. A blow-off evaporative cooling plant was used for the measurement carried out with prototypes L3.4 and L3.5, while a MARTA recirculating system [185] was used with L2.1. During the measurement, the heaters are connected to an external power supply. A varying heat flux is generated in the

heaters depending on the input voltage. The TFM is measured for different flux values up to 0.7 W cm^{-2} , corresponding to the expected module dissipation.

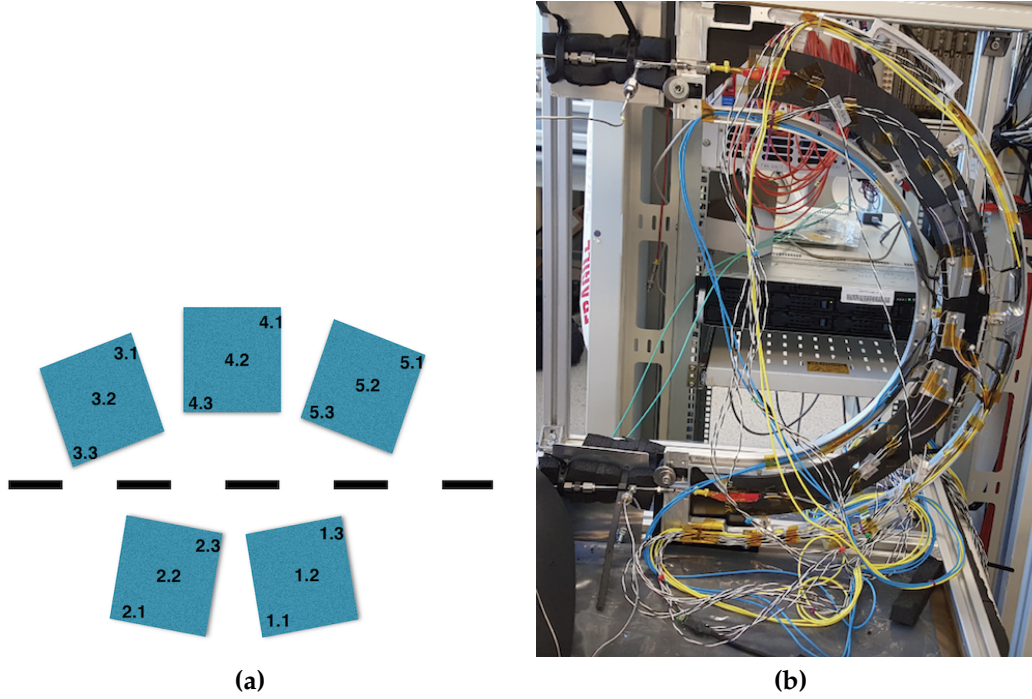


Figure 4.23.: Schematic of the NTC sensors configuration on the heaters occupying the central region of a HR (a). Setup of the HR attached to the cooling system for the TFM measurement (b).

Average values of TFM measured with Layer 3 prototypes (L3.4 and L3.5) are reported in fig. 4.24. The TFM value slightly increases after 10 thermal cycles and is stable afterwards. The plots also suggest a possible worsening after 50 pressure cycles. In particular, the heaters placed on the defective area (fig. 4.16b) showed a larger increment of the TFM value after pressure cycling. This would support the hypothesis of deterioration of the defect, also observed with the IR measurement after the removal of the heaters. The TFM values are still well within design specifications for Layer 3 local supports, but are close to the limits for Layer 2. However, a large safe factor was applied in the requirements, meaning the thermal runaway threshold is far from the measured values. After a careful evaluation of the TFM results and of the thermal conductivity spread of the carbon foam blocks⁶, it was decided to change the type of foam to increase its density by a

⁶The production procedure of the carbon foam does not guarantee a uniform thermal conductivity and density. The average values were measured to be respectively about 20 W mK^{-1} and 0.22 g cm^{-3} , both with large spread.

factor 2 as a safety measure [186]. A denser foam has a larger thermal conductivity and will guarantee the *TFM* requirement will be satisfied even if the foam density is lower than the average value.

After mounting the heaters on prototype L2.1, it also underwent thermal and pressure cycling. The average *TFM* after a different number of cycles is reported in fig. 4.25. The *TFM* value is given separately for three different zones of the HR: the central region corresponds to the standard 3 + 2 heaters placed at the middle of the HR, the minor defect corresponds to the T_{pipe} peak observed in fig. 4.22a (the no-glue region) and the major defect corresponds to the peak in fig. 4.22b. The central and minor defect regions do not present signs of degradation after cycling. On the other hand, the major defect has significantly worse results, which are also unstable. The non-stability of the results might be caused by environmental effects and changes in the experimental setup (the cooling system broke after 50 pressure cycles), but it is not possible to assign a specific trend. Given the high *TFM* values, which will be mitigated by the employment of the denser foam, a local support with a defect this large would not pass the QC requirement during production.

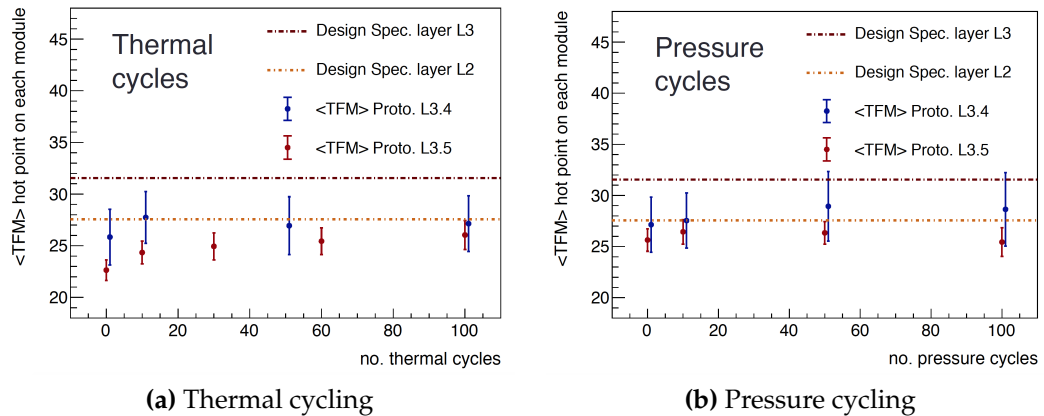


Figure 4.24.: Average *TFM* measured with prototypes L3.4 (blue) and L3.5 (red) as a function of the number of cumulative thermal and pressure cycles. The *TFM* values are expressed in $\text{K cm}^2 \text{W}^{-1}$. The uncertainties correspond to the RMS of the measurement. Design limits to the *TFM* are also shown with dashed lines for Layer 2 (orange) and Layer 3 (brown) [187]⁷.

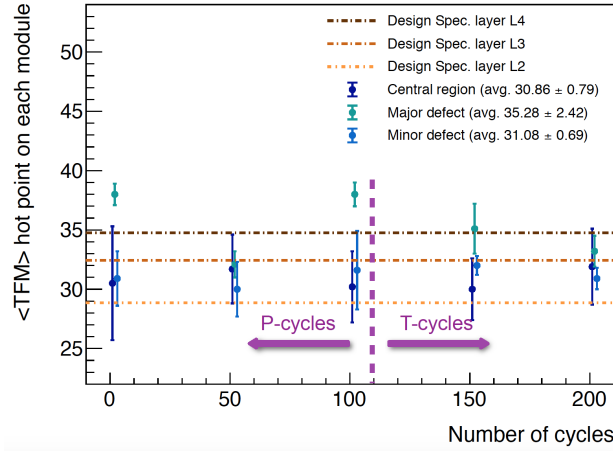


Figure 4.25.: Average TFM measured with prototype L2.1 as a function of the number of cumulative thermal and pressure cycles. The TFM values are expressed in $\text{K cm}^2 \text{W}^{-1}$. The results are given separately for the central region of the HR (blue), for the minor defect corresponding to fig. 4.22a (light blue) and for the major defect corresponding to fig. 4.22b (green). Design limits to the TFM are also shown with dashed lines for Layer 2 (orange), Layer 3 (brown) and Layer 4 (black). [188].

4.5. Towards production of the local supports

The ITk pixel OEC local supports' production is expected to begin in early 2024, with a joint effort between several institutes in the United Kingdom and Italy. About half of the total number of bare local supports, corresponding to the full set of Layer 3 HRs and half of Layer 2 ones, will be manufactured at the University of Manchester's facilities.

The HRs construction will be carried-out in a serialised production chain, in such a way that the goodness of the products can be assessed between different steps of the assembly procedure, and for each finalised local support. The Quality Control schedule is currently being optimised, and includes the evaluation of the thermal performance with the technique described in this thesis. Due to time constraints, and to prevent the prototype from undergoing unnecessary stresses during production, the thermal QC procedure will involve a reduced amount of thermal and pressure cycling compared to those used for the design qualification (QA). Currently, each produced HR is foreseen to be subject to a single pressure and thermal cycle, with a potential smaller temperature variation in the latter (the full temperature operating range of the Pixels ranges from -45°C to 40°C).

The thermal characterisation measurement with the infrared camera will be performed at least once after the cycling procedure, to single out poorly performing HRs. The peak residual temperature from the T_{pipe} distribution will be employed to determine whether the local supports meet the requirements, as illustrated in section 4.4. The TFM values measured with the (intentionally-built) defective prototype L2.1, reported in section 4.4.4, are at the limit of the design tolerance. Therefore, a HR presenting a peak of similar or larger magnitude than that observed in fig. 4.22b will be flagged during production, and it will be either discarded or kept as a spare part. The selection criteria will be further optimised with more data being gathered with newly-built HRs, as prototype L2.1 currently represents the sole case that was found to be in tension with the design specifications.

Blank Page

Chapter 5.

Differential cross-section of $ZZ + jj$ production at $\sqrt{s} = 13$ TeV

This chapter describes the measurement of unfolded differential cross-sections of $pp \rightarrow ZZjj \rightarrow \ell^+ \ell^- \ell^+ \ell^- jj$ ($\ell = e, \mu$) production performed with a dataset collected by the ATLAS experiment at $\sqrt{s} = 13$ TeV [2]. Section 5.1 introduces the analysis and its motivations. The data and MC samples used for the measurement are described in section 5.2. Section 5.3 defines the analysis phase space and the event selection. It also defines the measured observables and the signal regions used to obtain the results. The background estimation is outlined in section 5.5. An unfolding procedure is used to correct for detector effects and measure the cross-sections at fiducial-level. This is described in section 5.6. The evaluation of systematic uncertainties is discussed in section 5.8. The unfolded differential cross-sections are reported in section 5.9. Lastly, an Effective Field Theory (EFT) interpretation of the unfolded results is given in section 5.10. The studies described in this chapter, except the non-prompt background estimation and the EFT fits, were carried out by the author of this thesis and led to the publication of the measurement by ATLAS.

5.1. Introduction

The EW production of $ZZjj$ is a rare process, as pointed out in fig. 2.1. The high energy collisions at the LHC offer a unique condition to study this otherwise elusive process. The EW $ZZjj$ production mechanism is dominated by the t -channel exchange of weak bosons, which interact to form a pair of Z bosons in the final state. The two Z bosons successively decay leptonically into a $\ell^+ \ell^-$

pair, while the deflected initial partons form two jets in the final state. Despite the small $Z \rightarrow \ell^+ \ell^-$ branching ratio of 3.36(5)% per flavour [17], the leptonic decay channel provides the cleanest measurable final state of the $ZZjj$ production. The $4\ell jj$ final state can be fully reconstructed and presents a small background, mainly originating from the associated $t\bar{t} + Z$ production or triboson processes. Some characteristic diagrams describing the EW $ZZjj$ production can be seen in fig. 5.1. The non-abelian gauge structure of the EW interaction provides WWZ and $WWZZ$ vertices at tree-level, which can be used to probe weak boson self-interactions and search for anomalous couplings [189–192]. The VBS scattering amplitude from the self-interactions would diverge at high energy and violate unitarity at the TeV scale if not for precise cancellations caused by the presence of the diagrams containing the Higgs boson [193]. The $ZZjj$ production cross-section can therefore be used to test for a variety of New Physics models.

Alongside the EW production, the $ZZjj$ final state can also originate from strong interactions, as shown in fig. 5.2. In this case, the final-state jets mainly arise from the strong interaction. These processes are not additionally suppressed by higher α_{EW} order interactions, as in the EW case, and constitute the principal production mechanism of $ZZjj$ events. The final state particles produced in EW and strong interactions are indistinguishable from each other. However, the peculiar kinematic properties of the VBS mechanism can help to separate the two contributions, as discussed in section 5.3.2. The study of strong $ZZjj$ production is also of great interest, as the cross-section predictions depend on the accuracy of perturbative QCD calculations, which could be unreliable in extreme phase space regions. A differential measurement of strong $ZZjj$ production cross-section can help to compare and further constrain the modelling of QCD interactions in these regions (e.g. at large values of the dijet invariant mass). This would be extremely valuable for future measurements that rely on accurate modelling of the strong background, often one of the leading sources of systematic uncertainties. The measurement described in this thesis is inclusive of both the EW and strong production mechanisms, exploiting two different phase space regions where either of the two components is enhanced (see section 5.3.3).

The ATLAS experiment provided a strong effort to measure different VBS processes, including $Z\gamma jj$ [194, 195], same-sign $WWjj$ [196] and $WZjj$ [197] production. Concerning the ZZ final state, ATLAS recently measured the inclusive 4ℓ production cross-section with a complete Run 2 dataset [198]. The phase space

explored in the measurement is an extension of the one targeted in this thesis, as it contains the $ZZ \rightarrow 4\ell$ final state without requirements on the jets. The EW $ZZjj$ production was also recently observed by ATLAS with a significance greater than five standard deviations [199]. Similarly, the CMS experiment conducted a complementary search for the EW process, providing evidence with a significance greater than three standard deviations [200]. In Ref. [199], only the total EW $ZZjj$ production cross section was measured. The results presented in this thesis represent the first attempt to measure the inclusive $ZZjj$ cross-section differentially, in a phase-space where the EW contribution is enhanced. The differential nature of the measurement is instrumental, as it not only allows to test the production rate but is also sensitive to effects which depend on the shape of the measured observables. For example, this is particularly relevant for some New Physics models where the BSM contribution increases at high energy (e.g. as a function of the dijet or ZZ invariant mass) or for some CP-odd observables, which could present an asymmetric distribution. The measured differential cross-sections are also extrapolated at fiducial-level with an unfolding procedure, thus allowing a direct comparison with the expected values predicted by the theory. The model-independent EFT approach, described later in section 5.10, can be used to probe New Physics from the unfolded differential cross-sections, comparing the results with the EFT-corrected SM predictions and setting limits on the coupling constants of higher-dimension operators. The cross-sections presented here also complement the measurement in Ref. [198], as the latter corresponds to a more inclusive phase space where the EW production represents only a small fraction of the total. The presence of two jets in the final state also makes the measurement more sensitive to the effect of missing higher-order corrections in perturbative QCD.

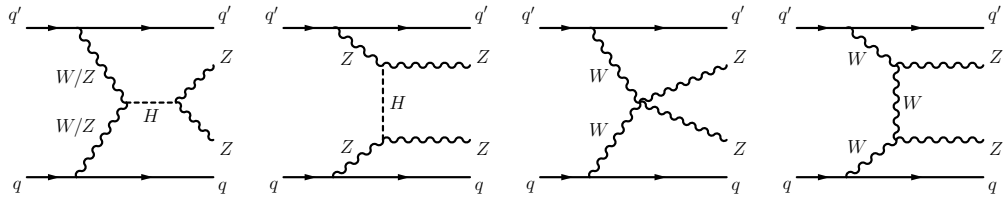


Figure 5.1.: Typical diagrams for the EW production of $ZZjj$.

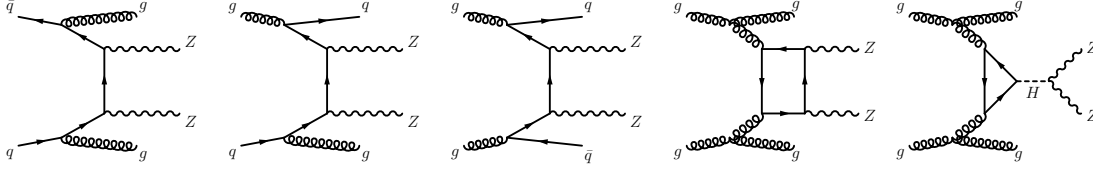


Figure 5.2.: Typical diagrams for the strong production of $ZZjj$.

5.2. Data and MC simulation

The measurement uses a complete Run 2 dataset corresponding to an integrated luminosity of $140.1 \pm 1.2 \text{ fb}^{-1}$ [98]. The pile-up profile varies between different years of data taking and corresponds to that shown in fig. 3.3. The average number of interactions per bunch crossing increased from 13.4 in 2015 to 36.1 in 2018. Data events are selected with a logical OR combination of different single and di-lepton unpre-scaled triggers. The trigger menu also changes across the years, as kinematic thresholds might need to be adjusted due to the changing beam conditions. A list of the selected electron, muon and combined triggers from the Run 2 trigger menu [124–126, 201–203] is given in table 5.1. All events are also subject to essential data quality criteria, such as stable conditions of the beams, when acquired.

Along with data, a set of simulated events allows to study the different processes contributing to the measured phase space, and it is used to define the analysis configuration. Monte Carlo simulations are also used to compare the results with the predictions. Generated events at particle-level are processed with a complete simulation of the ATLAS detector, previously described in section 3.4. Physical objects at detector-level are eventually reconstructed with the same procedure applied to data, also discussed in section 3.3. Simulated samples are produced in three separate campaigns, corresponding to the different $\langle \mu \rangle$ profiles of the 2015-2016, 2017 and 2018 data-taking periods (respectively named mc16a, mc16d and mc16e). A pile-up re-weighting (PRW) procedure [204] is carried out to account for instantaneous luminosity differences in data and simulation. In the procedure, generated events are overlaid with the predicted pile-up events, estimated with an ad hoc simulation, and are consequently re-weighted in such a way as to match the $\langle \mu \rangle$ distribution observed in the data. Corrections are then applied to the simulation on an object-by-object basis to match the momentum

Year	Electron trigger	Muon trigger	Combined trigger
2015	e24_lhmedium_L1EM20VH	mu20_iloose_L1MU15	e7_lhmedium_mu24
	e60_lhmedium	mu50	e17_lhloose_mu14
	e120_lhloose	2mu10	
	2e12_lhloose_L12EM10VH	mu18_mu8noL1	
2016	e26_lhtight_nod0_ivarloose	mu26_ivarmedium	e7_lhmedium_nod0_mu24
	e60_lhmedium_nod0	mu50	e17_lhloose_nod0_mu14
	e140_lhloose_nod0	2mu14	
	2e17_lhvloose_nod0	mu22_mu8noL1	
2017	e26_lhtight_nod0_ivarloose	mu26_ivarmedium	e17_lhloose_nod0_mu14
	e60_lhmedium_nod0	mu50	e26_lhmedium_nod0_mu8noL1
	e140_lhloose_nod0	2mu14	
	2e24_lhvloose_nod0	mu22_mu8noL1	
2018	e26_lhtight_nod0_ivarloose	mu26_ivarmedium	e17_lhloose_nod0_mu14
	e60_lhmedium_nod0	mu50	e26_lhmedium_nod0_mu8noL1
	e140_lhloose_nod0	2mu14	
	2e24_lhvloose_nod0	mu22_mu8noL1	

Table 5.1.: List of the year-dependant electron, muon and combined unrescaled triggers used in the analysis.

and energy scales of electrons and jets measured with data. Differences between the trigger efficiency in data and simulation are corrected using lepton-dependent scale factors, also applied as event weights. Similarly, per-lepton data-driven scale factors account for differences in lepton identification, isolation and reconstruction efficiencies between the data and simulation. All these scale factors are applied to the simulation as multiplicative event weights.

Different processes contribute to the signal and background events and are simulated independently. The signal is defined as the pair production of Z bosons in association with two jets, with the bosons decaying leptonically into electrons or muons: $pp \rightarrow Z^{(*)}Z^{(*)} \rightarrow 4\ell jj$ ($\ell = e, \mu$). The measured final state corresponds to $4\ell jj$, which, at $m_{4\ell} > 2m_Z$, is largely dominated by the on-shell $ZZ \rightarrow 4\ell$ process. The signal also includes contributions from Z^* and γ^* at lower energies. If not otherwise specified, the label " $ZZjj$ " is intended to include these off-shell contributions and is interchangeably used with " $4\ell jj$ ". The signal comprises both the strong and electroweak $ZZjj$ production, the latter corresponding to the VBS mechanism. Background events originate from other interactions that present the same reconstructed final state, thus mimicking the signal. These are categorised as prompt and non-prompt backgrounds, depending on the origin of the final state

leptons. The first case corresponds to four prompt leptons produced in the decays of other particles, such as in triboson processes or $t\bar{t}Z$ production. In the second, one or more non-prompt leptons stem from interactions occurring alongside the hard-scatter event or from misidentified leptons. The MC samples used for the measurement are listed in table 5.2 and are described in more detail below.

Process	Filter	Generator	PS	PDF	Accuracy
Signal samples					
$q\bar{q} \rightarrow Z^{(*)}Z^{(*)} \rightarrow 4\ell$	inclusive strong ≥ 2 jets (EW), $m_{4\ell} > 130$ GeV	SHERPA 2.2.2 MADGRAPH5	SHERPA PYTHIA 8	NNPDF3.0NNLO NNPDF3.0NNLO	$0, 1j$ @NLO + $2, 3j$ @LO $\geq 2j$ @LO
$gg \rightarrow Z^{(*)}Z^{(*)} \rightarrow 4\ell$	$m_{4\ell} > 130$ GeV	SHERPA 2.2.2	SHERPA	NNPDF3.0NNLO	$0, 1j$ @LO
Alternative signal samples					
$q\bar{q} \rightarrow Z^{(*)}Z^{(*)} \rightarrow 4\ell$	inclusive strong	MADGRAPH5_AMC@NLO	PYTHIA 8	PDF4LHC15NLO	$0, 1j$ @NLO
$q\bar{q} \rightarrow Z^{(*)}Z^{(*)} \rightarrow 4e jj$	t -channel (EW)	POWHEG BOX v2	PYTHIA 8	NNPDF3.0LO	$\geq 2j$ @NLO
$q\bar{q} \rightarrow Z^{(*)}Z^{(*)} \rightarrow 4\mu jj$	t -channel (EW)	POWHEG BOX v2	PYTHIA 8	NNPDF3.0LO	$\geq 2j$ @NLO
$q\bar{q} \rightarrow Z^{(*)}Z^{(*)} \rightarrow 2e 2\mu jj$	t -channel (EW)	POWHEG BOX v2	PYTHIA 8	NNPDF3.0LO	$\geq 2j$ @NLO
$pp \rightarrow W^{(*)}Z^{(*)}Z^{(*)} \rightarrow 4\ell jj$	inclusive	SHERPA 2.2.2	SHERPA	NNPDF3.0NNLO	$0j$ @NLO + $1, 2j$ @LO
$pp \rightarrow Z^{(*)}Z^{(*)}Z^{(*)} \rightarrow 4\ell jj$	inclusive	SHERPA 2.2.2	SHERPA	NNPDF3.0NNLO	$0j$ @NLO + $1, 2j$ @LO
Prompt background samples					
$pp \rightarrow t\bar{t} + \ell\ell$	$m_{\ell\ell} > 5$ GeV	SHERPA 2.2.0	SHERPA	NNPDF3.0NNLO	LO
$pp \rightarrow W^{(*)}W^{(*)}Z^{(*)} \rightarrow 4\ell 2\nu$	inclusive	SHERPA 2.2.2	SHERPA	NNPDF3.0NNLO	$0j$ @NLO + $1, 2j$ @LO
$pp \rightarrow W^{(*)}Z^{(*)}Z^{(*)} \rightarrow 5\ell 1\nu$	inclusive	SHERPA 2.2.2	SHERPA	NNPDF3.0NNLO	$0j$ @NLO + $1, 2j$ @LO
$pp \rightarrow Z^{(*)}Z^{(*)}Z^{(*)} \rightarrow 6\ell$	inclusive	SHERPA 2.2.2	SHERPA	NNPDF3.0NNLO	$0j$ @NLO + $1, 2j$ @LO
$pp \rightarrow Z^{(*)}Z^{(*)}Z^{(*)} \rightarrow 4\ell 2\nu$	inclusive	SHERPA 2.2.2	SHERPA	NNPDF3.0NNLO	$0j$ @NLO + $1, 2j$ @LO
Non-prompt background samples					
$pp \rightarrow Z^{(*)} \rightarrow 2e + \text{jets}$	inclusive	SHERPA 2.2.1	SHERPA	NNPDF3.0NNLO	$0, 1, 2j$ @NLO + $3, 4j$ @LO
$pp \rightarrow Z^{(*)} \rightarrow 2\mu + \text{jets}$	inclusive	SHERPA 2.2.1	SHERPA	NNPDF3.0NNLO	$0, 1, 2j$ @NLO + $3, 4j$ @LO
$pp \rightarrow Z^{(*)} \rightarrow 2\tau + \text{jets}$	inclusive	SHERPA 2.2.1	SHERPA	NNPDF3.0NNLO	$0, 1, 2j$ @NLO + $3, 4j$ @LO
$pp \rightarrow \ell\nu\ell\ell$	inclusive	SHERPA 2.2.2	SHERPA	NNPDF3.0NNLO	$0, 1j$ @NLO + $2, 3j$ @LO
$pp \rightarrow t\bar{t} \rightarrow 2\ell$	inclusive	POWHEG BOX v2	PYTHIA 8	NNPDF3.0NLO	NLO

Table 5.2.: List of MC samples used in the analysis.

Quark-initiated production, $q\bar{q} \rightarrow 4\ell$, constitutes the leading signal process contributing to the analysed data. The fully leptonic final state was generated with SHERPA 2.2.2 [56] using the NNPDF3.0NNLO [28] PDF set. The accuracy of matrix element computations in QCD corresponds to NLO for the emission of 0, 1 jets and LO for the additional emission of up to 3 jets. A Catani–Seymour dipole factorisation [66, 67] approach, following the MEPS@NLO prescription [52–54, 205], was used for the combination of matrix elements with the SHERPA parton shower. Virtual QCD corrections were provided by the OPENLOOPS library [68–70].

An alternative $q\bar{q} \rightarrow 4\ell$ sample is used to compare the predictions obtained with different modelling of the process. The sample was produced with the MADGRAPH5_AMC@NLO 2.6.2 [58] generator and the PDF4LHC15NLO PDF set [31], with a NLO accuracy in perturbative QCD for the emission of up to one jet. The

events were interfaced with PYTHIA 8 [57] to produce the hadronic final state. The A14 set of tuned parameters [206] was adopted in the parton shower and hadronisation. The FxFx prescription [63] was employed at the merging stage to account for underlying processes with different parton multiplicity. EVTGEN 1.6.0 [207] was used to simulate the bottom and charm hadrons decays.

The loop-induced, gluon-initiated 4ℓ production [208] was simulated with a similar configuration as the SHERPA $q\bar{q} \rightarrow 4\ell$ sample. The same PDF set and parton shower algorithm were used. Matrix elements computations were executed with a LO precision for the 0 and 1 jet final state. The $gg \rightarrow Z^{(*)}Z^{(*)} \rightarrow 4\ell$ sample includes the contributions from the s -channel decay with an intermediate Higgs boson and its interference with the $gg \rightarrow 4\ell$ box diagram. A minimum $m_{4\ell} > 130$ GeV threshold was applied to the generation. The cut doesn't entail a loss of events since the low $m_{4\ell}$ region is excluded from the analysis phase space. The simulated events were re-weighted following the procedure detailed in [198, 209]. An $m_{4\ell}$ -dependent k -factor was applied to correct the prediction with NLO QCD calculations [210, 211]. An additional constant k -factor accounts for differences between NNLO and NLO QCD predictions [212, 213]. The combination of this sample with the SHERPA quark-initiated production is referred to as strong $4\ell jj$ ($ZZjj$). Similarly, the combination with the alternative $q\bar{q} \rightarrow 4\ell$ sample is labelled as MG5_NLO+PY8 strong $4\ell jj$ ($ZZjj$).

The EW (order α_{EW}^6) $q\bar{q} \rightarrow Z^{(*)}Z^{(*)} \rightarrow 4\ell jj$ process was generated with MADGRAPH 5 [58] at LO accuracy in perturbative QCD. The A14 set of parameters was used to tune the MPI and parton shower modelling provided by PYTHIA 8. The NNPDF3.0NLO [28] PDF set was used. The simulation includes contributions from off-shell Higgs production and other processes occurring at the same α_{EW} order, such as triboson production where one boson decays hadronically: $ZZV(\rightarrow jj)$. The same minimum $m_{4\ell}$ requirement as the previous case was also applied here. This sample is referred to as MG5+PY8 EW $4\ell jj$ ($ZZjj$).

A second set of EW $ZZjj$ predictions is used to compare the results obtained with MG5+PY8, particularly to assess the impact of NLO correction on the event yield and physics modelling. Three simulations were carried out separately for different permutations of the two Z bosons' leptonic decays. Excluding the τ -lepton channel, these corresponds to the $4ejj$, $4\mu jj$ and $2e2\mu jj$ final states. The samples were produced with POWHEG BOX v2 [50, 51, 59, 60], using the generator's implementation of EW $ZZjj$ production [78]. The matrix elements were computed

with a NLO precision in perturbative QCD. The NNPDF3.0LO [28] PDF set was used, along with PYTHIA 8 for the modelling of parton shower, hadronisation and underlying event. The parameters for the latter were taken from the A14 tune. Differently from the MG5+PY8 EW $ZZjj$ sample, the contribution from triboson processes was not included in the generation, and it was estimated from an independent simulation made with SHERPA 2.2.2. This was carried out at NLO and LO accuracy, respectively for the 0 jet and 1, 2 jets final states, employing the NNPDF3.0NNLO PDF set. Parton shower and tuned parameters were provided by SHERPA. $ZZV(\rightarrow jj)$ events were added to those from the POWHEG BOX v2 samples to obtain the full EW $ZZjj$ prediction. This is henceforth referred to as EW POWHEG+PY8 $ZZjj$.

The main source of prompt background originates from $t\bar{t}Z$ production. This process is modelled with SHERPA 2.2.0 [56] at LO accuracy. The NNPDF3.0NNLO PDF set was used. The SHERPA parton shower was matched to matrix elements following the MEPS@LO prescription [52, 53] with up to one additional parton, for whose the CKKW scale was set to 30 GeV. A constant k-factor was applied to the sample's cross-section to match previous ATLAS measurements [214]. A second prompt background process corresponds to triboson (VVV) production. The fully-leptonic decays of WWZ , WZZ and ZZZ were generated with SHERPA 2.2.2, using the same set-up as for $ZZV(\rightarrow jj)$ events. Hadronic decays of the bosons were forbidden, thus ensuring no overlap with the EW $ZZjj$ predictions. Decay channels with $4\ell 2\nu$, $5\ell\nu$ and 6ℓ were individually simulated. Similarly to $t\bar{t}Z$ production, the cross-section was scaled to match the value measured by ATLAS [215].

The contribution from non-prompt background processes is evaluated with a data-driven procedure described in section 5.5. MC simulations are used alongside the data to study the control regions and validate the background estimate. $Z + \text{jets}$ production was generated with SHERPA 2.2.1 [56] and its corresponding parton shower algorithm and tuned parameters. The simulation was carried out separately for the three lepton flavours arising from the $Z \rightarrow \ell^+ \ell^-$ decay and performed in slices of H_T ¹. The matrix elements were computed at NLO accuracy in perturbative QCD for up to two jets in the final state and at LO accuracy for up to four jets, using the Comix [66] and OPENLOOPS libraries. The parton shower merging was performed following the MEPS@NLO prescription, and the

¹Scalar p_T sum of the jets and leptons.

NNPDF3.0NNLO PDF set was used. The samples were normalised to a NNLO QCD prediction [216]. The leptonic decays of $WZjj \rightarrow \ell\nu\ell\ell$ were generated with SHERPA 2.2.2, with the same configuration of the triboson simulations described before. Non-prompt background coming from $t\bar{t}$ production was modelled with POWHEG BOX v2 at a NLO, using the NNPDF3.0NLO PDF set. The simulation was configured with the h_{damp} parameter, a resummation parameter controlling the matrix elements merging in POWHEG, set to the top mass increased by a factor 1.5 [217]. The parton shower was provided by PYTHIA 8, using the A14 tune and the NNPDF2.3LO PDF set [218]. Bottom and charm hadrons decays were simulated with EVTGEN 1.6.0.

All the MC samples were interfaced with a simulation of the ATLAS detector to reproduce events as reconstructed by the experiment. The datasets were slimmed and skimmed to avoid processing a large quantity of data and retain only the interesting events. Only those satisfying a dilepton filter or firing a dilepton trigger were selected to ensure the presence of at least a ee , $e\mu$ or $\mu\mu$ pair in the final state. The tagging electrons and muons were also required to have $p_T > 15$ GeV, $|\eta| < 2.6$ and to pass basic quality selection criteria.

5.3. Analysis definition and event selection

5.3.1. Object reconstruction and identification

The reconstruction of electrons, muons and jets is carried out with the procedure described in section 3.3. The objects are then categorised into two classes: baseline and signal. Loose identification criteria are applied to the reconstructed objects to single out those in the first category. These objects constitute the basis for reconstructing the event's final state. Signal objects are a subset of the baseline entities and are selected with additional tighter requirements to reduce the contamination from pile-up interactions. Baseline and signal requirements for electrons, muons and jets are listed in table 5.3.

Baseline electrons are selected in the region $|\eta| < 2.47$ and must have $p_T > 7$ GeV. Relaxed likelihood-based identification criteria are applied by imposing the electron candidate to pass the VeryLoose [138] working point selection. The electrons are also required to be associated with a reconstructed hard-scatter PV, in such a way that $|z_0 \sin \theta| < 0.5$. A more stringent identification is imposed on the

Cut	Electrons	Muons	Jets
Baseline selection			
Kinematic	$ \eta < 2.47$ $p_T > 7 \text{ GeV}$	$ \eta < 2.7$ $p_T > 5 \text{ GeV}$ $p_T > 15 \text{ GeV}$ (Calo-tagged)	$ \eta < 4.5$ $p_T > 30 \text{ GeV}$
Identification	VeryLoose	Loose	–
Vertex association	$ z_0 \sin \theta < 0.5$	$ z_0 \sin \theta < 0.5$	–
Overlap removal	Lepton-favoured	Lepton-favoured	Lepton-favoured
Signal selection			
Baseline selection	Pass	Pass	Pass
Identification	LooseAndBLayer	Loose	Tight JVT ($ \eta < 2.4$) Tight fJVT ($2.5 < \eta < 4.5$)
Isolation	Loose	Loose (particle-flow)	–
Impact parameters	$\sigma_{d_0}/d_0 < 5$	$\sigma_{d_0}/d_0 < 3$	–

Table 5.3.: Baseline and signal requirements for the selection of electron muons and jets.

signal electrons, which are required to satisfy LooseAndBLayer [138] identification criteria. In addition to the likelihood discriminant and a requirement on the number of hits, this working point also demands the presence of a hit in the innermost pixel detector layer to limit the background from converted photons. Signal electrons must also be isolated. The Loose isolation [136] working point is chosen to achieve good selection efficiency and rejection of non-prompt electrons. The significance of the transverse impact parameter is required to be $\sigma_{d_0}/d_0 < 5$.

Baseline muons are required to have $|\eta| < 2.7$ and $p_T > 5 \text{ GeV}$. They are identified through the Loose [141] working point selection, which includes a combination of different muon classes depending on the detector region. Combined and inside-out combined muons are used within the full ID acceptance, whereas MS extrapolated muons extend the coverage to $2.5 < |\eta| < 2.7$. Calorimeter-tagged and segment-tagged muons are included within $|\eta| < 0.1$ to account for the MS acceptance gap in this region. Calorimeter-tagged muons are additionally required to have $p_T > 15 \text{ GeV}$. The TTVA is ensured with a similar $|z_0 \sin \theta| < 0.5$ prerequisite as for baseline electrons. Signal muons have further isolation and vertex association requirements, which correspond to the Loose isolation [141] selection and the $\sigma_{d_0}/d_0 < 3$ threshold.

The jets used in the measurement correspond to PFlow jets, reconstructed with the particle-flow procedure and the $R = 0.4$ anti- k_T algorithm. Baseline jets are defined only with a kinematic selection, requiring $|\eta| < 4.5$ and $p_T > 30 \text{ GeV}$. The

signal requirements include a selection based on the JVT and its forward variant fJVT to discriminate hard-scatter jets from pile-up jets. The Tight working point selection is chosen for the two discriminants.

As the reconstruction of jets and leptons proceeds independently and simultaneously, ambiguities could rise, resulting in leptons reconstructed as jets. To avoid double-counting, a lepton-favoured overlap removal is performed by discarding all the jets that are too close to electrons ($\Delta R_{e,j} < 0.2$). Similarly, jets which overlap with muons in the same $\Delta R_{\mu,j} < 0.2$ cone are rejected if they contain up to 3 ghost-associated ID tracks. The algorithm also removes overlapping leptons sharing tracks or calorimeter deposits. In the case of two electrons sharing the same track or cluster, the one with the highest p_T is preferred. Electrons are always rejected against overlapping muons, except for calorimeter-tagged muons, in which case they are retained.

5.3.2. Event selection

The event selection inherits from previous ATLAS measurements of inclusive 4ℓ production [198] and EW $ZZjj$ production [199], and was adapted to better match the physics goals of the current analysis. Being a rare process, one principal concern arises from the limited available data. The selection was optimised to retain as many events as possible to allow a differential measurement while containing the contributions from the reducible background and pile-up interactions. A summary of the cut-based selection is given in table 5.4.

The lepton quadruplet selection closely follows Ref [198]. At least four baseline leptons must be present in each event, with the p_T -leading and sub-leading ones having $p_T > 20$ GeV. Baseline electrons and muons are combined into SFOC pairs to form candidates of the two weak bosons' decay products. In this process, all leptons, regardless of their charge, must be separated from each other by at least $\Delta R > 0.05$. This requirement reduces possible contributions from misreconstructed leptons. All SFOC pairs are required to have an invariant mass $m_{\ell\ell} > 5$ GeV to reduce the small contribution arising from J/ψ production, which results to be negligible in the fiducial volume. The pairs are then ranked based on the distance of their mass from that of the Z boson, namely $|m_{\ell\ell} - m_Z|$. No on-shell requirement is imposed on the pairs' mass, as it was observed that it would significantly reduce the event yield of both EW and strong $4\ell jj$ production.

Selection stage	Requirement
Quadruplet selection	
Lepton kinematic	$p_T > 20$ GeV for the two leading leptons
Lepton separation	$\Delta R_{\ell_i \ell_j} > 0.05$
Lepton pairing	At least two SFOC lepton pairs $m_{\ell\ell} > 5$ GeV
Quadruplet candidate	Two SFOC pairs with smallest $ m_{\ell\ell} - m_Z $ Leading pair with highest $ y_{\ell\ell} $ $m_{4\ell} > 130$ GeV
Signal quadruplet	All four leptons passing the signal selection
Dijet selection	
Number of jets	At least two baseline jets
Dijet candidate	First two p_T -leading jets with $\eta_{j_1} \eta_{j_2} < 0$
Jet kinematic	$p_T > 40$ GeV for the leading jet
Rapidity separation	$ \Delta y_{jj} > 2$
Invariant mass	$m_{jj} > 300$ GeV
Signal jets	Both tagging jets passing the JVT or fJVT selection

Table 5.4.: Outline of the event selection requirements for the lepton quadruplet and dijet system.

A quadruplet candidate is constructed by selecting the two lepton pairs with the smallest $|m_{\ell\ell} - m_Z|$ that have $m_{4\ell} > 130$ GeV. The quadruplet pairs are ordered depending on their rapidity, rather than $m_{\ell\ell}$, with the leading pair chosen to be the one with the largest $|y_{\ell\ell}|$. This ordering strategy substantially reduces the fraction of mismatched pairs at fiducial and reconstruction-level. If the four leptons satisfy the signal requirements, the quadruplet candidate is retained as signal. Otherwise, the event is used to estimate the non-prompt background, as described in section 5.5.

The selection of the two jets is shaped around the topology of VBS-like events. In this type of interaction, the two initial state partons are deflected after radiating the weak bosons. The final state jets are characterised by a large invariant mass and rapidity separation due to the small p_T exchange with the bosons, favouring a back-to-back jet configuration. Having two jets in the final state makes the measurement particularly susceptible to contributions from pile-up jets. To reduce

their influence, jets with higher transverse momentum are preferred, as the soft activity increases at low p_T values. The selection strategy used in Ref. [199] introduced a varying jet p_T threshold, increasing at high pseudorapidity values to account for the missing ID information in the forward region of the detector. For the current measurement, a simplified constant threshold is preferred to avoid introducing complexities in the fiducial volume, which could affect the unfolding procedure. Moreover, the recent adaptation of the fJVT discriminant to PFlow jets already improves the purity of the selected events in the forward region. For this reason, the leading jet is required to have $p_T > 40$ GeV in addition to the baseline 30 GeV threshold. Different selection strategies have been studied by the author regarding the configuration of the dijet system. These include the selection of the two jets with the highest transverse momentum or the dijet pair with the largest invariant mass or rapidity separation. Eventually, a p_T -oriented selection has been chosen, as it provides good efficiency and enhances the concentration of the EW component. The dijet candidate is formed with the two leading jets that are also reconstructed in opposite sides of the detector (A/C sides), thus presenting an opposite rapidity sign ($\eta_{j1}\eta_{j2} < 0$). A requirement on the rapidity difference of the two jets, $|\Delta y_{jj}| > 2$, further enforces their separation. The dijet system must also have an invariant mass $m_{jj} > 300$ GeV. Lastly, the two tagging jets must satisfy the signal requirements on the Tight JVT and fJVT selections. A simplified selection cut-flow, with focus on the dijet system requirements, is provided in table 5.5 for the different signal and prompt-background MC samples.

The JVT (fJVT) requirement is essential, as it reduces the contribution from background events where a pile-up jet could be mistakenly selected as a VBS jet candidate. Figure 5.3 shows the impact of the JVT (fJVT) requirement in terms of selection efficiency and purity. The first corresponds to the fraction of baseline jets satisfying the JVT (fJVT) selection, while the latter is defined as the fraction of reconstructed jets which are geometrically matched with a particle-level jet within a cone $\Delta R < 0.3$. The efficiency and purity shown in the plots are computed from all the baseline jets belonging to an inclusive phase space, where only the lepton quadruplet signal selection is enforced. To reduce the amount of mismatched low- p_T jets due to migrations outside the fiducial volume, the p_T threshold of baseline jets at fiducial-level is lowered to 15 GeV. The jet signal selection improves the purity by 10% or more, especially in the low- p_T region. The selection efficiency is equal to unity for $p_T > 60$ GeV, as the JVT (fJVT) requirement is no longer applied.

Selection cut	Strong $qq \rightarrow 4\ell$		Strong $gg \rightarrow 4\ell$		EW $qq \rightarrow 4\ell jj$		$t\bar{t} + Z$		VVV	
	Events	Efficiency	Events	Efficiency	Events	Efficiency	Events	Efficiency	Events	Efficiency
Total events	7060	100%	1020	100%	84.4	100%	1290	100%	72.1	100%
Baseline quadruplet	5320	75%	802	79%	66.3	79%	469	36%	35.5	49%
Signal quadruplet	4260	60%	653	64%	52.8	63%	116	9%	26.6	37%
$n_{jet} > 1$	749	11%	126	12%	41.9	50%	96.4	7%	9.02	13%
AC-side jets	392	6%	71.2	7%	33.1	39%	63.5	5%	5.14	7%
Leading jet $p_T > 40$ GeV	353	5%	62.0	6%	32.8	39%	62.7	5%	4.93	7%
$ \Delta y_{jj} > 2$	228	3%	47.8	5%	28.8	34%	34.4	3%	2.95	4%
$m_{jj} > 300$ GeV	145	2%	31.1	3%	27.0	32%	23.7	2%	2.19	3%
Tight (f)JVT	118	2%	26.0	3%	26.2	31%	22.4	2%	1.95	3%
Signal events	118	100%	26.0	100%	26.2	100%	22.4	100%	1.95	100%
VBS-Enhanced region	77.6	66%	21.3	82%	24.1	92%	17.4	78%	1.37	70%
VBS-Suppressed region	40.8	34%	4.70	18%	2.12	8%	4.96	22%	0.580	30%

Table 5.5.: Simplified cut-flow of the event selection, with focus on the dijet requirements. Event yield and absolute change values are listed for the different signal and prompt-background MC samples. Along with the selection cuts, event yields are also shown for the VBS-Enhanced and VBS-Suppressed signal regions defined in section 5.3.3.

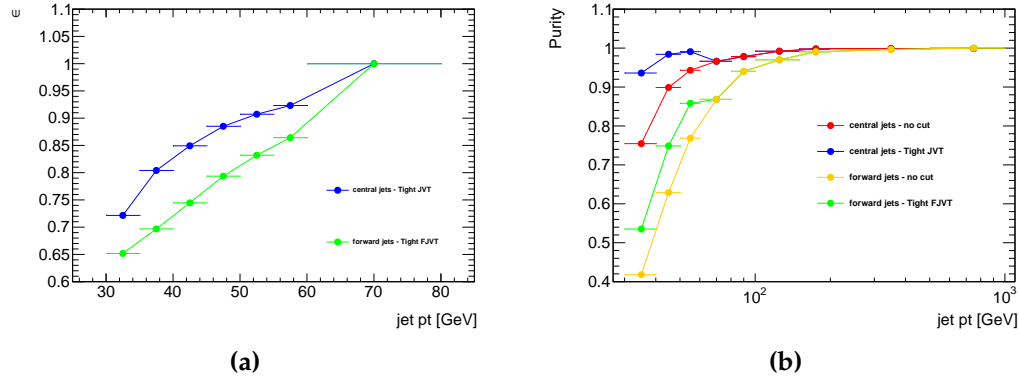


Figure 5.3.: Selection efficiency (left) and purity (right) corresponding to the JVT (fJVT) jet signal requirement. Baseline central (forward) jets are marked in red (yellow). Signal central (forward) jets are marked in blue (green). The plots are computed from all the baseline jets belonging to an inclusive phase space, without enforcing the signal dijet selection and with a reduced p_T threshold for the fiducial-level baseline jets (15 GeV).

5.3.3. Signal regions and measured observables

The measurement of differential $4\ell jj$ cross-section probes both strong and EW interactions. Two separate signal regions (SRs) are defined in such a way as to enhance the contribution from either production mechanism. In the VBS topology, the two bosons are centrally emitted with respect to the deflected partons, and there is no additional hadronic activity due to the lack of colour exchange between

the incoming partons. The centrality of the $4\ell jj$ system, which has a similar meaning as the Zeppenfeld observable [219], is defined as

$$\zeta = \left| \frac{y_{4\ell} - \langle y_j \rangle}{\Delta y_{jj}} \right|, \quad (5.1)$$

where $y_{4\ell}$ is the rapidity of the lepton quadruplet, $\langle y_j \rangle = (y_{j_1} + y_{j_2})/2$ is the average rapidity of the two tagging jets and Δy_{jj} their rapidity separation.

The centrality distribution for the signal processes is shown in fig. 5.4a. The plot indicates how the EW component is concentrated at small centrality values and nearly absent in the opposite direction. A VBS-Enhanced region is defined for centrality values up to $\zeta < 0.4$, while the remaining events constitute a VBS-Suppressed region. The centrality threshold is optimised to provide a good significance² and selection efficiency of the EW component over the strong production. The values of the significance and selection efficiency of the EW and strong processes for different centrality thresholds are shown respectively in green, blue and red in fig. 5.4b. In the VBS-Enhanced region, the fraction of events arising from the EW production is about 20% of the inclusive cross-section, increasing to 40 – 50% in some bins of the measured observables. The VBS-Suppressed region is primarily characterised by the strong interactions and has a $< 5\%$ contamination from the EW production.

The $4\ell jj$ production cross-section is measured differentially for several variables related to the kinematic of either the individual dijet (jj) and four-lepton (4ℓ) systems or the collective $4\ell jj$. The complete list of variables is

- The invariant mass, m_{jj} , and transverse momentum, $p_{T,jj}$, of the dijet system.
- The invariant mass, $m_{4\ell}$, and transverse momentum, $p_{T,4\ell}$, of the 4ℓ system.
- The rapidity separation of the two tagging jets, Δy_{jj} . The cross-section is measured as a function of the absolute value ($|\Delta y_{jj}|$).

²The significance of the EW component is calculated in the large background approximation as $s = \frac{N_{EW}}{\sqrt{N_{Strong}}}$. The measurement is not optimised to extract the EW component from the inclusive $4\ell jj$ production, and this significance value is only intended as an indicator of the concentration of the EW contribution.

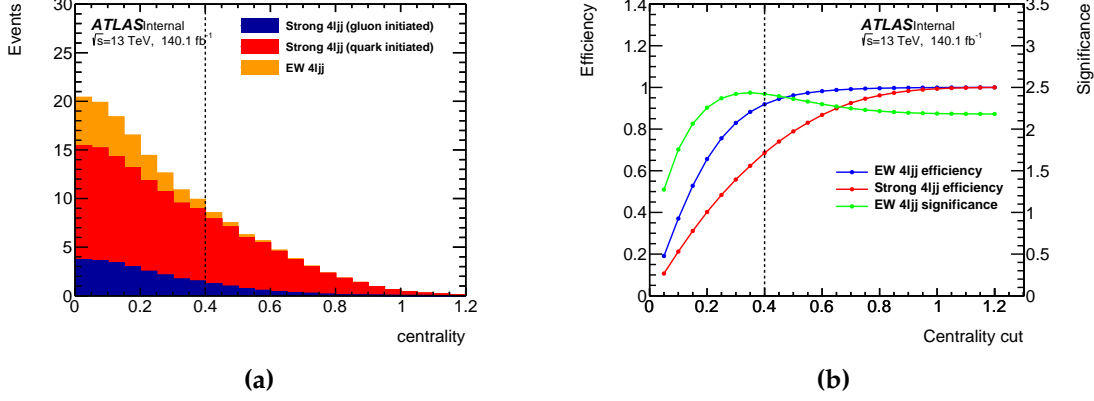


Figure 5.4.: (a) Measured distribution of the centrality of the $4\ell jj$ system from a simulation of the signal processes. EW production is shown in orange, while quark-initiated and gluon-initiated strong production is drawn respectively in red and blue. (b) Significance of the EW component (green) and EW and strong $4\ell jj$ selection efficiency (blue and red) for different centrality thresholds. The chosen cut value, corresponding to $\zeta = 0.4$, is highlighted with a dashed line.

- The azimuthal angle between the two tagging jets, $\Delta\phi_{jj}$, where the jets ordered with decreasing rapidity:

$$\Delta\phi_{jj} = \begin{cases} \phi(j_1) - \phi(j_2) & \text{if } y_{j_1} > y_{j_2} \\ \phi(j_2) - \phi(j_1) & \text{otherwise.} \end{cases} \quad (5.2)$$

$\Delta\phi_{jj}$ is a parity-odd observable and can be used to probe the CP nature of WWZ and WWZZ interactions [220].

- $\cos\theta_{12(34)}^*$ is the cosine of the decay angle of the negatively-charged lepton in the leading (sub-leading) pair in the Z boson centre-of-mass frame. This observable is sensitive to the polarisation of the boson.
- $p_{T,4\ell jj}$ and $S_{T,4\ell jj}$ are respectively the transverse momentum of the $4\ell jj$ system and the scalar sum of the transverse momenta of the two lepton pairs and jets.

The binning choice for the distribution of the observables is mainly driven by the necessity to achieve a reasonable statistical uncertainty. The binning was optimised using a simulation of the signal processes, separately in the two SRs. Given the limited overall event yield, each bin is required to have at least 20 (15) events in the VBS-Enhanced (VBS-Suppressed) region. The unfolding pro-

cedure is influenced by migrations over consecutive bins caused by the finite resolution of the detector (see section 5.6). To reduce this effect, the bins must be at least twice as large as the observable resolution in that bin. The resolution is estimated from the difference between the fiducial and measured value of the observable, taken from the simulation. Only events passing both the fiducial and reconstructed-level event selections, and with the two tagging jets truth-matched in a $\Delta R_{j(\text{Reco}), j(\text{Truth})} < 0.3$ cone, are used for this purpose. The *truth – measured* distribution is extracted in different slices of the true value and fitted with a Gaussian function. The resolution as a function of the observable is then obtained from the resulting standard deviation in the fits. The upper boundary of the last bin is also constrained so that the expected overflow event yield is smaller than unity. Overflow events in data are, therefore, largely suppressed, but they can still stem from statistical fluctuations or new Physics. In this case, they are added to the event yield in the last bin of the distribution. The motivation behind this strategy mainly concerns the EFT interpretation of the results, as some of the new Physics effects are more concentrated toward higher energies. A last condition is imposed on the $\Delta\phi_{jj}$, $\cos\theta_{12}^*$ and $\cos\theta_{34}^*$ bins, which are required to be symmetric about zero. The optimised binning for all the measured observables and the two SRs is listed in table 5.6.

5.4. Measured distributions

The expected and observed total event yields, after applying the event selection, are given in table 5.7. The overall event yield in the data amounts to 169 and 53 respectively in the VBS-Enhanced and VBS-Suppressed regions and is consistent with the predictions within uncertainties. The combined strong and EW $4\ell jj$ production represents the majority of the events, with a predicted background corresponding to about 15% of the total events. The events are measured differentially as a function of the different observables listed in section 5.3.3. The distributions in the two SRs for m_{jj} , $m_{4\ell}$, $p_{T,4\ell}$, $\Delta\phi_{jj}$, $\cos\theta_{12}^*$ and $S_{T,4\ell jj}$ are shown in figs. 5.5 to 5.10 respectively. Additional figures for the remaining observables are available in appendix A.1. In the plots, the predicted signal events originating from the strong and EW $4\ell jj$ production are depicted in red and orange, respectively. The expected prompt and non-prompt background contributions, the latter estimated with a data-driven method described later in section 5.5, are respectively

Selection stage	Requirement	
Observable	Binning	
	VBS-Enhanced region	VBS-Suppressed region
m_{jj} [GeV]	[300, 400, 530, 720, 1080, 3280]	[300, 410, 600, 1780]
$p_{T,jj}$ [GeV]	[0, 52, 82, 116, 172, 524]	[0, 80, 146, 448]
$m_{4\ell}$ [GeV]	[130, 210, 250, 304, 400, 1130]	[130, 226, 304, 752]
$p_{T,4\ell}$ [GeV]	[0, 50, 80, 116, 174, 512]	[0, 76, 140, 424]
$ \Delta y_{jj} $	[2, 3.08, 3.74, 4.32, 5.06, 7.4]	[2, 2.94, 3.78, 5.4]
$\Delta\phi_{jj}$ [rad]	$[-\pi, -2.1, 0, 2.1, \pi]$	$[-\pi, 0, \pi]$
$\cos\theta_{12}^*$	[-1, -0.5, 0, 0.5, 1]	[-1, 0, 1]
$\cos\theta_{34}^*$	[-1, -0.5, 0, 0.5, 1]	[-1, 0, 1]
$p_{T,4\ell jj}$ [GeV]	[0, 20, 42, 64, 298]	[0, 36, 70, 254]
$S_{T,4\ell jj}$ [GeV]	[70, 240, 320, 420, 580, 1410]	[70, 330, 500, 1210]

Table 5.6.: Binning of the observables' distributions in the VBS-Enhanced and VBS-Suppressed regions. Overflow events, if present, are added to the last bin of the distributions.

shown in violet and pink. Overall, the observed data distributions are in good agreement with the SM predictions across all the different observables. Figure 5.5 proves how the m_{jj} observable is particularly sensitive to the EW production. The kinematic properties of the two jets produced in VBS interactions favour a high- m_{jj} configuration, reflected in the fraction of EW events in the VBS-Enhanced region raising to about 40% in the last bin of the distribution.

5.5. Backgrounds

The event yield of prompt background processes is directly estimated from the simulation. Binned distributions for the different observables are measured from the $t\bar{t}V$ and VVV samples listed in section 5.2, and they are subtracted from the data before unfolding. The overall contribution from this source of background is typically small ($\approx 11\%$), showing a nearly flat distribution for several of the measured observables. In p_T -related observables, this background presents an increasing trend at higher energies. It is particularly evident in $p_{T,4\ell jj}$

Process	Event yield \pm stat. (\pm syst.)	
	Region	
	VBS-Enhanced	VBS-Suppressed
Strong $4\ell jj$	98.9 ± 0.5 (± 25.2)	45.5 ± 0.3 (± 12.9)
EW $4\ell jj$	24.1 ± 0.1 (± 1.8)	2.12 ± 0.02 (± 0.14)
Prompt background	18.8 ± 0.2 (± 2.2)	5.54 ± 0.12 (± 0.41)
Non-prompt background	3.02 ± 0.56 (± 3.22)	1.09 ± 0.45 (± 1.19)
Total pred.	144.8 ± 0.8 (± 26.5)	54.3 ± 0.6 (± 13.3)
Data	169 ± 13	53 ± 7

Table 5.7.: Event yield for the measured data and predictions in the VBS-Enhanced and VBS-Suppressed regions.

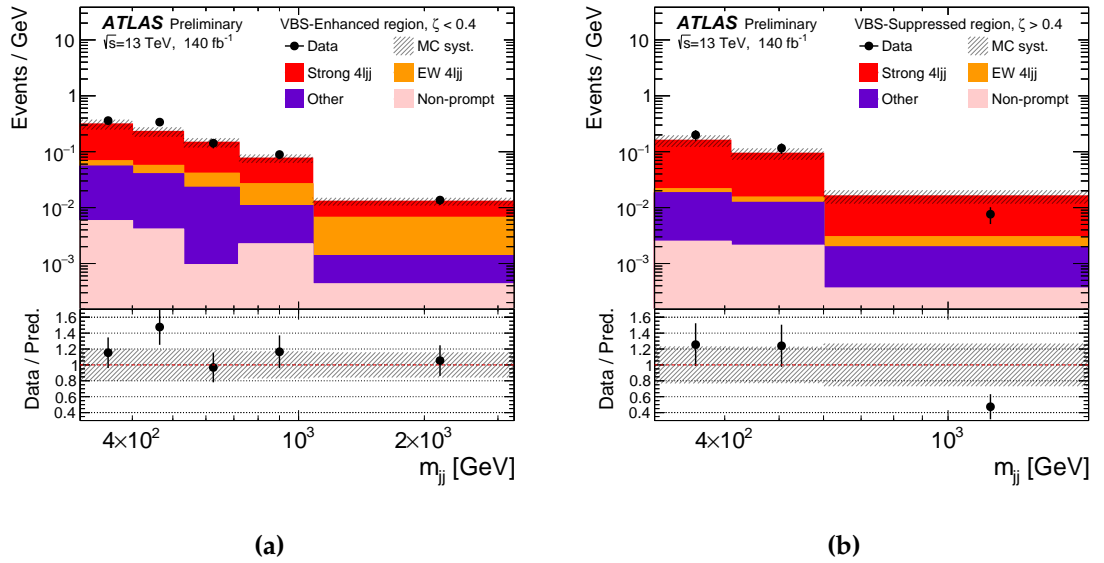


Figure 5.5.: Comparison of the measured m_{jj} distribution from the data (black) and the prediction in the VBS-Enhanced (left) and VBS-Suppressed (right) regions. The SHERPA strong $4\ell jj$ prediction is shown in red, while the MG5+PY8 EW $4\ell jj$ is in orange. The prompt and non-prompt backgrounds are illustrated respectively in violet and pink. The total uncertainty of the prediction is drawn with a dashed band.

(VBS-Enhanced), where it reaches around 30% of the event yield in the last bin of the distribution.

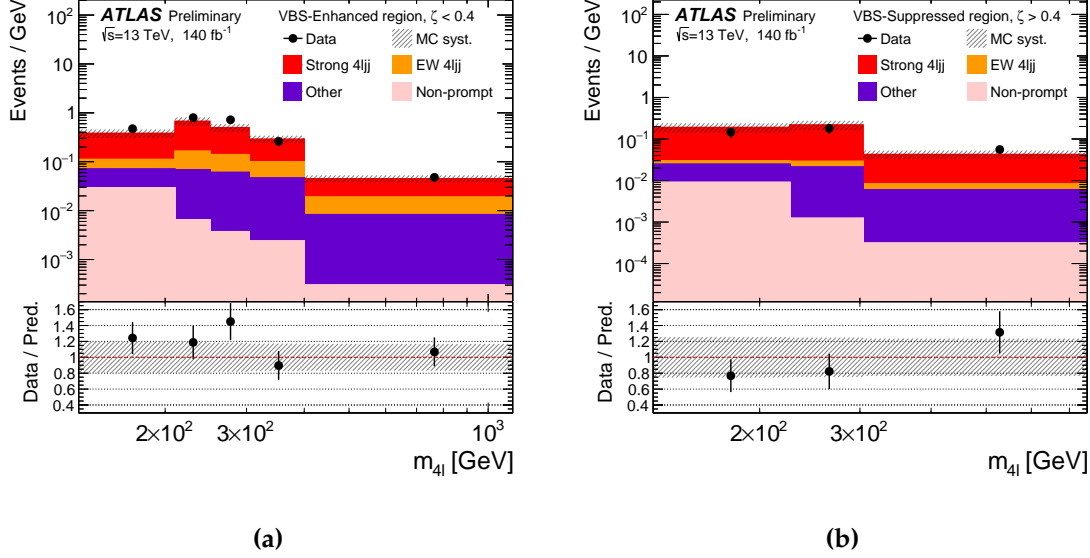


Figure 5.6.: Comparison of the measured $m_{4\ell}$ distribution from the data (black) and the prediction in the VBS-Enhanced (left) and VBS-Suppressed (right) regions. The SHERPA strong $4\ell jj$ prediction is shown in red, while the MG5+Py8 EW $4\ell jj$ is in orange. The prompt and non-prompt backgrounds are illustrated respectively in violet and pink. The total uncertainty of the prediction is drawn with a dashed band.

While the production and kinematics of prompt leptons are typically well-modelled in simulation, this is usually not the case for the additional non-prompt and misidentified (fake) leptons. Their production and selection rate strongly depends on the modelling accuracy of the detector material and the physics behind soft interactions, which can be unreliable in the non-perturbative regime. A data-driven procedure is therefore preferred when estimating this kind of background. The estimation was performed by another member of the analysis team and, therefore, only briefly described here. The measurement employs a "fake factor" method [221] with a similar strategy as done in Ref. [198]. The method relies on a two-level selection where the highest level corresponds to a tight lepton selection which provides a nearly pure set of real prompt leptons. The lowest level is characterised by a loose selection, thus forming a set which contains the tight one and has a larger fraction of non-prompt and fake leptons. In this measurement, the tight and loose sets respectively correspond to the events with signal and baseline quadruplet leptons. In a simplified case with only one lepton per event, the fake factor (F) is defined as the fraction of fake tight leptons divided by the

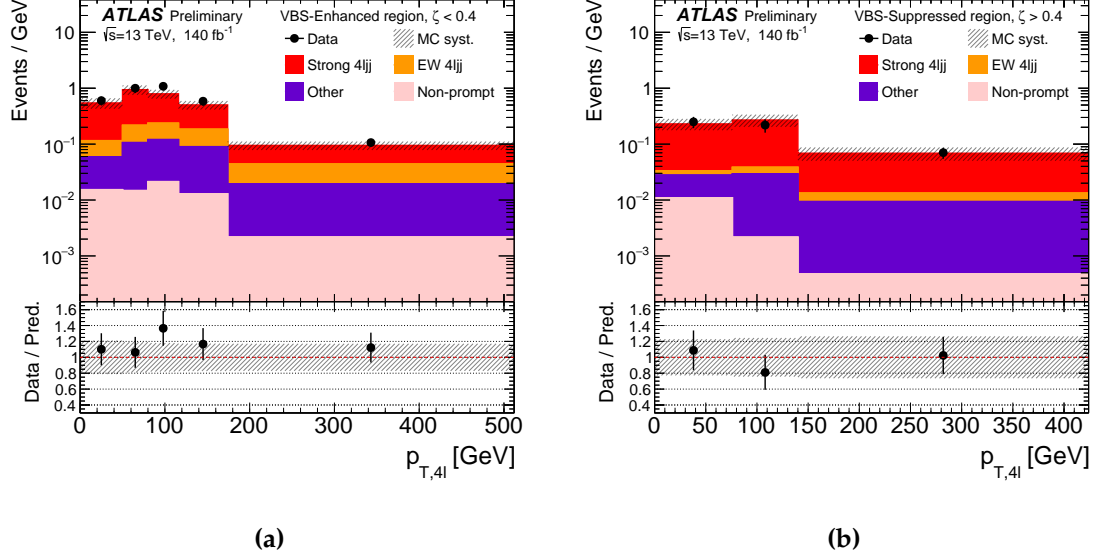


Figure 5.7.: Comparison of the measured $p_{T,4\ell}$ distribution from the data (black) and the prediction in the VBS-Enhanced (left) and VBS-Suppressed (right) regions. The SHERPA strong $4\ell jj$ prediction is shown in red, while the MG5+PY8 EW $4\ell jj$ is in orange. The prompt and non-prompt backgrounds are illustrated respectively in violet and pink. The total uncertainty of the prediction is drawn with a dashed band.

number of fake loose-non-tight leptons, namely

$$F = \frac{N_{fake}^{(Tight)}}{N_{fake}^{(Loose-non-Tight)}} = \frac{\epsilon_f}{1 - \epsilon_f}, \quad (5.3)$$

where the fake efficiency (ϵ_f) represents the fraction of fake tight leptons over fake loose leptons, i.e.

$$\epsilon_f = \frac{N_{fake}^{(Tight)}}{N_{fake}^{(Loose)}}. \quad (5.4)$$

Once the fake efficiency has been measured, the number of signal events containing fake leptons can then be estimated from eq. (5.3) by applying the fake factor to the non-signal leptons. The procedure can be generalised to the multiple-lepton case, considering the lepton fake factors as a set of multiplicative weights.

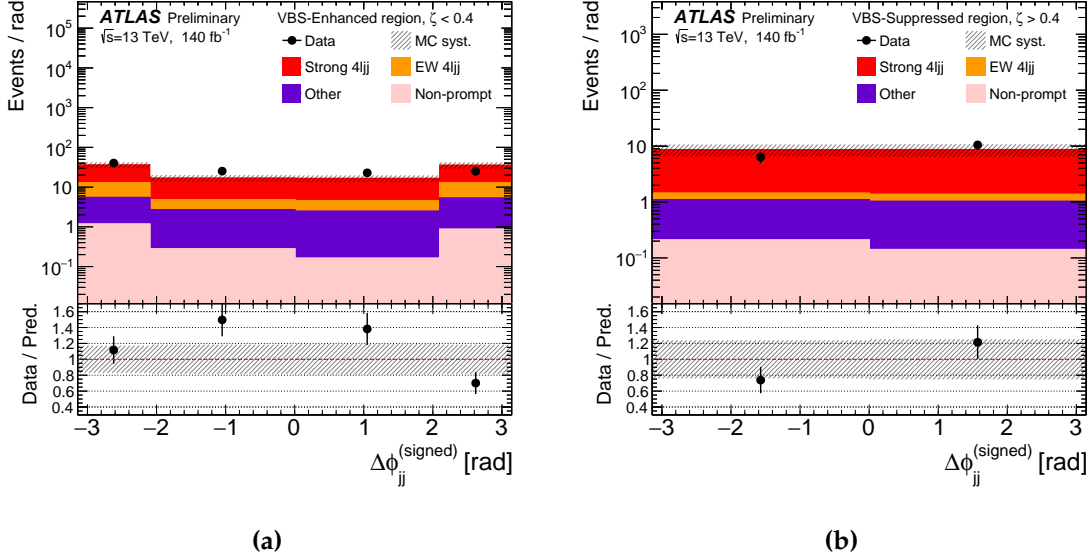


Figure 5.8.: Comparison of the measured $\Delta\phi_{jj}$ distribution from the data (black) and the prediction in the VBS-Enhanced (left) and VBS-Suppressed (right) regions. The SHERPA strong $4\ell jj$ prediction is shown in red, while the MG5+Py8 EW $4\ell jj$ is in orange. The prompt and non-prompt backgrounds are illustrated respectively in violet and pink. The total uncertainty of the prediction is drawn with a dashed band.

The fake efficiency measurement employs two dedicated control regions (CRs) characterised by an enhanced contribution from non-prompt leptons. The CRs are defined below.

- **Z+jets CR.** This region is characterised by two prompt leptons produced in the Z decay and additional leptons likely arising from hadron decays. The event selection uses a single or di-lepton trigger, similar to the SR. The leading and sub-leading leptons are required to satisfy respectively $p_T > 20$ GeV and $p_T > 15.0$ GeV. A SFOC lepton pair is then identified and required to have $76 < m_{\ell\ell} < 116$ GeV. An additional cut on the missing transverse momentum, $E_T^{\text{miss}} < 50$ GeV, reduces the contribution from additional prompt leptons originating from WZ production.
- **$t\bar{t}$ CR.** Candidate events are required to have a different-flavour opposite-charge (DFOC) lepton pair and additional baseline leptons, with similar lepton p_T requirements as in the previous CR. The events must also have at least one jet associated with a b -hadron [222].

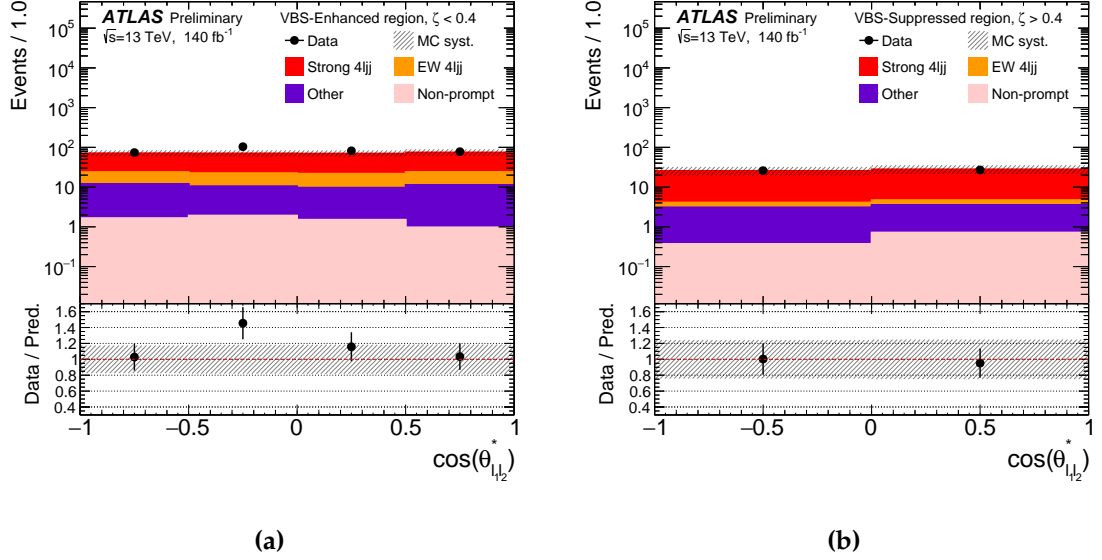


Figure 5.9.: Comparison of the measured $\cos\theta_{12}^*$ distribution from the data (black) and the prediction in the VBS-Enhanced (left) and VBS-Suppressed (right) regions. The SHERPA strong $4\ell jj$ prediction is shown in red, while the MG5+PY8 EW $4\ell jj$ is in orange. The prompt and non-prompt backgrounds are illustrated respectively in violet and pink. The total uncertainty of the prediction is drawn with a dashed band.

The fake efficiency is estimated from the Z +jets and $t\bar{t}$ CRs, after subtracting from the data the prompt component evaluated from the simulation, namely

$$\epsilon_f = \frac{N_{Data}^{(Signal)} - N_{MC}^{(Prompt\ Signal)}}{N_{Data}^{(Baseline)} - N_{MC}^{(Prompt\ Baseline)}}. \quad (5.5)$$

The two CRs are both largely dominated by the non-prompt contribution, with more than 80% (95%) of the baseline electrons (muons) not originating from the hard-scatter event. However, the sources of these non-prompt leptons differ in the two regions. About 80% of the fake electrons in the Z +jets CR correspond to the products of light hadrons decays, while they decrease to around 40% in the $t\bar{t}$ CR. A similar imbalance is observed for the non-prompt muons, which mainly come from heavy-flavour (b and c -hadrons) decays. To better describe the SR, whose leptons also have different origins, the two CRs are linearly combined in a way to reproduce the predicted flavour composition of the SR.

The fake efficiency is measured separately for electrons and muons in different bins of η and p_T , as it depends on the lepton kinematics. A residual dependence is

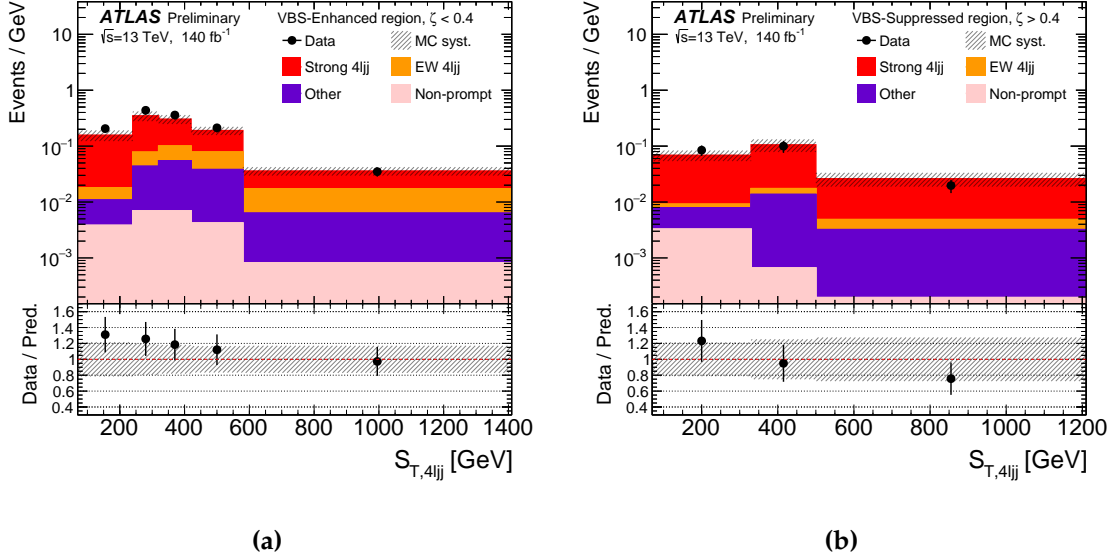


Figure 5.10.: Comparison of the measured $S_{T,4ljj}$ distribution from the data (black) and the prediction in the VBS-Enhanced (left) and VBS-Suppressed (right) regions. The SHERPA strong $4ljj$ prediction is shown in red, while the MG5+PY8 EW $4ljj$ is in orange. The prompt and non-prompt backgrounds are illustrated respectively in violet and pink. The total uncertainty of the prediction is drawn with a dashed band.

observed as a function of the number of jets in the event. This is attributed to the selection employing a lepton-favoured overlap removal and because the leptons are more likely to fail isolation requirements with additional hadronic activity. As a consequence, ϵ_f is also measured in two slices corresponding to $n_{jets} = 0$ and $n_{jets} > 0$. As an example, two-dimensional maps of the fake efficiency for electrons are reported in fig. 5.11. Analogous results are obtained also for muons. The efficiency values are converted into the fake factor, which is then applied on an event-by-event basis to the non-signal quadruplets to estimate the non-prompt background. The same procedure is carried out in two validation regions (VRs), a Different-flavour VR (VRDF) and a Same-charge VR (VRSC), to cross-check the goodness of the background estimate. The VRDF (VRSC) event selection is analogous to the SR but requires one pair in the quadruplet to be formed by leptons of a different flavour (same charge). Additionally, events are vetoed if they contain one or more b -jets to reduce the contribution from $t\bar{t}V$ events. The resulting predictions are found to agree with the data in both VRs.

To avoid discontinuities and negative values in the estimated background events, which could be caused by the MC subtraction in eq. (5.5), the distributions

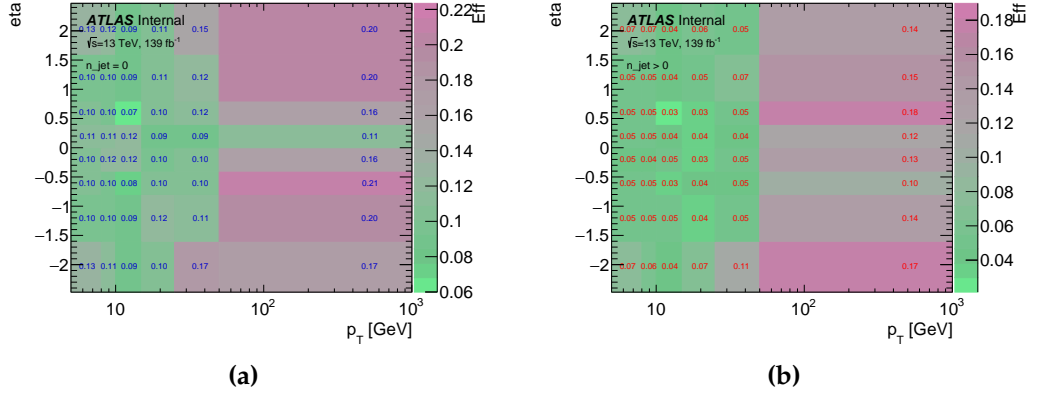


Figure 5.11.: Fake efficiency for electrons measured from the data in the combined Z +jets and $t\bar{t}$ CR. The efficiency is measured differentially as a function of the electron η and p_T , separately for events with zero (left) or more (right) jets.

are smoothed with a moving average after setting the negative bins to zero. The final non-prompt background estimate was previously shown for different observables in figs. 5.5 to 5.10, displayed in pink. Statistical and systematics uncertainties affecting the fake efficiency are propagated to the measured and unfolded distributions, as described in section 5.8.

5.6. Unfolding

The question of unfolding arises from the necessity to remove from the data all effects induced by the detector, which can alter a measured observable. Extrapolating the results to the level of theory predictions can be very important for their longevity and reproducibility. An unfolded observable can be compared to the theoretical predictions given by different models without having to interface them with a simulation of the detector used in the measurement. Similarly, the results obtained from different experiments, each with its characteristic detector, can be directly compared once unfolded. The process of unfolding is naively illustrated in fig. 5.12.

Consider an observable (e.g. the dijet invariant mass) described at particle-level by the true distribution $f(t)$. With a perfect detector, the corresponding measured distribution of the same observable would be identical. In practice, the detectors present a finite resolution and typically also have a limited efficiency. These attributes degrade the measured quantities, leading to a change in the original

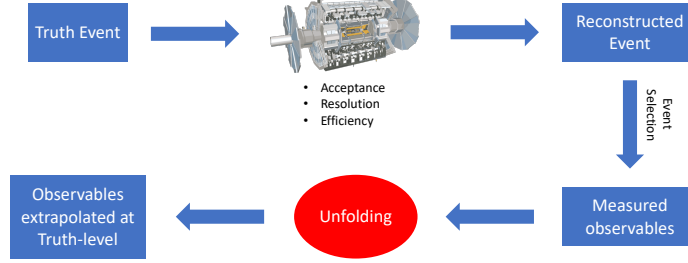


Figure 5.12.: Diagram of the different steps leading to the production of an unfolded measurement

distribution. Thus, $f(t)$ becomes $g(m)$ at detector-level. Parametrising the detector response with the kernel function $R(t, m)$, the relationship between the measured and the true distribution can be expressed with the Fredholm integral [223]

$$g(m) = \int_{\Omega} R(t, m) f(t) dt. \quad (5.6)$$

$R(t, m)$ can be evaluated from MC simulations, relating the particle-level predictions to the measured observables. Solving eq. (5.6) is referred to as folding, while the inverse process corresponds to the unfolding. The deconvolution of the measured distribution is a non-trivial problem, often non-solvable in a continuous space. In particle physics analyses, the observables are typically measured in binned distributions, and the problem becomes discrete. Assuming for simplicity the same number of K equally spaced bins for both distributions³, the true and measured yields are respectively $\mathbf{y} = (y_1, y_2, \dots, y_K)$ and $\mathbf{x} = (x_1, x_2, \dots, x_K)$, with

$$y_i = N_y \int_{\Delta t_i} f(t) dt \quad (5.7)$$

and

$$x_i = N_x \int_{\Delta m_i} g(m) dm, \quad (5.8)$$

³The problem can be easily generalised to the case of different numbers of bins and with varying bin width using the same formalism.

where $i \in \{1, 2, \dots, K\}$ is the bin index, the $f(t)$ and $g(m)$ distributions are assumed to be normalised to unity, and N_y, N_x respectively correspond to the number of true and measured events. The detector response also translates into a $K \times K$ square matrix $\mathbf{R} = (R_{ij})$, whose elements describe the conditional probability to measure the observable in the i -th bin, given the corresponding true value in the j -th bin:

$$R_{ij} = p(m' \in \Delta m_i | t' \in \Delta t_j). \quad (5.9)$$

Including the contribution from background events $\mathbf{b} = (b_1, b_2, \dots, b_K)$, eq. (5.6) translates to

$$\mathbf{x} = \mathbf{R} \cdot \mathbf{y} + \mathbf{b}. \quad (5.10)$$

For K -fixed bins, the response matrix is square, and the unfolded distribution can be naively obtained by inverting it. Considering the data vector $\mathbf{d} = (d_1, d_2, \dots, d_K)$ with expected values $E[d_i] = x_i$, we obtain from eq. (5.10) the estimate of the number of truth events as $\hat{\mathbf{y}} = \mathbf{R}^{-1}(\mathbf{d} - \mathbf{b})$. The matrix inversion approach can be problematic, as the response matrix binning must be carefully chosen to make it non-singular. This is particularly relevant for measurement with limited event yields or large bin migrations. Moreover, the results may have negative yields introduced by the inversion procedure and typically present very large statistical variances. It can be shown how the matrix inversion corresponds to the solution obtained by the maximum likelihood estimator for a data histogram with independent bins described by a Poisson distribution⁴ [224]. This is the solution to an ill-defined problem [225], where minimal changes in the input data can cause large fluctuations in the results. In case of a diagonal response matrix, i.e. if there are no migrations across the bins, a small-variance solution can be obtained by applying a bin-by-bin correction estimated from the simulation⁵. To overcome the issue of the large variance in a more generic case, an alternative solution can be found with the so-called regularised unfolding. In this procedure, the truth

⁴The likelihood for the data histogram can be written as $\mathcal{L} = \prod_{i=1}^K x_i^{d_i} \frac{e^{-x_i}}{d_i!}$, and the maximum likelihood estimator of \mathbf{x} is given by $\hat{\mathbf{x}} = \mathbf{d}$.

⁵The estimate of the number of truth events in each bin is given by $\hat{y}_i = C_i(d_i - b_i)$, where $C_i = \frac{y_i^{(MC)}}{x_i^{(MC)}}$ is an efficiency correction obtained by comparing the true and measured distributions in the simulation.

yield estimate is computed in a contour of the likelihood maximum where the fluctuations are more contained. This is achieved by adding a regularising function to the likelihood profile before performing the maximisation. Following [226], this can be expressed as

$$\mathcal{L}(y) = \mathcal{L}_0(y) + \tau S(y), \quad (5.11)$$

where $\mathcal{L}_0(y)$ is the original likelihood, $S(y)$ is a smoothing function, and the parameter τ controls the strength of the regularisation. The case limit with $\tau = 0$ corresponds to the non-regularised solution given by the matrix inversion. With larger values of τ , the smoothing increases up to the maximally-regularised solution, which is characterised by zero statistical variance and large bias⁶. Many alternative algorithms to solve the regularised unfolding have been implemented and used in particle physics measurement [226–233]. The measurement described in this thesis employs an iterative Bayesian unfolding, which is described in section 5.6.2.

5.6.1. Fiducial phase space

The fiducial volume represents the phase space region targeted by the measurement and to which the unfolded cross-sections are extrapolated. It is defined at the particle-level with a set of kinematic requirements applied to the final state particles to account for the limited acceptance of the ATLAS detector and ensure high reconstruction efficiency.

Physical objects at particle-level are defined in a way to resemble those reconstructed from the detector measurements [234]. Charged leptons are often accompanied by a QED final state radiation. The emitted photons are typically collinear to the lepton and, in the detector-level reconstruction, are re-absorbed via the clustering of energy deposits in the calorimeter. To reproduce this effect in theory predictions, particle-level leptons are combined with close-by photons which lie within a cone of aperture $\Delta R = 0.1$ centred on the lepton trajectory. This process is called dressing, and the p_T -corrected leptons are referred to as dressed leptons. Jets are defined with the same anti- k_T algorithm used in the reconstruction procedure described in section 3.3.4. A radius parameter of $R = 0.4$ is

⁶The unfolding bias is defined as the difference between the unfolded and true distributions:
 $bias_i = N_i^{(unfolded)} - N_i^{(truth)}.$

employed. Jets are found only after the electrons and muons have been identified and dressed to avoid ambiguities in the clustered objects.

Following the ID acceptance, dressed electrons are required to be in the range $|\eta| < 2.47$ and have a minimum transverse momentum of $p_T > 7$ GeV. With analogous considerations on the MS acceptance, muons are selected with $|\eta| < 2.7$ and $p_T > 5$ GeV. Leptons arising from τ decays are excluded from the fiducial volume. The expected event yield from such decays is small (per cent order), thus having little to no impact on the final result. Jets are required to have $p_T > 30$ GeV and be in the region $|\eta| < 4.5$. The fiducial event selection follows the detector-level selection previously introduced in section 5.3.2.

5.6.2. Iterative Bayesian unfolding

The unfolding algorithm used in this measurement corresponds to the "improved" version [235] of the iterative Bayesian unfolding method introduced by D'Agostini [233]. The algorithm is implemented in the RooUnfold package [226, 236] of the ROOT analysis framework [237]. The unfolding procedure is constructed upon some considerations based on Bayes' theorem, similar to the Lucy-Richardson algorithms [238, 239] employed respectively in the fields of optics and statistical astronomy. Given a set of independent causes, $\{C_i\}$, and effects, $\{E_j\}$, Bayes' theorem states that the probability that an effect E_j has been induced by the cause C_i is proportional to the probability of the cause to produce the effect, multiplied by the probability of the cause. Namely,

$$p(C_i|E) = \frac{p(E|C_i)p(C_i)}{\sum_{i=1}^{N_C} p(E|C_i)p(C_i)}. \quad (5.12)$$

The D'Agostini method applies Bayes' theorem to the unfolding problem in particle physics, relating the causes and effects to the true and measured observable bin contents. As seen in eq. (5.12), the formula depends on the prior distribution of the true events. The shape of this distribution is, in principle, unknown, and its parametrisation is one of the main caveats in many applications of the Bayes' theorem. The algorithm starts with a prior assumption based on the predicted truth distribution, corresponding to $p_0(C_i) = \frac{n_{C_i}}{\sum_{i=1}^{N_C} n_{C_i}}$, with n_{C_i} denoting the number of predicted events in the i -th truth bin. The prior choice

can be a strong assumption and may not correctly represent the underlying true distribution of a physics observable, thus introducing a bias in the unfolded spectra. This effect can be reduced with an iterative procedure, which updates the knowledge of the prior with the estimate of the true events found at the precedent step. The number of iterations has a similar meaning to the regularisation strength introduced in eq. (5.11). The result obtained with no iterations corresponds to the maximally-regularised solution, while the limit of infinite iterations tends to the zero-bias maximum likelihood estimator. The resulting unfolded distribution can be interpreted as a linear transformation of the input data. Calling \mathbf{A} the transformation matrix, this is equivalent to write $\hat{\mathbf{y}} = \mathbf{A}\hat{\mathbf{x}}$, with $\hat{\mathbf{x}}$ being the background-subtracted data. The propagation of the statistical uncertainty is then straightforwardly obtained by $\mathbf{C}_{\hat{\mathbf{y}}} = \mathbf{A}\mathbf{C}_{\hat{\mathbf{x}}}\mathbf{A}^T$, having indicated the statistical covariance matrices of the unfolded and measured distributions respectively with $\mathbf{C}_{\hat{\mathbf{y}}}$ and $\mathbf{C}_{\hat{\mathbf{x}}}$. Different bins of the measured distribution are assumed to be uncorrelated, meaning $\mathbf{C}_{\hat{\mathbf{x}}}$ has the form of a diagonal matrix with elements $C_{\hat{\mathbf{x}}, ii} = \sigma_{\hat{\mathbf{x}}, i}^2$. A different approach to propagate the statistical uncertainty with toy distributions is described in section 5.7.

The simulation of the signal processes is used to train the unfolding algorithm and apply corrections to the measured data. Particularly, fiducial and detector-level events provide the necessary inputs to the RooUnfold framework. The principal quantities characterising the unfolding procedure are described below. In the following, the fiducial and detector selections are labelled respectively as "Truth" and "Reco".

- **Reconstruction efficiency:** the reconstruction efficiency (ϵ) corresponds to the fraction of true events that are successfully observed. It is measured from the simulation from the ratio

$$\epsilon = \frac{N^{(\text{pass Reco and pass Truth})}}{N^{(\text{pass Truth})}}, \quad (5.13)$$

where $N^{(\text{pass Truth})}$ is the overall number of events passing the fiducial selection and $N^{(\text{pass Reco and pass Truth})}$ is the subset of events also passing the detector-level selection. The probability of reconstructing a true value can also be obtained from the resolution matrix by summing over all the corresponding bins of the measured observable. For the j -th true bin, this

corresponds to

$$\epsilon_j = \sum_{i=0}^K R_{ij}. \quad (5.14)$$

The reconstruction efficiency for m_{jj} and $m_{4\ell}$, in both the VBS-Enhanced and VBS-Suppressed regions, is shown with a red line in fig. 5.14. Its value typically ranges from 40% to 60% for all the observables.

- **Migration matrix:** the migration matrix (\mathbf{M}) corresponds to the joint probability of measuring an event in the i -th bin, while the true value falls in the j -th bin, $M_{ij} = p(m' \in \Delta m_i, t' \in \Delta t_j)$. \mathbf{M} is directly related to the response matrix through the equation

$$R_{ij} = \frac{M_{ij}}{\epsilon_j^{-1} \sum_{v=0}^K M_{vj}}. \quad (5.15)$$

The migration matrix is estimated from MC events satisfying both the fiducial and detector selection. A 2-dimensional matrix is constructed using the same binning defined in section 5.3.3, with the $x(y)$ -axis corresponding to the reconstructed (true) value. Examples of migration matrices for both m_{jj} and $m_{4\ell}$ in the two SRs are shown in fig. 5.13. In the plots, the entries are normalised to the total number of events in the corresponding true bin to help visualise the detector-level migrations. The width requirement in the binning optimisation procedure ensures the migrations over consecutive bins are typically small, varying between 10% to 30%.

- **Fiducial fraction:** the fiducial fraction (f) expresses the amount of measured events originating from the selected fiducial volume. It is evaluated from the fraction of events passing both fiducial and detector selections ($N^{(\text{pass Reco and pass Truth})}$) over the total measured events ($N^{(\text{pass Reco})}$), namely

$$f = \frac{N^{(\text{pass Reco and pass Truth})}}{N^{(\text{pass Reco})}}. \quad (5.16)$$

In the unfolding procedure, the fiducial fraction is used to correct the data (after the background subtraction) to account for events that do not originate from the fiducial volume and, as such, should not be extrapolated back to

the true spectrum. These events arise either from pile-up interactions or from the signal processes whose kinematic properties don't satisfy the event selection (e.g. low- p_T jets). The fiducial fraction for m_{jj} and $m_{4\ell}$ in the two SRs is shown in fig. 5.14 with a yellow line. On average, the fiducial fraction varies between 60 and 80%, decreasing at low energies due to the combined effect of a more abundant soft activity and migrations outside the fiducial volume caused by the lower resolution.

- **Purity and stability:** These two quantities are defined respectively as the fraction of measured or true events having both particle and reconstruction-level observable in the same bin. They are both closely connected to the migration matrix and are likewise evaluated from events passing both fiducial and detector selections. The purity (p) and stability (s) are defined as

$$p_i = \frac{M_{ii}}{\sum_j M_{ij}} \text{ and } s_j = \frac{M_{jj}}{\sum_i M_{ij}}, \quad (5.17)$$

where the i and j indexes respectively refer to the measured and true bins, as before. Both variables are not directly used to correct the data in the unfolding procedure but rather to quantify the balance of the distributions due to the binning choice. All the observables are characterised by high purity and stability, with values normally above 70%. Figure 5.14 shows the two quantities as a function of m_{jj} and $m_{4\ell}$ in both the VBS-Enhanced and VBS-Suppressed regions, respectively depicted with a blue and a green line.

Additional plots of migration matrix, reconstruction efficiency, fiducial fraction, purity and stability for the remaining observables are available in appendix A.1.

5.6.3. Regularisation of the unfolding procedure

As discussed in section 5.6.2, the number of iterations used in the unfolding algorithm influences both the variance and the bias of the results. The two quantities grow in opposite directions, as the bias decreases with more iterations due to a reduced dependence on the prior assumption, at the cost of an increased statistical uncertainty in the unfolded distribution. The unfolding regularisation must, therefore, be optimised to find an ideal compromise between the two. The number of iterations is chosen as the value which provides the lowest total uncertainty, corresponding to the sum in quadrature of the bias and the statistical uncertainty.

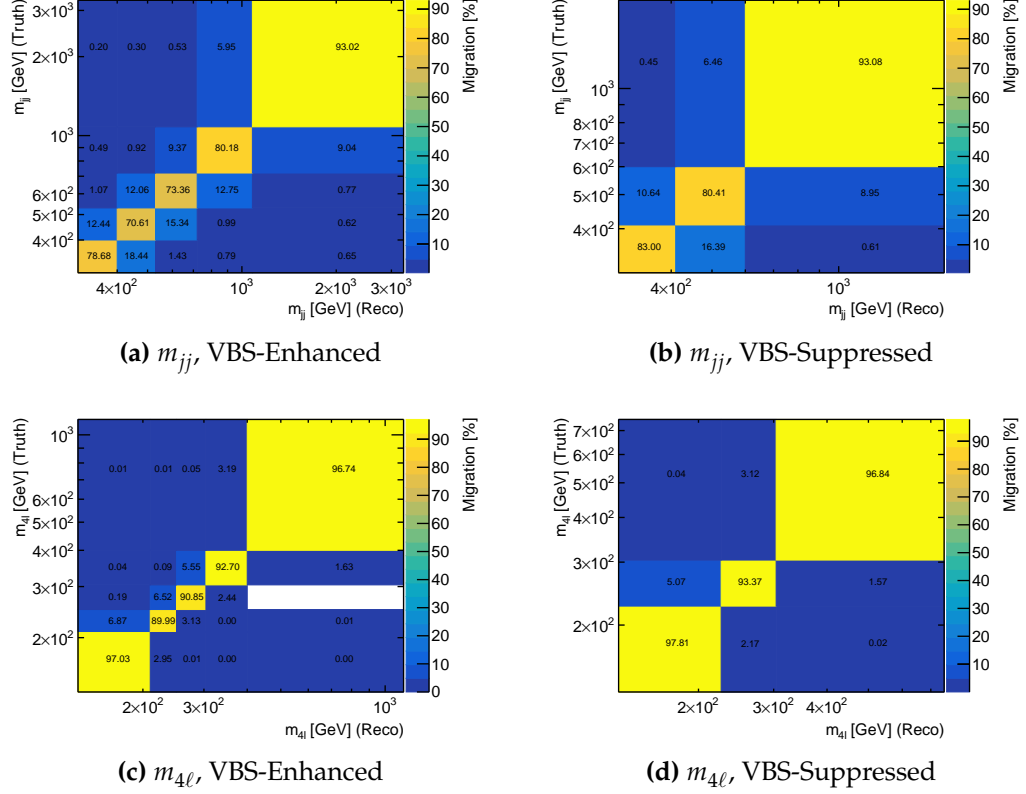


Figure 5.13.: Examples of migration matrices normalized to the number of events in each truth bin. The plots on the top (a, b) correspond to m_{jj} in the VBS-Enhanced (left) and VBS-Suppressed (right) regions. The plots on the bottom (c, d) are analogous for $m_{4\ell}$.

An additional constraint is placed on the total uncertainty, whose relative value must be greater than that of the input data, to prevent undercoverage of the statistical uncertainty, as discussed below.

While the statistical uncertainty is propagated through the unfolding procedure by the algorithm, the bias has to be estimated by varying the input parameters. Two different methods are used to evaluate the bias, one relying on the measured data and the other on the simulation. The first is referred to as the data-driven closure test and consists in altering the shape of the expected measured distribution to resemble that of the data. The procedure is illustrated in fig. 5.15. First, the unfolding algorithm is trained with the predicted measured (fig. 5.15a) and true distributions and the migration matrix evaluated from the simulation. The simulated events are then re-weighted at particle-level with an observable-dependent scale factor given by the data and MC prediction ratio. The ratio is derived in a

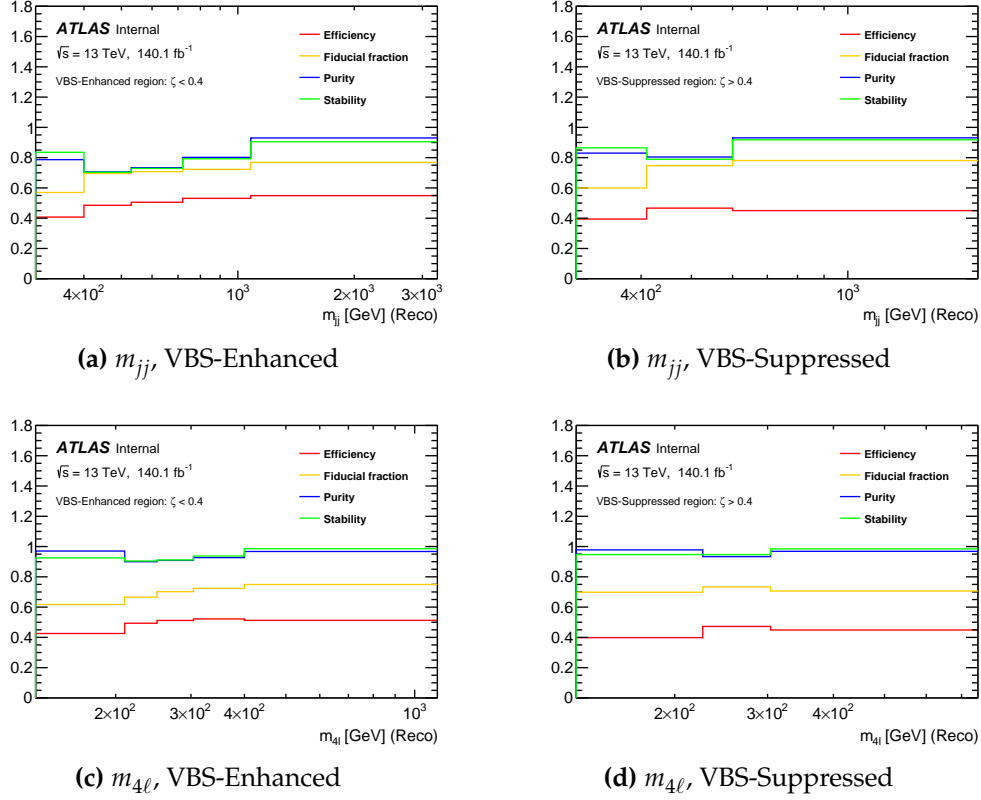


Figure 5.14.: Reconstruction efficiency (red), fiducial fraction (yellow), purity (blue) and stability (green). The plots on the top (a, b) correspond to m_{jj} in the VBS-Enhanced (left) and VBS-Suppressed (right) regions. The plots on the bottom (c, d) are analogous for $m_{4\ell}$.

binned distribution, as the data, and smoothed using a regression algorithm based on Friedman's Super Smoother [240] (fig. 5.15b). Border conditions are imposed, fixing the smoothed function to be constant at lower (higher) values than the first (last) bin and equal to the Data/MC ratio. The pseudo-dataset obtained from the re-weighting procedure (fig. 5.15c) is unfolded with the nominal response. The bias is eventually given by the difference between the unfolding result and the re-weighted true distribution (fig. 5.15d). The bias after one iteration is typically below 10 to 15% for all observables. The value is observed to significantly vary across different bins and observables. This is attributed to the limited amount of data available. The data-driven closure method depends on the precision with which the data is measured and can be susceptible to statistical fluctuations in the re-weighting procedure.

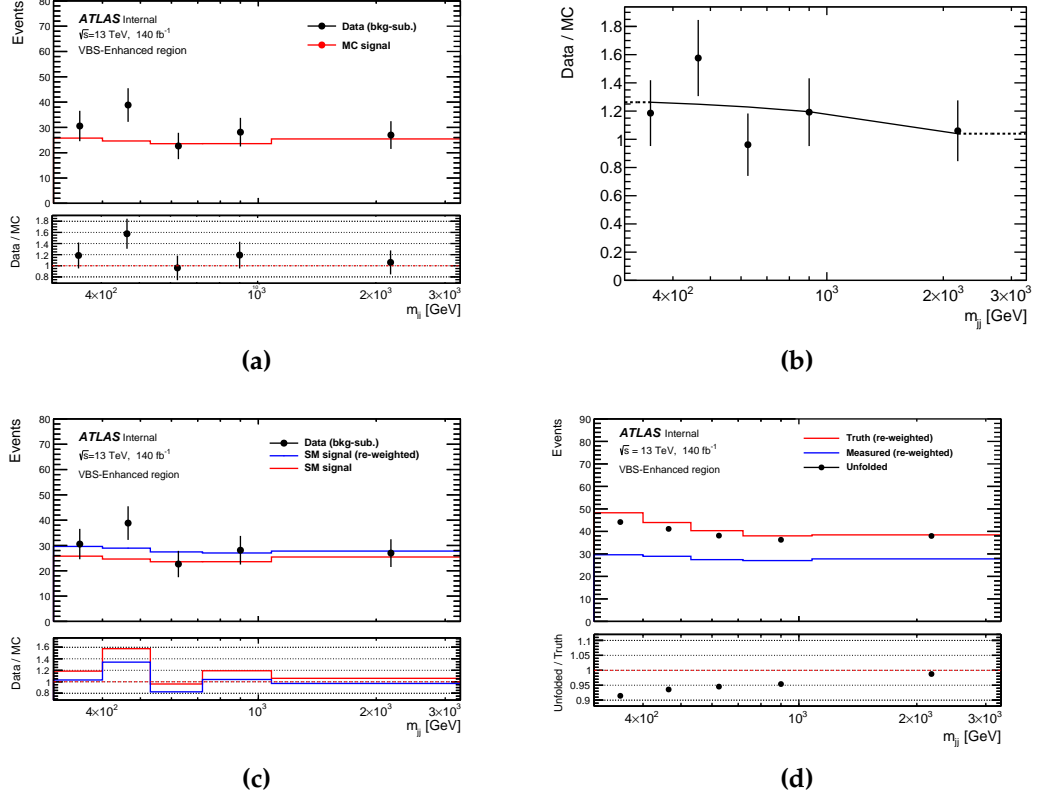


Figure 5.15.: Illustration of the data-driven closure test for m_{jj} in the VBS-Enhanced region. (a) Comparison of the background-subtracted data and the predicted measured distribution from the signal MC. Only statistical uncertainties are shown in the plot. (b) The ratio between data and MC is used as a re-weighting function and applied to the simulation at particle-level. The ratio is smoothed using Friedman’s Super Smoother, with fixed values at the first and last bin edges. (c) Comparison of data with the MC re-weighted (blue) and nominal (red) measured distributions. (d) The detector-level re-weighted distribution (blue) is unfolded with the nominal response (black) and compared to the re-weighted true distribution (red). The unfolded distribution is obtained with one iteration. The bias is estimated from the unfolded and truth difference.

A second approach derives the bias from the simulation, thus eliminating the data constraint. A set of 10000 toy replicas is constructed from the predicted true distribution of a given observable. Each bin is independently varied through a random sampling performed with a Gaussian distribution having mean equal to zero and standard deviation equal to the square root of the number of true events expected in the bin. The toy’s true distribution is folded with the nominal response matrix to obtain a pseudo-dataset at detector-level. In this process, the non-fiducial events are also included. The new distribution is unfolded back at fiducial-level

and compared with the toy's true distribution to estimate the bias. The process is repeated for all the toys. In each bin of the observable, the bias is averaged out in different slices of the toy's true value. This is shown in fig. 5.16a, where the toys' true values corresponding to the first bin of m_{jj} in the VBS-Enhanced region are arranged over the x axis. The average bias tends to zero when the toy approaches the original distribution and increases as it moves apart from it. The uncertainty associated with the unfolding bias is estimated at the intersection between the average bias curve and the 1σ confidence interval of the toys' true distribution, shown as a green band in the figure. The values corresponding to the upper and lower limits of the interval are averaged to obtain a symmetric uncertainty. The resulting uncertainty is shown as a function of the number of iterations in fig. 5.16b (red), along with the expected statistical uncertainty (blue) and their combination (black). Due to the limited event yield, the statistical uncertainty is the dominant contribution already at the single iteration case. Despite providing the smallest combined uncertainty, the 1-iteration case presents symptoms of undercoverage. The relative statistical uncertainty of the input measured distribution (shown with a dashed line in the plot) is observed to decrease after the unfolding, as displayed by the left-most point in fig. 5.16b. Figure 5.17 reports the statistical uncertainty as a function of m_{jj} , obtained from the data in the VBS-Enhanced region after unfolding with a different number of iterations. The comparison with the initial uncertainty of the background-subtracted data presents the same feature consistently among all bins of the observable. This is a non-physical effect, likely caused by a large bias induced by the prior choice, which over-constrains the unfolded spectrum. As a consequence, two iterations are used in the measurement of unfolded cross-sections. An additional third iteration is needed for the $p_{T, A\ell jj}$ observable in the VBS-Enhanced region.

Overall, the bias estimated with the MC-based method gives similar, or slightly larger, results than the data-driven closure. Being a more conservative solution, the MC-based method is used to estimate the uncertainty relative to the unfolding procedure in the cross-section measurement. The corresponding values, along with other sources of systematic uncertainties, are shown in section 5.8.4. The relatively large (still below the statistical uncertainty) unfolding bias is a common feature of VBS measurements and was observed in similar analyses. This is partly attributed to the large fraction of non-fiducial events, which can be as big as 40% in some bins of the observables, such as in the first bin of fig. 5.14. The origin of these events is further studied in the simulation. About half of these

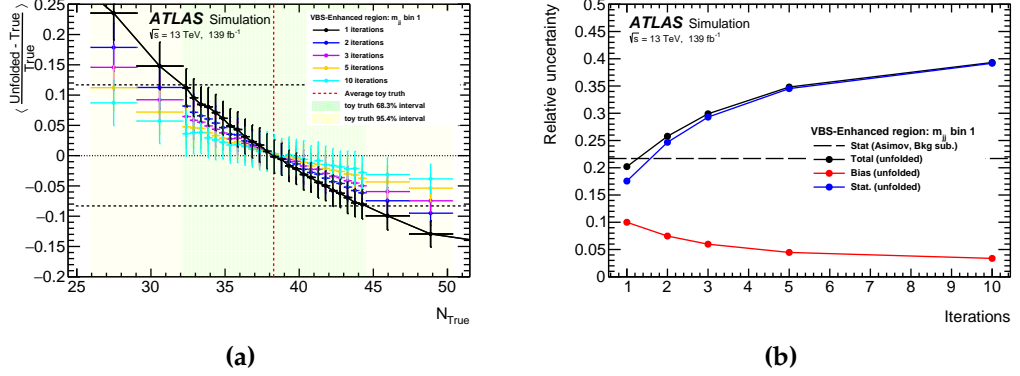


Figure 5.16.: MC-based estimation of the unfolding bias in the first bin of the m_{jj} distribution in the VBS-Enhanced region. (a) Average unfolding bias obtained with an increasing number of iterations in the unfolding procedure. The x axis corresponds to the toys' true yield. The dashed red line represents the average value of the toys' yield, while the green (yellow) band is the interval where 68.3% (95.5%) of the toys lie. The resulting uncertainty is evaluated from the intersection of the average bias curve with the green band, and it is shown with the horizontal black dashed lines for the 1-iteration case. (b) Unfolding bias (red) and statistical uncertainty (blue) as a function of the number of iterations. The black line corresponds to the combined uncertainty, retrieved as the sum in quadrature of the two. The expected statistical uncertainty of the background-subtracted measured distribution, before unfolding, is shown with a dashed line for comparison.

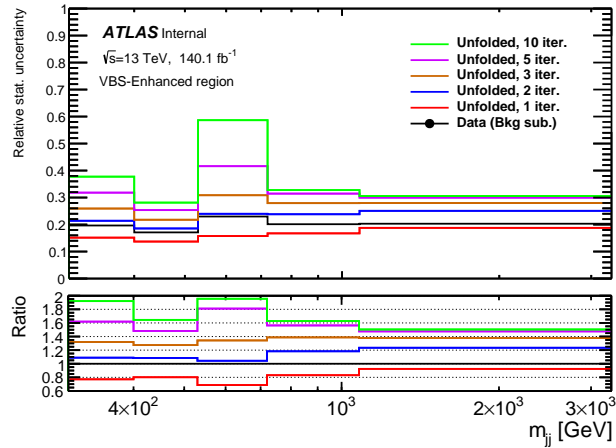


Figure 5.17.: Statistical uncertainty of the unfolded m_{jj} distribution in the VBS-Enhanced region obtained from the data. Different colours correspond to an increasing number of iterations. The statistical uncertainty of the background-subtracted data before unfolding is shown in black for comparison.

events are expected to come from pile-up interactions, while the remaining are caused by migrations outside the fiducial volume. The EW $4\ell jj$ production is

characterised by high purity, as the selected jets are likely to originate from the VBS interaction. Contrarily, pile-up jets are particularly relevant for the strong $4\ell jj$ production, as additional hadronic activity is expected to occur. The fraction of non-fiducial events in the quark-initiated strong production is shown in fig. 5.18 for the VBS-Enhanced region. The quantity is labelled as fake fraction in the plot and corresponds to the complement of the fiducial fraction. It is computed as the fraction of events selected at reconstruction-level, which fail the fiducial selection. The fraction has a clear dependence on the p_T and η of the two tagging jets, increasing at low- p_T and large η . This behaviour reflects the limitations of the hard-scatter jets identification in the region outside the acceptance of the ID. The possibility to further reduce the contribution of pile-up events with a cut-based selection was investigated with some pile-up sensitive observables, such as the p_T balance of the event, defined as the ratio between $p_{T,4\ell jj}$ and $S_{T,4\ell jj}$. The signal efficiency loss and the additional migrations outside the fiducial volume introduced by the additional cut were, however, found to be too large to have a positive impact on the measured cross-section and were not included in the event selection, as shown in fig. 5.19. At the same time, it is not possible to subtract the predicted non-fiducial events before unfolding, as the resulting uncertainty would be too large. The modelling of the non-fiducial events in the simulation is additionally cross-checked in a dedicated pile-up CR. This region is defined with the same event selection as in the SR, but the dijet candidate is formed by two jets both failing the JVT (fJVT) requirement, thus being enriched with pile-up jets. The measured data in the CR are observed to be consistent with the predictions given by both the nominal SHERPA and the alternative MG5_NLO+PY8 strong $4\ell jj$ samples.

5.6.4. Unfolding validation

Some tests are carried out to validate the unfolding procedure and check its robustness to physics variations. In particular, injection tests are performed to assess if the unfolding algorithm is capable of predicting the underlying true distribution originating from New Physics contributions. The expected detector-level distribution for a BSM process is measured from a dedicated simulation and added to the SM prediction. The resulting distribution is then unfolded with a response trained on the pure SM MC samples. The difference between the unfolded and the combined SM +BSM true distributions gives an estimate of the bias. As an example, the injection test for a dimension-8 EFT operator is illustrated

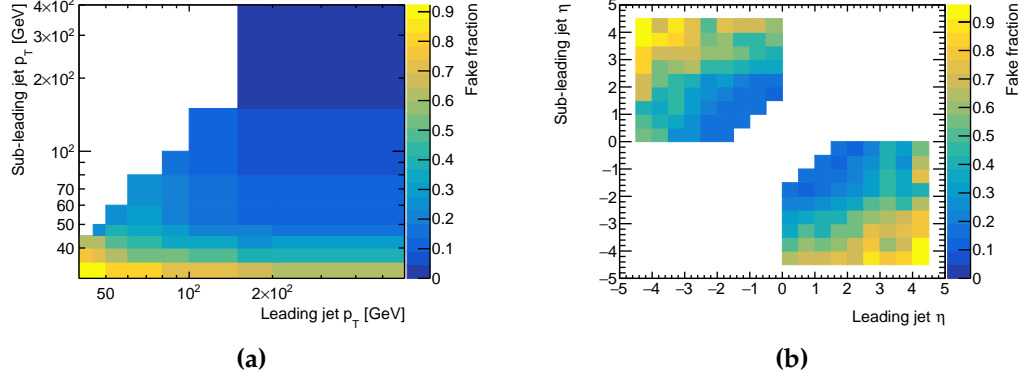


Figure 5.18.: Fraction of non-fiducial events in the quark-initiated strong $4\ell jj$ production as a function of the tagging jets transverse momentum (left) and pseudorapidity (right). The sample refers to the VBS-Enhanced region.

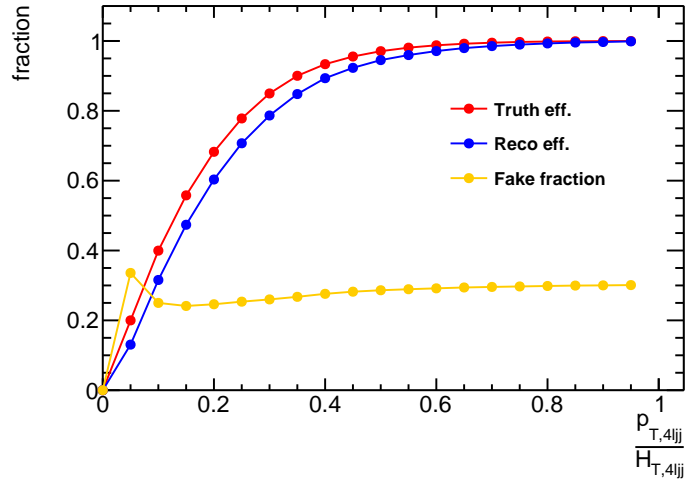


Figure 5.19.: Fiducial (red) and reconstruction-level (blue) selection efficiency when including an upper cut on the p_T balance of the event, $p_{T,4\ell jj} / S_{T,4\ell jj} < x_{cut}$, evaluated from the simulation of the signal processes. The observable H_T in the plot is analogous to $S_{T,4\ell jj}$ defined in section 5.3.3. The fraction of non-fiducial events is shown in yellow.

in fig. 5.20. The figure shows the contribution of the field strength operator⁷ $\mathcal{O}_{T,0}$ for a Wilson coefficient equal to $f_{T,0} = 0.6 \text{ TeV}^{-4}$. The unfolded distribution is consistent with the MC truth well below uncertainties.

⁷A description of the EFT formalism and the operators' definitions are given in section 5.10, along with details of the simulated samples.

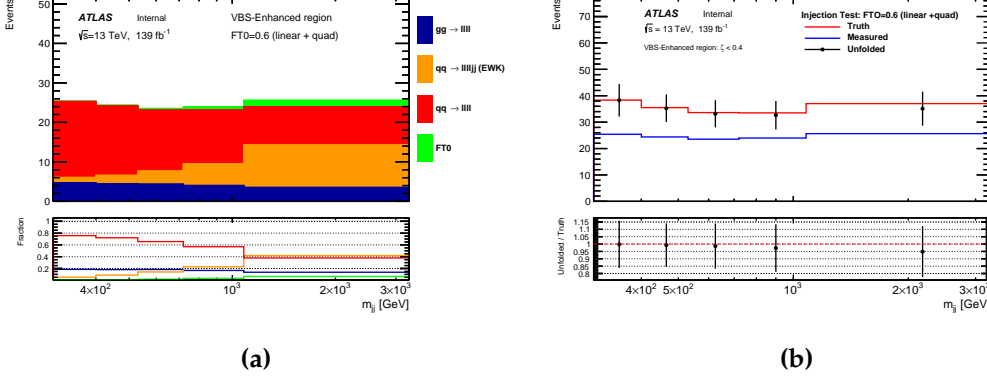


Figure 5.20.: Detector-level MC prediction (left) and result of the unfolding injection test (right) when including the contribution from the dimension-8 EFT operator $\mathcal{O}_{T,0}$ with a Wilson coefficient equal to $f_{T,0} = 0.6 \text{ TeV}^{-4}$. The distribution corresponds to m_{jj} in the VBS-Enhanced region and is comprehensive of the contributions from the pure BSM process and its interference with the SM diagrams. The unfolding is performed with one iteration.

5.7. Bootstrap and statistical correlation

The statistical uncertainty of the unfolded distribution, as well as the statistical correlation between different bins of the measured observables, can be evaluated using a bootstrap technique [241]. The method consists in generating a set of replicas of the measured distributions by means of statistical fluctuations of the observed events. The variations are obtained event-by-event, applying a weight randomly generated from a Poisson distribution with mean $\lambda = 1$. The set of weights is distinctively determined for each dataset with a univocal random generator seed. The full unfolding procedure is performed on the replicas, thus retrieving a set of unfolded distributions. Similar statistical fluctuations can also be applied to the simulated sample before computing the response matrix to propagate the MC uncertainty in the unfolding procedure. The covariance between the i -th and j -th bins of two generic observables a and b can be computed from the unfolded replicas as

$$C(a_i, b_j) = \sum_{n=1}^{N_{\text{replicas}}} (a_{i,n} - \langle a_i \rangle)(b_{j,n} - \langle b_j \rangle), \quad (5.18)$$

where $\langle a_i \rangle$ and $\langle b_j \rangle$ are the averages of the unfolded replicas in the two bins.

A set of 10000 replicas is used to evaluate the unfolded distributions and cross-check the values provided by the RooUnfold framework. The uncertainties obtained with the two methods are found to be in agreement at the order of per cent, which corresponds to the precision of the bootstrap technique. The unfolded replicas are also used to measure the statistical correlation between bins of different observables. The correlation values are trivially obtained from eq. (5.18), dividing $C(a_i, b_j)$ by the product of the standard deviations in the two bins. Correlation matrices for all the measured observables are reported in figs. 5.21 and 5.22, separately for the VBS-Enhanced and VBS-Suppressed regions.

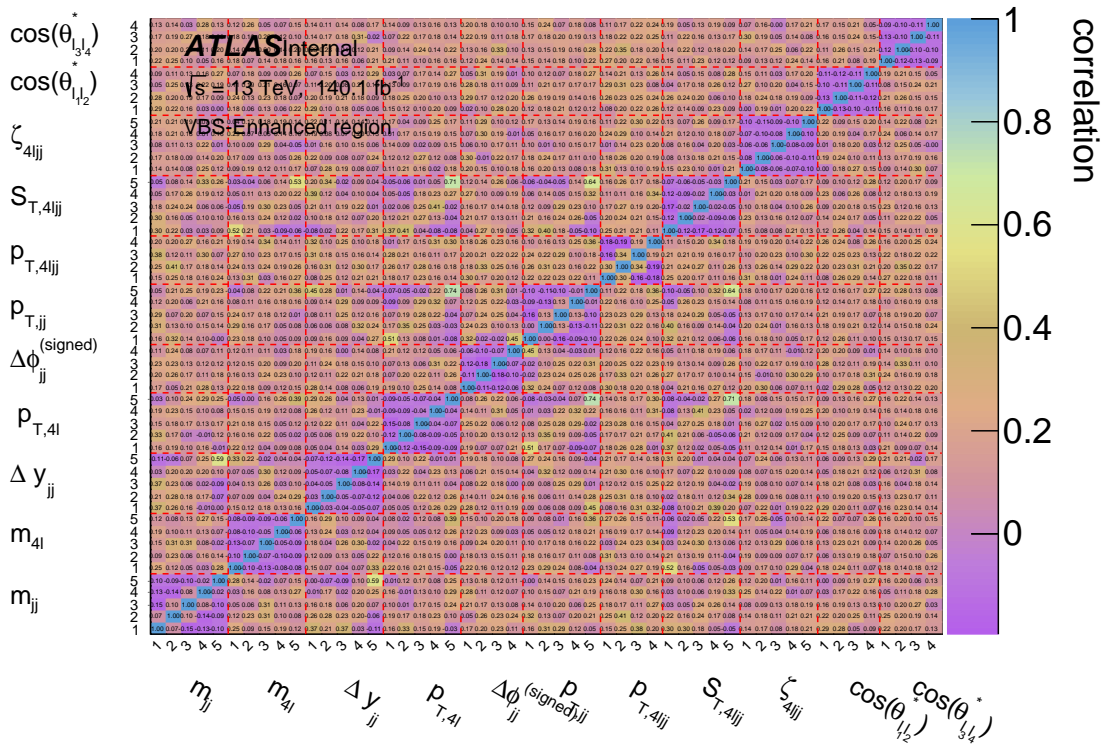


Figure 5.21.: Correlation matrix for all the measured observables in the VBS-Enhanced region after unfolding. The statistical correlation is evaluated from a set of 10000 bootstrap replicas which are unfolded using two iterations.

5.8. Systematic uncertainties

This section outlines the different sources of systematic uncertainties which affect the measurement and describes the procedure used to evaluate the corresponding uncertainties on the unfolded cross-section. Uncertainties on the fiducial-level

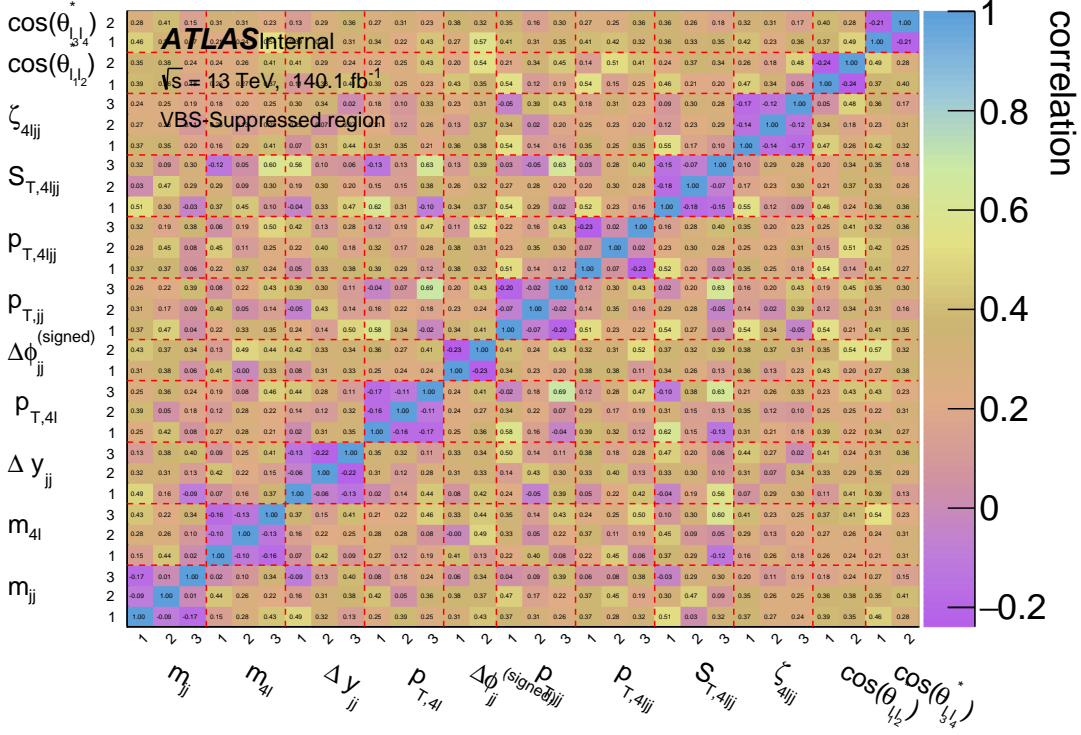


Figure 5.22.: Correlation matrices for all the measured observables in the VBS-Suppressed region after unfolding. The statistical correlation is evaluated from a set of 10000 bootstrap replicas which are unfolded using two iterations.

distributions correspond to theoretical variations in the models and parameters used to generate the MC events. The detector-level uncertainties include the aforementioned theoretical systematics and the uncertainties associated with the reconstruction and calibration procedures. The fiducial and reconstruction-level predictions are used in the unfolding algorithm, whose result is subject to both sources of systematics. Additionally, the uncertainty at the unfolded-level includes systematics directly related to the unfolding procedure, such as the bias.

Typically, the different sources of systematics produce an alteration of the nominal distribution. At fiducial and reconstruction-level, the uncertainty is directly derived from the difference between the two:

$$\sigma_i = \frac{N_i^{(\text{Syst})} - N_i^{(\text{Nominal})}}{N_i^{(\text{Nominal})}}, \quad (5.19)$$

where the index i runs over the bins of the observable distribution. In case $\pm 1\sigma$ variations, also referred to as "up" and "down", are available, the systematic uncer-

tainty is symmetrised by averaging the absolute variation in the two directions, i.e.

$$\sigma_i = \frac{|\sigma_i^{up}| + |\sigma_i^{down}|}{2}. \quad (5.20)$$

The bootstrap method introduced in section 5.7 can be used to estimate the statistical uncertainty relative to the systematic variation. Before performing the average, a set of replicas of the simulated samples was used to validate the assumption of symmetric variations. In the case of multiple-points variations, the uncertainty is taken as the envelope of the absolute values corresponding to single variations,

$$\sigma_i = \max_{v \in \{\text{variations}\}} (|\sigma_{i,v}|), \quad (5.21)$$

thus selecting the maximum spread.

The systematic uncertainties associated with the unfolded cross-section measurement are evaluated from the simulation and later applied to the data as a relative value. The systematic variations can be propagated through the unfolding procedure either by altering the response matrix or varying the distribution to be unfolded. The methods are equivalent and only differ in the sign of the resulting variation, which is opposite in the two. The measurement described in this thesis uses the second approach, where the varied measured distribution is unfolded with the nominal response. All the different sources of systematics are independent of each other. The total systematic uncertainty is obtained by the sum in quadrature of the terms, namely

$$\sigma_i^{\text{Tot}} = \sqrt{\sum_{s \in \{\text{syst.}\}} \sigma_{i,s}^2}. \quad (5.22)$$

5.8.1. Theoretical uncertainties

Systematic variations related to uncertainties in the theory are typically obtained with on-the-fly event weights that are applied to the simulated events. The leading source of theoretical uncertainty comes from QCD scale variations, which can produce large differences in the predictions. As an example, the QCD scale uncertainty of the strong SHERPA $4\ell jj$ production is typically of the order of 20 – 30%. This large variation is suppressed at the unfolded-level, as the unfolding

algorithm is primarily susceptible to alterations in the shape of the distributions rather than their normalisation, provided there are no changes in efficiency. The different sources of theoretical uncertainties are described below.

- QCD scale:** The variations account for the uncertainties of the QCD factorisation (μ_F) and renormalisation (μ_R) scales due to missing higher-order corrections. The two parameters are independently shifted by a factor 0.5 and 2, thus producing a 7-points variation corresponding to $(\mu_R, \mu_F) \times \{(0.5, 0.5), (0.5, 1), (1, 0.5), (1, 1), (1, 2), (2, 1), (2, 2)\}$. The opposite variations (0.5, 2) and (2, 0.5) are not included to avoid large logarithms in the calculations. The envelope of the different variations is considered as the final uncertainty. The QCD scale variations are evaluated separately for the different signal processes. The strong $gg \rightarrow 4\ell$ sample includes corrections related to higher-order predictions. In this case, the QCD scale variations are normalised to the nominal event yield to avoid double-counting the uncertainty associated with the k-factors. As an example, unfolded-level QCD scale uncertainties for the strong $qq \rightarrow 4\ell$ production are shown in fig. 5.23 as a function of m_{jj} in both SRs.
- PDF and α_S :** The uncertainties in the signal samples are evaluated following the NNPDF3.0 prescription [28]. The MC samples present 100 internal variation of the PDF tune, along with variations given by the use of the alternative CT14 [29] and MMHT2014 [30] PDF sets. The uncertainty is evaluated as the envelope between the standard deviation of the internal variations and those due to the alternative sets. The strong coupling constant is also varied by ± 0.001 , corresponding to $\alpha_S = \{0.117, 0.119\}$, and the resulting uncertainty is combined with that of the PDF set. The alternative sample for the strong $4\ell jj$ production utilises a different set of internal PDF variations accordingly with the PDF4LHC15NLO recipe [31]. The combination of PDF and α_S uncertainties for the strong $qq \rightarrow 4\ell$ production is illustrated in fig. 5.24, again as a function of m_{jj} in both SRs.
- $gg \rightarrow 4\ell$ re-weighting:** The uncertainties associated with the higher-order QCD k-factors are propagated through the MC predictions.
- $t\bar{t}Z$ and VVV cross-sections:** The cross-sections used to normalise the MC predictions are varied accordingly with uncertainties derived in previous

ATLAS measurements [214, 215]. The variations correspond to 15% and 10% respectively for the two processes.

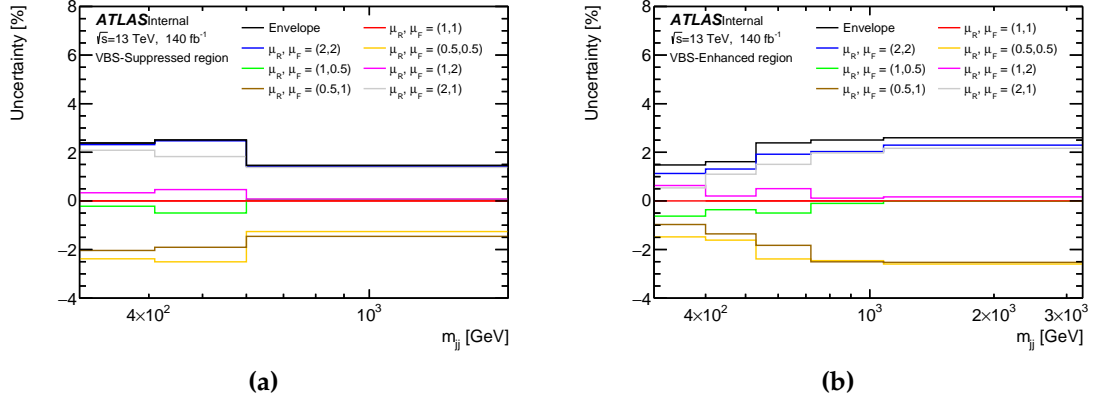


Figure 5.23.: QCD scale systematic uncertainty as a function of m_{jj} in the VBS-Suppressed (left) and VBS-Enhanced (right) regions for the strong $qq \rightarrow 4\ell$ sample. The uncertainties correspond to the unfolded-level and are derived with two iterations. The seven-points variations of the μ_R and μ_F parameters are shown with coloured lines, including the nominal case in red. The envelope displayed in black represents the final uncertainty.

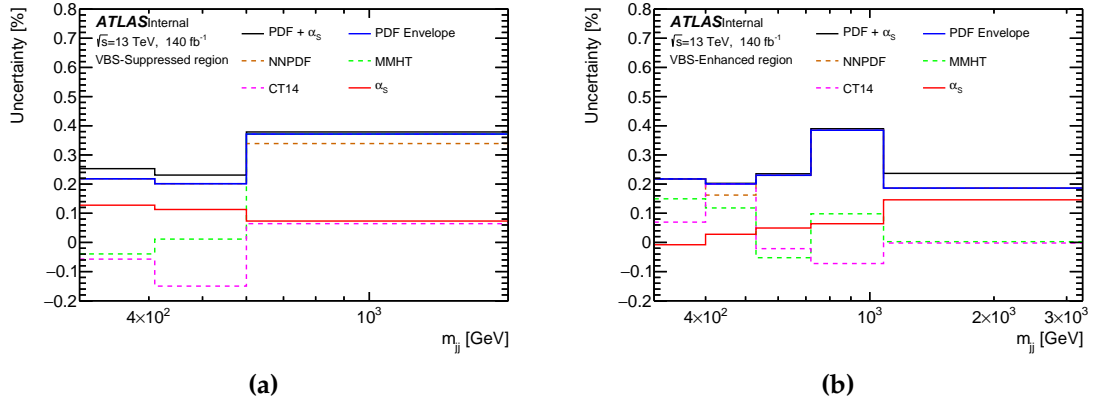


Figure 5.24.: Combined PDF and α_s systematic uncertainty (black) as a function of m_{jj} in the VBS-Suppressed (left) and VBS-Enhanced (right) regions for the strong $qq \rightarrow 4\ell$ sample. The uncertainties correspond to the unfolded-level and are derived with two iterations. The uncertainty associated with the internal NNPDF PDF set is displayed with a dashed brown line, while the alternative CT14 and MMHT2014 sets are shown in fuchsia and green, respectively. The blue solid line gives the envelope of the three PDF sets. The red solid line corresponds to the uncertainty associated with the α_s variations only.

5.8.2. Experimental systematics

Systematic variations related to the uncertainties of the different scale factors applied to the simulation are obtained by applying a multiplicative event weight corresponding to the scale factor variation. Contrarily, uncertainties affecting the momentum and energy calibrations are propagated through the reconstruction procedure, thus producing a set of varied datasets. The new samples undergo the complete analysis event selection to obtain the corresponding observable distributions, from which the systematic uncertainties are estimated with the usual procedure. All the systematic variations associated with the reconstruction and selection of physical objects are coherently propagated to both signal and background predictions, including the non-prompt component estimated from the data CRs, to account for the uncertainties in the background subtraction procedure. The different sources of experimental systematics are described below.

- **Jet energy scale:** JES uncertainties come from the different procedures used to calibrate the energy of the jets described in section 3.3.4, such as the in-situ calibrations of the measured JES with respect to well-calibrated objects. These uncertainties typically depend on the pseudorapidity and transverse momentum of the jets and are provided by the ATLAS software [242]. The JES uncertainties are parametrised with a set of 23 nuisance parameters, which are shifted by $\pm 1\sigma$, corresponding to a total of 46 variations. Among these, two parameters account for the varying response to quark and gluon jets, which is estimated by comparing the hadronisation predictions provided by different generators. The evaluation strongly depends on the assumed flavour composition of the jets and can yield very large uncertainties if it is not representative of the measured phase space. The fraction of quark and gluon jets was measured in the fiducial volume of the measurement before the nuisance parameter variation and propagated through the evaluation of the systematics. The procedure was observed to strongly reduce the jet flavour uncertainties.
- **Jet energy resolution:** Systematics related to the JER are mainly driven by resolution differences in the data and the simulation and by the evaluation of the noise term in eq. (3.10). When the measured resolution in the data differs from the predicted values, the simulation is smeared with a Gaussian distribution until the average resolution matches the data. The smearing pro-

cedure is performed only if the data resolution is larger than in the simulation. A total of 13×2 variations cover the JER uncertainties.

- **JVT (fJVT) efficiency:** The uncertainties of the JVT (fJVT) efficiency scale factors are propagated through the measurement.
- **Electron reconstruction and selection:** The uncertainties of trigger, identification, reconstruction and isolation efficiencies are included in the form of additional event weights. A single nuisance parameter, corresponding to 1×2 variations, accounts for the uncertainties of the trigger scale factor. A set of 25×2 and 34×2 variations covers the electron reconstruction and identification efficiency respectively. Two variations of a single parameter correspond to the uncertainty of the isolation efficiency. Two additional nuisance parameters (2×2) are used for the systematics related to the electron momentum resolution and scale uncertainties.
- **Muon reconstruction and selection:** The systematics corresponding to the reconstruction and selection efficiency of the muons are similar to those listed for the electrons. A set of 2×2 , 4×2 , 2×2 and 2×2 variation are used respectively for the uncertainties of the trigger, combined reconstruction and identification, isolation and TTVA efficiencies, for a total of 10 nuisance parameters. The momentum resolution and scale are covered by 2 and 1 parameters respectively, with an additional 2 for the sagitta correction, all with upward and downward variations.
- **Pile-up re-weighting:** One nuisance parameter with upward and downward variations accounts for uncertainties in the scale factor applied to the simulation to match the $\langle\mu\rangle$ profile in the data.
- **Luminosity:** The simulation is normalised to the Run 2 luminosity, which was measured with a precision of 0.83% [98]. Upward and downward variations are obtained by re-scaling the distributions, which are then used in the unfolding procedure. The luminosity value also contributes to the cross-section computation via eq. (3.4). The final uncertainty is determined as the combination of the luminosity uncertainty and the unfolded-level value, assuming the two terms are fully correlated.

- **Non-prompt background estimate:** The statistical and systematic uncertainties associated with the measurement of the fake efficiency are propagated through the non-prompt background estimate.

The leading contribution among these systematics stems from the uncertainties associated with the jet energy scale and resolution. A breakdown of the different terms composing the JES and JER systematics is shown in fig. 5.25 as a function of m_{jj} in both SRs. The figure reports the uncertainties at the unfolded-level, which are typically below 10%.

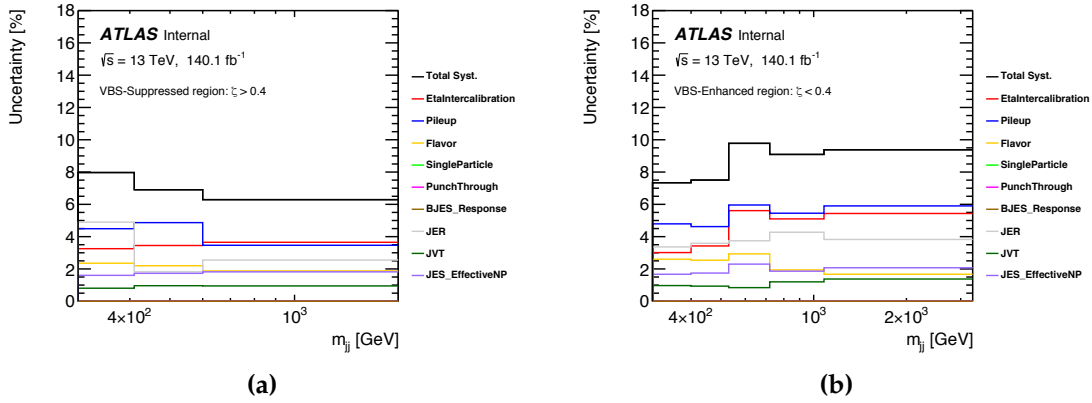


Figure 5.25.: Different sources of systematic uncertainties associated with the JES and JER as a function of m_{jj} in the VBS-Suppressed (left) and VBS-Enhanced (right) regions. The uncertainties correspond to the unfolded-level and are derived with two iterations.

5.8.3. Unfolding systematics

The sources of systematic uncertainty described below directly affect the unfolding procedure and, as such, are not included in the fiducial or reconstruction-level uncertainties.

- **Unfolding bias:** The uncertainty relative to the precision of the unfolding algorithm is given by the bias introduced in section 5.6. The bias is evaluated with the MC-based procedure described in section 5.6.3.
- **Generator choice:** The response matrix is based on the modelling of the signal processes that is intertwined with the specific MC generators used to simulate the events. This systematic uncertainty accounts for the model independence of the unfolding procedure and is estimated using the alternative samples listed in section 5.2. Only the uncertainty relative to the modelling

of the quark-initiated strong $4\ell jj$ production is considered, as the predictions of the MG5+PY8 and POWHEG+PY8 EW $4\ell jj$ are found to be very similar. A different Asimov dataset is constructed replacing the SHERPA $qq \rightarrow 4\ell$ sample with the alternative one generated with MG5_NLO+PY8. The latter is re-weighted at particle level to match the SHERPA line-shape using the smoothed ratio between the detector-level predictions given by the two generators. The process is analogous to the re-weighting procedure performed in the data-driven closure and prevents the double-counting of the unfolding bias uncertainty. The re-weighted measured distribution is unfolded with the nominal response computed from SHERPA, and the uncertainty is given by the difference between the unfolded and the re-weighted true distributions. As an example, the procedure for m_{jj} in the VBS-Enhanced region is illustrated in fig. 5.26.

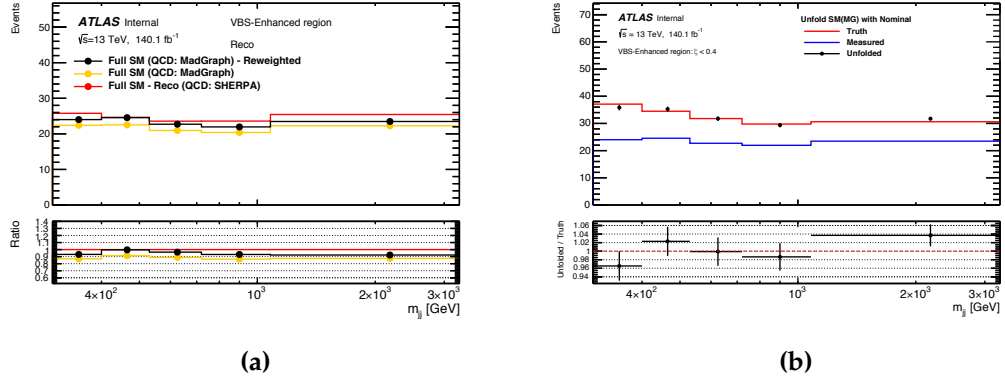


Figure 5.26.: (a) Comparison of the predicted measured m_{jj} distributions in the VBS-Enhanced region obtained with the nominal SHERPA (red) or the alternative MG5_NLO+PY8 (yellow) $qq \rightarrow 4\ell$ samples. The reducible background is not included in the distributions. The alternative sample is re-weighted at particle-level to match the nominal line-shape (black line). (b) The re-weighted measured MC (blue) is unfolded with the nominal response (black) and compared to the re-weighted true distribution (red). The unfolding algorithm is executed with two iterations.

5.8.4. Breakdown of the uncertainties

The impact of the different sources of systematics on the total uncertainty is shown in figs. 5.27 and 5.28. The uncertainties in the figures correspond to the unfolded values after two iterations, respectively for m_{jj} and $m_{4\ell}$ in the two SRs. Plots for the remaining observables are reported in appendix A.1. The total uncertainty ranges on average between 20% and 30% and is dominated by the

statistical uncertainty. However, the latter can get as large as $\approx 60\%$ in some low-populated bins of the VBS-Suppressed region. Among the systematic uncertainties, the largest contributions are delivered by the systematics associated with the reconstruction of the jets and the unfolding bias. The different contributions are also listed with more detail in tables 5.8 and 5.9.

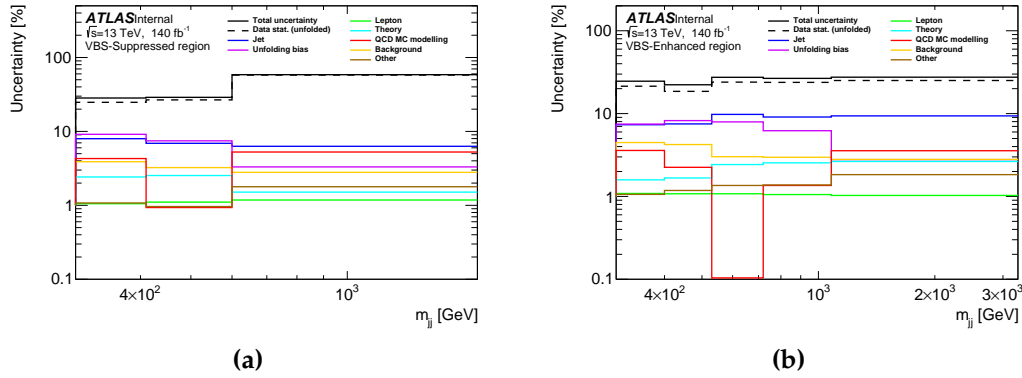


Figure 5.27.: Different sources of uncertainties at unfolded-level as a function of m_{jj} in the VBS-Suppressed (left) and VBS-Enhanced (right) regions. The total uncertainty is depicted with a continuous black line, while the statistical uncertainty is shown with a dashed line. The different colours represent the various sources of systematic uncertainties. The plots correspond to the unfolded values after two iterations.

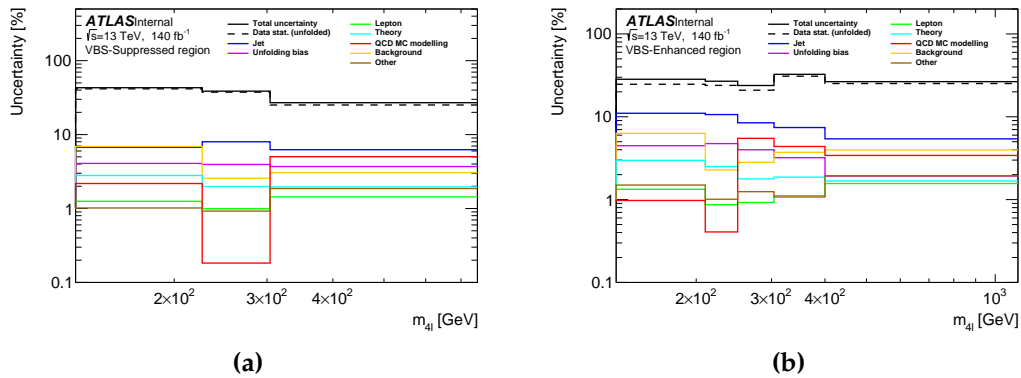


Figure 5.28.: Different sources of uncertainties at unfolded-level as a function of $m_{4\ell}$ in the VBS-Suppressed (left) and VBS-Enhanced (right) regions. The total uncertainty is depicted with a continuous black line, while the statistical uncertainty is shown with a dashed line. The different colours represent the various sources of systematic uncertainties. The plots correspond to the unfolded values after two iterations.

VBS-Suppressed Region			
Bin			
m_{jj} [GeV]	[300, 410)	[410, 600)	[600, 1780)
Strong $qq \rightarrow 4\ell jj$ modelling	4.3%	0.93%	5.3%
Jet	8%	6.9%	6.3%
Trigger	0.076%	0.059%	0.063%
Leptons	1.1%	1.1%	1.2%
PRW	0.52%	0.036%	0.16%
Theory (Strong $qq \rightarrow 4\ell jj$)	2.4%	2.5%	1.5%
Theory (EW $qq \rightarrow 4\ell jj$)	0.071%	0.029%	0.082%
Theory (Strong $gg \rightarrow 4\ell jj$)	0.34%	0.27%	0.044%
Prompt background	1.6%	1.8%	1.5%
Non-prompt background	3.5%	2.7%	2.4%
Luminosity	0.71%	0.68%	0.69%
Unfolding bias	9.1%	7.5%	3.3%
Total syst.	14%	11%	9.5%
Stat.	25%	27%	58%

Table 5.8.: Breakdown of the systematic uncertainties for m_{jj} in the VBS-Suppressed region at unfolded level after 2 iterations.

VBS-Enhanced Region					
Bin					
m_{jj} [GeV]	[300, 400)	[400, 530)	[530, 720)	[720, 1080)	[1080, 3280)
Strong $qq \rightarrow 4\ell jj$ modelling	3.6%	2.2%	0.1%	1.4%	3.6%
Jet	7.3%	7.5%	9.8%	9.1%	9.4%
Trigger	0.07%	0.059%	0.059%	0.058%	0.05%
Leptons	1.1%	1.1%	1.1%	1.1%	1%
PRW	0.28%	0.6%	0.93%	0.98%	0.56%
Theory (Strong $qq \rightarrow 4\ell jj$)	1.5%	1.6%	2.4%	2.5%	2.6%
Theory (EW $qq \rightarrow 4\ell jj$)	0.44%	0.34%	0.28%	0.13%	0.26%
Theory (Strong $gg \rightarrow 4\ell jj$)	0.29%	0.18%	0.23%	0.15%	0.33%
Prompt background	2.9%	2.8%	2.5%	1.7%	0.86%
Non-prompt background	3.4%	3.2%	1.7%	2.4%	2.7%
Luminosity	0.62%	0.63%	0.67%	0.67%	0.71%
Unfolding bias	7.5%	8.2%	7.9%	6.2%	2.8%
Total syst.	12%	12%	13%	12%	11%
Stat.	21%	19%	24%	24%	25%

Table 5.9.: Breakdown of the systematic uncertainties for m_{jj} in the VBS-Enhanced region at unfolded level after 2 iterations.

5.9. Unfolded differential cross-sections

The measured data distributions are unfolded with the iterative algorithm introduced in section 5.6.2 after the prompt and non-prompt background estimates are subtracted. All the observables are unfolded with two iterations, except $p_{T,4\ell jj}$ in the VBS-Enhanced region, which needed three iterations to prevent the undercoverage of the statistical uncertainty, as described in section 5.6.3. Following eq. (3.4), the unfolded distributions are divided by the total integrated luminosity of the dataset to obtain differential cross-sections.

The results for all the measured observables are reported in figs. 5.29 and 5.30, respectively for the VBS-Suppressed and VBS-Enhanced regions. The data cross-sections are compared with the MC predictions at fiducial-level. The nominal signal predictions provided by the SHERPA strong and MG5+PY8 EW $4\ell jj$ samples are displayed in red in the figures. The results are compared with a second set of predictions obtained by interchanging the quark-initiated strong production with the alternative MG5_NLO+PY8 sample. The first set of predictions is found to be in sufficient agreement with the observed data in all bins of the measured observable. On the other hand, the strong MG5_NLO+PY8 $4\ell jj$ sample is less consistent with the data, generally underestimating the production cross-section. This feature can be seen, for example, at low energies in the m_{jj} and $m_{4\ell}$ distributions (figs. 5.30a and 5.30b) belonging to the VBS-Enhanced region or towards the central part of the angular distributions $\Delta\phi_{jj}$ and $\cos\theta^*$ (figs. 5.30e, 5.30i and 5.30j), also in the VBS-Enhanced region. Similar trends are observed in the VBS-Suppressed region. A possible explanation for the discrepancies observed between the two sets of predictions can be found in the different multi-jet final state accuracy in the two generators. Although both samples are at NLO accuracy for the 0, 1 jet final states, the additional parton emission in the MG5_NLO+PY8 sample is purely handled by the parton shower algorithm, while SHERPA has a LO accuracy for up to 3 additional jets. The event selection and SR definition rely on the angular configuration of the two tagging jets, which could be different for the sub-leading one. The uncertainties of the two simulations are also very different from each other, with SHERPA being more conservative and presenting an uncertainty more than twice as large as MG5_NLO+PY8. The disparity mainly originates from the systematic uncertainty related to the QCD scale variations. The uncertainty associated with the PDF set is also computed from different internal variations of the sets employed by the two generators. However, it is found to

be significantly smaller than the QCD scale uncertainty. Predictions for the pure EW $4\ell jj$ production are also included in the plots to assess the sensitivity of the observable to the VBS process. These are compared with the cross-section obtained from the alternative combined EW POWHEG+PY8 $4\ell jj$ + SHERPA $ZZV(\rightarrow jj)$ samples. The two are observed to be very similar across all bins of the measured observables.

The unfolded cross-sections presented above represent the first ATLAS differential measurement of $4\ell jj$ production. The previous ATLAS observation of EW $ZZjj$ production only reported an inclusive cross-section, for both the $4\ell jj$ and $\ell\ell\nu\nu jj$ decay channels. The cross-section values were extrapolated to the fiducial volume by means of a single multiplicative correction factor, defined as the fraction of events passing the detector-level events to the total events selected at particle-level in the simulation. The resulting fiducial cross-section for the inclusive $ZZjj$ production in the $4\ell jj$ channel was measured to be $1.2 \pm 0.12(\text{stat}) \pm 0.02(\text{theory}) \pm 0.07(\text{experimental}) \pm 0.01(\text{background}) \pm 0.12(\text{luminosity})$ [199]. This value is of the same order of magnitude as the results presented in this thesis (after integrating the differential cross-section), though a direct comparison is not possible due to the different fiducial volumes studied in the two measurements. Similarly, the measurement reported by the CMS collaboration [200] focused on the determination of the EW production signal strength, and reported the total cross-sections for the EW-only and EW +Strong production.

5.10. EFT interpretation

The unfolded differential cross-sections presented in section 5.9 are used to search for contributions from New Physics events in the context of a SM Effective Field Theory (EFT). This study was carried out by another member of the analysis team and is only briefly described here to complement the measurement's results.

The EFT represents a model-independent approach to extend the SM theory, where BSM contributions are parametrised with higher-dimension operators acting at a much larger energy scale. Thus, the EFT Lagrangian (\mathcal{L}_{EFT}) assumes the form of a series expansion in powers of a cut-off energy scale Λ , where the lowest-energy term corresponds to the SM Lagrangian discussed in section 2.2.5.

Namely,

$$\mathcal{L}_{EFT} = \mathcal{L}_{SM} + \sum_{d>4} \sum_i^{n_d} \left(\frac{c_i^{(d)}}{\Lambda^{d-4}} \mathcal{O}_i^{(d)} \right) + O\left(\Lambda^{-(n_d+1)}\right), \quad (5.23)$$

where d denotes the dimension of the operators $\mathcal{O}_i^{(d)}$, c_i are coupling constants called Wilson coefficients, and n_d is the maximum order of the series expansion. Typically, operators of an odd dimension are not included in the expansion, as they violate baryon and lepton number conservation. Of particular interest for the $ZZjj$ measurement are dimension-8 operators, as they correspond to the first order at which quartic weak boson self-interactions occur. The measurement is also sensitive to some dimension-6 operators, some of which have a CP-odd nature which could help explain the baryon asymmetry problem. Both dimension-6 and dimension-8 terms have a known set of orthogonal operators, commonly represented in the Warsaw [243] basis and Eboli [189] model, respectively.

The total scattering amplitude corresponding to the combined SM and EFT production is commonly obtained with the decomposition method, namely

$$|\mathcal{M}|^2 = |\mathcal{M}_{SM}|^2 + 2\Re(\mathcal{M}_{SM}^* \mathcal{M}_{\mathcal{O}}) + |\mathcal{M}_{\mathcal{O}}|^2, \quad (5.24)$$

where the first term is the SM scattering amplitude, the remaining two correspond respectively to the interference with the SM and the pure EFT process, and we neglected the contributions from operators other than \mathcal{O} . For a dimension- d operator the interference and pure EFT terms are proportional to c_i/Λ^{d-4} and $c_i^2/\Lambda^{2(d-4)}$, respectively. These correspond to contributions of the order $1/\Lambda^4$ and $1/\Lambda^8$ for dimension-8 operators.

Theory predictions are obtained from independent simulations of a single operator's interference and pure EFT contributions. The samples were generated at LO accuracy in perturbative QCD using MADGRAPH 5 with the NNPDF3.0NLO PDF set. The generator was interfaced with PYTHIA 8 to simulate the $Z \rightarrow \ell^+ \ell^-$ decays, as well as the parton shower and hadronisation. The A14 set of tuned parameters was used. The interactions from the dimension-6 operators were provided by the SMEFTsim [244] package, parametrised in the Warsaw basis. The aforementioned Eboli model was, instead, used for the dimension-8 interactions. The generated events were processed with a Rivet [245] routine to provide particle-level predictions and emulate the fiducial selection of the measurement. The

resulting fiducial distributions of the interference and pure EFT contributions are added to the strong SHERPA $4\ell jj$ and MG5+PY8 EW $4\ell jj$ predictions, providing the overall SM +EFT prediction. The Wilson coefficients were set to unity in the simulation. Still, the interference and pure EFT contributions can be re-scaled to any desired value accordingly to their linear and quadratic behaviour.

The couplings of several EFT operators are constrained using a profile-likelihood test statistic [246], using a Python-based framework previously employed in Refs. [198, 247]. Assuming Gaussian-distributed uncertainties, a χ^2 variable is constructed as

$$\chi^2(c_X, \vec{\theta}) = \left(\vec{\sigma}_{unf} - \vec{\sigma}_{SM+EFT}(c_X) - \sum_{\theta} \theta \cdot \vec{e}_{\theta} \right)^T \mathbf{C}^{-1} \left(\vec{\sigma}_{unf} - \vec{\sigma}_{SM+EFT}(c_X) - \sum_{\theta} \theta \cdot \vec{e}_{\theta} \right), \quad (5.25)$$

where $\vec{\sigma}_{unf}$ and $\vec{\sigma}_{SM+EFT}(c_X)$ are respectively the unfolded cross-section, and the combined SM +EFT predicted cross-section corresponding to the operator X with coupling c_X . $\vec{\theta}$ is a set of Gaussian-constrained nuisance parameters of magnitude \vec{e}_{θ} , corresponding to the fiducial-level uncertainties of the theory prediction (QCD scale, PDF, etc.). The covariance matrix $\mathbf{C} = \mathbf{C}_{stat} + \mathbf{C}_{syst}$ accounts for the statistical and systematic uncertainties of the unfolded cross-section. The systematic term contains all the different sources of uncertainty shown previously in section 5.8.4, which are all independent. The covariance matrix for a single systematic uncertainty is constructed assuming full correlation between the bins of an observable.

Using the χ^2 defined in eq. (5.25), the likelihood function⁸ can be written as

$$\mathcal{L}(c_X, \vec{\theta}) = \frac{1}{\sqrt{(2\pi)^K |\mathbf{C}|}} e^{-\frac{1}{2} \chi^2(c_X, \vec{\theta})} \prod_{\theta} \mathcal{G}(\theta), \quad (5.26)$$

where K corresponds to the number of bins in the cross-section measurement and $\mathcal{G}(\theta)$ is the Gaussian distribution describing the nuisance parameter θ . The test

⁸The symbol \mathcal{L} in eq. (5.26) represents the likelihood function and should not be confused with the Lagrangian density, e.g. in eq. (5.23).

statistic ($q(c_X)$) is then given by the likelihood ratio

$$q(c_X) = -2 \log \frac{\mathcal{L}(c_X, \hat{\vec{\theta}})}{\mathcal{L}(\hat{c}_X, \hat{\vec{\theta}})}, \quad (5.27)$$

having indicated with \hat{c}_X and $\hat{\vec{\theta}}$ the maximum likelihood estimators of c_X and $\vec{\theta}$, respectively. The term $\hat{\vec{\theta}}$ represents the value of $\vec{\theta}$ which maximises the likelihood for a given choice of c_X . Assuming Wilks' theorem [248], eq. (5.25) is described by a χ^2 distribution with one degree of freedom, and we can evaluate the 95% confidence interval for c_X from the integral relation

$$\int_0^{q(c_X)} \chi^2(d.o.f = 1) dq > 95\%. \quad (5.28)$$

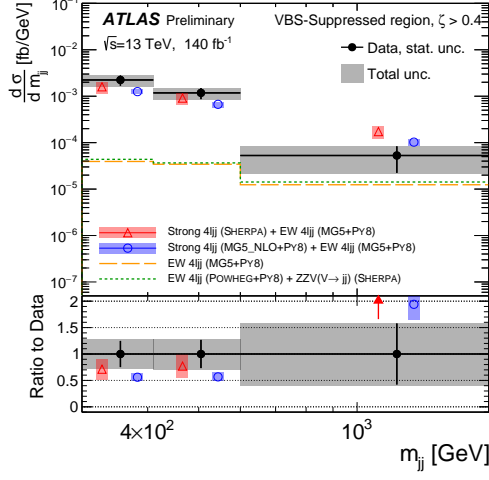
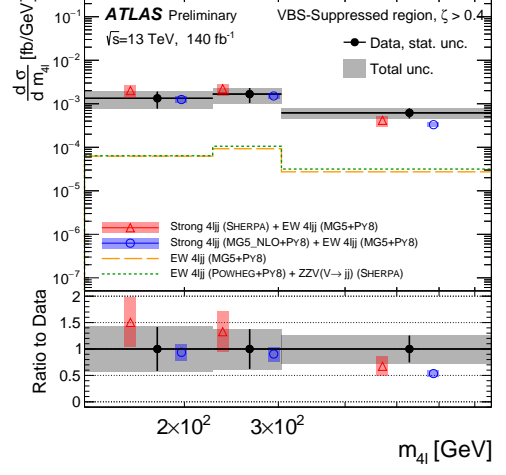
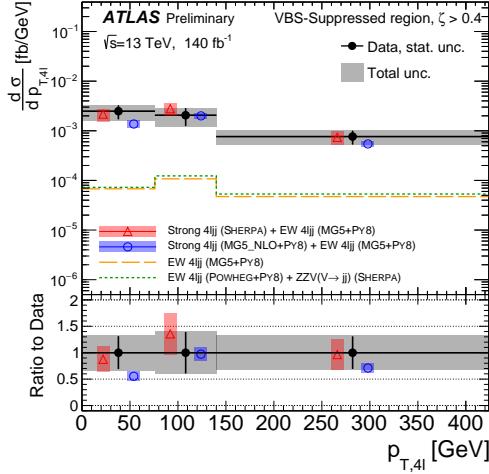
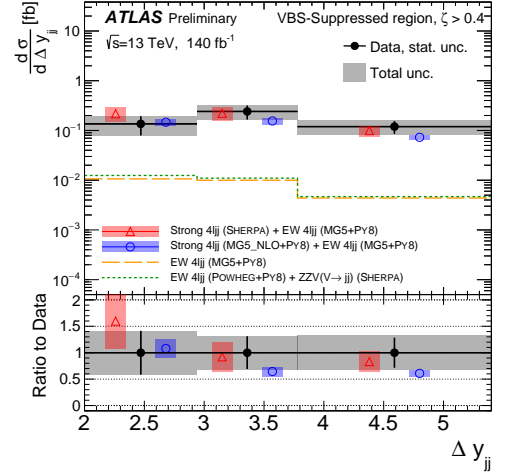
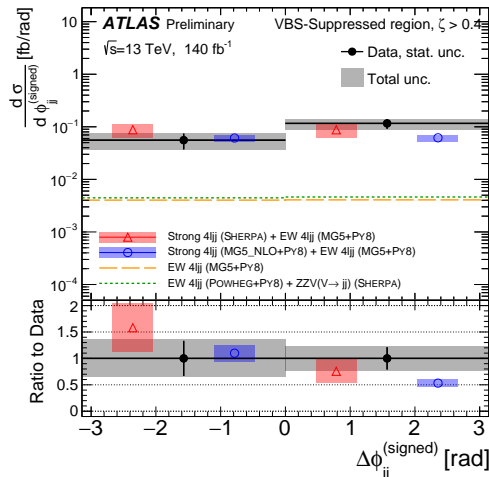
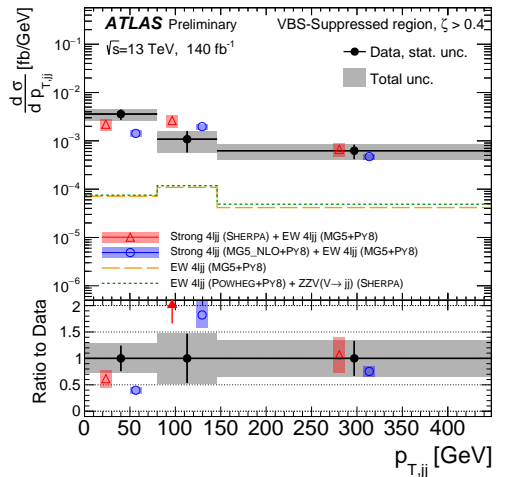
A total of six dimension-6 and eight dimension-8 operators are selected in their respective basis, as they are the ones to which the measurement is most sensitive. The 95% confidence interval is evaluated with the above procedure for each operator, using the combined $m_{jj} + m_{4\ell}$ unfolded cross-section in the VBS-Enhanced region. Both m_{jj} and $m_{4\ell}$ are particularly sensitive to the BSM contribution, which is typically enhanced towards high energies, and their combination provides the most stringent limit among the measured observables. When combining the two differential cross-sections, the first bin of $m_{4\ell}$ ($130 < m_{4\ell} < 210$ GeV) is dropped. The bin removal prevents a possible overconstraint of the confidence interval caused by a close-to-zero eigenvalue in the covariance matrix. The EFT contribution in the first $m_{4\ell}$ bin is negligible, and the bin removal does not diminish the sensitivity to New Physics. The statistical correlation between bins of the m_{jj} and $m_{4\ell}$ distributions is evaluated with the bootstrap method described in section 5.7 and is included in the combined covariance matrix. The observed and expected 95% confidence interval for the dimension-6 and dimension-8 operators are reported in tables 5.10 and 5.11, respectively. Limits are provided for the inclusive linear and quadratic and the linear-only EFT contributions. The interference contribution would be zero for some CP-odd dimension-6 operators ($c_{\tilde{W}}$, $c_{H\tilde{W}B}$ and $c_{H\tilde{B}}$ in table 5.10) due to the parity-even nature of m_{jj} and $m_{4\ell}$. In this case, the linear-only limit is evaluated using the $\Delta\phi_{jj}$ distribution, which is characterised by large asymmetries produced by the interference of the CP-odd operator. All the measured intervals are compatible with the assumption of no EFT contribution,

with the tightest constraints placed on the Wilson coefficients of the dimension-8 $\mathcal{O}_{T,0}$ and $\mathcal{O}_{T,1}$ field strength operators.

Although the $4\ell jj$ production is sensitive to dimension-6 operators, more stringent limits can be obtained from measurements of diboson production and vector boson fusion, as the effect of anomalous triple gauge couplings can be more significant in these processes, and such measurements are generally less statistically limited. As an example, comparable or tighter limits on some of the dimension-6 Wilson coefficients listed in table 5.10 have been established by measurements of 4ℓ [198], Zjj [247] and $W^+W^- (+ \geq 1j)$ [249, 250] production at ATLAS, and by measurements of WZ [251] and $W^\pm \gamma$ [252] production at CMS. Analogous limits on the couplings of the dimension-8 operators $\mathcal{O}_{T,0}$, $\mathcal{O}_{T,1}$, $\mathcal{O}_{T,2}$, $\mathcal{O}_{T,8}$ and $\mathcal{O}_{T,9}$ were measured by CMS from $ZZjj$ events [200]. Both ATLAS and CMS limits are compatible with the SM prediction, though the latter are about four times tighter than those presented in table 5.11. The difference arises from the fact that the CMS measurement was performed at detector-level, contrarily to the ATLAS measurement presented in this thesis, which employed unfolded cross-sections. The binning requirement introduced in section 5.3.3, necessary to execute the unfolding, results in very wide bins at high values of m_{jj} and $m_{4\ell}$, where the EFT contribution is more prominent. Requiring at least 20 SM predicted events in the last bin of the distributions reduces the concentration of EFT events, thus lowering the significance of the BSM component. On the other hand, the detector-level measurement of Ref. [200] is free from such constraint, allowing limits to be obtained from bins with zero observed events and a large predicted EFT contribution. Even if less competitive, the limits presented above represent an independent and complementary measurement to that of CMS, which can be used to consolidate the current knowledge of the dimension-8 EFT interpretation.

Wilson coefficient	$ \mathcal{M}_{d6} ^2$ Included	95% confidence interval [TeV^{-2}]	
		Expected	Observed
c_W/Λ^2	yes	[-1.3, 1.3]	[-1.2, 1.2]
	no	[-32, 32]	[-37, 28]
$c_{\tilde{W}}/\Lambda^2$	yes	[-1.3, 1.3]	[-1.2, 1.2]
	no	[-17, 17] [*]	[0, 30] [*]
c_{HWB}/Λ^2	yes	[-16, 7]	[-16, 6]
	no	[-12, 12]	[-15, 10]
$c_{H\tilde{W}B}/\Lambda^2$	yes	[-1.3, 1.3]	[-1.2, 1.2]
	no	[-67, 67] [*]	[-25, 130] [*]
c_{HB}/Λ^2	yes	[-13, 13]	[-12, 12]
	no	[-38, 38]	[-38, 38]
$c_{H\tilde{B}}/\Lambda^2$	yes	[-13, 13]	[-12, 12]
	no	[-420, 420] [*]	[-200, 790] [*]

Table 5.10.: Expected and observed 95% confidence interval for several Wilson coefficients of dimension-6 EFT operators. Limits are provided when including the quadratic pure EFT contribution to the SM predictions. The results are evaluated from the combined $m_{jj} + m_{4\ell}$ distribution in the VBS-Enhanced region, except for those marked with a (*), obtained using $\Delta\phi_{jj}$.

(a) m_{jj} (b) $m_{4\ell}$ (c) $p_{T,4\ell}$ (d) Δy_{jj} (e) $\Delta\phi_{jj}$ (f) $p_{T,jj}$

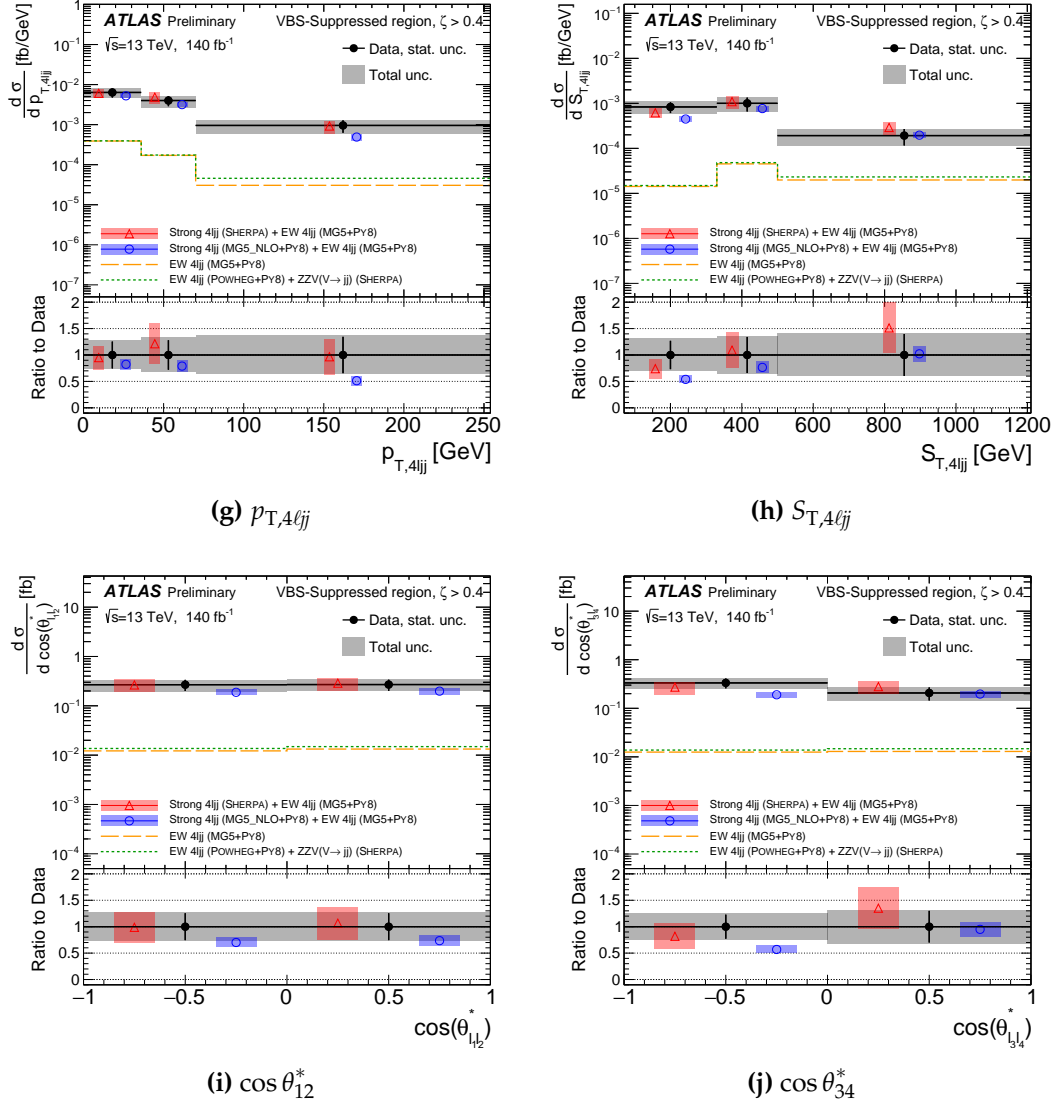
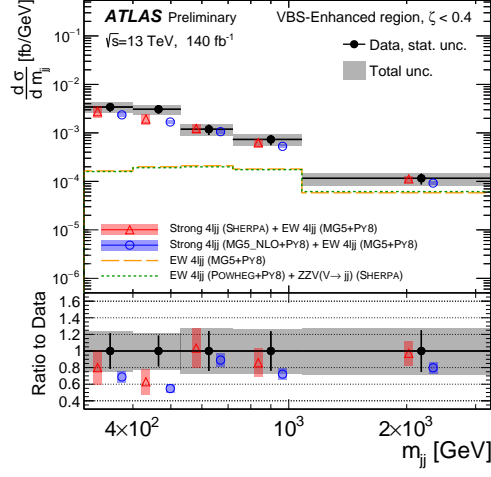
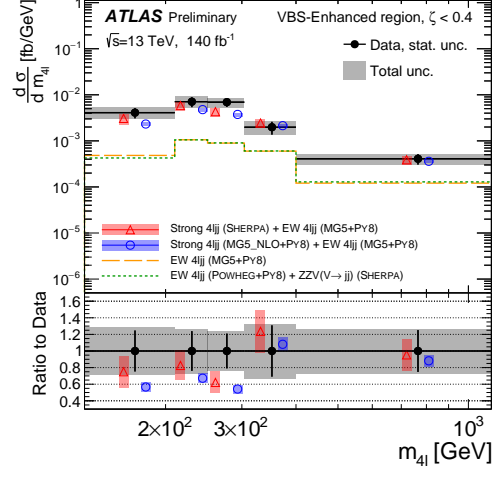
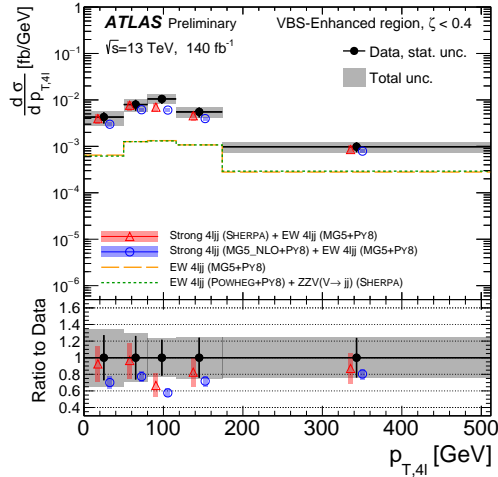
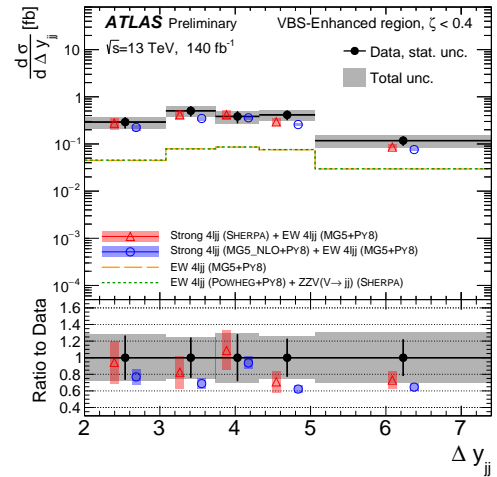
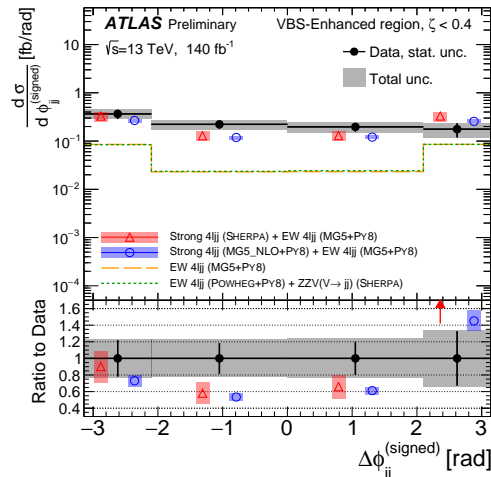
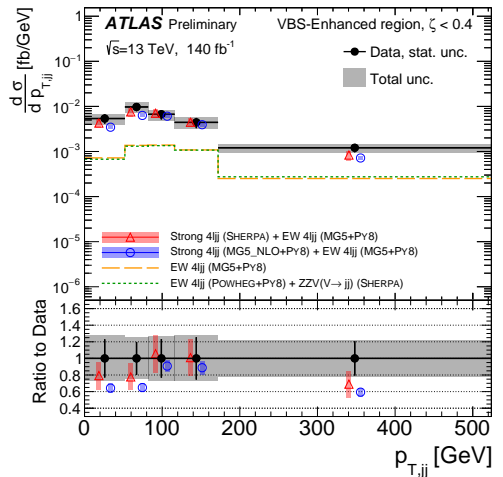


Figure 5.29.: Unfolded differential cross-sections from data (black) as a function of the different measured observables in the VBS-Suppressed region. All the unfolded distributions are obtained with two iterations. The error bars and grey hashed bands on the data points correspond respectively to the statistical and total. Fiducial-level predictions of the signal processes obtained with the SHERPA (MG5_NLO+PY8) strong $4\ell jj$ sample are displayed in red (blue). The pure EW $4\ell jj$ production is shown with an orange dashed line. Additionally, the predictions given by the alternative POWHEG+PY8 EW $4\ell jj$ production are also included for comparison and marked with a green dotted line. The alternative EW sample is missing the contribution from ZZV($\rightarrow jj$) production, which is estimated from SHERPA.

(a) m_{jj} (b) $m_{4\ell}$ (c) $p_{T,4\ell}$ (d) Δy_{jj} (e) $\Delta\phi_{jj}$ (f) $p_{T,jj}$

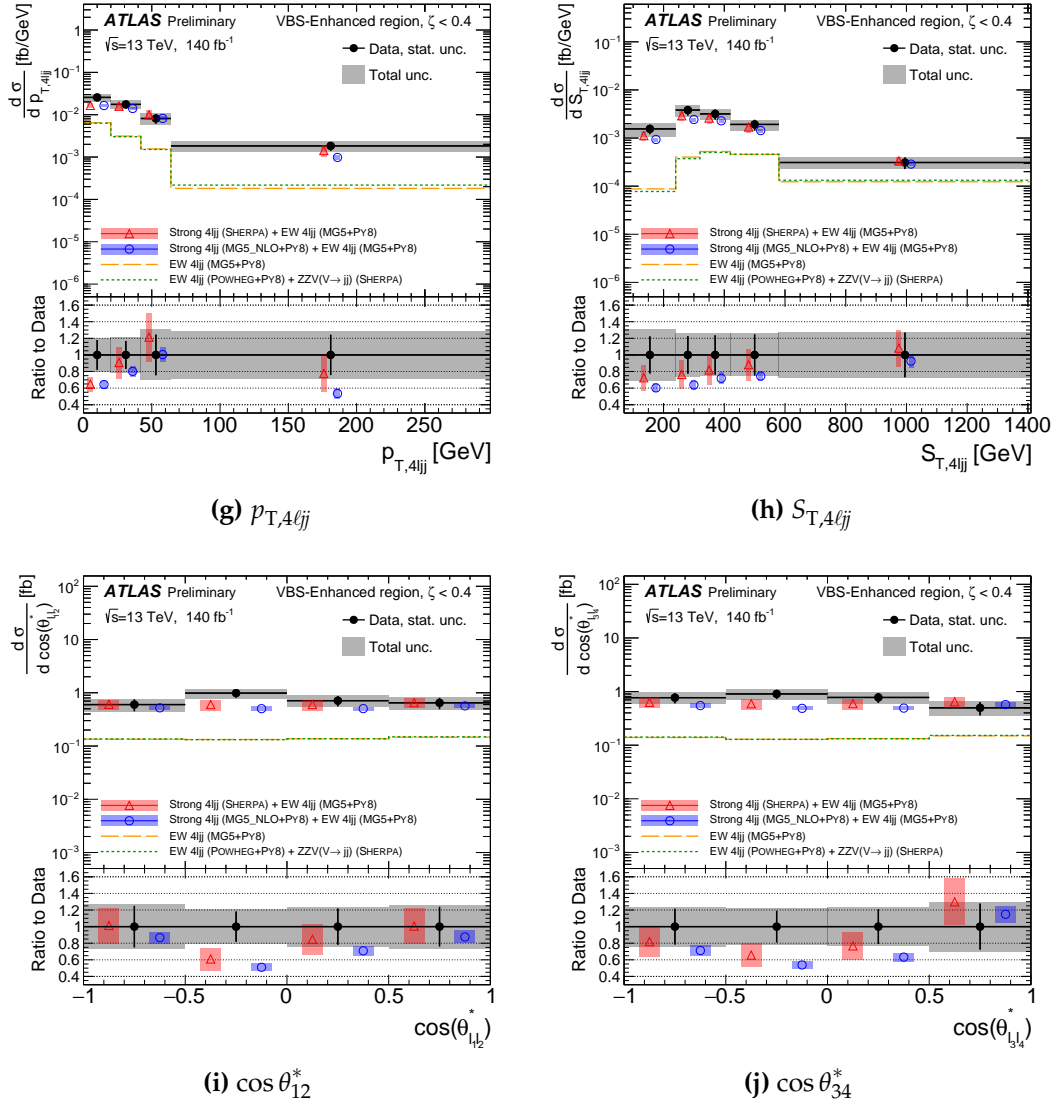


Figure 5.30.: Unfolded differential cross-sections from data (black) as a function of the different measured observables in the VBS-Enhanced region. All the unfolded distributions are obtained with two iterations, except for $p_{T,4\ell jj}$ (g), where three iterations were used. The error bars and grey hashed bands on the data points correspond respectively to the statistical and total. Fiducial-level predictions of the signal processes obtained with the SHERPA (MG5_NLO+Py8) strong $4\ell jj$ sample are displayed in red (blue). The pure EW $4\ell jj$ production is shown with an orange dashed line. Additionally, the predictions given by the alternative POWHEG+Py8 EW $4\ell jj$ production are also included for comparison and marked with a green dotted line. The alternative EW sample is missing the contribution from ZZV($\rightarrow jj$) production, which is estimated from SHERPA.

Wilson coefficient	$ \mathcal{M}_{d8} ^2$	95% confidence interval [TeV^{-4}]	
	Included	Expected	Observed
$f_{T,0}/\Lambda^4$	yes	[-1.00, 0.97]	[-0.98, 0.93]
	no	[-19, 19]	[-23, 17]
$f_{T,1}/\Lambda^4$	yes	[-1.3, 1.3]	[-1.2, 1.2]
	no	[-140, 140]	[-160, 120]
$f_{T,2}/\Lambda^4$	yes	[-2.6, 2.5]	[-2.5, 2.4]
	no	[-63, 62]	[-74, 56]
$f_{T,5}/\Lambda^4$	yes	[-2.6, 2.5]	[-2.5, 2.4]
	no	[-68, 67]	[-79, 60]
$f_{T,6}/\Lambda^4$	yes	[-4.1, 4.1]	[-3.9, 3.9]
	no	[-550, 540]	[-640, 480]
$f_{T,7}/\Lambda^4$	yes	[-8.8, 8.4]	[-8.5, 8.1]
	no	[-220, 220]	[-260, 200]
$f_{T,8}/\Lambda^4$	yes	[-2.2, 2.2]	[-2.1, 2.1]
	no	$[-3.9, 3.8] \times 10^4$	$[-4.6, 3.1] \times 10^4$
$f_{T,9}/\Lambda^4$	yes	[-4.7, 4.7]	[-4.5, 4.5]
	no	$[-6.4, 6.3] \times 10^4$	$[-7.5, 5.5] \times 10^4$

Table 5.11.: Expected and observed 95% confidence interval for several Wilson coefficients of dimension-8 EFT operators. Limits are provided when including the quadratic pure EFT contribution to the SM predictions. The results are evaluated from the combined $m_{jj} + m_{4\ell}$ distribution in the VBS-Enhanced region.

Blank Page

Chapter 6.

Conclusions

The thermal characterisation of several ITk pixel outer end-caps local support prototypes was presented. The measurements were carried out by recording infrared thermal images of the subject under study during a cooling process to assess its thermal performance. In particular, a controlled environment allowed to simulate the foreseen workload during the detector operation. The thermal performance was evaluated with a *Python*-based analysis framework which employs pattern recognition algorithms. The measurement and analysis methods were optimised for their employment in the Quality Control procedure during the production chain of the local supports. The temperature of the local support surface corresponding to a position perpendicular to the embedded pipe (T_{pipe}) was observed to be an observable sensitive to structural defects. This was proven by the measurements carried out on a prototype with intentionally implanted defects, which were successfully identified.

Measurements obtained with three prototypes were reported, including two different Layer-3 and one Layer-2 Half-Rings. The T_{pipe} distributions showed, in large part, the expected behaviour of a nearly-linear increment of temperature from the inlet position to the outlet position. Some peaks were observed in the distributions that hint at zones of poorer cooling capabilities, the largest of which reaches an amplitude of about 1 °C. The Layer-3 prototypes underwent a series of stress tests to evaluate their resistance to extreme temperature and pressure. Such tests were performed in several steps, alternating measurements of their thermal performance. These showed no worsening of the prototypes' cooling capabilities, up to a cumulative value of 100 thermal and 100 pressure cycles, except for one of the observed peaks in prototype L3.4, which increased in

amplitude after the stress tests. The results of the infrared measurements were compared to complementary measurements of the Thermal Figure of Merit, which confirmed a worsening of the thermal performance around the peak area. Despite the slight worsening, all the measured TFM values were below the thresholds imposed by the detector requirements, proving the robustness of the local support design. Only the (intentional) defective region mentioned above was found to be incompatible with the requirements, but still in a regime which would not cause compromising damage to the pixel sensors. The correlation of infrared and TFM measurements in this particular region will be used as a reference to identify faulty local supports in the production chain.

Unfolded differential cross-sections for the $pp \rightarrow 4\ell jj$ process were measured with 140 fb^{-1} of collision data recorded by the ATLAS experiment at a centre-of-mass energy of $\sqrt{s} = 13 \text{ TeV}$. The measurement complements the previous ATLAS observation of EW $ZZjj$ production, exploring two phase space regions characterised by an enhanced contribution from events originating respectively from strong and EW interactions. The fiducial volume was defined by a lepton quadruplet containing two SFOC e^+e^- or $\mu^+\mu^-$ pairs and two highly energetic jets separated by a rapidity gap of $|\Delta y_{jj}| > 2$. Two signal regions, VBS-Enhanced and VBS-Suppressed, were defined using the centrality of the $4\ell jj$ system, with a larger contribution from VBS-like events at small centrality values. Reducible prompt background stemming from $t\bar{t}Z$ and VVV production was evaluated from state-of-the-art ATLAS MC simulations and subtracted from the measured data. A data-driven technique was employed to evaluate background contributions from non-prompt leptons. A total event yield of $N_{\text{VBS-Enhanced}} = (169 \pm 13)$ and $N_{\text{VBS-Suppressed}} = (53 \pm 7)$ was observed in the two regions before background subtraction, which constitutes about 15% of the total events. Nearly 17% of the total events in the VBS-Enhanced region are expected to originate from the EW production.

Differential distributions were measured for ten observables describing the final state's kinematic properties and were then unfolded with an iterative Bayesian algorithm to extrapolate cross-section values at fiducial-level. The unfolding regularisation was optimised according to its combined effect on the statistical uncertainty and unfolding bias, resulting in two iterations used for most observables. The unfolding bias was estimated with a MC-based procedure and found to be typically below 10%. Systematic uncertainties were evaluated from simulations

and propagated through the unfolding procedure, with leading contributions deriving from JES and JER uncertainties. Average values of the total systematic uncertainty were found to be between 10% and 15%, with few isolated cases reaching around 20% (e.g. at small $p_{T,4\ell}$ and $S_{T,4\ell jj}$ values in the VBS-Enhanced region). A total of 20 unfolded differential cross-sections, 10 for each SR, were reported. As a function of the dijet invariant mass (m_{jj}) in the VBS-Enhanced region, the unfolded cross-section was measured to vary from

$$\sigma_{\text{VBS-Enhanced}}^{(\text{Unf})}(pp \rightarrow 4\ell jj)_{m_{jj} \text{ bin } 1} = 0.342 \pm 0.073 \text{ (stat.)} \pm 0.041 \text{ (syst.) fb}$$

in the first bin ($300 \text{ GeV} < m_{jj} < 400 \text{ GeV}$) down to

$$\sigma_{\text{VBS-Enhanced}}^{(\text{Unf})}(pp \rightarrow 4\ell jj)_{m_{jj} \text{ bin } 5} = 0.254 \pm 0.064 \text{ (stat.)} \pm 0.028 \text{ (syst.) fb}$$

in the last bin ($1.08 \text{ TeV} < m_{jj} < 3.28 \text{ TeV}$). The latter represents one of the bins most sensitive to the EW production, with a purity of about 40%. The unfolded cross-sections were compared with state-of-the-art particle-level predictions, showing a reasonable agreement considering the large uncertainties. Several MC generators were employed to compare different modelling of the processes. LO predictions of the EW production obtained from MG5+PY8 yielded very close results to NLO ones produced with POWHEG+PY8, resulting in negligible differences in the measured cross-sections. Differently, the modelling of strong $4\ell jj$ production provided respectively by SHERPA and MG5_NLO+PY8 showed significant differences among all the measured distributions. Overall, the SHERPA sample was found to better describe the unfolded data, while MG5_NLO+PY8 typically underestimates it. A possible cause for the discrepancy was attributed to the different modelling of high-multiplicity jet final states. In MG5_NLO+PY8, the additional partonic emission beyond one final-state jet is controlled only by the parton shower. At the same time, SHERPA has LO-accurate matrix elements for up to 3 jets in the final state.

The measured cross-sections were also used to search for New Physics contributions in the form of anomalous weak boson self-interactions. A model-independent EFT approach was used to constrain the couplings of dimension-6 and dimension-8 operators through a simultaneous profile-likelihood fit to the combined m_{jj} and $m_{4\ell}$ unfolded distributions. A total of six operators in the Warsaw basis (dimension-6) and eight operators of the EboLi model (dimension-8)

were tested, and their coupling was found to be consistent with zero in all cases. The most stringent constraint was set to the dimension-8 $\mathcal{O}_{T,0}$ operator, with an observed 95% CL limit on its Wilson coefficient equal to $[-1.0, 0.97] \text{ TeV}^{-4}$.

The measurement presented in this thesis is currently limited by its statistical precision due to the rarity of the $4\ell jj$ production. The current LHC Run 3, and the future HL-LHC phase, will offer an opportunity to collect more data on this elusive process and further improve the precision of the measured cross-sections.

Appendix A.

Appendix

A.1. Additional plots of the $ZZjj$ cross-section measurement

This appendix contains additional plots related to the measurement of $ZZjj$ cross-section described in chapter 5. Figures A.1 to A.4 show the measured distribution in the VBS-Enhanced and VBS-Suppressed regions respectively for the Δy_{jj} , $p_{T,jj}$, $\cos \theta_{34}^*$ and $p_{T,4\ell jj}$ observables. Migration matrices for $p_{T,4\ell}$, $\Delta \phi_{jj}$, Δy_{jj} , $p_{T,jj}$, $\cos \theta_{12}^*$, $\cos \theta_{34}^*$, $p_{T,4\ell jj}$ and $S_{T,4\ell jj}$ are shown in figs. A.5 to A.12. Reconstruction efficiency, fiducial fraction, purity and stability for the above observable are also reported in figs. A.13 to A.20. Figures A.21 to A.28 show a breakdown of the unfolded-level uncertainties, again for the same observables mentioned before.

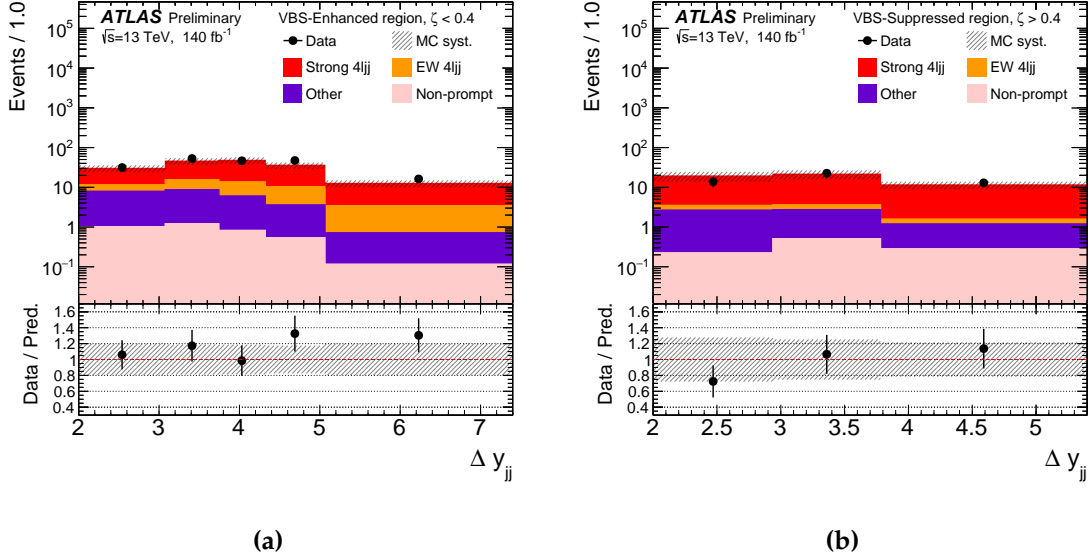


Figure A.1.: Comparison of the measured Δy_{jj} distribution from the data (black) and the prediction in the VBS-Enhanced (left) and VBS-Suppressed (right) regions. The SHERPA strong 4 ℓjj prediction is shown in red, while the MG5+PY8 EW 4 ℓjj is in orange. The prompt and non-prompt backgrounds are illustrated respectively in violet and pink. The total uncertainty of the prediction is drawn with a dashed band.

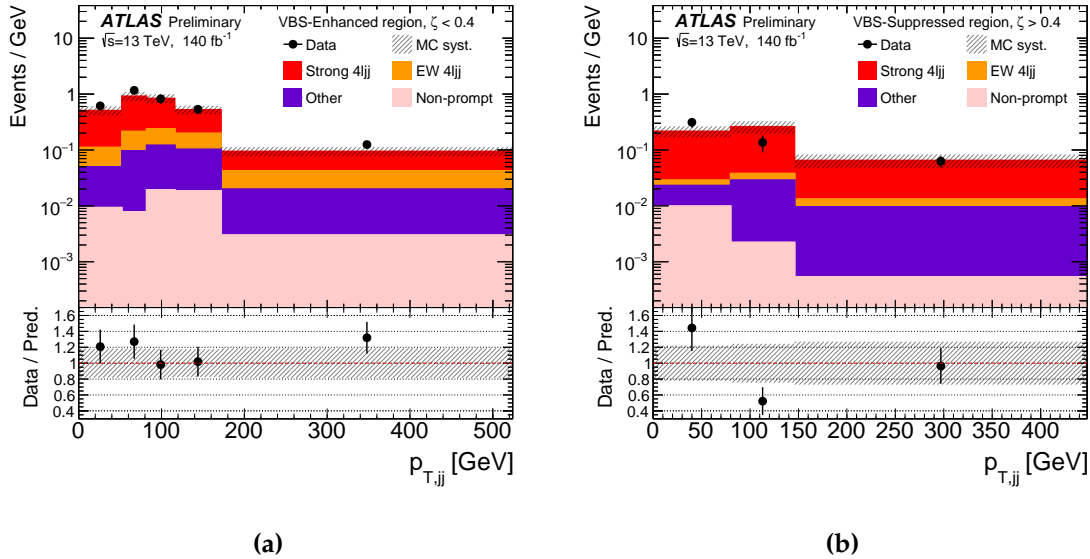


Figure A.2.: Comparison of the measured $p_{T,jj}$ distribution from the data (black) and the prediction in the VBS-Enhanced (left) and VBS-Suppressed (right) regions. The SHERPA strong 4 ℓjj prediction is shown in red, while the MG5+PY8 EW 4 ℓjj is in orange. The prompt and non-prompt backgrounds are illustrated respectively in violet and pink. The total uncertainty of the prediction is drawn with a dashed band.

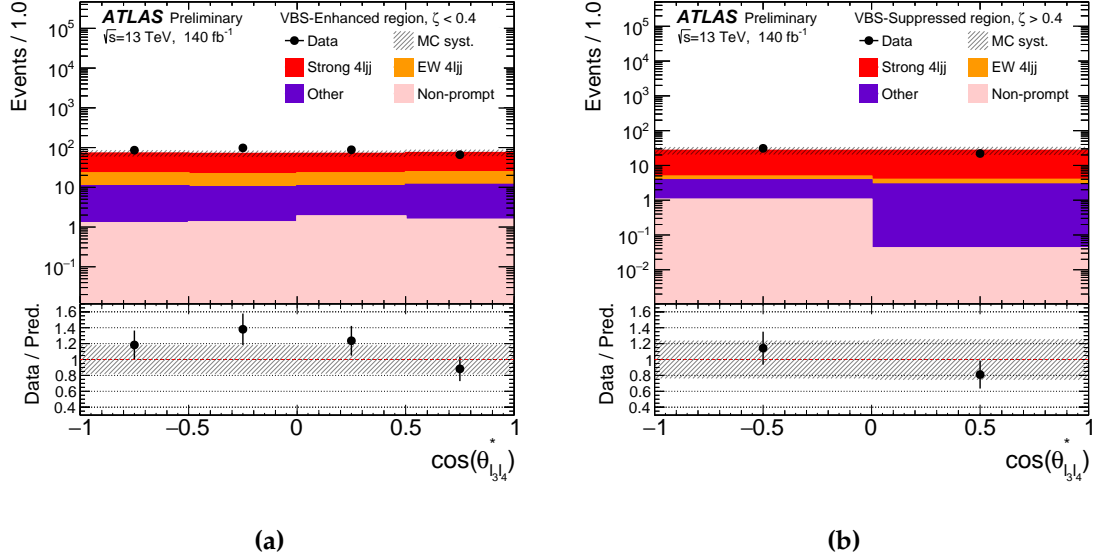


Figure A.3.: Comparison of the measured $\cos \theta_{34}^*$ distribution from the data (black) and the prediction in the VBS-Enhanced (left) and VBS-Suppressed (right) regions. The SHERPA strong $4\ell jj$ prediction is shown in red, while the MG5+PY8 EW $4\ell jj$ is in orange. The prompt and non-prompt backgrounds are illustrated respectively in violet and pink. The total uncertainty of the prediction is drawn with a dashed band.

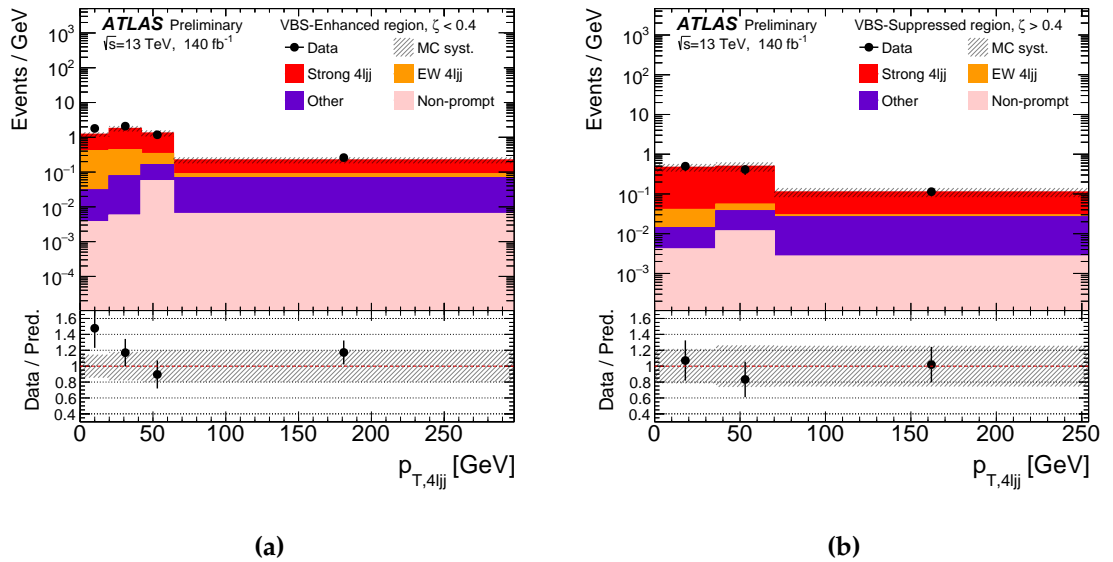


Figure A.4.: Comparison of the measured $p_{T,4\ell jj}$ distribution from the data (black) and the prediction in the VBS-Enhanced (left) and VBS-Suppressed (right) regions. The SHERPA strong $4\ell jj$ prediction is shown in red, while the MG5+PY8 EW $4\ell jj$ is in orange. The prompt and non-prompt backgrounds are illustrated respectively in violet and pink. The total uncertainty of the prediction is drawn with a dashed band.

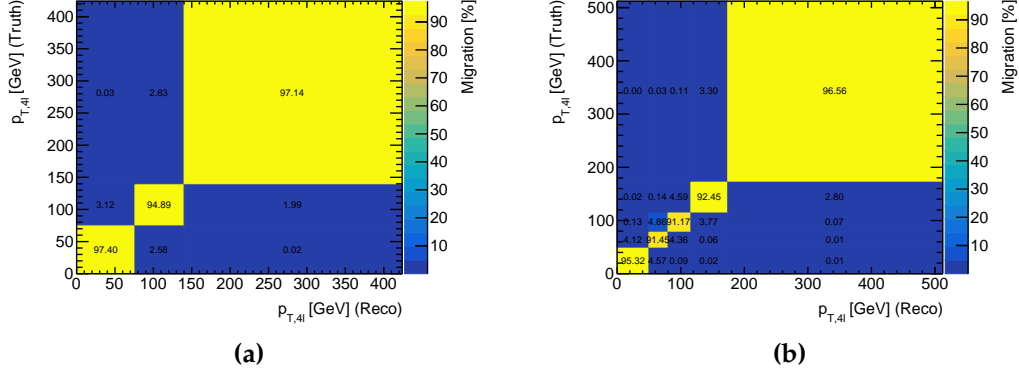


Figure A.5.: Migration matrices for $p_{T,4\ell}$ in the VBS-Suppressed (left) and VBS-Enhanced (right) regions. The bin values are normalized to the number of events in each truth bin.

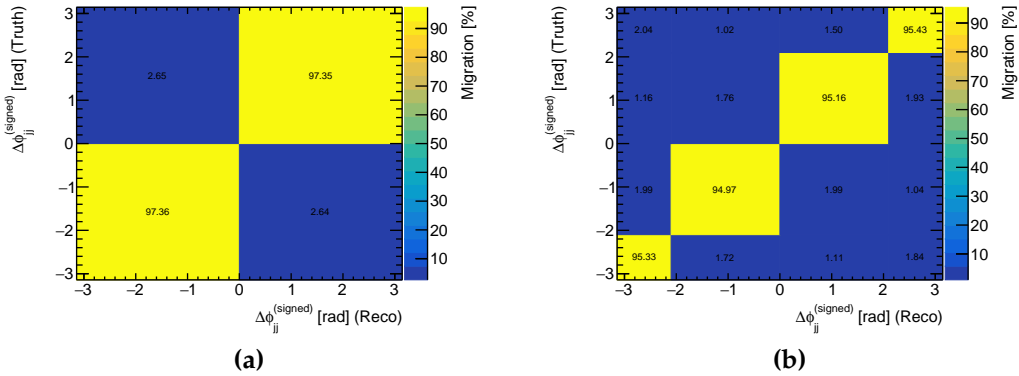


Figure A.6.: Migration matrices for $\Delta\phi_{jj}$ in the VBS-Suppressed (left) and VBS-Enhanced (right) regions. The bin values are normalized to the number of events in each truth bin.

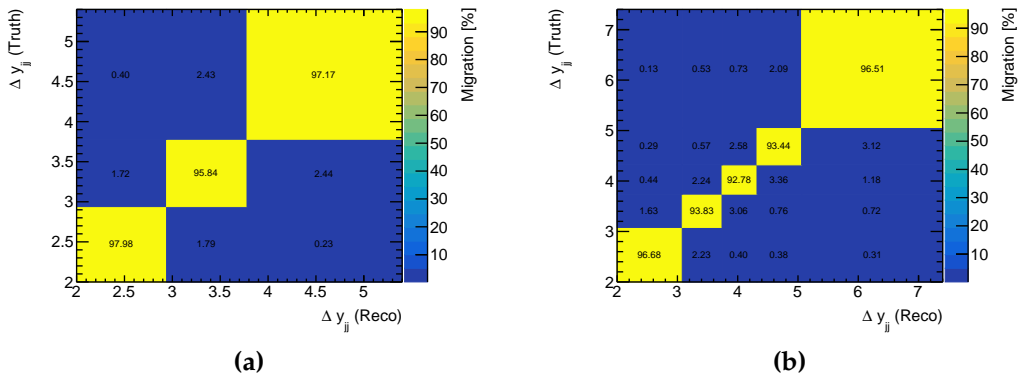


Figure A.7.: Migration matrices for Δy_{jj} in the VBS-Suppressed (left) and VBS-Enhanced (right) regions. The bin values are normalized to the number of events in each truth bin.

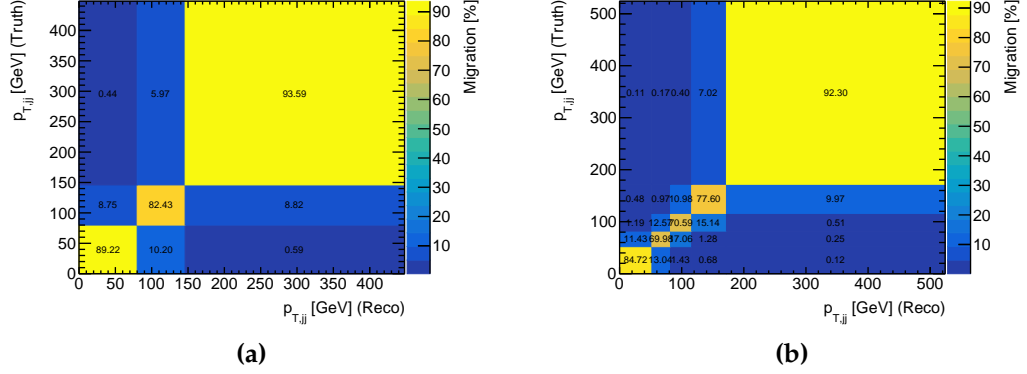


Figure A.8.: Migration matrices for $p_{T,jj}$ in the VBS-Suppressed (left) and VBS-Enhanced (right) regions. The bin values are normalized to the number of events in each truth bin.

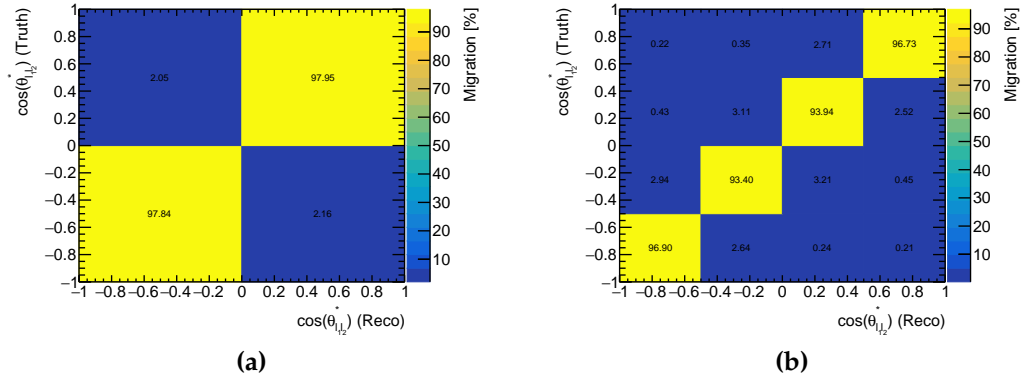


Figure A.9.: Migration matrices for $\cos \theta_{12}^*$ in the VBS-Suppressed (left) and VBS-Enhanced (right) regions. The bin values are normalized to the number of events in each truth bin.

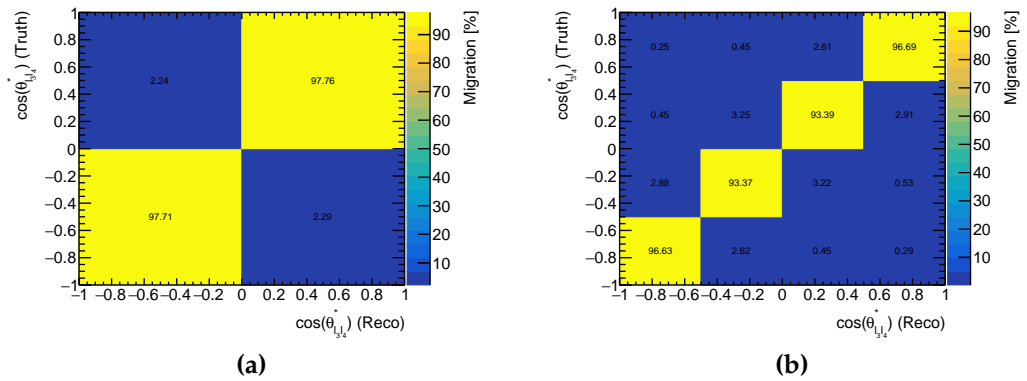


Figure A.10.: Migration matrices for $\cos \theta_{34}^*$ in the VBS-Suppressed (left) and VBS-Enhanced (right) regions. The bin values are normalized to the number of events in each truth bin.

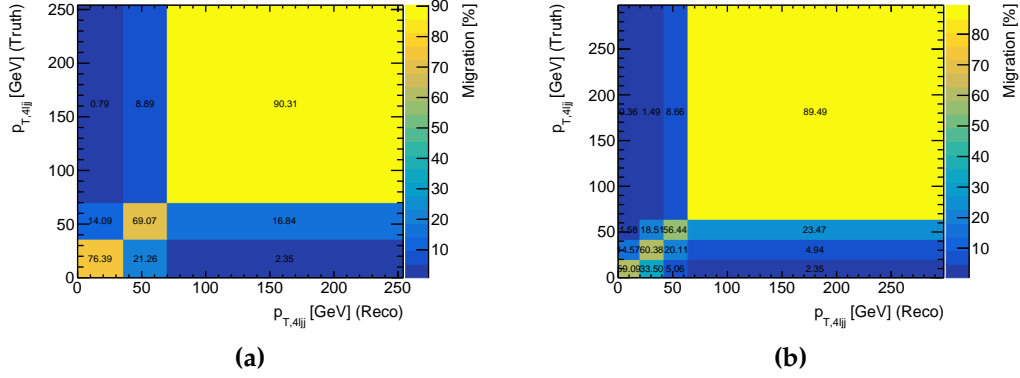


Figure A.11.: Migration matrices for $p_{T,4\ell j}$ in the VBS-Suppressed (left) and VBS-Enhanced (right) regions. The bin values are normalized to the number of events in each truth bin.

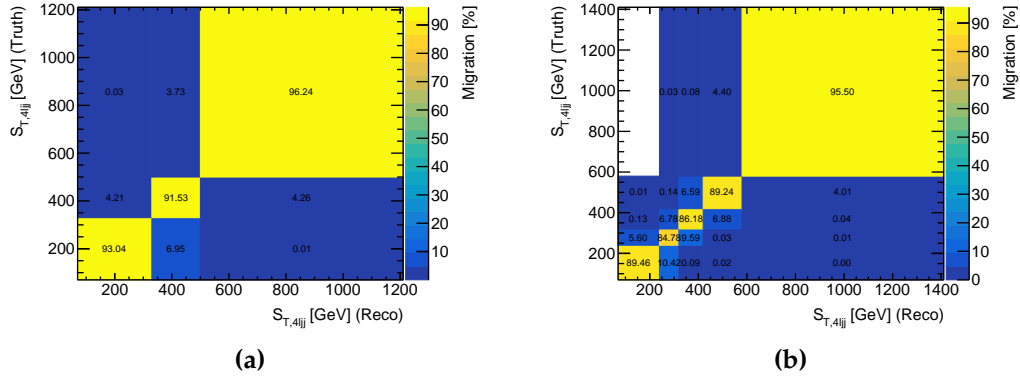


Figure A.12.: Migration matrices for $S_{T,4\ell j}$ in the VBS-Suppressed (left) and VBS-Enhanced (right) regions. The bin values are normalized to the number of events in each truth bin.

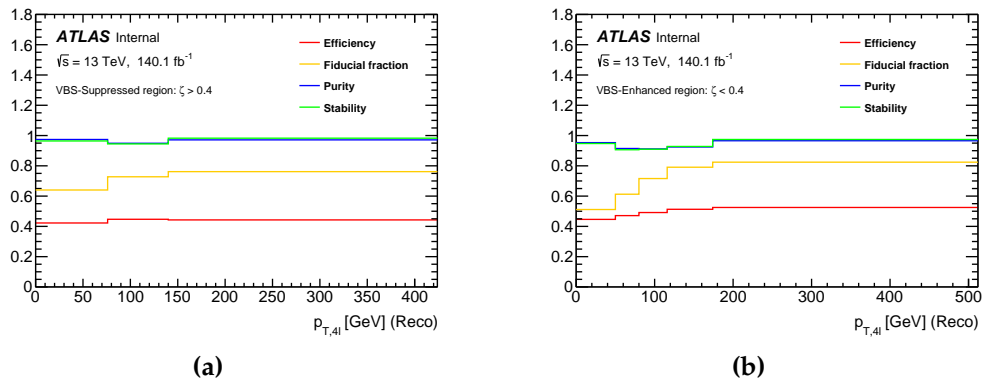


Figure A.13.: Reconstruction efficiency (red), fiducial fraction (yellow), purity (blue) and stability (green) for $p_{T,4\ell}$ in the VBS-Suppressed (left) and VBS-Enhanced (right) regions.

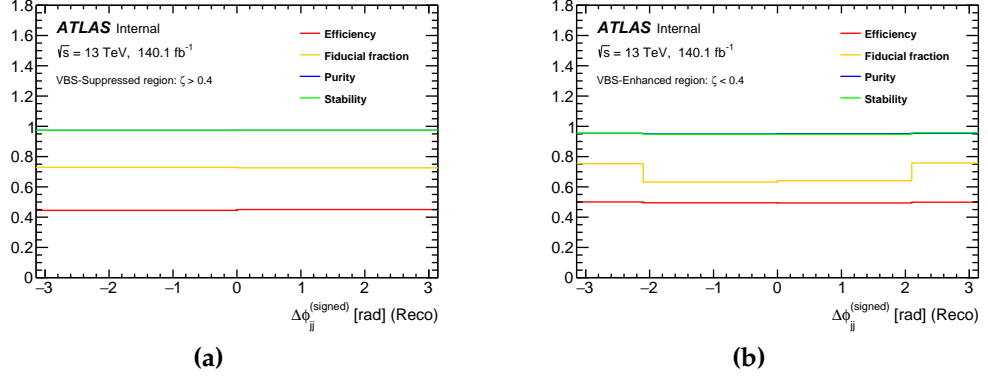


Figure A.14.: Reconstruction efficiency (red), fiducial fraction (yellow), purity (blue) and stability (green) for $\Delta\phi_{jj}$ in the VBS-Suppressed (left) and VBS-Enhanced (right) regions.

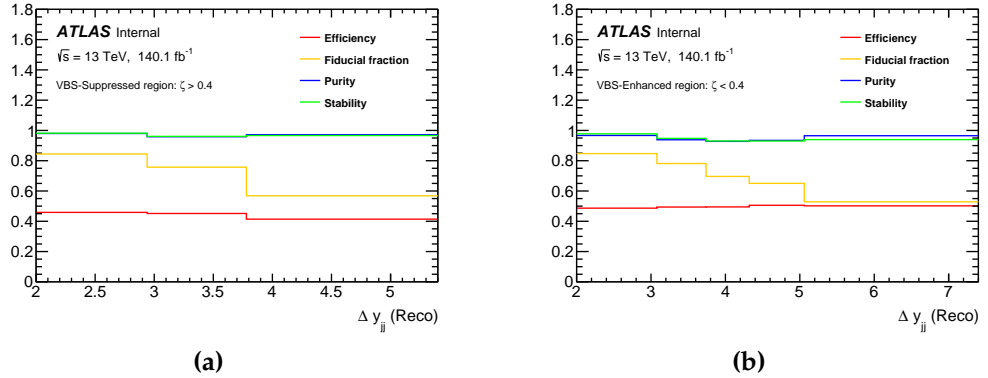


Figure A.15.: Reconstruction efficiency (red), fiducial fraction (yellow), purity (blue) and stability (green) for Δy_{jj} in the VBS-Suppressed (left) and VBS-Enhanced (right) regions.

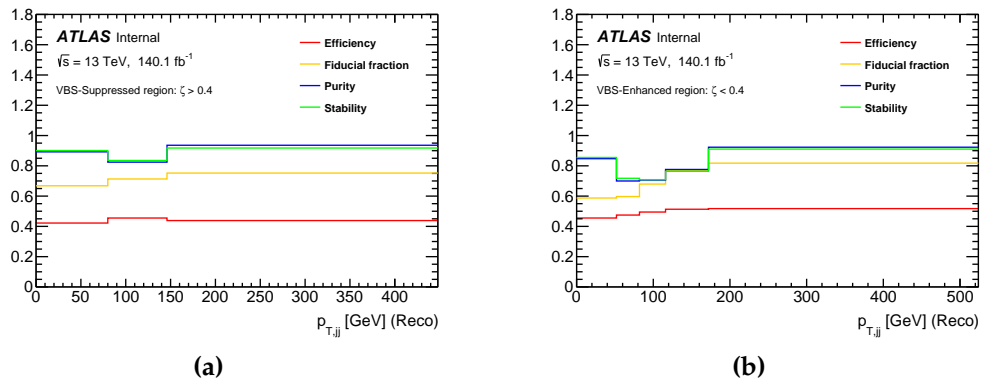


Figure A.16.: Reconstruction efficiency (red), fiducial fraction (yellow), purity (blue) and stability (green) for $p_{T,jj}$ in the VBS-Suppressed (left) and VBS-Enhanced (right) regions.

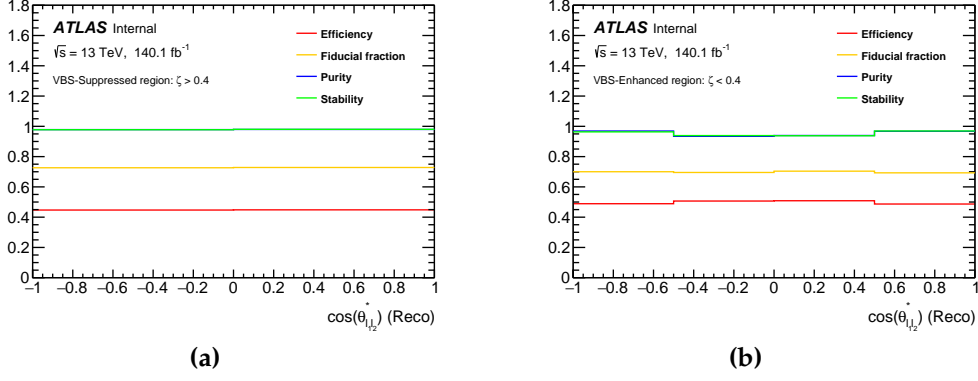


Figure A.17.: Reconstruction efficiency (red), fiducial fraction (yellow), purity (blue) and stability (green) for $\cos \theta_{12}^*$ in the VBS-Suppressed (left) and VBS-Enhanced (right) regions.

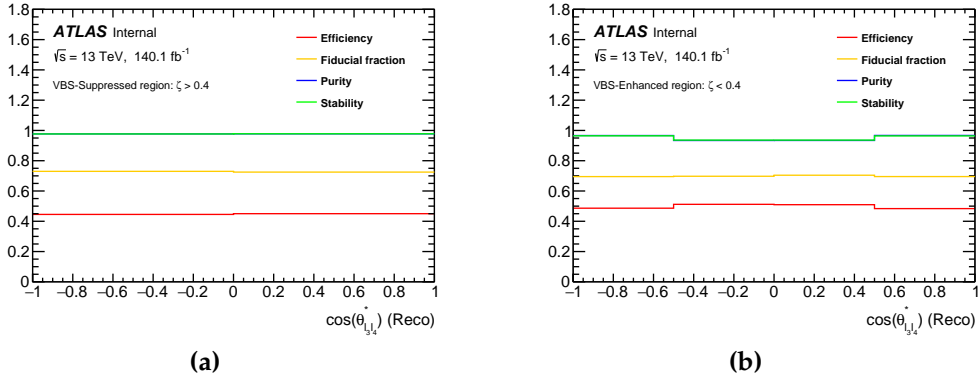


Figure A.18.: Reconstruction efficiency (red), fiducial fraction (yellow), purity (blue) and stability (green) for $\cos \theta_{34}^*$ in the VBS-Suppressed (left) and VBS-Enhanced (right) regions.

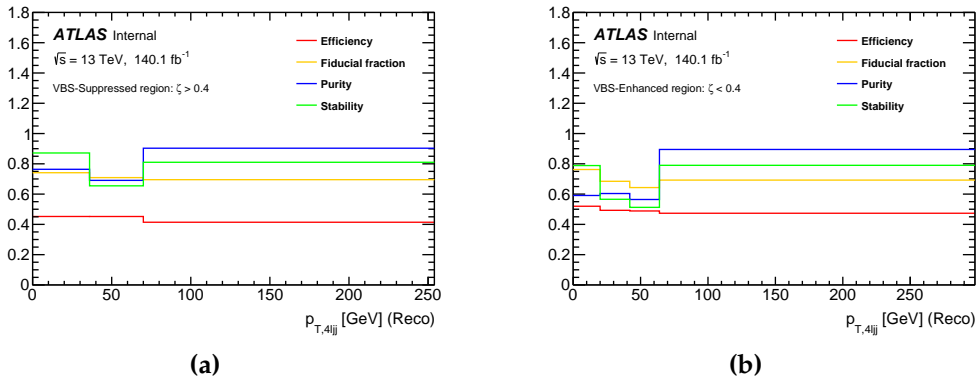


Figure A.19.: Reconstruction efficiency (red), fiducial fraction (yellow), purity (blue) and stability (green) for $p_{T,4ljj}$ in the VBS-Suppressed (left) and VBS-Enhanced (right) regions.

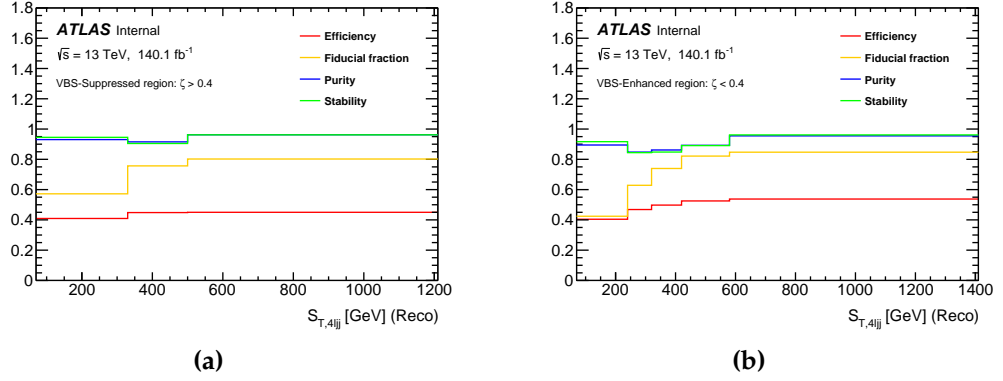


Figure A.20.: Reconstruction efficiency (red), fiducial fraction (yellow), purity (blue) and stability (green) for $S_{T,4\ell jj}$ in the VBS-Suppressed (left) and VBS-Enhanced (right) regions.

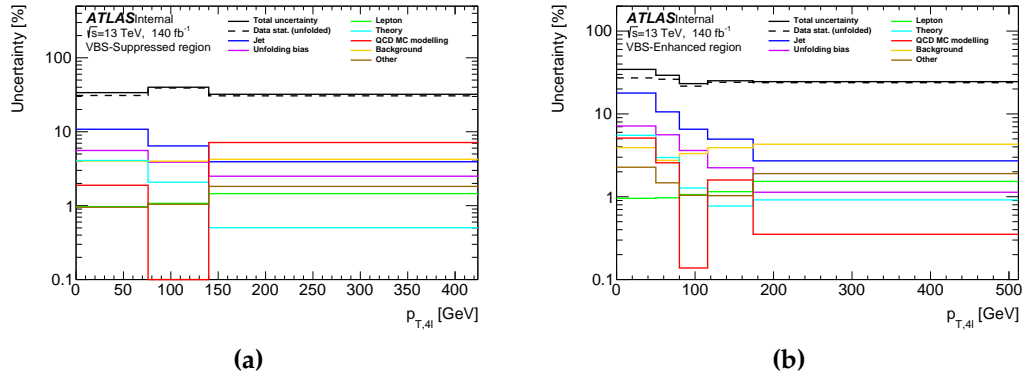


Figure A.21.: Different sources of uncertainties at unfolded-level as a function of $p_{T,4\ell}$ in the VBS-Suppressed (left) and VBS-Enhanced (right) regions. The total uncertainty is depicted with a continuous black line, while the statistical uncertainty is shown with a dashed line. The different colours represent the various sources of systematic uncertainties. The plots correspond to the unfolded values after two iterations.

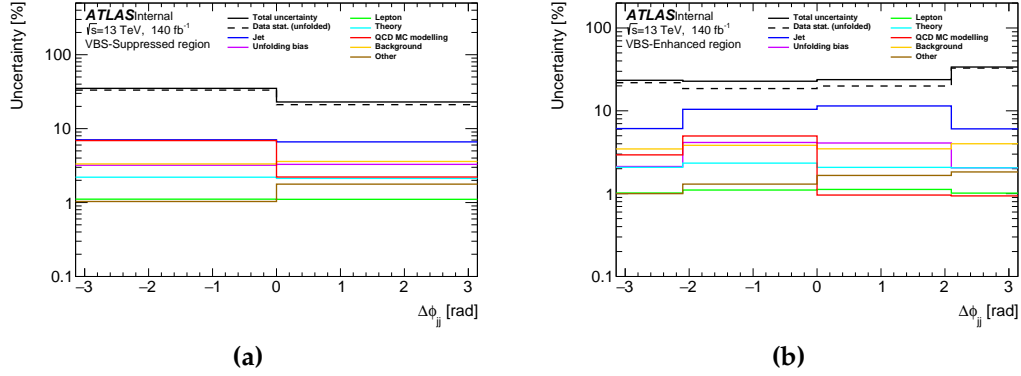


Figure A.22.: Different sources of uncertainties at unfolded-level as a function of $\Delta\phi_{jj}$ in the VBS-Suppressed (left) and VBS-Enhanced (right) regions. The total uncertainty is depicted with a continuous black line, while the statistical uncertainty is shown with a dashed line. The different colours represent the various sources of systematic uncertainties. The plots correspond to the unfolded values after two iterations.

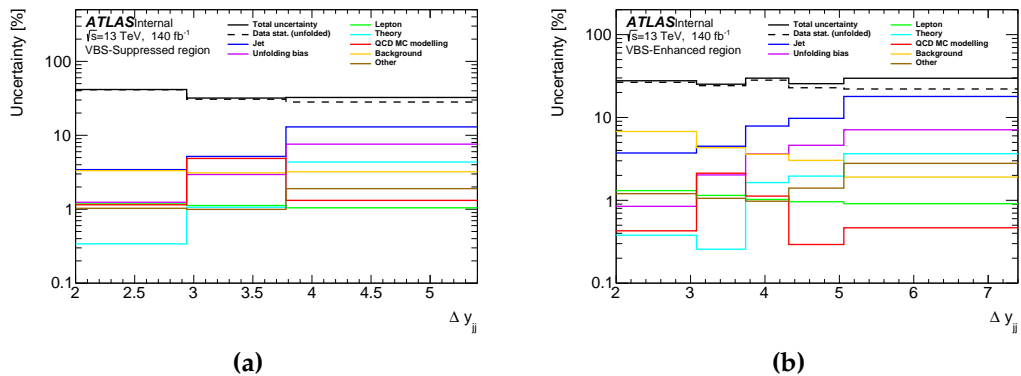


Figure A.23.: Different sources of uncertainties at unfolded-level as a function of Δy_{jj} in the VBS-Suppressed (left) and VBS-Enhanced (right) regions. The total uncertainty is depicted with a continuous black line, while the statistical uncertainty is shown with a dashed line. The different colours represent the various sources of systematic uncertainties. The plots correspond to the unfolded values after two iterations.

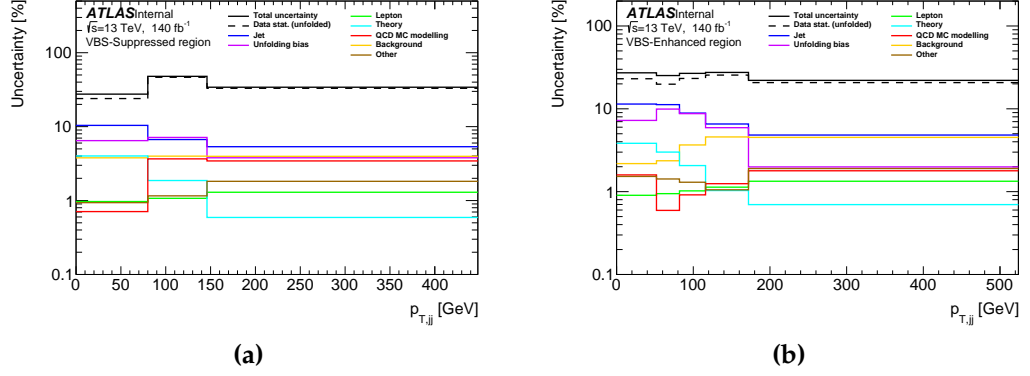


Figure A.24.: Different sources of uncertainties at unfolded-level as a function of $p_{T,jj}$ in the VBS-Suppressed (left) and VBS-Enhanced (right) regions. The total uncertainty is depicted with a continuous black line, while the statistical uncertainty is shown with a dashed line. The different colours represent the various sources of systematic uncertainties. The plots correspond to the unfolded values after two iterations.

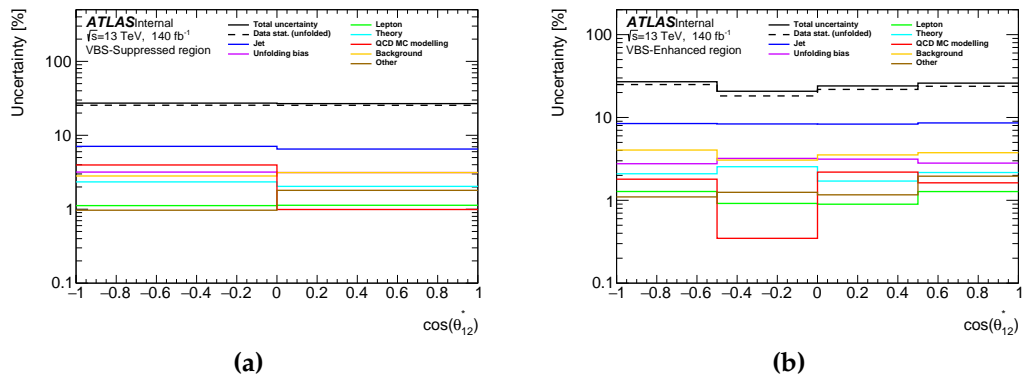


Figure A.25.: Different sources of uncertainties at unfolded-level as a function of $\cos \theta_{12}^*$ in the VBS-Suppressed (left) and VBS-Enhanced (right) regions. The total uncertainty is depicted with a continuous black line, while the statistical uncertainty is shown with a dashed line. The different colours represent the various sources of systematic uncertainties. The plots correspond to the unfolded values after two iterations.

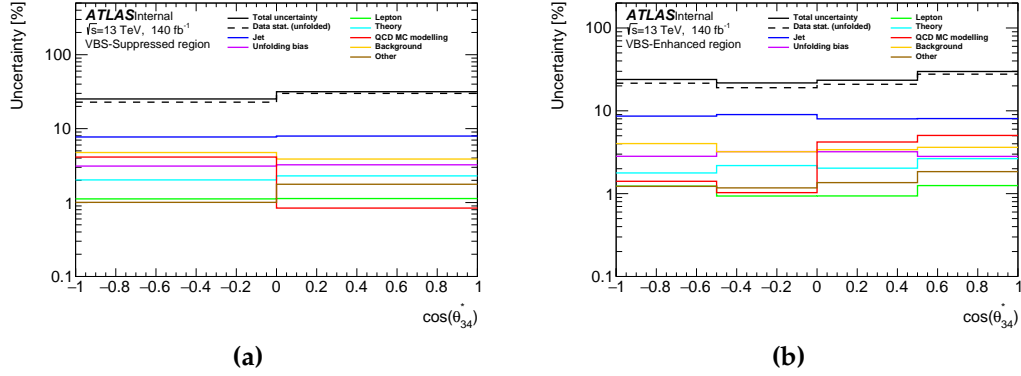


Figure A.26.: Different sources of uncertainties at unfolded-level as a function of $\cos \theta_{34}^*$ in the VBS-Suppressed (left) and VBS-Enhanced (right) regions. The total uncertainty is depicted with a continuous black line, while the statistical uncertainty is shown with a dashed line. The different colours represent the various sources of systematic uncertainties. The plots correspond to the unfolded values after two iterations.

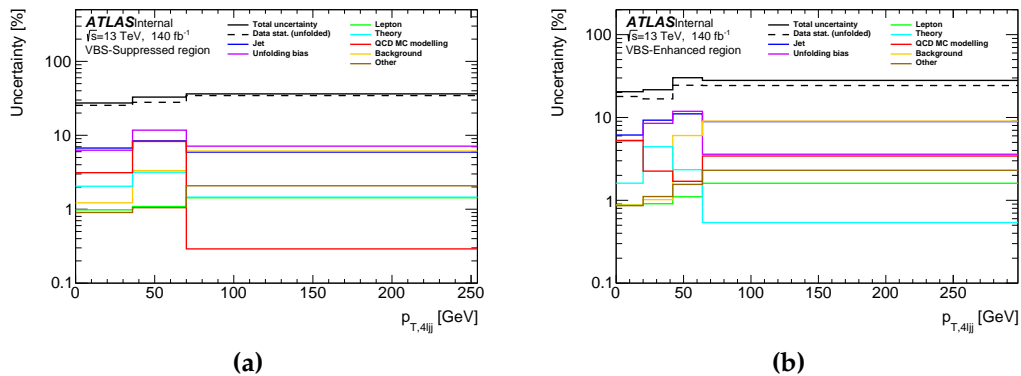


Figure A.27.: Different sources of uncertainties at unfolded-level as a function of $p_{T,4ljj}$ in the VBS-Suppressed (left) and VBS-Enhanced (right) regions. The total uncertainty is depicted with a continuous black line, while the statistical uncertainty is shown with a dashed line. The different colours represent the various sources of systematic uncertainties. The plots correspond to the unfolded values after three iterations.

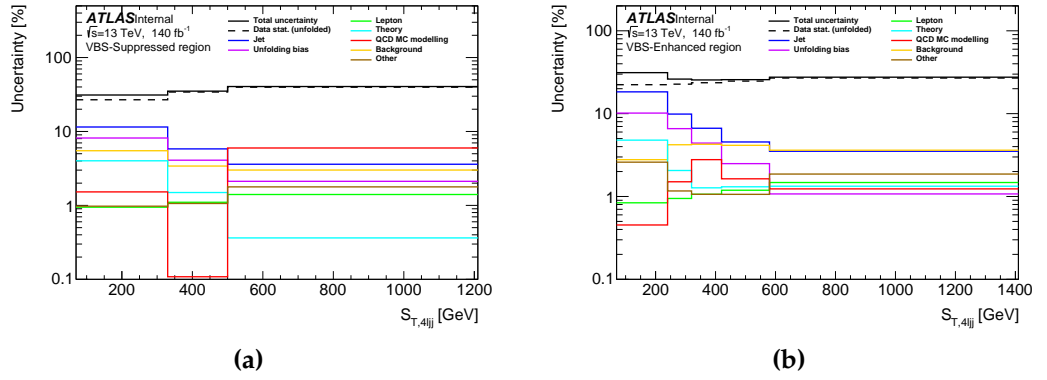


Figure A.28.: Different sources of uncertainties at unfolded-level as a function of $S_{T,4\ell jj}$ in the VBS-Suppressed (left) and VBS-Enhanced (right) regions. The total uncertainty is depicted with a continuous black line, while the statistical uncertainty is shown with a dashed line. The different colours represent the various sources of systematic uncertainties. The plots correspond to the unfolded values after two iterations.

Blank Page

Colophon

This thesis was made in $\text{\LaTeX} 2_{\epsilon}$ using the “hepthesis” class.

Blank Page

Bibliography

- [1] *Thermal characterisation of thermo-active support structures and its application in the ATLAS pixel outer endcap local supports*, tech. rep., CERN, 2021, URL: <https://cds.cern.ch/record/2752933> (cit. on pp. 27, 98, 101, 104, 107–112, 117–119).
- [2] *Differential cross-section measurements of the production of four charged leptons in association with two jets using the ATLAS detector*, tech. rep., CERN, 2023, URL: <https://cds.cern.ch/record/2859349> (cit. on pp. 27, 127).
- [3] Sheldon L. Glashow, *Partial-symmetries of weak interactions*, *Nuclear Physics* **22** (1961) 579, ISSN: 0029-5582, URL: <https://www.sciencedirect.com/science/article/pii/0029558261904692> (cit. on pp. 29, 44).
- [4] Steven Weinberg, *A Model of Leptons*, *Phys. Rev. Lett.* **19** (21 1967) 1264, URL: <https://link.aps.org/doi/10.1103/PhysRevLett.19.1264> (cit. on pp. 29, 44).
- [5] Abdus Salam, *Weak and Electromagnetic Interactions*, *Conf. Proc. C* **680519** (1968) 367 (cit. on pp. 29, 44).
- [6] Peter W. Higgs, *Broken Symmetries and the Masses of Gauge Bosons*, *Phys. Rev. Lett.* **13** (16 1964) 508, URL: <https://link.aps.org/doi/10.1103/PhysRevLett.13.508> (cit. on pp. 29, 45).
- [7] G. S. Guralnik, C. R. Hagen, and T. W. B. Kibble, *Global Conservation Laws and Massless Particles*, *Phys. Rev. Lett.* **13** (20 1964) 585, URL: <https://link.aps.org/doi/10.1103/PhysRevLett.13.585> (cit. on pp. 29, 45).
- [8] F. Englert and R. Brout, *Broken Symmetry and the Mass of Gauge Vector Mesons*, *Phys. Rev. Lett.* **13** (9 1964) 321, URL: <https://link.aps.org/doi/10.1103/PhysRevLett.13.321> (cit. on pp. 29, 45).

- [9] ATLAS Collaboration, *Observation of a new particle in the search for the Standard Model Higgs boson with the ATLAS detector at the LHC*, *Physics Letters B* **716** (2012) 1, ISSN: 0370-2693, URL: <https://www.sciencedirect.com/science/article/pii/S037026931200857X> (cit. on pp. 29, 47).
- [10] CMS Collaboration, *Observation of a new boson at a mass of 125 GeV with the CMS experiment at the LHC*, *Physics Letters B* **716** (2012) 30, ISSN: 0370-2693 (cit. on pp. 29, 47).
- [11] G. Arnison et al., *Experimental observation of lepton pairs of invariant mass around 95 GeV/c² at the CERN SPS collider*, *Physics Letters B* **126** (1983) 398, ISSN: 0370-2693, URL: <https://www.sciencedirect.com/science/article/pii/0370269383901880> (cit. on p. 29).
- [12] P. Bagnaia et al., *Evidence for $Z^0 \rightarrow e^+e^-$ at the CERN $\bar{p}p$ Collider*, *Physics Letters B* **129** (1983) 130, ISSN: 0370-2693, URL: <https://www.sciencedirect.com/science/article/pii/037026938390744X> (cit. on p. 29).
- [13] Franz Mandl and Graham Shaw, *Quantum Field Theory*, en, 2nd ed., Wiley-Blackwell, 2007 (cit. on pp. 33, 36).
- [14] Michael E Peskin and Daniel V Schroeder, *An introduction to quantum field theory*, en, Westview Press, 1995 (cit. on p. 33).
- [15] Yorikiyo Nagashima, *Elementary particle physics: Elementary particle physics quantum field theory and particles volume 1*, en, Wiley-VCH Verlag, 2010 (cit. on pp. 33, 50).
- [16] Christoph Englert, *Quantum Field Theory*, <https://conference.ippp.dur.ac.uk/event/785/attachments/3688/4135/QFTnotes.pdf>, 2014 (cit. on pp. 33, 35).
- [17] R. L. Workman et al., *Review of Particle Physics*, *PTEP* **2022** (2022) 083C01 (cit. on pp. 37, 38, 128).
- [18] E. Noether, *Invariante Variationsprobleme*, ger, Nachrichten von der Gesellschaft der Wissenschaften zu Göttingen, Mathematisch-Physikalische Klasse **1918** (1918) 235, URL: <http://eudml.org/doc/59024> (cit. on p. 38).
- [19] David J. Gross and Frank Wilczek, *Ultraviolet Behavior of Non-Abelian Gauge Theories*, *Phys. Rev. Lett.* **30** (26 1973) 1343, URL: <https://link.aps.org/doi/10.1103/PhysRevLett.30.1343> (cit. on p. 42).

- [20] T. D. Lee and C. N. Yang, *Question of Parity Conservation in Weak Interactions*, *Phys. Rev.* **104** (1 1956) 254, URL: <https://link.aps.org/doi/10.1103/PhysRev.104.254> (cit. on p. 42).
- [21] C. S. Wu, E. Ambler, R. W. Hayward, D. D. Hoppes, and R. P. Hudson, *Experimental Test of Parity Conservation in Beta Decay*, *Phys. Rev.* **105** (4 1957) 1413, URL: <https://link.aps.org/doi/10.1103/PhysRev.105.1413> (cit. on p. 42).
- [22] Nicola Cabibbo, *Unitary Symmetry and Leptonic Decays*, *Phys. Rev. Lett.* **10** (12 1963) 531, URL: <https://link.aps.org/doi/10.1103/PhysRevLett.10.531> (cit. on p. 43).
- [23] Makoto Kobayashi and Toshihide Maskawa, *CP-Violation in the Renormalizable Theory of Weak Interaction*, *Progress of Theoretical Physics* **49** (1973) 652, ISSN: 0033-068X, eprint: <https://academic.oup.com/ptp/article-pdf/49/2/652/5257692/49-2-652.pdf>, URL: <https://doi.org/10.1143/PTP.49.652> (cit. on p. 43).
- [24] *Standard Model Summary Plots February 2022*, tech. rep., CERN, 2022, URL: <https://cds.cern.ch/record/2804061> (cit. on p. 49).
- [25] Super-Kamiokande Collaboration, *Evidence for Oscillation of Atmospheric Neutrinos*, *Phys. Rev. Lett.* **81** (8 1998) 1562, URL: <https://link.aps.org/doi/10.1103/PhysRevLett.81.1562> (cit. on p. 49).
- [26] SNO Collaboration, *Direct Evidence for Neutrino Flavor Transformation from Neutral-Current Interactions in the Sudbury Neutrino Observatory*, *Phys. Rev. Lett.* **89** (1 2002) 011301, URL: <https://link.aps.org/doi/10.1103/PhysRevLett.89.011301> (cit. on p. 49).
- [27] Andrei D Sakharov, *Violation of CP invariance, C asymmetry, and baryon asymmetry of the universe*, *Soviet Physics Uspekhi* **34** (1991) 392, URL: <https://dx.doi.org/10.1070/PU1991v034n05ABEH002497> (cit. on p. 50).
- [28] Richard D. Ball et al., *Parton distributions for the LHC run II*, *JHEP* **04** (2015) 040, arXiv: 1410.8849 [hep-ph] (cit. on pp. 51, 132–134, 170).
- [29] Sayipjamal Dulat et al., *New parton distribution functions from a global analysis of quantum chromodynamics*, *Phys. Rev. D* **93** (2016) 033006, arXiv: 1506.07443 [hep-ph] (cit. on pp. 51, 52, 170).

- [30] L. A. Harland-Lang, A. D. Martin, P. Motylinski, and R. S. Thorne, *Parton distributions in the LHC era: MMHT 2014 PDFs*, *Eur. Phys. J. C* **75** (2015) 204, arXiv: 1412.3989 [hep-ph] (cit. on pp. 51, 170).
- [31] Jon Butterworth et al., *PDF4LHC recommendations for LHC Run II*, *J. Phys. G* **43** (2016) 023001, arXiv: 1510.03865 [hep-ph] (cit. on pp. 51, 132, 170).
- [32] V. N. Gribov and L. N. Lipatov, *Deep inelastic $e p$ scattering in perturbation theory*, *Sov. J. Nucl. Phys.* **15** (1972) 438 (cit. on p. 51).
- [33] V. N. Gribov and L. N. Lipatov, *$e^+ e^-$ pair annihilation and deep inelastic $e p$ scattering in perturbation theory*, *Sov. J. Nucl. Phys.* **15** (1972) 675 (cit. on p. 51).
- [34] Guido Altarelli and G. Parisi, *Asymptotic Freedom in Parton Language*, *Nucl. Phys. B* **126** (1977) 298 (cit. on p. 51).
- [35] Yuri L. Dokshitzer, *Calculation of the Structure Functions for Deep Inelastic Scattering and $e^+ e^-$ Annihilation by Perturbation Theory in Quantum Chromodynamics.*, *Sov. Phys. JETP* **46** (1977) 641 (cit. on p. 51).
- [36] J C Collins and D E Soper, *The Theorems of Perturbative QCD*, *Annual Review of Nuclear and Particle Science* **37** (1987) 383, eprint: <https://doi.org/10.1146/annurev.ns.37.120187.002123>, URL: <https://doi.org/10.1146/annurev.ns.37.120187.002123> (cit. on p. 52).
- [37] Andy Buckley et al., *General-purpose event generators for LHC physics*, *Physics Reports* **504** (2011) 145, URL: <https://doi.org/10.1016%2Fj.physrep.2011.03.005> (cit. on pp. 54, 59).
- [38] Stefan Höche, *Introduction to parton-shower event generators*, 2015, arXiv: 1411.4085 [hep-ph] (cit. on p. 55).
- [39] D.R Yennie, S.C Frautschi, and H Suura, *The infrared divergence phenomena and high-energy processes*, *Annals of Physics* **13** (1961) 379, ISSN: 0003-4916, URL: <https://www.sciencedirect.com/science/article/pii/0003491661901518> (cit. on p. 55).
- [40] Torbjörn Sjöstrand and Maria van Zijl, *A multiple-interaction model for the event structure in hadron collisions*, *Phys. Rev. D* **36** (7 1987) 2019, URL: <https://link.aps.org/doi/10.1103/PhysRevD.36.2019> (cit. on p. 56).

- [41] B. Andersson, G. Gustafson, G. Ingelman, and T. Sjöstrand, *Parton fragmentation and string dynamics*, **Physics Reports** **97** (1983) 31, ISSN: 0370-1573, URL: <https://www.sciencedirect.com/science/article/pii/0370157383900807> (cit. on p. 57).
- [42] Bo Andersson, *The Lund Model*, Cambridge Monographs on Particle Physics, Nuclear Physics and Cosmology, Cambridge University Press, 1998 (cit. on p. 57).
- [43] B.R. Webber, *A QCD model for jet fragmentation including soft gluon interference*, **Nuclear Physics B** **238** (1984) 492, ISSN: 0550-3213, URL: <https://www.sciencedirect.com/science/article/pii/055032138490333X> (cit. on p. 57).
- [44] J.-C. Winter, F. Krauss, and G. Soff, *A modified cluster-hadronisation model*, **The European Physical Journal C** **36** (2004) 381, URL: <https://doi.org/10.1140/2Fepjc%2Fs2004-01960-8> (cit. on p. 57).
- [45] Yorikiyo Nagashima, *Elementary particle physics: Foundations of the Standard Model volume 2*, en, Wiley-VCH Verlag, 2013 (cit. on p. 57).
- [46] D. Amati and G. Veneziano, *Preconfinement as a property of perturbative QCD*, **Physics Letters B** **83** (1979) 87, ISSN: 0370-2693, URL: <https://www.sciencedirect.com/science/article/pii/0370269379908967> (cit. on p. 58).
- [47] A. Bassetto, M. Ciafaloni, and G. Marchesini, *Inelastic distributions and color structure in perturbative QCD*, **Nuclear Physics B** **163** (1980) 477, ISSN: 0550-3213, URL: <https://www.sciencedirect.com/science/article/pii/0550321380904137> (cit. on p. 58).
- [48] G. Marchesini, L. Trentadue, and G. Veneziano, *Space-time description of colour screening via jet calculus techniques*, **Nuclear Physics B** **181** (1981) 335, ISSN: 0550-3213, URL: <https://www.sciencedirect.com/science/article/pii/0550321381903576> (cit. on p. 58).
- [49] Stefano Frixione and Bryan R. Webber, *Matching NLO QCD computations and parton shower simulations*, **JHEP** **06** (2002) 029, arXiv: [hep-ph/0204244](https://arxiv.org/abs/hep-ph/0204244) (cit. on p. 58).
- [50] Paolo Nason, *A new method for combining NLO QCD with shower Monte Carlo algorithms*, **JHEP** **11** (2004) 040, arXiv: [hep-ph/0409146](https://arxiv.org/abs/hep-ph/0409146) (cit. on pp. 58, 59, 133).

- [51] Stefano Frixione, Paolo Nason, and Carlo Oleari, *Matching NLO QCD computations with parton shower simulations: the POWHEG method*, [JHEP 11 \(2007\) 070](#), arXiv: [0709.2092 \[hep-ph\]](#) (cit. on pp. [58](#), [59](#), [133](#)).
- [52] S. Catani, F. Krauss, B. R. Webber, and R. Kuhn, *QCD Matrix Elements + Parton Showers*, [JHEP 11 \(2001\) 063](#), arXiv: [hep-ph/0109231](#) (cit. on pp. [58](#), [132](#), [134](#)).
- [53] Stefan Höche, Frank Krauss, Steffen Schumann, and Frank Siegert, *QCD matrix elements and truncated showers*, [JHEP 05 \(2009\) 053](#), arXiv: [0903.1219 \[hep-ph\]](#) (cit. on pp. [58](#), [132](#), [134](#)).
- [54] Stefan Höche, Frank Krauss, Marek Schönherr, and Frank Siegert, *QCD matrix elements + parton showers. The NLO case*, [JHEP 04 \(2013\) 027](#), arXiv: [1207.5030 \[hep-ph\]](#) (cit. on pp. [58](#), [132](#)).
- [55] J. M. Campbell et al., *Event Generators for High-Energy Physics Experiments*, 2022, arXiv: [2203.11110 \[hep-ph\]](#) (cit. on p. [59](#)).
- [56] Enrico Bothmann et al., *Event generation with Sherpa 2.2*, [SciPost Phys. 7 \(2019\) 034](#), arXiv: [1905.09127 \[hep-ph\]](#) (cit. on pp. [59](#), [132](#), [134](#)).
- [57] Torbjörn Sjöstrand et al., *An introduction to PYTHIA 8.2*, [Comput. Phys. Commun. 191 \(2015\) 159](#), arXiv: [1410.3012 \[hep-ph\]](#) (cit. on pp. [59](#), [133](#)).
- [58] J. Alwall et al., *The automated computation of tree-level and next-to-leading order differential cross sections, and their matching to parton shower simulations*, [JHEP 07 \(2014\) 079](#), arXiv: [1405.0301 \[hep-ph\]](#) (cit. on pp. [59](#), [132](#), [133](#)).
- [59] Stefano Frixione, Giovanni Ridolfi, and Paolo Nason, *A positive-weight next-to-leading-order Monte Carlo for heavy flavour hadroproduction*, [JHEP 09 \(2007\) 126](#), arXiv: [0707.3088 \[hep-ph\]](#) (cit. on pp. [59](#), [133](#)).
- [60] Simone Alioli, Paolo Nason, Carlo Oleari, and Emanuele Re, *A general framework for implementing NLO calculations in shower Monte Carlo programs: the POWHEG BOX*, [JHEP 06 \(2010\) 043](#), arXiv: [1002.2581 \[hep-ph\]](#) (cit. on pp. [59](#), [133](#)).
- [61] T. Sjöstrand and P. Z. Skands, *Transverse-momentum-ordered showers and interleaved multiple interactions*, [The European Physical Journal C 39 \(2005\) 129](#), URL: <https://doi.org/10.1140/2Fepjc%2Fs2004-02084-y> (cit. on p. [59](#)).
- [62] Leif Lönnblad and Stefan Prestel, *Matching tree-level matrix elements with interleaved showers*, [JHEP 03 \(2012\) 019](#), arXiv: [1109.4829 \[hep-ph\]](#) (cit. on p. [59](#)).

- [63] Rikkert Frederix and Stefano Frixione, *Merging meets matching in MC@NLO*, [JHEP **12** \(2012\) 061](#), arXiv: [1209.6215 \[hep-ph\]](#) (cit. on pp. [59](#), [133](#)).
- [64] F. Krauss, R. Kuhn, and G. Soff, *AMEGIC++ 1.0: A Matrix element generator in C++*, [JHEP **02** \(2002\) 044](#), arXiv: [hep-ph/0109036](#) (cit. on p. [59](#)).
- [65] Tanju Gleisberg and Stefan Höche, *Comix, a new matrix element generator*, [Journal of High Energy Physics **2008** \(2008\) 039](#), URL: <https://doi.org/10.1088%2F1126-6708%2F2008%2F12%2F039> (cit. on p. [59](#)).
- [66] Tanju Gleisberg and Stefan Höche, *Comix, a new matrix element generator*, [JHEP **12** \(2008\) 039](#), arXiv: [0808.3674 \[hep-ph\]](#) (cit. on pp. [60](#), [132](#), [134](#)).
- [67] Steffen Schumann and Frank Krauss, *A parton shower algorithm based on Catani–Seymour dipole factorisation*, [JHEP **03** \(2008\) 038](#), arXiv: [0709.1027 \[hep-ph\]](#) (cit. on pp. [60](#), [132](#)).
- [68] Federico Buccioni et al., *OpenLoops 2*, [Eur. Phys. J. C **79** \(2019\) 866](#), arXiv: [1907.13071 \[hep-ph\]](#) (cit. on pp. [60](#), [132](#)).
- [69] Fabio Cascioli, Philipp Maierhöfer, and Stefano Pozzorini, *Scattering Amplitudes with Open Loops*, [Phys. Rev. Lett. **108** \(2012\) 111601](#), arXiv: [1111.5206 \[hep-ph\]](#) (cit. on pp. [60](#), [132](#)).
- [70] Ansgar Denner, Stefan Dittmaier, and Lars Hofer, *COLLIER: A fortran-based complex one-loop library in extended regularizations*, [Comput. Phys. Commun. **212** \(2017\) 220](#), arXiv: [1604.06792 \[hep-ph\]](#) (cit. on pp. [60](#), [132](#)).
- [71] Jan-Christopher Winter, Frank Krauss, and Gerhard Soff, *A modified cluster-hadronization model*, [Eur. Phys. J. C **36** \(2004\) 381](#), arXiv: [hep-ph/0311085](#) (cit. on p. [60](#)).
- [72] Johan Alwall, Michel Herquet, Fabio Maltoni, Olivier Mattelaer, and Tim Stelzer, *MadGraph 5 : Going Beyond*, [JHEP **06** \(2011\) 128](#), arXiv: [1106.0522 \[hep-ph\]](#) (cit. on p. [60](#)).
- [73] Adam Alloul, Neil D. Christensen, Céline Degrande, Claude Duhr, and Benjamin Fuks, *FeynRules 2.0 — A complete toolbox for tree-level phenomenology*, [Computer Physics Communications **185** \(2014\) 2250](#), URL: <https://doi.org/10.1016%2Fj.cpc.2014.04.012> (cit. on p. [60](#)).
- [74] Valentin Hirschi et al., *Automation of one-loop QCD computations*, [Journal of High Energy Physics **2011** \(2011\)](#), URL: <https://doi.org/10.1007%2Fjhep05%282011%29044> (cit. on p. [60](#)).

- [75] M. Bähr et al., *Herwig++ physics and manual*, *Eur. Phys. J. C* **58** (2008) 639, arXiv: 0803.0883 [hep-ph] (cit. on p. 60).
- [76] Johannes Bellm et al., *Herwig 7.0/Herwig++ 3.0 release note*, *Eur. Phys. J. C* **76** (2016) 196, arXiv: 1512.01178 [hep-ph] (cit. on p. 60).
- [77] R. Frederix, S. Frixione, S. Prestel, and P. Torrielli, *On the reduction of negative weights in MC@NLO-type matching procedures*, *Journal of High Energy Physics* **2020** (2020), URL: <https://doi.org/10.1007%2Fjhep07%282020%29238> (cit. on p. 60).
- [78] Barbara Jäger, Alexander Karlberg, and Giulia Zanderighi, *Electroweak ZZjj production in the Standard Model and beyond in the POWHEG-BOX V2*, *JHEP* **03** (2014) 141, arXiv: 1312.3252 [hep-ph] (cit. on pp. 61, 133).
- [79] A. Hrynevich, *ATLAS jet and missing energy reconstruction, calibration and performance in LHC Run-2*, *Journal of Instrumentation* **12** (2017) C06038, URL: <https://dx.doi.org/10.1088/1748-0221/12/06/C06038> (cit. on pp. 61, 90).
- [80] Oliver Sim Brüning et al., *LHC Design Report*, CERN Yellow Reports: Monographs, CERN, 2004, URL: <https://cds.cern.ch/record/782076> (cit. on pp. 63, 67).
- [81] Oliver Sim Brüning et al., *LHC Design Report*, CERN Yellow Reports: Monographs, CERN, 2004, URL: <http://cds.cern.ch/record/815187> (cit. on p. 63).
- [82] Michael Benedikt, Paul Collier, V Mertens, John Poole, and Karlheinz Schindl, *LHC Design Report*, CERN Yellow Reports: Monographs, CERN, 2004, URL: <http://cds.cern.ch/record/823808> (cit. on p. 63).
- [83] *LEP design report*, CERN, 1983, URL: <https://cds.cern.ch/record/98881> (cit. on p. 64).
- [84] *LEP design report*, CERN, 1984, URL: <https://cds.cern.ch/record/102083> (cit. on p. 64).
- [85] L Arnaudon et al., *Linac4 Technical Design Report*, tech. rep., CERN, 2006, URL: <https://cds.cern.ch/record/1004186> (cit. on p. 64).
- [86] Esma Mobs, *The CERN accelerator complex. Complexe des accélérateurs du CERN*, (2016), URL: <https://cds.cern.ch/record/2197559> (cit. on p. 64).

- [87] ATLAS Collaboration, *The ATLAS Experiment at the CERN Large Hadron Collider*, [JINST 3 \(2008\) S08003](#), Also published by CERN Geneva in 2010, URL: <https://cds.cern.ch/record/1129811> (cit. on pp. 65, 71, 75, 77).
- [88] S Chatrchyan et al., *The CMS experiment at the CERN LHC. The Compact Muon Solenoid experiment*, [JINST 3 \(2008\) S08004](#), Also published by CERN Geneva in 2010, URL: <https://cds.cern.ch/record/1129810> (cit. on p. 65).
- [89] A Augusto Alves et al., *The LHCb Detector at the LHC*, [JINST 3 \(2008\) S08005](#), Also published by CERN Geneva in 2010, URL: <http://cds.cern.ch/record/1129809> (cit. on p. 65).
- [90] K Aamodt et al., *The ALICE experiment at the CERN LHC. A Large Ion Collider Experiment*, [JINST 3 \(2008\) S08002](#), Also published by CERN Geneva in 2010, URL: <http://cds.cern.ch/record/1129812> (cit. on p. 65).
- [91] G Ruggiero et al., *The TOTEM Detector at LHC*, (2010), URL: <https://cds.cern.ch/record/1247067> (cit. on p. 66).
- [92] O Adriani et al., *The LHCf detector at the CERN Large Hadron Collider*, [JINST 3 \(2008\) S08006](#), URL: <http://cds.cern.ch/record/1129808> (cit. on p. 66).
- [93] James Pinfold et al., *Technical Design Report of the MoEDAL Experiment*, tech. rep., 2009, URL: <https://cds.cern.ch/record/1181486> (cit. on p. 66).
- [94] Henso Abreu et al., *The FASER Detector*, tech. rep., CERN, 2022, arXiv: 2207.11427, URL: <https://cds.cern.ch/record/2816452> (cit. on p. 66).
- [95] G. Acampora et al., *SND@LHC: The Scattering and Neutrino Detector at the LHC*, tech. rep., 2022, arXiv: 2210.02784, URL: <https://cds.cern.ch/record/2838901> (cit. on p. 66).
- [96] P. Grafström and W. Kozanecki, *Luminosity determination at proton colliders*, [Progress in Particle and Nuclear Physics 81 \(2015\) 97](#), ISSN: 0146-6410, URL: <https://www.sciencedirect.com/science/article/pii/S0146641014000878> (cit. on p. 67).
- [97] ATLAS Collaboration, *Improved luminosity determination in pp collisions at $\sqrt{s} = 7$ TeV using the ATLAS detector at the LHC*, [Eur. Phys. J. C 73 \(2013\) 2518](#), arXiv: 1302.4393 [hep-ex] (cit. on p. 67).
- [98] ATLAS Collaboration, *Luminosity determination in pp collisions at $\sqrt{s} = 13$ TeV using the ATLAS detector at the LHC*, 2022, URL: <https://arxiv.org/abs/2212.09379> (cit. on pp. 67, 68, 83, 130, 173).

- [99] ATLAS Collaboration, *Public ATLAS Luminosity Results for Run-2 of the LHC*, <https://twiki.cern.ch/twiki/bin/view/AtlasPublic/LuminosityPublicResultsRun2> (cit. on p. 68).
- [100] ATLAS Collaboration, *ATLAS central solenoid: Technical Design Report*, Technical design report. ATLAS, CERN, 1997, URL: <https://cds.cern.ch/record/331067> (cit. on p. 69).
- [101] ATLAS Collaboration, *ATLAS barrel toroid: Technical Design Report*, Technical design report. ATLAS, CERN, 1997, URL: <http://cds.cern.ch/record/331065> (cit. on p. 69).
- [102] ATLAS Collaboration, *ATLAS end-cap toroids: Technical Design Report*, Technical design report. ATLAS, CERN, 1997, URL: <http://cds.cern.ch/record/331066> (cit. on p. 69).
- [103] ATLAS Collaboration, *ATLAS inner detector: Technical Design Report, 1*, Technical design report. ATLAS, CERN, 1997, URL: <https://cds.cern.ch/record/331063> (cit. on p. 71).
- [104] ATLAS Collaboration, *ATLAS inner detector: Technical Design Report, 2*, Technical design report. ATLAS, CERN, 1997, URL: <https://cds.cern.ch/record/331064> (cit. on p. 71).
- [105] ATLAS Collaboration, *Alignment of the ATLAS Inner Detector in Run-2*, *Eur. Phys. J. C* **80** (2020) 1194, arXiv: 2007.07624, URL: <https://cds.cern.ch/record/2724037> (cit. on p. 72).
- [106] ATLAS Collaboration, *Study of the material of the ATLAS inner detector for Run 2 of the LHC. Study of the material of the ATLAS inner detector for Run 2 of the LHC*, *JINST* **12** (2017) P12009, arXiv: 1707.02826, URL: <https://cds.cern.ch/record/2273894> (cit. on p. 72).
- [107] ATLAS Collaboration, *ATLAS pixel detector: Technical Design Report*, Technical design report. ATLAS, CERN, 1998, URL: <https://cds.cern.ch/record/381263> (cit. on p. 72).
- [108] G Aad et al., *ATLAS pixel detector electronics and sensors*, *Journal of Instrumentation* **3** (2008) P07007, URL: <https://dx.doi.org/10.1088/1748-0221/3/07/P07007> (cit. on p. 73).
- [109] M Capeans et al., *ATLAS Insertable B-Layer Technical Design Report*, tech. rep., 2010, URL: <https://cds.cern.ch/record/1291633> (cit. on p. 73).

- [110] B. Abbott et al., *Production and integration of the ATLAS Insertable B-Layer*, *Journal of Instrumentation* (2018) T05008, URL: <https://doi.org/10.1088/1748-0221/13/05/T05008> (cit. on p. 73).
- [111] A. Abdesselam et al., *The barrel modules of the ATLAS semiconductor tracker*, *Nuclear Instruments and Methods in Physics Research Section A: Accelerators, Spectrometers, Detectors and Associated Equipment* **568** (2006) 642, ISSN: 0168-9002, URL: <https://www.sciencedirect.com/science/article/pii/S016890020601388X> (cit. on p. 73).
- [112] A. Abdesselam et al., *The ATLAS semiconductor tracker end-cap module*, *Nuclear Instruments and Methods in Physics Research Section A: Accelerators, Spectrometers, Detectors and Associated Equipment* **575** (2007) 353, ISSN: 0168-9002, URL: <https://www.sciencedirect.com/science/article/pii/S0168900207003270> (cit. on p. 73).
- [113] The ATLAS TRT collaboration et al., *The ATLAS Transition Radiation Tracker (TRT) proportional drift tube: design and performance*, *Journal of Instrumentation* **3** (2008) P02013, URL: <https://dx.doi.org/10.1088/1748-0221/3/02/P02013> (cit. on p. 73).
- [114] The ATLAS TRT collaboration et al., *The ATLAS TRT Barrel Detector*, *Journal of Instrumentation* **3** (2008) P02014, URL: <https://dx.doi.org/10.1088/1748-0221/3/02/P02014> (cit. on p. 73).
- [115] The ATLAS TRT collaboration et al., *The ATLAS TRT end-cap detectors*, *Journal of Instrumentation* **3** (2008) P10003, URL: <https://dx.doi.org/10.1088/1748-0221/3/10/P10003> (cit. on p. 73).
- [116] ATLAS Collaboration, *ATLAS liquid-argon calorimeter: Technical Design Report*, Technical design report. ATLAS, CERN, 1996, URL: <https://cds.cern.ch/record/331061> (cit. on pp. 74, 76, 77).
- [117] ATLAS Collaboration, *ATLAS tile calorimeter: Technical Design Report*, Technical design report. ATLAS, CERN, 1996, URL: <https://cds.cern.ch/record/331062> (cit. on p. 76).
- [118] A Artamonov et al., *The ATLAS Forward Calorimeter*, *Journal of Instrumentation* **3** (2008) P02010, URL: <https://dx.doi.org/10.1088/1748-0221/3/02/P02010> (cit. on p. 77).

- [119] ATLAS Collaboration, *ATLAS muon spectrometer: Technical Design Report*, Technical design report. ATLAS, CERN, 1997, URL: <https://cds.cern.ch/record/331068> (cit. on p. 78).
- [120] ATLAS Collaboration, *Performance of the ATLAS RPC detector and Level-1 muon barrel trigger at $\sqrt{s} = 13$ TeV*, *Journal of Instrumentation* **16** (2021) P07029, URL: <https://dx.doi.org/10.1088/1748-0221/16/07/P07029> (cit. on p. 80).
- [121] ATLAS Collaboration, *ATLAS level-1 trigger: Technical Design Report*, Technical design report. ATLAS, CERN, 1998, URL: <http://cds.cern.ch/record/381429> (cit. on p. 80).
- [122] Peter Jenni, Marzio Nessi, Markus Nordberg, and Kenway Smith, *ATLAS high-level trigger, data-acquisition and controls: Technical Design Report*, Technical design report. ATLAS, CERN, 2003, URL: <http://cds.cern.ch/record/616089> (cit. on p. 81).
- [123] The ATLAS TDAQ Collaboration, *The ATLAS Data Acquisition and High Level Trigger system*, *Journal of Instrumentation* **11** (2016) P06008, URL: <https://dx.doi.org/10.1088/1748-0221/11/06/P06008> (cit. on p. 81).
- [124] ATLAS Collaboration, *Trigger Menu in 2016*, tech. rep., CERN, 2017, URL: <https://cds.cern.ch/record/2242069> (cit. on pp. 81, 130).
- [125] ATLAS Collaboration, *Trigger Menu in 2017*, tech. rep., CERN, 2018, URL: <https://cds.cern.ch/record/2625986> (cit. on pp. 81, 130).
- [126] ATLAS Collaboration, *Trigger menu in 2018*, tech. rep., CERN, 2019, URL: <https://cds.cern.ch/record/2693402> (cit. on pp. 81, 130).
- [127] G. Avoni et al., *The new LUCID-2 detector for luminosity measurement and monitoring in ATLAS*, *Journal of Instrumentation* **13** (2018) P07017, URL: <https://dx.doi.org/10.1088/1748-0221/13/07/P07017> (cit. on p. 82).
- [128] Oleksandr Viazlo and ATLAS LUCID Collaboration, *ATLAS LUCID detector upgrade for LHC Run 2*, tech. rep., CERN, 2015, URL: <https://cds.cern.ch/record/2062038> (cit. on p. 82).
- [129] V Cindro et al., *The ATLAS Beam Conditions Monitor*, *Journal of Instrumentation* **3** (2008) P02004, URL: <https://dx.doi.org/10.1088/1748-0221/3/02/P02004> (cit. on p. 82).
- [130] S van der Meer, *Calibration of the effective beam height in the ISR*, tech. rep., CERN, 1968, URL: <https://cds.cern.ch/record/296752> (cit. on p. 83).

- [131] ATLAS Collaboration, *Performance of the ATLAS Track Reconstruction Algorithms in Dense Environments in LHC Run 2*, *Eur. Phys. J. C* **77** (2017) 673, arXiv: 1704.07983 [hep-ex] (cit. on p. 84).
- [132] R. Fruhwirth, *Application of Kalman filtering to track and vertex fitting*, *Nucl. Instrum. Meth. A* **262** (1987) 444 (cit. on p. 84).
- [133] T Cornelissen et al., *The new ATLAS track reconstruction (NEWT)*, *Journal of Physics: Conference Series* **119** (2008) 032014, URL: <https://dx.doi.org/10.1088/1742-6596/119/3/032014> (cit. on p. 84).
- [134] G Piacquadio, K Prokofiev, and A Wildauer, *Primary vertex reconstruction in the ATLAS experiment at LHC*, *Journal of Physics: Conference Series* **119** (2008) 032033, URL: <https://dx.doi.org/10.1088/1742-6596/119/3/032033> (cit. on p. 85).
- [135] ATLAS Collaboration, *Reconstruction of primary vertices at the ATLAS experiment in Run 1 proton–proton collisions at the LHC*, *The European Physical Journal C* **77** (2017), URL: <https://doi.org/10.1140%2Fepjc%2Fs10052-017-4887-5> (cit. on p. 85).
- [136] ATLAS Collaboration, *Electron and photon performance measurements with the ATLAS detector using the 2015–2017 LHC proton-proton collision data*, *Journal of Instrumentation* **14** (2019) P12006, URL: <https://dx.doi.org/10.1088/1748-0221/14/12/P12006> (cit. on pp. 86, 87, 136).
- [137] ATLAS Collaboration, *Improved electron reconstruction in ATLAS using the Gaussian Sum Filter-based model for bremsstrahlung*, tech. rep., CERN, 2012, URL: <https://cds.cern.ch/record/1449796> (cit. on p. 86).
- [138] ATLAS Collaboration, *Electron reconstruction and identification in the ATLAS experiment using the 2015 and 2016 LHC proton-proton collision data at $\sqrt{s} = 13$ TeV*, *The European Physical Journal C* **79** (2019), URL: <https://doi.org/10.1140%2Fepjc%2Fs10052-019-7140-6> (cit. on pp. 87, 135, 136).
- [139] ATLAS Collaboration, *Measurement of the photon identification efficiencies with the ATLAS detector using LHC Run 2 data collected in 2015 and 2016*, *The European Physical Journal C* **79** (2019), URL: <https://doi.org/10.1140%2Fepjc%2Fs10052-019-6650-6> (cit. on p. 87).

- [140] J. Illingworth and J. Kittler, *A survey of the hough transform*, *Computer Vision, Graphics, and Image Processing* **44** (1988) 87, ISSN: 0734-189X, URL: <https://www.sciencedirect.com/science/article/pii/S0734189X88800331> (cit. on p. 88).
- [141] ATLAS Collaboration, *Muon reconstruction and identification efficiency in ATLAS using the full Run 2 pp collision data set at $\sqrt{s} = 13$ TeV*, *The European Physical Journal C* **81** (2021), URL: <https://doi.org/10.1140/epjc/s10052-021-09233-2> (cit. on pp. 88, 89, 136).
- [142] ATLAS Collaboration, *Studies of the muon momentum calibration and performance of the ATLAS detector with pp collisions at $\sqrt{s}=13$ TeV*, (2022), arXiv: 2212.07338 [hep-ex] (cit. on p. 89).
- [143] ATLAS Collaboration, *Jet reconstruction and performance using particle flow with the ATLAS Detector*, *The European Physical Journal C* **77** (2017), URL: <https://doi.org/10.1140/2Fepjc%2Fs10052-017-5031-2> (cit. on p. 90).
- [144] ATLAS Collaboration, *Jet energy scale and resolution measured in proton-proton collisions at $\sqrt{s} = 13$ TeV with the ATLAS detector*, *The European Physical Journal C* **81** (2021) 689, URL: <https://doi.org/10.1140/epjc/s10052-021-09402-3> (cit. on pp. 90, 91).
- [145] Matteo Cacciari and Gavin P. Salam, *Pileup subtraction using jet areas*, *Physics Letters B* **659** (2008) 119, ISSN: 0370-2693, URL: <https://www.sciencedirect.com/science/article/pii/S0370269307011094> (cit. on p. 91).
- [146] Matteo Cacciari, Gavin P Salam, and Gregory Soyez, *The catchment area of jets*, *Journal of High Energy Physics* **2008** (2008) 005, URL: <https://doi.org/10.1088%2F1126-6708%2F2008%2F04%2F005> (cit. on p. 91).
- [147] ATLAS Collaboration, *Performance of pile-up mitigation techniques for jets in pp collisions at $\sqrt{s} = 8$ TeV using the ATLAS detector*, *The European Physical Journal C* **76** (2016), URL: <https://doi.org/10.1140/2Fepjc%2Fs10052-016-4395-z> (cit. on p. 92).
- [148] Andreas Hoecker et al., *TMVA - Toolkit for Multivariate Data Analysis*, 2007, arXiv: physics/0703039 [physics.data-an] (cit. on p. 92).

- [149] ATLAS Collaboration, *Identification and rejection of pile-up jets at high pseudo-rapidity with the ATLAS detector*, *The European Physical Journal C* **77** (2017), URL: <https://doi.org/10.1140%2Fepjc%2Fs10052-017-5081-5> (cit. on p. 93).
- [150] *Measurement of the tau lepton reconstruction and identification performance in the ATLAS experiment using pp collisions at $\sqrt{s} = 13$ TeV*, tech. rep., CERN, 2017, URL: <https://cds.cern.ch/record/2261772> (cit. on p. 94).
- [151] *Reconstruction, Energy Calibration, and Identification of Hadronically Decaying Tau Leptons in the ATLAS Experiment for Run-2 of the LHC*, tech. rep., CERN, 2015, URL: <https://cds.cern.ch/record/2064383> (cit. on p. 94).
- [152] *Identification of hadronic tau lepton decays using neural networks in the ATLAS experiment*, tech. rep., CERN, 2019, URL: <https://cds.cern.ch/record/2688062> (cit. on p. 94).
- [153] ATLAS Collaboration, *Performance of missing transverse momentum reconstruction with the ATLAS detector using proton-proton collisions at $\sqrt{s} = 13$ TeV*, *The European Physical Journal C* **78** (2018), URL: <https://doi.org/10.1140%2Fepjc%2Fs10052-018-6288-9> (cit. on p. 94).
- [154] E_T^{miss} performance in the ATLAS detector using 2015-2016 LHC p-p collisions, tech. rep., CERN, 2018, URL: <https://cds.cern.ch/record/2625233> (cit. on p. 95).
- [155] ATLAS Collaboration, *The ATLAS Simulation Infrastructure*, *The European Physical Journal C* **70** (2010) 823, URL: <https://doi.org/10.1140%2Fepjc%2Fs10052-010-1429-9> (cit. on p. 95).
- [156] Marilena Bandieramonte, Joseph Boudreau, and Riccardo Maria Bianchi, *FullSimLight: ATLAS standalone Geant4 simulation*, tech. rep., CERN, 2020, URL: <https://cds.cern.ch/record/2712863> (cit. on p. 95).
- [157] S. Agostinelli et al., *Geant4—a simulation toolkit*, *Nuclear Instruments and Methods in Physics Research Section A: Accelerators, Spectrometers, Detectors and Associated Equipment* **506** (2003) 250, ISSN: 0168-9002, URL: <https://www.sciencedirect.com/science/article/pii/S0168900203013688> (cit. on p. 95).
- [158] O. Aberle et al., *High-Luminosity Large Hadron Collider (HL-LHC): Technical design report*, CERN Yellow Reports: Monographs, CERN, 2020, URL: <https://cds.cern.ch/record/2749422> (cit. on p. 97).

- [159] *ATLAS Phase-II Upgrade Scoping Document*, tech. rep., CERN, 2015, URL: <http://cds.cern.ch/record/2055248> (cit. on p. 97).
- [160] *Technical Design Report for the ATLAS Inner Tracker Pixel Detector*, tech. rep., CERN, 2017, URL: <http://cds.cern.ch/record/2285585> (cit. on pp. 97, 99, 102).
- [161] *Technical Design Report for the ATLAS Inner Tracker Strip Detector*, tech. rep., CERN, 2017, URL: <http://cds.cern.ch/record/2257755> (cit. on p. 97).
- [162] Nicolas Scharmberg, “Measurement of the production cross section of a Higgs boson in combination with two top quarks at the ATLAS experiment”, PhD thesis: Manchester U., University of Manchester, Manchester U., 2021 (cit. on p. 98).
- [163] *Expected tracking and related performance with the updated ATLAS Inner Tracker layout at the High-Luminosity LHC*, tech. rep., CERN, 2021, URL: <https://cds.cern.ch/record/2776651> (cit. on pp. 98, 99).
- [164] J. Pater et al., *Design Overview of Bare Local Supports for the ITk Pixel Outer Endcaps*, <https://edms.cern.ch/document/2632350>, ATLAS Project document No: AT2-IP-ER-0012, 2021 (cit. on pp. 100, 101).
- [165] Tim Jones, *Nearly Glue less IBL prototype*, https://indico.cern.ch/event/114520/contributions/1322917/attachments/47099/67736/Cocuring_of_Foam_and_Structures.pdf, ATLAS meeting, Upgrade for High Luminosity, Insertable B-layer (IBL), 2010 (cit. on p. 100).
- [166] F.C. Campbell, *Manufacturing Processes for Advanced Composites*, Elsevier Science, 2003, ISBN: 9780080510989, URL: <https://books.google.co.uk/books?id=VkX5NXymelEC> (cit. on p. 100).
- [167] *Hysol EA 9396 AERO*, Technical Data Sheet, URL: https://www.henkel-adhesives.com/vn/en/product/adhesives/loctite_ea_9396_aero.html (cit. on p. 100).
- [168] Lin, Fang-Ming, *Heat Transfer Interface to Graphitic Foam. Master’s Theses. 4942*, https://scholarworks.sjsu.edu/etd_theses/4942, 2018 (cit. on p. 100).

- [169] G. Lindström, M. Moll, and E. Fretwurst, *Radiation hardness of silicon detectors – a challenge from high-energy physics*, *Nuclear Instruments and Methods in Physics Research Section A: Accelerators, Spectrometers, Detectors and Associated Equipment* **426** (1999) 1, ISSN: 0168-9002, URL: <https://www.sciencedirect.com/science/article/pii/S0168900298014624> (cit. on p. 101).
- [170] Graham Beck and Georg Viehhauser, *Analytic model of thermal runaway in silicon detectors*, *Nuclear Instruments and Methods in Physics Research Section A: Accelerators, Spectrometers, Detectors and Associated Equipment* **618** (2010) 131, ISSN: 0168-9002, URL: <https://www.sciencedirect.com/science/article/pii/S0168900210005498> (cit. on p. 102).
- [171] J. Pater et al., *ITK Pixel Local Support Design Specifications*, <https://edms.cern.ch/document/1534572>, ATLAS Project document No: AT2-IP-EN-0017, 2021 (cit. on p. 102).
- [172] *FLIR SC7000 Series - datasheet*, FLIR Systems, Inc., URL: https://www.flirmedia.com/MMC/THG/Brochures/RND_017/RND_017_US.pdf (cit. on p. 103).
- [173] *Dynamic climate chambers for rapid temperature changes with extended low temperature range. Model MKT 720*, Binder GmbH, URL: <https://www.binder-world.com/en/products/dynamic-climate-chambers/series-mkt/mkt-720> (cit. on p. 104).
- [174] *Datasheet Evaluation Kit EK-H4*, SENSIRION the sensor company, URL: <https://www.sensirion.com/en/environmental-sensors/humidity-sensors/evaluation-kit-ek-h4/> (cit. on p. 104).
- [175] Arcus Technology, URL: <https://www.arcus-technology.com> (cit. on p. 104).
- [176] *Instruction Manual Circulator C10 including all Baths*, Thermo Haake, URL: https://archive-resources.coleparmer.com/Manual_pdfs/12206-00,-05.pdf (cit. on p. 104).
- [177] Inc. Thorlabs, URL: <https://www.thorlabs.com/thorproduct.cfm?partnumber=BK5> (cit. on p. 105).
- [178] <https://docs.python.org/3/>, Python 3.X official documentation (cit. on p. 105).

- [179] Stéfan van der Walt et al., *scikit-image: image processing in Python*, *PeerJ* **2** (2014) e453, ISSN: 2167-8359, URL: <http://dx.doi.org/10.7717/peerj.453> (cit. on p. 106).
- [180] J. Canny, *A Computational Approach to Edge Detection*, *IEEE Transactions on Pattern Analysis and Machine Intelligence* **PAMI-8** (1986) 679, ISSN: 0162-8828 (cit. on p. 106).
- [181] N. Otsu, *A Threshold Selection Method from Gray-Level Histograms*, *IEEE Transactions on Systems, Man, and Cybernetics* **9** (1979) 62, ISSN: 2168-2909 (cit. on p. 106).
- [182] Martin A. Fischler and Robert C. Bolles, *Random Sample Consensus: A Paradigm for Model Fitting with Applications to Image Analysis and Automated Cartography*, *Commun. ACM* **24** (1981) 381, ISSN: 0001-0782, URL: <https://doi.acm.org/10.1145/358669.358692> (cit. on p. 106).
- [183] Abhishek Sharmaa and Carlos Solansb, “Voltage to Temperature ReadOut INstrument”, manual, 2017 (cit. on p. 121).
- [184] URL: <https://store.arduino.cc/arduino-mega-2560-rev3> (cit. on p. 121).
- [185] MARTA (Monoblock Approach for a Refrigeration Technical Application), <https://icp.mech.pk.edu.pl/martaco2/index.php/2-uncategorised/1-overall-features> (cit. on p. 121).
- [186] J. Pater et al., *Allcomp Foam for the ITk Pixel Local Supports*, <https://edms.cern.ch/document/2390267>, ATLAS Project document No: AT2-IP-EN-0017, 2020 (cit. on p. 123).
- [187] Quake Y. Qin, *TFM measurements of the end-cap L3 half-ring prototypes*, https://indico.cern.ch/event/964939/contributions/4060686/attachments/2121827/3571464/2020_09_28_TFMupdate.pdf, ATLAS meeting, ITk Pixel endcap mechanics, 2020 (cit. on p. 123).
- [188] Quake Y. Qin, *TFM measurements of the end-cap half-ring prototype L2.1*, https://indico.cern.ch/event/1062679/contributions/4466140/attachments/2290912/3895021/2021_08_02_TFMupdate.pdf, ATLAS meeting, ITk Pixel endcap mechanics, 2021 (cit. on p. 124).
- [189] O. J. P. Éboli and M. C. Gonzalez–Garcia, *Classifying the bosonic quartic couplings*, *Physical Review D* **93** (2016), URL: <https://doi.org/10.1103/PhysRevD.93.093013> (cit. on pp. 128, 180).

- [190] O. J. P. Éboli, M. C. Gonzalez-Garcia, and J. K. Mizukoshi, $pp \rightarrow jje^{\pm}\mu^{\pm}\nu\nu$ and $jje^{\pm}\mu^{\mp}\nu\nu$ at $\mathcal{O}(\alpha_{\text{em}}^6)$ and $\mathcal{O}(\alpha_{\text{em}}^4\alpha_s^2)$ for the study of the quartic electroweak gauge boson vertex at CERN LHC, *Phys. Rev. D* **74** (7 2006) 073005, URL: <https://link.aps.org/doi/10.1103/PhysRevD.74.073005> (cit. on p. 128).
- [191] R. Bellan et al., *A sensitivity study of VBS and diboson WW to dimension-6 EFT operators at the LHC*, *Journal of High Energy Physics* **2022** (2022), URL: [https://doi.org/10.1007/JHEP05\(2022\)29039](https://doi.org/10.1007/JHEP05(2022)29039) (cit. on p. 128).
- [192] Raquel Gomez-Ambrosio, *Studies of dimension-six EFT effects in vector boson scattering*, *The European Physical Journal C* **79** (2019), URL: <https://doi.org/10.1140/EPJC%2Fs10052-019-6893-2> (cit. on p. 128).
- [193] Benjamin W. Lee, C. Quigg, and H. B. Thacker, *Strength of Weak Interactions at Very High Energies and the Higgs Boson Mass*, *Phys. Rev. Lett.* **38** (16 1977) 883, URL: <https://link.aps.org/doi/10.1103/PhysRevLett.38.883> (cit. on p. 128).
- [194] ATLAS Collaboration, *Measurement of electroweak $Z(\nu\bar{\nu})\gamma jj$ production and limits on anomalous quartic gauge couplings in pp collisions at $\sqrt{s} = 13$ TeV with the ATLAS detector*, 2022, arXiv: 2208.12741 [hep-ex] (cit. on p. 128).
- [195] ATLAS Collaboration, *Evidence for electroweak production of two jets in association with a $Z\gamma$ pair in pp collisions at $\sqrt{s} = 13$ TeV with the ATLAS detector*, *Physics Letters B* **803** (2020) 135341, URL: <https://doi.org/10.1016/J.physletb.2020.135341> (cit. on p. 128).
- [196] ATLAS Collaboration, *Observation of electroweak production of a same-sign W boson pair in association with two jets in pp collisions at $\sqrt{s} = 13$ TeV with the ATLAS detector*, *Physical Review Letters* **123** (2019), URL: <https://doi.org/10.1103/PhysRevLett.123.161801> (cit. on p. 128).
- [197] ATLAS Collaboration, *Observation of electroweak $W^{\pm}Z$ boson pair production in association with two jets in pp collisions at $\sqrt{s} = 13$ TeV with the ATLAS detector*, *Physics Letters B* **793** (2019) 469, URL: <https://doi.org/10.1016/J.physletb.2019.05.012> (cit. on p. 128).
- [198] ATLAS Collaboration, *Measurements of differential cross-sections in four-lepton events in 13 TeV proton-proton collisions with the ATLAS detector*, *JHEP* **07** (2021) 005, arXiv: 2103.01918 [hep-ex] (cit. on pp. 128, 129, 133, 137, 146, 181, 183).

- [199] ATLAS Collaboration, *Observation of electroweak production of two jets and a Z-boson pair*, *Nature Physics* (2023), eprint: 2004.10612, URL: <https://doi.org/10.1038%2Fs41567-022-01757-y> (cit. on pp. 129, 137, 139, 179).
- [200] CMS Collaboration, *Evidence for electroweak production of four charged leptons and two jets in proton-proton collisions at $\sqrt{s} = 13$ TeV*, *Physics Letters B* **812** (2021) 135992, URL: <https://doi.org/10.1016%2Fj.physletb.2020.135992> (cit. on pp. 129, 179, 183).
- [201] ATLAS Collaboration, *Performance of the ATLAS Trigger System in 2015*, *Eur. Phys. J. C* **77** (2017) 317, arXiv: 1611.09661, URL: <https://cds.cern.ch/record/2235584> (cit. on p. 130).
- [202] ATLAS Collaboration, *Performance of electron and photon triggers in ATLAS during LHC Run 2*, *The European Physical Journal C* **80** (2020), URL: <https://doi.org/10.1140%2Fepjc%2Fs10052-019-7500-2> (cit. on p. 130).
- [203] ATLAS Collaboration, *Performance of the ATLAS muon triggers in Run 2*, *Journal of Instrumentation* **15** (2020) P09015, URL: <https://doi.org/10.1088%2F1748-0221%2F15%2F09%2Fp09015> (cit. on p. 130).
- [204] William Buttinger, *Using Event Weights to account for differences in Instantaneous Luminosity and Trigger Prescale in Monte Carlo and Data*, tech. rep., CERN, 2015, URL: <https://cds.cern.ch/record/2014726> (cit. on p. 130).
- [205] Stefan Höche, Frank Krauss, Marek Schönherr, and Frank Siegert, *A critical appraisal of NLO+PS matching methods*, *JHEP* **09** (2012) 049, arXiv: 1111.1220 [hep-ph] (cit. on p. 132).
- [206] ATLAS Pythia 8 tunes to 7 TeV data, tech. rep., CERN, 2014, URL: <https://cds.cern.ch/record/1966419> (cit. on p. 133).
- [207] D. J. Lange, *The EvtGen particle decay simulation package*, *Nucl. Instrum. Meth. A* **462** (2001) 152 (cit. on p. 133).
- [208] F. Cascioli et al., *Precise Higgs-background predictions: merging NLO QCD and squared quark-loop corrections to four-lepton + 0,1 jet production*, *Journal of High Energy Physics* **2014** (2014), URL: <https://doi.org/10.1007%2Fjhep01%282014%29046> (cit. on p. 133).

- [209] ATLAS Collaboration, *Measurement of the four-lepton invariant mass spectrum in 13 TeV proton-proton collisions with the ATLAS detector*, *Journal of High Energy Physics* **2019** (2019), URL: <https://doi.org/10.1007%2Fjhep04%282019%29048> (cit. on p. 133).
- [210] Fabrizio Caola, Kirill Melnikov, Raoul Röntsch, and Lorenzo Tancredi, *QCD corrections to ZZ production in gluon fusion at the LHC*, *Physical Review D* **92** (2015), URL: <https://doi.org/10.1103%2Fphysrevd.92.094028> (cit. on p. 133).
- [211] Fabrizio Caola, Matthew Dowling, Kirill Melnikov, Raoul Röntsch, and Lorenzo Tancredi, *QCD corrections to vector boson pair production in gluon fusion including interference effects with off-shell Higgs at the LHC*, *Journal of High Energy Physics* **2016** (2016), URL: <https://doi.org/10.1007%2Fjhep07%282016%29087> (cit. on p. 133).
- [212] Giampiero Passarino, *Higgs CAT*, *The European Physical Journal C* **74** (2014), URL: <https://doi.org/10.1140%2Fepjc%2Fs10052-014-2866-7> (cit. on p. 133).
- [213] CERN, *CERN Yellow Reports: Monographs, Vol 2 (2017): Handbook of LHC Higgs cross sections: 4. Deciphering the nature of the Higgs sector*, en, 2017, URL: <https://e-publishing.cern.ch/index.php/CYRM/issue/view/32> (cit. on p. 133).
- [214] ATLAS Collaboration, *Measurement of the $t\bar{t}Z$ and $t\bar{t}W$ cross sections in proton-proton collisions at $\sqrt{s} = 13$ TeV with the ATLAS detector*, *Phys. Rev. D* **99** (2019) 072009, arXiv: 1901.03584 [hep-ex] (cit. on pp. 134, 171).
- [215] ATLAS Collaboration, *Evidence for the production of three massive vector bosons with the ATLAS detector*, *Phys. Lett. B* **798** (2019) 134913, arXiv: 1903.10415 [hep-ex] (cit. on pp. 134, 171).
- [216] Charalampos Anastasiou, Lance Dixon, Kirill Melnikov, and Frank Petriello, *High-precision QCD at hadron colliders: Electroweak gauge boson rapidity distributions at next-to-next-to leading order*, *Phys. Rev. D* **69** (2004) 094008, arXiv: hep-ph/0312266 (cit. on p. 135).
- [217] ATLAS Collaboration, *Studies on top-quark Monte Carlo modelling for Top2016*, ATL-PHYS-PUB-2016-020, 2016, URL: <https://cds.cern.ch/record/2216168> (cit. on p. 135).

- [218] Richard D. Ball et al., *Parton distributions with LHC data*, *Nucl. Phys. B* **867** (2013) 244, arXiv: 1207.1303 [hep-ph] (cit. on p. 135).
- [219] D. Rainwater, R. Szalapski, and D. Zeppenfeld, *Probing color-singlet exchange in $Z + 2$ -jet events at the CERN LHC*, *Phys. Rev. D* **54** (11 1996) 6680, URL: <https://link.aps.org/doi/10.1103/PhysRevD.54.6680> (cit. on p. 141).
- [220] V. Hankele, G. Klmke, D. Zeppenfeld, and T. Figy, *Anomalous Higgs boson couplings in vector boson fusion at the CERN LHC*, *Physical Review D* **74** (2006), URL: <https://doi.org/10.1103/PhysRevD.74.095001> (cit. on p. 142).
- [221] *Tools for estimating fake/non-prompt lepton backgrounds with the ATLAS detector at the LHC*, (2022), arXiv: 2211.16178 [hep-ex] (cit. on p. 146).
- [222] ATLAS Collaboration, *ATLAS b -jet identification performance and efficiency measurement with $t\bar{t}$ events in pp collisions at $\sqrt{s} = 13$ TeV*, *The European Physical Journal C* **79** (2019), URL: <https://doi.org/10.1140/epjc%2Fs10052-019-7450-8> (cit. on p. 148).
- [223] Volker Blobel, *Unfolding methods in high-energy physics experiments*, (1985), URL: <https://cds.cern.ch/record/157405> (cit. on p. 152).
- [224] Glen Cowan, *Statistical Data Analysis*, en, Oxford science publications, Clarendon Press, 1998 (cit. on p. 153).
- [225] Per Christian Hansen, *The Discrete Picard Condition for Discrete Ill-Posed Problems*, *BIT* **30** (1990) 658, ISSN: 0006-3835, URL: <https://doi.org/10.1007/BF01933214> (cit. on p. 153).
- [226] Lydia Brenner et al., *Comparison of unfolding methods using RooFitUnfold*, 2020, arXiv: 1910.14654 [physics.data-an] (cit. on pp. 154, 155).
- [227] Volker Blobel, *Unfolding Methods in Particle Physics*, (2011) 240, URL: <https://cds.cern.ch/record/2203257> (cit. on p. 154).
- [228] G. Cowan, *A survey of unfolding methods for particle physics*, *Conf. Proc. C* **0203181** (2002) 248, ed. by M. R. Whalley and L. Lyons (cit. on p. 154).
- [229] Francesco Spano, *Unfolding in particle physics: a window on solving inverse problems*, *EPJ Web Conf.* **55** (2013) 03002, ed. by T. Delemontex and Arnaud Lucotte (cit. on p. 154).

- [230] Andreas Höcker and Vakhtang Kartvelishvili, *SVD approach to data unfolding*, [Nuclear Instruments and Methods in Physics Research Section A: Accelerators, Spectrometers, Detectors and Associated Equipment](#) **372** (1996) 469, URL: <https://doi.org/10.1016%2F0168-9002%2895%2901478-0> (cit. on p. 154).
- [231] S Schmitt, *TUnfold, an algorithm for correcting migration effects in high energy physics*, [Journal of Instrumentation](#) **7** (2012) T10003, URL: <https://doi.org/10.1088%2F1748-0221%2F7%2F10%2Ft10003> (cit. on p. 154).
- [232] Bogdan Malaescu, *An iterative, dynamically stabilized method of data unfolding*, 2009, arXiv: 0907.3791 [[physics.data-an](#)] (cit. on p. 154).
- [233] G. D'Agostini, *A multidimensional unfolding method based on Bayes' theorem*, [Nuclear Instruments and Methods in Physics Research Section A: Accelerators, Spectrometers, Detectors and Associated Equipment](#) **362** (1995) 487, ISSN: 0168-9002, URL: <https://www.sciencedirect.com/science/article/pii/016890029500274X> (cit. on pp. 154, 155).
- [234] *Proposal for particle-level object and observable definitions for use in physics measurements at the LHC*, tech. rep., CERN, 2015, URL: <https://cds.cern.ch/record/2022743> (cit. on p. 154).
- [235] G. D'Agostini, *Improved iterative Bayesian unfolding*, 2010, arXiv: 1010.0632 [[physics.data-an](#)] (cit. on p. 155).
- [236] *RooUnfold*, <https://gitlab.cern.ch/RooUnfold/RooUnfold> (cit. on p. 155).
- [237] Rene Brun and Fons Rademakers, *ROOT — An object oriented data analysis framework*, [Nuclear Instruments and Methods in Physics Research Section A: Accelerators, Spectrometers, Detectors and Associated Equipment](#) **389** (1997) 81, *New Computing Techniques in Physics Research V*, ISSN: 0168-9002, URL: <https://www.sciencedirect.com/science/article/pii/S016890029700048X> (cit. on p. 155).
- [238] L. B. Lucy, *An iterative technique for the rectification of observed distributions*, [The Astronomical Journal](#) **79** (1974) 745 (cit. on p. 155).
- [239] William Hadley Richardson, *Bayesian-Based Iterative Method of Image Restoration*, [J. Opt. Soc. Am.](#) **62** (1972) 55, URL: <https://opg.optica.org/abstract.cfm?URI=josa-62-1-55> (cit. on p. 155).

- [240] J H Friedman, *A variable span smoother*, tech. rep., SLAC, 1984, URL: <https://cds.cern.ch/record/155846> (cit. on p. 160).
- [241] *Evaluating statistical uncertainties and correlations using the bootstrap method*, tech. rep., CERN, 2021, URL: <https://cds.cern.ch/record/2759945> (cit. on p. 166).
- [242] ATLAS Collaboration, *Athena*, URL: <https://doi.org/10.5281/zenodo.2641996> (cit. on p. 172).
- [243] B. Grzadkowski, M. Iskrzyński, M. Misiak, and J. Rosiek, *Dimension-six terms in the Standard Model Lagrangian*, *Journal of High Energy Physics* **2010** (2010), URL: <https://doi.org/10.1007%2Fjhep10%282010%29085> (cit. on p. 180).
- [244] Ilaria Brivio, Yun Jiang, and Michael Trott, *The SMEFTsim package, theory and tools*, *Journal of High Energy Physics* **2017** (2017), URL: <https://doi.org/10.1007%2Fjhep12%282017%29070> (cit. on p. 180).
- [245] Christian Bierlich et al., *Robust Independent Validation of Experiment and Theory: Rivet version 3*, *SciPost Physics* **8** (2020), URL: <https://doi.org/10.21468%2Fscipostphys.8.2.026> (cit. on p. 180).
- [246] Gary J. Feldman and Robert D. Cousins, *Unified approach to the classical statistical analysis of small signals*, *Physical Review D* **57** (1998) 3873, URL: <https://doi.org/10.1103%2Fphysrevd.57.3873> (cit. on p. 181).
- [247] ATLAS Collaboration, *Differential cross-section measurements for the electroweak production of dijets in association with a Z boson in proton–proton collisions at ATLAS*, *The European Physical Journal C* **81** (2021) 163, URL: <https://doi.org/10.1140/epjc/s10052-020-08734-w> (cit. on pp. 181, 183).
- [248] S. S. Wilks, *The Large-Sample Distribution of the Likelihood Ratio for Testing Composite Hypotheses*, *The Annals of Mathematical Statistics* **9** (1938) 60, URL: <https://doi.org/10.1214/aoms/1177732360> (cit. on p. 182).
- [249] ATLAS Collaboration, *Measurement of fiducial and differential W^+W^- production cross-sections at $\sqrt{s} = 13$ TeV with the ATLAS detector*, *The European Physical Journal C* **79** (2019), URL: <https://doi.org/10.1140%2Fepjc%2Fs10052-019-7371-6> (cit. on p. 183).

- [250] ATLAS collaboration, *Measurements of $W^+W^- + \geq 1$ jet production cross-sections in pp collisions at $\sqrt{s} = 13$ TeV with the ATLAS detector*, [JHEP 06 \(2021\) 003](#), arXiv: [2103.10319 \[hep-ex\]](#) (cit. on p. 183).
- [251] CMS Collaboration, *Measurement of the inclusive and differential WZ production cross sections, polarization angles, and triple gauge couplings in pp collisions at $\sqrt{s} = 13$ TeV*, [Journal of High Energy Physics 2022 \(2022\)](#), URL: <https://doi.org/10.1007%2Fjhep07%282022%29032> (cit. on p. 183).
- [252] CMS Collaboration, *Measurement of $W^\pm\gamma$ differential cross sections in proton-proton collisions at $\sqrt{s} = 13$ TeV and effective field theory constraints*, [Phys. Rev. D 105 \(5 2022\) 052003](#), URL: <https://link.aps.org/doi/10.1103/PhysRevD.105.052003> (cit. on p. 183).